Water and Carbon Dioxide in Basaltic Magmas

Thesis by

Jacqueline Eaby Dixon

In Partial Fulfillment of the Requirements

for the Degree of

Doctor of Philosophy

California Institute of Technology

Pasadena, California

1992

(Submitted February 3, 1992)

Acknowledgements

I would like to thank all the members of my committee for their guidance and support. I am especially grateful to Ed Stolper, who provided clear vision and an example of the highest scientific integrity. Ed has taught me that "good enough" really isn't good enough, and this is a better thesis for it. In addition to providing an academic standard to which I will always aspire, Ed was extremely supportive of my decision to initiate the big experiment and start a family. John Holloway taught me the tricks of the experimental trade, and more importantly, the joy of experimenting; for this I will always be grateful. George Rossman was a continual source of enlightenment on the vagaries of FTIR instrumentation and the rigors of data analysis. Don Burnett got me started doing experiments at Caltech, and has always encouraged me. Peter Wyllie kindly shared his time and ideas on the mantle beneath Hawaii. Dave Clague kindled my interest in igneous petrology in general and Hawaii in particular, and has remained a valued friend and colleague during the long incubation of this thesis.

The experimental portion of this thesis was carried out at Arizona State University. Experiments originally planned to take 3 months ended up taking three years, causing me to impose on the hospitality of many people at ASU. In particular, Tracy Paul provided a home away from home, including nourishing meals while I was pregnant. I am especially grateful to David Joyce for keeping my spirits up at a time when Murphy's Law was controlling my experiments. David Joyce, Tom Stanton, Gordon Moore, Hanna Nevaskil, Gisli Gimundsson, Tracy Paul, Jeff Roberts, Vivian Pan, and Alison Pawley provided invaluable assistance in the lab. I will always value them as colleagues and friends.

At Caltech, I am indebted to Paula Rosener, Sieger Van der Laan, John Beckett, Mike Carroll, Greg Miller, Mary Johnson, Astrid Howard, Mike Baker, Sally Newman, and Phil Ihinger for their advice and help in the lab. I especially thank Phil Ihinger, David Bell, David Pyle, Sally Newman, Laurie Watson, and Jen Blank for their assistance, support, and many stimulating discussions. I consider myself extremely fortunate to have

shared my many years at Caltech with an exceptional group of classmates, including David Bell, Joel Blum, Yigal Erel, Diane Knott, Wei Lu, Sally McGill, Charlie Rubin, Phil Shaller, Jack Sheng, and Mike Wolf.

Last but not least, I would like to thank my family for their support. My mother is largely responsible for inspiring me on to higher education, though she never dreamed it would take this long. My stepsons, Robert and Alex, helped polish samples and kept their father busy while I was working late. My son, Ian, has given my life a sense of balance and joy and forced me to "keep it all in perspective". And finally, I would like to thank my husband, Tim, without whose constant encouragement this thesis could never have been completed.

Abstract

Experiments were conducted in which basaltic melts were equilibrated with a vapor phase consisting of pure water, pure carbon dioxide, and water-carbon dioxide mixtures at 1200°C and 200 to 980 bars in order to develop a basis for interpreting the behavior of these volatiles during the evolution and degassing of submarine magmas. Molar absorptivities for the 4500 cm^{-1} band for hydroxyl groups and for the 5230 and 1630 cm^{-1} bands of molecular water were calibrated to be 0.67 ± 0.04, 0.62 ± 0.08, and 25 ± 3 l/mole-cm, respectively. The solubility of water in MORB liquid was determined from the experiments in which MORB melt was equilibrated with pure H_2O vapor. Results are in agreement with the higher-pressure results of Hamilton et al. (1964) on Columbia River basalt. Trends observed in the concentrations of molecular water and hydroxyl groups with respect to total water concentration in the quenched, experimental, basaltic glasses are similar to those observed in albitic glasses (Silver and Stolper, 1989). Moreover, the concentration of molecular water measured in the quenched basaltic glasses is approximately proportional to water fugacity in all samples regardless of the composition of the vapor (X_{CO_2}), demonstrating that molecular water solubility in basaltic melts is closely approximated by Henry's law at pressures less than 1 kbar. Total water concentrations and the speciation of water in vapor-saturated basaltic melt are fit by a regular ternary solution model with the coefficients for albitic glasses (Silver and Stolper, 1989), where the activity of water in the melt is given by Henry's law for molecular water. At pressures higher than about 1 kbar, the effect of the molar volume of water in the melt ($V^{0,m}_{H_2O}$) on the activity of water in vapor-saturated melts is no longer negligible; a ($V^{0,m}_{H_2O}$) of ~12 cm^3/mole fits the data of Hamilton et al. (1964).

Concentrations of CO_2 dissolved as carbonate in the experimental glasses range from 63 to 315 ppm CO_2. Carbonate was the only species of dissolved carbon observed. The mole fraction of CO_2 in the vapor varied from 0.39 to 0.93. Concentrations of CO_2

dissolved as carbonate in the melt for all the experiments are proportional to f_{CO_2}. The data for pure CO_2-saturated and mixed H_2O-CO_2-saturated experiments are fit with a straight line through the origin with a slope of 40 ppm/100 bar f_{CO_2} (equivalent to 47 ppm/km water depth). These results suggest Henrian behavior for CO_2; that is, the solubility of CO_2 in the basaltic melt is essentially proportional to the fugacity of CO_2, with the same constant of proportionality, whether the vapor contains pure CO_2 or H_2O+CO_2. These results do not support the widely held view that water enhances the solubility of carbon dioxide in basaltic melts.

Results of degassing calculations show that the vapor phase in equilibrium with MORB magmas at typical midoceanic eruption depths is CO_2-rich and that the dissolved CO_2 contents should vary linearly with depth of eruption. Basaltic magmas containing <1.0 wt.% H_2O will not degas significant quantities of water until pressures <100 bars are reached. As water contents increase, either through fractional crystallization or variations in the initial water contents, an inverse correlation is predicted between dissolved CO_2 and H_2O contents in melts saturated with a mixed H_2O-CO_2 vapor phase. These predictions were tested by examining the water and carbon dioxide concentrations in suites of basaltic glasses from the Juan de Fuca Ridge and Hawaii.

Concentrations of dissolved H_2O and CO_2 were measured in a suite of basaltic glasses from the Juan de Fuca Ridge. CO_2 contents dissolved as carbonate range from about 45 to 360 ppm by weight. In contrast to the predictions based on vapor-saturated degassing, samples erupted at a given depth exhibit a large range in dissolved CO_2 contents that we interpret to be the result of variable amounts of degassing. The lowest CO_2 contents at each depth are in reasonable agreement with the experimentally determined CO_2 solubility curve for basalt at low pressures. All glasses with CO_2 values higher than the experimentally determined solubility at the eruption depth are oversaturated because of incomplete degassing. The highest CO_2 contents are spatially associated with the local topographic highs for each ridge segment. Lavas from relatively deep areas may have had

greater opportunity to degas during ascent from a relatively deeper magma chamber or during lateral flow in dikes or seafloor lava flows. The highest observed CO_2 concentrations are from the axial seamount and lead to an estimate of a minimum depth to the magma chamber of 2.7 kilometers beneath the ridge axis. Water contents were not modified during degassing and were found to behave incompatibly during partial melting and crystal fractionation. Variations in ratios of water to other incompatible elements suggest that water has a bulk partition coefficient similar to La during partial melting (D~0.010).

Major, minor, and dissolved volatile element concentrations were measured in tholeiitic glasses from the submarine portion (Puna Ridge) of the east rift zone of Kilauea Volcano, Hawaii. Dissolved H_2O and S concentrations display a wide range relative to nonvolatile incompatible elements at all depths. This range cannot be readily explained by fractional crystallization, degassing of H_2O and S during eruption on the seafloor, or source region heterogeneities. Dissolved CO_2 concentrations, in contrast, show a positive correlation with eruption depth and typically agree within error with the solubility at that depth. Magmas along the Puna Ridge can be modelled as resulting from (1) mixing of a relatively volatile-rich, undegassed component with magmas that experienced low pressure (perhaps subaerial) degassing during which substantial H_2O, S, and CO_2 were lost, followed by (2) fractional crystallization of olivine, clinopyroxene, and plagioclase from this mixture to generate a residual liquid; and (3) further degassing, principally of CO_2 for samples erupted deeper than 1000 m, during eruption on the seafloor. The degassed end member may form at upper levels of the summit magma chamber (assuming less than lithostatic pressure gradients), during residence at shallow levels in the crust, or during sustained summit eruptions. The final phase of degassing during eruption on the seafloor occurs slowly enough to achieve melt/vapor equilibrium during exsolution of the typically CO_2-rich vapor phase. According to the model, an average Kilauean primary magma with 16.0 % MgO should contain ~0.47 wt. % H_2O and ~900 ppm S. The model predicts that

submarine lavas from wholly submarine volcanoes (i.e., Loihi), for which there is no opportunity to generate the degassed end member by low pressure degassing, will be enriched in volatiles relative to those from volcanoes whose summits have breached the sea surface (i.e., Kilauea and Mauna Loa).

Table of Contents:

Introduction

This thesis was undertaken to characterize the behavior of water and carbon dioxide in submarine basaltic glasses. First, I conducted an experimental study of solubilities of water and carbon dioxide in basaltic melts in order to develop a basis for interpreting the behavior of these volatiles during the evolution and degassing of submarine magmas. Second, I measured the water and carbon dioxide concentrations in suites of basaltic glasses from several tectonic environments using infrared spectroscopy. Variations in these data were modelled in terms of degassing, crystal fractionation, partial melting, and source region heterogeneity. The thesis is written as three separate papers (Chapters 1-3) and three appendices. Each paper appears here with separate abstracts, introductions and bibliographies. Variations in style among the manuscripts are a function of the format of the journal to which they were submitted.

In Chapter 1, to be submitted to Contributions to Mineralogy and Petrology, I report results of experiments in which basaltic melts were equilibrated with a vapor phase consisting of pure water, pure carbon dioxide, and water-carbon dioxide mixtures at 1200°C and 200 to 980 bars. Water solubility at these pressures was found to be consistent with previous studies at higher pressures. The solubilities of molecular water and carbon dioxide were found to obey Henry's law, such that the amount of each species dissolved in the melt is simply proportional to the fugacity of that species in the vapor. The solubility of CO_2 was not higher in hydrous melts than anhydrous melts, in contrast to the results of previous studies at much higher pressures. Results of degassing calculations, described in Appendix 3, show that the vapor phase in equilibrium with MORB magmas at typical midoceanic eruption depths is CO_2-rich and that the dissolved CO_2 contents should vary linearly with depth of eruption (pressure). Basaltic magmas containing <1.0 wt.% H_2O will not degas significant quantities of water until pressures <100 bars are reached. As water contents increase, either through fractional crystallization or variations in the initial water contents, an inverse correlation is predicted between dissolved CO_2 and H_2O

contents. These predictions will be tested by examining the water and carbon dioxide concentrations in suites of basaltic glasses from the Juan de Fuca Ridge (Chapter 2) and Hawaii (Chapter 3).

In Chapter 2, published in Earth and Planetary Science Letters (v. 90, 87-104, 1988), concentrations of dissolved H_2O and CO_2 were measured in a suite of basaltic glasses from the Juan de Fuca Ridge. This study was significant because it marked the first time that the variation in water and carbon dioxide was examined in detail in a geochemically and tectonically well constrained suite of samples from a single rift environment. A large range in CO_2 contents was observed in samples erupted at similar depths and was interpreted to be the result of variable amounts of degassing. These data showed the importance of understanding the kinetics of degassing in modelling the chemistry of volatile species in these glasses. Because the solubility of water is much higher than that of carbon dioxide in basalt, and because the concentrations of water in MORB are low, water contents were not modified during degassing and were found to behave incompatibly during partial melting and crystal fractionation. Variations in ratios of water to other incompatible elements suggest that water has a bulk partition coefficient similar to La during partial melting (D~0.010).

One way of further testing the influence of eruption kinetics on volatile species chemistry in basaltic magmas is to investigate nonridge environments, where we might expect much slower eruption rates. In Chapter 3, published in Journal of Geology (v. 99, 371-394, 1991), the concentrations of major and minor elements, water, sulfur, and carbon dioxide in a suite of samples from the submarine portion of the Kilauea east rift zone are discussed. The major and minor element data, including sulfur, were generated by David Clague at the USGS. The concentrations of water and carbon dioxide were measured using infrared spectroscopy by myself at Caltech. In contrast to the MORB data, the CO_2 concentrations were found to be in equilibrium with the solubility of CO_2 in basalt for the depth of eruption, while water and sulfur showed a large range in values that could not be

explained by simple crystal-liquid fractionation processes or degassing during submarine eruption. A model was developed to explain the variations in major, minor, and volatile element geochemistry involving (1) mixing of a relatively volatile-rich, undegassed component with magmas that experienced low pressure degassing during which substantial H_2O, S, and CO_2 were lost, followed by (2) fractional crystallization of olivine, clinopyroxene, and plagioclase from this mixture to generate a residual liquid; and (3) further degassing, principally of CO_2 for samples erupted deeper than 1000 m, during eruption on the seafloor. This study shows that the degassing history of magmas erupted from volcanoes that have breached the sea surface (popped their tops), is much more complicated than those that are completely submarine.

Appendix 1 is a preprint of a manuscript in press in American Mineralogist on the development of the rapid-quench, internally heated pressure vessel with John Holloway as first author. Appendix 2 is a preprint of a paper describing the determination of the molar absorptivity for dissolved carbonate in basanitic glass, which will be submitted to American Mineralogist. Appendix 3 is a detailed description of the method used to determine degassing paths of basaltic magmas based on the thermodynamic development of H_2O and CO_2 solubilities described in Chapter 1.

Chapter 1

An experimental study of water and carbon dioxide in midoceanic ridge basalt

Abstract

A series of experiments were conducted to determine the solubilities of H_2O and CO_2 and the nature of their mixing behavior in basaltic liquid at pressures and temperature relevant to seafloor eruption. MORB liquid was saturated at 1200°C with pure H_2O at pressures of 176-717 bars and H_2O-CO_2 vapor at pressures up to 980 bars. Experiments were performed in conventional and rapid-quench, internally heated pressure vessels. Iron loss was controlled using foils of Pt-Fe alloy. Oxygen fugacity was controlled by using mixtures of Ar and H_2 as the pressurizing medium. Vapor compositions had X_{CO_2} ranging from 0 to 0.93. Concentrations and speciation of H_2O and CO_2 dissolved in the quenched glasses were measured using infrared spectroscopy. Molar absorptivities for the 4500 cm^{-1} band for hydroxyl groups and for the 5230 and 1630 cm^{-1} bands of molecular water were calibrated to be 0.67 ± 0.04, 0.62 ± 0.08, and 25 ± 3 l/mole-cm, respectively.

The solubility of water in MORB liquid was determined from the experiments in which MORB melt was equilibrated with pure H_2O vapor. Results are in agreement with the higher-pressure results of Hamilton et al. (1964) on Columbia River basalt. Trends observed in the concentrations of molecular water and hydroxyl groups with respect to total water concentration in the quenched, experimental basaltic glasses are similar to those observed in albitic glasses (Silver and Stolper, 1989). Moreover, the concentration of molecular water measured in the quenched basaltic glasses is approximately proportional to water fugacity in all samples regardless of the composition of the vapor (X_{CO_2}), demonstrating that molecular water solubility in basaltic melts is closely approximated by Henry's law at pressures less than 1 kbar. Total water concentrations and the speciation of water in vapor-saturated basaltic melt are fit by a regular ternary solution model with the coefficients for albitic glasses (Silver and Stolper, 1989), where the activity of water in the melt is given by Henry's law for molecular water. At pressures higher than about 1 kbar, the effect of the molar volume

of water in the melt ($V^{0,m}_{H_2O}$) on the activity of water in vapor-saturated melts is no longer negligible; a ($V^{0,m}_{H_2O}$) of ~12 cm^3/mole fits the data of Hamilton et al. (1964).

Concentrations of CO_2 dissolved as carbonate in the experimental glasses range from 63 to 315 ppm CO_2. Carbonate was the only species of dissolved carbon observed. The mole fraction of CO_2 in the vapor varied from 0.39 to 0.93. Concentrations of CO_2 dissolved as carbonate in the melt for all the experiments are proportional to f_{CO_2}. The data for pure CO_2-saturated and mixed H_2O-CO_2-saturated experiments are fit with a straight line through the origin with a slope of 40 ppm/100 bar f_{CO_2} (equivalent to 47 ppm/km water depth). These results suggest Henrian behavior for CO_2; that is, the solubility of CO_2 in the basaltic melt is essentially proportional to the fugacity of CO_2, with the same constant of proportionality, whether the vapor contains pure CO_2 or H_2O+CO_2. These results do not support the widely held view that water enhances the solubility of carbon dioxide in basaltic melts. Degassing processes in basaltic magmas rich in both water and carbon dioxide can be accurately modelled using these results in the end-member systems and the assumption of Henry's law.

1. Introduction

Magmas erupted subaerially solidify at a pressure of about 1 bar, but the pressure on submarine magmas depends on the water depth at which they erupt and may range from near 1 bar to several hundred bars. Even over this small range in pressure, the vesicularity of magma and the composition of gas in vesicles can change dramatically, reflecting the enormous differences in volume between vapor and melt, the large compressibility of the gas phase at these low pressures, and the differing solubilities of various gaseous species. The degassing of submarine magmas as they erupt at progressively shallower depths is largely responsible for the negative correlation between eruption depth and vesicularity of submarine magmas (e. g., Moore , 1965 , 1970 , 1979 ; Moore and Schilling, 1973). It also leads to changes in the composition of the vapor in the vesicles with depth (e.g., Moore, 1965, 1970; Gerlach, 1986) and might result in systematic changes in the oxidation state of iron in erupting magmas (e.g., Sato and Wright, 1966; Sato, 1978; Mathez, 1984; Carmichael and Ghiorso, 1986).

In view of the importance of the exsolution of a vapor phase from submarine magmas to understanding their vesicle contents, their eruptive histories, aspects of their chemistry (especially oxidation state), and the chemistry of the atmosphere and ocean (Des Marais, 1985), it is surprising how little is really known about the behavior of volatile components in these systems. Only recently has the solubility of carbon dioxide, the major degassing species in MORBs (Killingley and Muenow, 1975; Moore et al., 1977; Delaney et al., 1978; Jambon and Zimmermann, 1987) been measured in MORB melt by experiment (Stolper and Holloway, 1988; Mattey, 1991; Pan et al., 1991; Pawley and Holloway, 1991).

Although the solubility of water in MORB magmas is expected to be much greater than that of carbon dioxide under equivalent conditions, prior to this study there had been no measurements of the solubility of water in MORB systems, though some

work does exist on other basaltic compositions. Hamilton et al. (1964) measured the solubility of water in a Columbia River basaltic melt at 1-6 kbar, using several analytical techniques for bulk-water contents. There is also some Russian work on water solubility in basaltic melts at pressures between 1 and 3 kbar (Khitarov et al., 1959; Kadik et al., 1971), but the results differ in some ways from those of Hamilton et al. (1964). Also, the absence of speciation data in these previous studies prevented the development of a thermodynamic model for water solubility.

In the context of MORB petrogenesis, the concentration of water in basaltic liquids in equilibrium with pure water vapor is less important than the concentration of water in liquids in equilibrium with H_2O-CO_2 fluids, because the vapor that exsolves from MORBs on decompression contains both volatile components. Except at very low pressures (<50 bars based on Moore, 1970) or for magmas in which water is highly enriched (e.g., Byers et al., 1983, 1984), the vapor phase that exsolves from MORB magmas is predominantly carbon dioxide (Killingley and Muenow, 1975; Moore et al., 1977; Delaney et al., 1978; Jambon and Zimmermann, 1987). If both water and carbon dioxide solubility in the mixed volatile system can be approximated by Henry's law (where the activity of a species dissolved in the melt is proportional to its fugacity in the vapor) under the conditions of MORB genesis, then the behavior of the mixed volatile system can be understood simply with reference to the two end-member systems. Given the Henrian approximation and knowledge of the solubilities of CO_2 and H_2O in melts in the end-member systems, the degassing paths of magmas as they decompress can be readily calculated. Such calculations have been carried out by Shilobreyeva et al. (1983); Gerlach (1986); and Newman (1989, 1990) for basaltic systems and by Newman et al. (1988) for rhyolitic systems.

There have been reasons to suspect, however, that the Henrian approximation may be inaccurate, particularly at the CO_2-rich end of the system, where data at much higher pressures in other silicate-H_2O-CO_2 systems have indicated that the presence of

water enhances the solubility of carbon dioxide by as much as 50% (Holloway and Lewis, 1974; Mysen, 1976; Brey and Green, 1976; Eggler and Rosenhauer, 1978). The explanation offered for this is that addition of water depolymerizes the melt, thereby enhancing the solubility of carbon dioxide as carbonate. Kadik et al. (1972) reported mixed CO_2 and H_2O solubilities in basaltic melts at 1-3 kbar and did not report the expected effect of water on CO_2 solubility. Their experiments, however, did not extend to the CO_2-rich part of the system, and the CO_2 contents they reported are inconsistent with later studies (Stolper and Holloway, 1988).

I will show that the expected enhancement in CO_2 solubility does not occur in MORB at pressures relevant to eruption conditions over the range of vapor compositions investigated, and that both molecular water and carbon dioxide solubilities appear to follow Henry's law. These measurements provide a basis for interpreting the water and carbon contents of submarine magmas and for assessing the factors controlling the extent to which they degas on ascent and emplacement.

2. Experimental Techniques

Experiments were conducted by equilibrating basaltic melt with pure H_2O, pure CO_2, and mixed H_2O-CO_2 vapors at 1200°C at pressures between 200 and 980 bars in conventional and rapid-quench, internally heated pressure vessels. After quenching, the water and carbon dioxide contents dissolved in the basaltic glass were measured using infrared spectroscopy. Details of each run are given in Table 1.

2.1 Starting materials

Experiments were conducted on two starting materials, both Fe-rich basalt from the Juan de Fuca Ridge, chosen for their low liquidus temperatures (~1165°C). Compositions of the starting materials are listed with the compositions of the run products in Table 2. One composition (TT152-51-3) is the same starting material used

in the CO_2 solubility study of Stolper and Holloway (1988). Several grams of this composition were powdered, pressed into pellets, and held at 940°C for 14 hrs at 1 atm in a CO_2-CO gas mixture corresponding to the quartz-fayalite-magnetite (QFM) buffer. The pellet was repowdered, and the powder was stored in a dessicator. The other composition (TT152-51-3) was held at 900°C for 36 hrs in an H_2-CO_2 gas mix corresponding to the nickel-nickel oxide (Ni-NiO) buffer. Vapor compositions were produced by addition of water, oxalic acid dihydrate ($H_2C_2O_4 \cdot 2H_2O$), and silver oxalate ($Ag_2C_2O_4$). Powdered basalt (50 to 100 mg) and various combinations of water, oxalic acid dihydrate, or silver oxalate were loaded into Pt capsules (0.15" outside diameter Pt tubing) that were then sealed by arc welding.

2.2 Control of Fe-Loss

It has long been recognized that a major problem in high-temperature experiments on basaltic compositions is the loss of iron from the melt to the Pt container (see Grove, 1981 for a review). Reduction of iron as FeO in the melt results in production of an Fe-Pt alloy and liberation of excess O_2. The extent of iron loss is related to the oxidation state of the system in that O_2 is produced during the reaction, and the proportion of the total iron present as FeO varies as a function of oxygen fugacity. A higher oxidation state results in lower concentrations of Fe in the Fe-Pt alloy in equilibrium with the melt, and therefore less Fe will be lost from the melt. For example, the concentrations of Fe in alloys in equilibrium with a basalt containing 12.4 wt.% FeO* (total Fe as FeO) at 1200°C at the hematite-magnetite (HM), Ni-NiO, and QFM buffers are 0.16, 6.5, and 8.7 wt.%, respectively. Techniques used to control iron loss in these experiments are discussed below. Control of oxygen fugacity is discussed in the sections on conventional and rapid-quench, internally heated pressure vessels.

In the first approach, loss of Fe to the Pt capsule was minimized by use of a double-capsule technique. Outer capsules of pure platinum were lined with cylindrical

Pt-Fe alloy foils having activities of Fe calculated to be in equilibrium with the basalt at the run conditions (Grove, 1981; Van der Laan and Koster van Groos, 1991). The Pt-Fe alloy inserts were generated by electroplating Fe onto Pt-foils (0.002" thick) followed by annealing at high temperature (1450°C) in a reducing gas (f_{O_2} ~two log units below the iron-wustite (IW) buffer) to produce a homogeneous alloy. Unfortunately, the Pt-Fe alloy foils proved to be brittle, prone to breakage during capsule preparation, and they complicated the process of arc-welding the capsules.

The second approach to minimizing Fe loss involved the use of Pt capsules presaturated with Fe. Presaturation was performed by melting powdered TT152-21-35 in open Pt capsules at 1 atm at 1250°C in an H_2-CO_2 gas mix corresponding to QFM-1/2 (log units) for 14 hrs. After presaturation, the glass was dissolved out of the capsules by soaking in warm HF followed by dilute HCl. The major disadvantage to capsule presaturation was that the capsules became brittle and tended to rupture during quench.

A few runs were also performed in pure Pt capsules (without a Pt-Fe alloy insert or Fe-presaturation). These runs also cracked before or during quench similar to the Fe-presaturated capsules.

2.3 Conventional, Internally Heated Pressure Vessel (IHPV)

Several low pressure (200-300 bar) runs were conducted in a horizontal, internally heated gas-pressure vessel (Holloway, 1971). Ar gas was used as the pressurizing medium; pressures were monitored with a Bourdon tube gauge. Samples were heated with a single-wound Kanthal furnace. Temperatures were monitored with two chromel-alumel thermocouples bracketing the position of the capsule.

Experiments were brought up to the run conditions by first prefilling the vessel with a small volume of H_2, calculated using a modified Redlich-Kwong (MRK) equation of state (Holloway, 1977) to be in equilibrium with H_2O at QFM at the run conditions, pressurizing the Ar gas to about two-thirds of the desired final pressure at

room temperature, increasing the temperature to the final T, and then adjusting the pressure to the desired value. Hydrogen pressures in the Ar gas were monitored using a AgPd Shaw membrane. Temperature gradients were about 30°C along the length of the capsule. Pressures varied by <1% of the run pressure. Single-pressure runs were held at the run conditions for 2.5 hrs . Reversals were held at a higher pressure for 2.5 hrs, and then the pressure was decreased and held at the final value for an additional 2.5 hrs.

Runs in the conventional, internally heated pressure vessels were terminated by shutting off power to the furnace. Quench rates of about 8°C/sec were achieved. Glasses were produced for runs ≤300 bars. Melts did not quench to glass at this quench rate for runs >300 bars.

2.4 Rapid-quench, Internally Heated Pressure Vessel (RQIHPV)

Because of the difficulty in quenching hydrous basaltic melts to glass, and the requirement for glass material for FTIR analysis, it was necessary to design a rapid-quench mechanism for the internally heated pressure vessel for use in the higher-pressure experiments. Details of the design are given in Holloway et al. (1992) (Appendix 1) and summarized below. The pressure vessel was mounted in a vertical position. Samples were heated with a Kanthal double-wound furnace. The sample was hung from a thin Pt wire. The quenching mechanism used a high surge current from a discharging capacitor to burn out the Pt-hanging wire, allowing the sample to drop down to the head, which maintained a temperature of about 25°C. Four sheathed, chromel-alumel thermocouples (or Pt-Rh thermocouples in some runs) bracketed the location of the sample providing information on thermal gradients during the runs. Temperature gradients were typically less than 10°C over about 1.5 cm. The inclusion of quench wire leads through the head left insufficient room for a Shaw membrane; therefore, control of f_{H_2} was done by using premixed mixtures of Ar and H_2 as the pressure medium. This technique has been shown to provide an "infinite reservoir" of

H_2 for the duration of the experiments (Joyce and Holloway, 1992). Several runs were conducted using pure Ar gas as the pressure medium.

Experiments were brought up to the run conditions in a manner similar to those conducted in the conventional, internally heated pressure vessels. Run times were similar to those run in the conventional, internally heated pressure vessels (Table 1). All runs quenched to glass successfully.

3. Analytical Techniques

All run products were clear, brown glass. Most had bubbles ranging in size from 10s to 1000s of microns that were concentrated along the capsule walls. Several runs had a large bubble in the center of the quenched glass. Glass in the bottoms of the capsules of the CO_2-rich runs were a milky, bluish-green color and contained disseminated streaks of silver from the silver oxalate.

3.1 Electron Microprobe

Electron microprobe analyses of the run products were carried out at the California Institute of Technology on a JEOL JXA-733 Superprobe (15 kV accelerating potential, 15 nA beam current, 20 μm spot size). Standards used for the glass analyses were VG-2 for Mg, Al, Si, Ca, and Fe; TiO_2 for Ti, a synthetic Mn-olivine for Mn, albite for Na, and microcline for K. Data reduction was done using the CITZAF program (Armstrong, 1988), employing the absorption correction of Armstrong (1982), the atomic number correction of Love et al. (1978), and the fluorescence correction of Reed (1965) as modified by Armstrong (1988). Glass analyses reported in Table 2 are averages of 4 to 8 analyses of different spots.

The concentration of Fe in the Fe-Pt foils were also determined after the runs by electron microprobe. Standards used were pure Pt and Fe metals. Backgrounds were 0.01 wt.% for Fe in Pt and 0.05 for Pt in Fe. Iron concentrations in the foils

determined by microprobe were within 8% of those determined by mass balance before the run.

3.2 Fe^{2+}/Fe^{3+}

Ferrous iron was measured by Dr. Ian Carmichael at the University of California at Berkeley by a colorimetric, wet-chemical method (Wilson, 1960) corrected for time-dependent, ferric-iron interference as described in Lange and Carmichael (1989). Precision of the ferrous iron analyses is about 2% of the amount present based on multiple analyses of an internal lab standard (JDFD-2; $10.93 \pm 0.21\%$ (2σ)). Ferric iron was determined by subtracting ferrous iron from total iron determined by microprobe. These data are listed in Table 2.

3.3 Spectroscopic Data Analysis

3.3.1 Determination of concentrations

Dissolved, total H_2O and CO_2 concentrations were determined by transmission infrared spectroscopy on doubly polished glass chips, using the procedures and calibrations described by Dixon et al. (1988). In general, concentrations are calculated using the Beer-Lambert law as follows:

$$c = \frac{(MW)\,(Abs)}{(\rho)\,(d)\,(\varepsilon)}, \qquad (1)$$

where c is the concentration in weight fraction, MW is the molecular weight of the species of interest in g/mole (18.015 for H_2O, 44.01 for CO_2), Abs is absorbance (dimensionless), ρ is the glass density in g/l, d is the sample thickness in centimeters, and ε is the molar absorptivity in l/(mol cm). If integrated absorbance (cm^{-1}) is used

instead of absorbance, ε is replaced by ε^*, the integrated molar absorptivity, with units of l/(mol cm^2). Previous studies have documented the equivalence of concentrations calculated using band heights and integrated absorbances (Fine and Stolper, 1986; Newman et al., 1986; Silver, 1988). Concentrations in this study are calculated using band heights (absorbances) only. Glass densities (Table 1) were calculated using the Gladstone-Dale rule and the Church-Johnson equation as described by Silver (1988). Thicknesses of glasses were measured using a digital micrometer having an accuracy and precision of about 1-2 μm. The validity of Lambert's law (i.e., that absorbance is proportional to sample thickness) for these samples was confirmed by measuring band intensities on several pieces of the same sample ground to different thicknesses.

3.3.2 Infrared region (1500-3800 cm^{-1})

A typical spectrum in the infrared region (1500-3800 cm^{-1}) is shown in Figure 1a. Note the broad asymmetric band centered at ~3550 cm^{-1} corresponding to the fundamental OH-stretching vibration (Nakamoto, 1978). The band at 1630 cm^{-1} is due to the fundamental bending mode of water molecules (Nakamoto, 1978). The bands at 1515 and 1430 cm^{-1} correspond to antisymmetric stretching of distorted carbonate (CO_3^{2-}) groups (Brey and Green, 1975; Sharma, 1979; Sharma et al., 1979; Mysen and Virgo, 1980a and b; Fine and Stolper, 1986). No absorptions at ~2350, corresponding to the ν_3 antisymmetric stretch of molecular CO_2, were observed.

At least three glass chips were separated from each experiment for spectroscopic analysis. Precision of the measurements of total water in the infrared region are about 2% based on duplicate analyses of a single glass chip. When the 3550 cm^{-1} band was analyzed on the same spot in both the infrared and near-infrared regions, however, the data were not as reproducible and differences of up to 14% were observed. Accuracy is limited by the uncertainty in the molar absorptivity and is about 10%. Accuracy for the 1630 cm^{-1} band is discussed below in the calibration section.

The intensities (band heights) of the carbonate bands were measured separately after numerical subtraction of the spectrum of a decarbonated basaltic glass, either TT152-21-35 or 519BL, and a concentration was calculated from the intensity of each band. Figure 1b shows typical sample, reference, and reference-subtracted spectra in the carbonate region. Analyses of the same spot are reproducible to about 8% of the amount present for CO_2 concentrations >50 pm. Accuracy is limited by the uncertainty in the molar absorption coefficient and in the background correction procedure and is estimated to be about 15%.

3.3.3 Near-infrared region (3800-7600 cm^{-1})

Band assignments for hydrous species in the near-infrared region (3800-7600 cm^{-1}) in basaltic glasses are similar to those for rhyolitic glasses (see review in Newman et al., 1986). The main bands of interest for this study are the 5230 cm^{-1} band, resulting from the combination stretching + bending mode of water molecules (Scholze, 1960; Bartholomew et al., 1980), and the 4500 cm^{-1} band, resulting from a combination mode for Si-OH and Al-OH groups (Scholze, 1966; Stolper, 1982a). Determination of the band heights for the near-infrared bands for molecular water (5230 cm^{-1}) and hydroxyl groups (4500 cm^{-1}) were complicated by the presence of two broadly overlapping absorption bands corresponding to the crystal-field transitions in octahedrally and tetrahedrally coordinated Fe^{2+} ions (Bell et al. 1976; Goldman and Berg, 1980) in the near-infrared region at about 9500 and 5500 cm^{-1} (1.06 and 1.8 μm, respectively) and an absorption at 4000 cm^{-1} (Figure 2). The band at 4000 cm^{-1} correlates with total water content (Stolper, 1982a), but the mechanism of absorption is uncertain (Newman et al. 1986; Silver and Stolper, 1989). The spectrum of a single, devolatilized reference glass cannot be used for subtraction for all the samples, because the Fe absorption bands are a function of the total iron concentration and oxidation state, and these quantities may change during the experimental runs. Another complicating

factor is the presence of the large, asymmetric OH absorption at 3550 cm^{-1}. Unfortunately, the shape of the 3550 cm^{-1} absorption narrows slightly as water concentrations increase (Silver and Stolper, 1989), over the range of concentrations found in the experimental glasses. Therefore, the effect of the 3550 cm^{-1} absorption could not be removed by simply subtracting out a generic 3550 cm^{-1} band shape.

In order to have a consistent background-subtraction method for the near-infrared region, we fit the background using a nonlinear curve-fitting routine. Nonlinear least-squares fits to the backgrounds were calculated using a curve-fit routine modified from Bevington (1969) (Program 11-5, p. 237). The backgrounds were modeled as a sum of 5 Gaussian curves: two for the Fe absorptions centered at about 9500 and 5500 cm^{-1}, one centered at about 4000 cm^{-1}, and two to fit the left-hand shoulder of the 3550 cm^{-1} absorption. A typical spectrum, the modeled fit, and the resulting background-subtracted spectrum are shown in Figure 2. Note the flat background on the background-subtracted spectrum, the asymmetric shape of the 5230 cm^{-1} band and the symmetric Gaussian shape of the 4500 cm^{-1} band. Band heights were measured by hand on the background-subtracted spectra.

3.4 Manometry

The composition of the mixed H_2O-CO_2 vapor phase in two runs (20M and 21M) were measured using manometry by P. Ihinger at Caltech (Ihinger, 1991). Capsules were loaded in a vacuum-tight, capsule-piercing device and pierced under vacuum at room temperature. Vapor was extracted by a series of cycles of expansion of the gas into an evacuated volume followed by condensation in the cold trap at liquid-nitrogen temperatures. After pumping away a small volume of non-condensible gas (<4 %), the CO_2 was released by bathing the trap in a slurry of dry ice and M17 (an organic solvent consisting of methylene chloride, methyl chloroform, and tetrahydrofuran) and passed through a Toepler pump into a calibrated volume for manometric analysis. The

pure water remaining in the cold trap was converted to H_2 by expanding over hot (750°C) uranium using the procedure of Bigeleisen et al. (1952) and passed into a calibrated volume for manometric analysis. Analytical uncertainty of the manometric measurement is estimated to be less than one percent of the volume of the sample (Ihinger, 1991).

4. Results and Discussion

4.1 Calibration of molar absorptivities

In order to calculate concentrations of water dissolved as hydroxyl groups and molecular water from the measured absorbances, the molar absorptivities for the 4500, 5230, and 1630 cm^{-1} bands had to be determined for basaltic glass. We solved for the molar absorptivities of these bands, assuming that the concentrations of molecular water and hydroxyl groups had to add up to the concentration of total water measured using the 3550 cm^{-1} band. Thus, assuming that molecular water + hydroxyl groups = total water, the Beer-Lambert law yields:

$$\frac{MW*Abs^{5230}}{\varepsilon^{5230}*\rho*d} + \frac{MW*Abs^{4500}}{\varepsilon^{4500}*\rho*d} = \frac{MW*Abs^{3550}}{\varepsilon^{3550}*\rho*d}, \qquad (2)$$

where the variables are the same as in Equation (1). This is equivalent to:

$$\frac{\varepsilon^{3550}}{\varepsilon^{5230}}Abs^{5230} + \frac{\varepsilon^{3550}}{\varepsilon^{4500}}Abs^{4500} = Abs^{3550}. \qquad (3)$$

We performed a multiple regression on all the absorbance data (Table 4) to solve simultaneously for ε^{5230} and ε^{4500}, assuming $\varepsilon^{3550} = 63 \pm 5$ l/mole-cm (Dobson,

Newman, Epstein, and Stolper, unpublished). Similarly, we performed a multiple regression to solve simultaneously for ε^{1630} and ε^{4500}. We also performed a linear regression to solve for the ratio of the molar absorptivities for the two molecular water bands by assuming that the concentrations for the two bands were equivalent:

$$\frac{\varepsilon^{1630}}{\varepsilon^{5230}} \mathrm{Abs}^{5230} = \mathrm{Abs}^{1630} \quad . \qquad (4)$$

The molar absorptivities for the 4500 cm^{-1} band for hydroxyl groups and for the 5230 and 1630 cm^{-1} bands of molecular water have been calibrated to be 0.67 ± 0.04, 0.62 ± 0.08, and 25 ± 3 l/mole-cm, respectively (Table 3). Reported errors include propagation of error for the value of ε^{3550}. The errors in the molar absorptivities (about 6% for the 4500 cm^{-1} band and about 12% for the 5230 and 1630 cm^{-1} bands) are the limiting error source in the accuracy of determinations of hydroxyl and molecular water concentrations.

The internal consistency of our procedure and the quality of the derived values for the molar absorptivities can be demonstrated in two ways. First, total water as calculated by the sum of molecular water and hydroxyl groups can be plotted versus total water measured using the 3550 cm^{-1} band (Figure 3). A fit through these data shows about 4% deviation from the ideal slope of 1 (well within 2 standard deviations of the 1:1 line) and negligible deviation from the ideal intercept of 0. Second, the concentration of molecular water determined from the 1630 cm^{-1} band can be plotted versus that determined from the 5230 cm^{-1} band (Figure 4). The data in Figure 4 also lie within 2 standard deviations of the 1:1 line, showing that the concentrations of molecular water determined from the 5230 and 1630 cm^{-1} bands are equivalent.

Our best-fit molar absorptivities for molecular water and hydroxyl groups in basaltic glasses are significantly lower (~60%) than those determined for rhyolitic glasses (Newman et al., 1986; Ihinger, 1991), showing the importance of accurate molar absorptivity calibrations for each composition of interest.

4.2 Fe-loss and oxidation state

The use of the double-capsule technique successfully minimized Fe-loss from the basaltic melt to the Pt capsule. The runs performed using the Pt-Fe alloy inserts lost less than 7% of the total FeO present (<0.9 wt.% FeO). One run (17H) actually gained iron from the Fe-Pt alloy foil, going from an initial Fe content of 12.3 wt.% to a final value of 13.1 wt.%. Another advantage of the double-capsule technique is that the outer platinum capsules remained relatively pure and were not weakened by interaction with the iron in the melt. Only the double-capsule runs were able to withstand quenching without cracking.

The extent of iron loss in the nondouble capsule runs is a function of their oxidation state during the run. Runs 32 through 35 were performed in pure Pt capsules, but lost less than 10% of their initial iron. These runs were highly oxidized (>NiNiO) because H_2 was lost from the capsule to the pure Ar gas outside the capsule during the run (discussed in more detail below). Several of these quenched glasses were red in color consistent with their high oxidation states. Only two experiments (28B and 29B) run in pure Pt capsules lost significant iron (52% and 85%, respectively), producing glasses that were pale green in color. Though the final f_{O_2} of these runs were between NiNiO and QFM, these runs initially experienced reducing conditions relative to the others for two reasons. First, oxalic acid dihydrate was used to generate the vapor phase, resulting in production of excess H_2 (H_2:H_2O:CO_2 = 1:2:2). Second, these runs ruptured during the run (fugacities of H_2O and CO_2 are in the correct ratio but both

diminished by about 60%) resulting in equilibration with the reducing Ar/H_2 pressure medium gas.

Oxygen fugacities were calculated from Fe_2O_3/FeO ratios measured in the glasses using the empirical relationships of Kilinc et al. (1983) and Kress and Carmichael (1991). These two methods give results within about 0.4 log units of each other. We list the values calculated using Kilinc et al. (1983) in Table 2 to be consistent with oxygen fugacities presented in previous studies of natural MORB glasses (Christie et al., 1986). Most runs are within a log unit of the QFM buffer at 1200°C. Runs 17H, 20M, and 33A have oxygen fugacities more oxidizing than QFM, having log f_{O_2}s 1.8 to 3.5 log units greater than QFM (0.8 to 2.5 more oxidizing than Ni-NiO at 1200°C).

The fact that the oxygen fugacity of all of the runs is >QFM at 1200°C is important because it allows us to estimate the effect of CO on the composition of the vapor phase. Recently, it has been shown that CO_2 behaves in a Henrian fashion in the C-O system (Holloway et al., 1992; Pawley and Holloway, 1991; Pawley et al., 1992). As a consequence, CO_2 solubility is strongly dependent on the oxygen fugacity of the system since, for example, under graphite-saturated conditions where the proportion of CO in the vapor is 50-90%, the fugacity of CO_2 is 50-90% less than under conditions where the fluid is nearly pure CO_2. Because the f_{O_2} of our experiments was >QFM, the proportion of CO in the vapor phase is <5% (Deines et al., 1974) allowing us to assume in our calculation of fugacities that CO_2 is the only carbon species.

4.3 Solubility of water in basaltic melts

Run conditions are listed in Table 1; absorbance and concentration data for dissolved water species are given in Table 4 and summarized in Table 7.

4.3.1 Concentrations of water

Six successful experiments using pure water were conducted at about 1200°C with total pressure (~P_{H_2O} in these experiments) ranging between 200 and 717 bars.

Three experiments (7, 8, and 9) were conducted in the conventional, internally heated vessel, and three others (17H, 20H, and 21H) were conducted in the rapid-quench, internally heated vessel. Fugacities of water were calculated assuming pure water in the vapor using a MRK equation of state (Holloway, 1977).

Three successful experiments (18M, 20M, and 21M) using oxalic acid dihydrate to produce a mixed H_2O-CO_2 vapor phase were carried out at about 1200°C and total pressure ranging from 310 to 980 bars. The vapor phase composition of two of these runs (20H and 21H) was measured using manometry and found to contain about 0.4 volume percent H_2O and 0.6 volume percent CO_2. These proportions of H_2O and CO_2 in the vapor are consistent with mass balance calculations if the starting material contained about 0.1 wt.% H_2O, possibly dissolved in the glassy starting material or adsorbed on the powder surface. The vapor phase composition of the third oxalic acid dihydrate run (18M) was calculated by mass balance, assuming 0.1 wt.% H_2O in the starting material, and also was found to be about 0.4 vol.% H_2O and 0.6 vol.% CO_2. Fugacities of H_2O and CO_2 were calculated using the mole fractions of the species in the vapor and a MRK equation of state (Holloway, 1977). Though additional mixed H_2O-CO_2 vapor experiments were conducted, the pure water and oxalic acid dihydrate experiments provide a data set in which the water fugacities are well constrained, allowing the relation between water fugacity in the vapor and concentration of total and molecular water to be determined.

Figure 5 shows total dissolved water, determined from the 3550 cm^{-1} band, plotted against water fugacity. Water concentrations in these runs range from 1 to 2.5 wt.% and are typically homogeneous to better than 7% of the amount present. The water concentrations of runs 7 (held at 200 bars for 2.5 hrs) and 8 (held at 400 bars for 2.25 hrs and then held at 200 bars for 2.75 hrs) are the same within errors, indicating that equilibrium was reached on the time scales of the experiments. Also note that the water concentrations of runs 9 (run in the IHPV) and 20H (run in the RQIHPV) are the

same within errors, showing that quench rate does not affect the total dissolved water concentration at these pressures. Finally, note that the water concentration in runs 21M (mixed H_2O-CO_2 vapor with f_{H_2O} = 200 bar) and 7 and 8 (pure H_2O vapor with f_{H_2O} = 200 bar) are the same within errors, showing that the solubility of water is a simple function of H_2O fugacity regardless of the composition of the vapor.

Figure 6 compares our results with those of Hamilton et al. (1964). Although the earlier results were obtained at higher pressures and with a different basalt composition (Columbia River basalt), the data from both studies are clearly compatible.

4.3.2 Validity of Henry's law

The interaction between vapor and water molecules dissolved in the melt can be described by the following reaction:

$$H_2O^{vapor} \leftrightarrow H_2O^{melt}_{molecular} . \qquad (5)$$

The equilibrium constant for the reaction is:

$$K = \frac{a^m_{H_2O,\,mol}}{a^v_{H_2O}} = \frac{X^m_{H_2O,\,mol}}{(f_{H_2O}/f^0_{H_2O})} , \qquad (6)$$

where f_{H_2O} is the fugacity of water in the vapor, $f^0_{H_2O}$ is the fugacity of water in the standard state of the vapor, taken as pure water vapor at P and T (Burnham et al., 1969), and the activity of water molecules in the melt, $a^m_{H_2O,\,mol}$, defined relative to a standard state of pure water molecules at P and T (Shaw, 1964; Stolper, 1982b; Silver and Stolper, 1985). If Henry's law is valid for water in basaltic systems, the activity of molecular water in the melt should be equal to its mole fraction in the melt ($X^m_{H_2O,\,mol}$).

Using the calibration discussed above, the concentrations of water dissolved as molecular water and hydroxyl groups were determined for each run. Mole fractions were calculated on a single oxygen basis according to the equations listed in the key to Table 4. The concentration of molecular water measured in the quenched basaltic glasses is approximately proportional to water fugacity in all samples (Figure 8), confirming that molecular water solubility in basaltic melts is closely approximated by Henry's law at pressures less than 1 kbar, as has been previously observed for more silicic, more highly polymerized melts (Stolper , 1982a, b; Silver and Stolper, 1989; Silver et al., 1990). Note that at the low pressures of these experiments, the effect of the molar volume of water ($V_{H_2O}^{0,m}$) can be neglected and it is acceptable to compare data obtained at different total pressures directly with those obtained from different vapor phase compositions. A fit through the data forced through the origin has an R^2 of 0.97 and yields the relation:

$$X_{H_2O,\,mol}^{m} = 2.93 \times 10^{-5} * f_{H_2O}\,(bar)\,. \qquad (7)$$

This equation can be used to calculate the fugacity of water in equilibrium with basalt at 1200°C and pressures <1 kbar based on the measured concentrations of molecular water in quenched, natural basaltic glasses and in the mixed H_2O-CO_2 runs where direct measurement of the vapor composition may not be possible. This will be important in cases where the capsule ruptured prematurely.

The fact that the proportionality between molecular water and water fugacity holds regardless of the composition of the vapor phase (Figure 8), suggests that H_2O-CO_2 mixtures can be modelled as ideal. A better way to illustrate the validity of Henry's law for molecular water in H_2O-CO_2 mixtures is shown in Figure 9. From Equation (6) we can derive:

$$\frac{X^{m}_{H_2O,\,mol}}{X^{0,\,m}_{H_2O,\,mol}} = \frac{f_{H_2O}}{f^{0}_{H_2O}}, \qquad (8)$$

where $X^{m}_{H_2O,\,mol}$ is the mole fraction of molecular water dissolved in a melt in equilibrium with pure water vapor at P and T. Thus, if the species in the melt behave ideally, the ratio of the amount of molecular water dissolved in a melt in equilibrium with mixed H_2O-CO_2 vapor phase with respect to that dissolved in the melt in equilibrium with a pure H_2O vapor phase (y-axis in Figure 9) should be simply equal to the ratio of the water fugacities in the mixed and pure vapors (x-axis in Figure 9). In fact, this is exactly what we observe; the mixed vapor runs fall within errors of the 1:1 line (Figure 9). This observation considerably simplifies modelling of the thermodynamics of hydrous basaltic melts.

Figure 8 also shows that there is no difference in the proportion of molecular water between the slow (conventional IHPV) and fast (RQIHPV) quench experiments, suggesting that the speciation of water is not altered on quenching. This contrasts with observations for rhyolitic melts (Silver et al., 1990; Ihinger, 1991) and suggests that the speciation of water in basaltic melts is less dependent on temperature than that in rhyolitic melts.

4.3.3 Speciation of water in basalt

Previous studies of hydrous silicate melts (Stolper, 1982a, b; Stolper et al., 1983; Newman et al., 1986; Silver and Stolper, 1989; Silver et al., 1990; Ihinger, 1991) have shown that the speciation of water varies systematically with total water concentration. At low water concentrations, water dissolves in the melt dominantly as hydroxyl groups. As the concentration of water increases, the concentration of hydroxyl groups levels off, while the concentration of molecular water increases. Thus,

the proportion of molecular water increases as the amount of total dissolved water increases.

Concentrations of molecular water and hydroxyl groups in the quenched basaltic glasses with respect to total water concentration are shown in Figures 7a and b along with the data for albitic glass (Silver and Stolper, 1989). The trends observed in these experiments on MORB are essentially identical to those observed in albitic glasses (Silver and Stolper, 1989) and similar to those found in other silicate melt compositions (Stolper, 1982a, b; Stolper et al., 1983; Newman et al., 1986; Silver et al., 1990; Ihinger, 1991). Though the water concentrations observed in this study are not high enough to allow us to determine the crossover point at which the concentration of molecular water equals that of hydroxyl groups, based on the coincidence of the MORB and albitic glass data sets, we assume this occurs at about 4 wt.% total dissolved H_2O, equivalent to a mole fraction of total dissolved H_2O (X_B) of 0.12.

Several recent studies (Stolper, 1982a; Silver and Stolper, 1985; Silver and Stolper, 1989; Silver et al., 1990) have focussed on development of simple thermodynamic models involving homogeneous equilibria among melt species that can account for the trends in the spectroscopically determined water speciation data. Once water molecules enter the melt, they will react with the silicate portion of the melt to form hydroxyl groups as described by the reaction:

$$H_2O^{melt}_{molecular} + O^{melt} \leftrightarrow 2OH^{melt} \quad . \tag{9}$$

The equilibrium constant for this reaction is:

$$K = \frac{(a^m_{OH})^2}{(a^m_{H_2O,\,mol})(a^m_O)} \quad . \tag{10}$$

The simplest type of thermodynamic model (Wasserburg, 1957; Stolper, 1982b; and Silver and Stolper, 1985) involves ideal mixing of water molecules, hydroxyl groups, and oxygens in the melt, allowing the activities to be replaced by mole fractions in the expression of the equilibrium constant. This ideal mixing model provides a qualitative fit to the shape of the trends in the speciation data at low water concentrations, but tends to diverge progressively from the measured concentrations at high water contents; the measured hydroxyl group concentrations flatten out more sharply relative to the ideal mixing model calculations (Silver and Stolper, 1989).

Silver and Stolper (1989) use the ideal mixing model as a basis for development of several more complex models to account for the speciation data by including the effects of nonideal interactions, mixing properties of polymeric groups, and a range of distinguishable types of oxygens in the melt. Any of these three nonideal models are able to reproduce the measured variations in speciation; the data cannot distinguish among the models. For simplicity, I will limit my treatment of water solubility in basalt to the regular solution model developed by Silver and Stolper (1989) for albitic glass.

Possible nonideal interactions between water molecules, hydroxyl groups, and oxygens can be modelled in terms of a regular ternary solution, where the entropy of mixing is taken to be identical to that in an ideal mixture, but the possible configurations of the three species over the quasi-crystalline lattice sites are not energetically identical. The activities of the three species are (Guggenheim, 1952; Prigogine and Defay, 1954, Equation 16.90):

$$a^{m}_{H_2O,\,mol} = X^{m}_{H_2O,\,mol}\exp\{\frac{1}{RT}(X^{m}_{O}X^{m}_{OH}(W_{H_2O,\,mol\text{-}O}-W_{O\text{-}OH}+W_{H_2O,\,mol\text{-}OH})$$

$$+(X^{m}_{O})^{2}W_{H_2O,\,mol\text{-}O}+(X^{m}_{OH})^{2}W_{H_2O,\,mol\text{-}OH})\}, \qquad (11.1)$$

$$a_O^m = X_O^m \exp\{\frac{1}{RT}(X_{H_2O,\,mol}^m X_{OH}^m (W_{O\text{-}OH} - W_{H_2O,\,mol\text{-}OH} + W_{H_2O,\,mol\text{-}O}) + (X_{H_2O,\,mol}^m)^2 W_{H_2O,\,mol\text{-}O} + (X_{OH}^m)^2 W_{O\text{-}OH})\}, \quad (11.2)$$

$$a_{OH}^m = X_{OH}^m \exp\{\frac{1}{RT}(X_{H_2O,\,mol}^m X_O^m (W_{H_2O,\,mol\text{-}OH} - W_{H_2O,\,mol\text{-}O} + W_{O\text{-}OH}) + (X_{H_2O,\,mol}^m)^2 W_{H_2O,\,mol\text{-}OH} + (X_O^m)^2 W_{O\text{-}OH})\}, \quad (11.3)$$

where the W_{ij} are binary interaction parameters, have units of energy, and are independent of temperature and pressure.

Following Silver and Stolper (1989), the activity expressions given above can be substituted into the definition of K (Equation 10) and rearranged to give:

$$-\ln\left[\frac{(X_{OH}^m)^2}{(X_{H_2O,\,mol}^m)(1 - X_{OH}^m - X_{H_2O,\,mol}^m)}\right] = A' + B' X_{OH}^m + C' X_{H_2O,\,mol}^m, \quad (12)$$

where

$$A' = -\ln K + (2W_{O\text{-}OH} - W_{H_2O,\,mol\text{-}O})/RT\,; \quad (13.1)$$

$$B' = (W_{H_2O,\,mol\text{-}O} - 3W_{O\text{-}OH} - W_{H_2O,\,mol\text{-}OH})/RT\,; \quad (13.2)$$

$$C' = 2(W_{H_2O,\,mol\text{-}O} - W_{O\text{-}OH})/RT\,. \quad (13.3)$$

Given values for these coefficients and $X_{H_2O,\,mol}^m$ (from Henry's law as discussed above), Equation 12 can be solved iteratively to give X_{OH}^m. The mole fraction of total dissolved water can then be specified using:

$$X_{total\,H_2O}^m = X_B = X_{H_2O,\,mol}^m + \frac{X_{OH}^m}{2}. \quad (14)$$

For water in albitic glasses, Silver and Stolper (1989) used the method of least squares to determine the best fit values for the coefficients in Equation 10 of A'=0.403, B'=15.333, C'=10.894. Because the water speciation data for basaltic glass determined in this study are coincident with the data for albitic glass determined by Silver and Stolper (1989), and because the albitic glass data span a much larger range in water concentrations, allowing a more robust determination of the values for the coefficients, I will use the values for albitic glasses in the modelling of water speciation in basaltic systems. The applicability of these coefficients for calculating the speciation of water in basaltic glasses having water contents greater than about 3 wt. % needs to be confirmed by experimentally producing basaltic glasses with higher water contents.

Curves representing the mole fractions of molecular water, hydroxyl groups, and total water calculated using Henry's law (Equation 6) and the regular ternary solution model are shown along with the spectroscopically measured data on Figures 5 and 7b. The model accurately predicts the observed speciation and total water concentration for basaltic glass at pressures <1 kbar.

At pressures higher than about 1 kbar, however, the effect of the molar volume of water in the melt ($V^{0,m}_{H_2O}$) on the activity of water in vapor-saturated melts is no longer negligible, and it must be included in the expression to constrain the activity of water in the melt. It has been shown previously (Silver and Stolper, 1989) that the solubility of molecular water can be expressed as:

$$a^{m}_{mol.\ H_2O}(P, T) = a^{0,m}_{mol.\ H_2O}(P_0, T_0)\,\frac{f_{H_2O}(P, T)}{f^{0}_{H_2O}(P_0, T_0)}\,\exp\left\{\frac{-V^{0,m}_{H_2O,\,mol}(P-P_0)}{RT} - \frac{\Delta H^{0}_{r}(P_0)}{R}\left(\frac{1}{T}-\frac{1}{T_0}\right)\right\} \quad , \quad (15)$$

where $a^{m}_{mol.\ H_2O}(P, T)$ is the activity of molecular water in the vapor-saturated melt at P and T, relative to standard states defined by the pure melt species at the temperature and pressure of interest; $a^{0,\,m}_{mol.\ H_2O}(P_0, T_0)$ is the activity of molecular water in the melt in equilibrium with pure water at a reference pressure and temperature of P_0 and T_0; $f_{H_2O}(P,T)$ is the fugacity of H_2O in the vapor at P and T ; $f^{0}_{H_2O}(P_0, T_0)$ is the fugacity of pure H_2O in the vapor at P_0 and T_0; $V^{0,\,m}_{H_2O,\,mol}$ is the molar volume of molecular water in the melt in its standard state; $\Delta H^{0}_{r}(P_0)$ is the enthalpy change of the reaction. Because these experiments were done at a single temperature, the temperature term can be neglected. At low pressures, the exponent of the $P\text{-}P_0$ term is small and can be neglected, but becomes significant at pressures greater than about 1 kbar. Because of the weak pressure dependence of the speciation of water in silicate liquids, it has been suggested that the partial molar volume of molecular water in a silicate melt may be similar to that of a hydroxyl group (Stolper, 1989). If this assumption is valid, then determinations of the partial molar volume of molecular water should be equivalent to the partial molar volume of water $\left(V^{0,\,m}_{H_2O}\right)$ in silicate melts. In the following discussion, I will simply refer to the molar volume of water in the melt $\left(V^{0,\,m}_{H_2O}\right)$.

Figure 6 shows the calculated water solubilities for basalt at 1200°C using the regular solution model and several different values for $V^{0,\,m}_{H_2O}$. A value of $V^{0,\,m}_{H_2O}=0$ is equivalent to neglecting the pressure term. The levelling off of water solubility at elevated pressures is due to a nonzero, partial molar volume of water in the melt. Using a reference pressure and temperature of 1 bar and 1200°C and assuming a regular solution model, the water solubility data of Hamilton et al. (1964) are best fit by the following pressure dependent equation for the activity of water in the melt:

$$a^{m}_{H_2O} = X^{m}_{mol.\ H_2O} = 3.102 \times 10^{-5} \frac{f_{H_2O}}{1} \exp\left\{\frac{-12(P-1)}{RT}\right\}. \qquad (16)$$

Note that the data are best fit by a $V_{H_2O}^{0,m}$ of 12 cm^3/mole. Values for water solubility and speciation based on equations 12 and 16 are provided in Table 8.

Recently, estimates for the partial molar volume of water in silicate liquids have been compiled by Lange and Carmichael (1990) and are listed in Table 5. The estimates of $V_{H_2O}^{0,m}$ constrained by data at pressures >1 kbar range from 17 to 25 cm^3/mol. The $V_{H_2O}^{0,m}$ in Ca-Al-Mg-silicate melts appear to be lower than the Na-Al-K-silicate melts. The estimate of $V_{H_2O}^{0,m}$ for basalt is even lower than those for the simple synthetic compositions, and may reflect to addition of Fe to the melt. It is difficult to assess, however, if the variations in $V_{H_2O}^{0,m}$ are due to compositional effects or to uncertainties in the thermodynamic analysis.

4.5 Mixed-volatile (CO_2+H_2O) solubility relations in basaltic melts

Nine successful experiments using a mixed H_2O-CO_2 vapor phase were conducted at 1200°C with total pressure ranging between 210 and 980 bars. Run conditions are listed in Table 1. Carbonate absorbance data for individual spectra from each run are reported in Table 6. The mean and 1 standard deviation of all of the CO_2 concentrations measured from all spectra on glass chips from the same run are reported in Table 7. All mixed H_2O-CO_2 runs were conducted in the rapid-quench, internally heated pressure vessel. The three experiments (18M, 20M, and 21M) using oxalic acid dihydrate to produce a mixed H_2O-CO_2 vapor phase have well constrained H_2O and CO_2 fugacities as discussed above. The other mixed vapor experiments leaked (ruptured) either on quenching or when two capsules, run at the same time and had sintered together, were pulled apart. Thus, the composition of the vapor phase in these latter experiments could not be measured directly, and had to be determined by more indirect methods. The fugacity of water in the vapor phase in equilibrium with the melt

for these experiments was calculated using the linear relation between fugacity and the mole% of molecular water measured using the 5230 cm^{-1} band in the glass (Equation 6). We assumed that the vapor was composed of only H_2O and CO_2, consistent with the measured oxidation state of the glasses, and used the MRK equation of state (Holloway, 1977) to solve for the mole fractions of H_2O and CO_2 and the fugacity of CO_2 in the vapor at the run conditions.

It is interesting to note that the runs (30-35) (performed using pure Ar gas as the pressure medium in order to try to minimize the H_2 embrittlement of the Pt capsules) have calculated f_{H_2O}s in the vapor phase lower than that predicted by mass balance. Because H_2 will diffuse through the Pt capsule until the fugacity of hydrogen inside the capsule is the same as that in the Ar gas outside the capsule, it was expected that variable amounts of H_2 would be lost during these runs. The expected H_2 loss from the interior of the capsule did not become significant, however, until about the sixth run after switching to a pure Ar gas, showing that there was a substantial H_2-memory effect caused by slow diffusion of H_2 out of the vessel over the course of several runs. As the amount of residual H_2 in the vessel progressively decreased with each run, the amount of H_2-loss from the interior of the capsule increased.

CO_2 concentrations in two glasses equilibrated with pure CO_2 vapor (TT152-2 and 5 from Stolper and Holloway, 1988) were redetermined for this study so that all data were obtained using a consistent background-subtraction scheme. The highest pressure run of Stolper and Holloway (1988) was not reanalyzed because that run failed after an hour and could have anomalously low CO_2 concentrations (E. Stolper, personal communication). The revised CO_2 concentrations of the reanalyzed glasses are about 10% higher, but still within 2-σ errors, of those reported in Stolper and Holloway (1988). The resulting slope of a linear regression line through the two revised data points and forced through zero yields a slope of 47 ppm/100 bar pressure (equivalent to

47 ppm/(km water depth)), about 20% higher than the value of 38 ± 2 ppm/100 bar reported in Stolper and Holloway (1988).

Concentrations of CO_2 dissolved as carbonate in the experimental glasses range from 63 to 315 ppm CO_2. Carbonate was the only species of dissolved carbon observed consistent with the results of Fine and Stolper (1986). The mole fraction of CO_2 in the vapor varied from 0.39 to 0.95. The CO_2 concentrations of runs 33B (held at 503 bars for 2 hrs with f_{CO_2} = 207.2 bars) and 20M (held at 424 bars for 3 hrs and then held at 200 bars for 3 hrs with a final f_{CO_2} = 201 bars) are the same within errors, indicating that equilibrium was reached on the time scales of the experiments.

The CO_2 concentrations in the 33B-20M experiment pair (different run conditions, same f_{CO_2}), and also in runs 35B (mixed H_2O-CO_2 vapor, f_{CO_2} = 531 bars) and TT152-5 (pure CO_2 vapor, f_{CO_2} = 560 bars), are the same within errors, showing that the solubility of carbon dioxide is a simple function of f_{CO_2} regardless of the composition of the vapor. Concentrations of CO_2 dissolved as carbonate in the melt for all the experiments are proportional to f_{CO_2} (Figure 10). The data for pure CO_2 and mixed H_2O-CO_2 experiments are fit with a straight line through the origin with an R^2 of 0.99:

$$CO_2\,(\text{ppm}) = 0.395 * f_{CO_2} \,. \qquad (17)$$

Alternatively, the data can be cast in terms of mole fractions, and a fit through these data gives:

$$a^m_{CO_2} = X^m_{CO_2} = 3.292 \times 10^{-7} * f_{CO_2} \,. \qquad (18)$$

Equations 15 and 16 allow the the fugacity of CO_2 in a mixed H_2O-CO_2 vapor phase to be calculated based on the measured concentrations of CO_2 dissolved in the natural basaltic glasses that last equilibrated at pressures <1 kbar.

As discussed for water, at pressures higher than about 1 kbar, the pressure effect of $V^{0,m}_{CO_2}$ is no longer negligible. Using a $V^{0,m}_{CO_2}$ of 23.14 cm^3/mole (Pan et al., 1991), the data are fit by:

$$a^m_{CO_2} = X^m_{CO_2} = 3.817 \text{ X } 10^{-7} \frac{f_{CO_2}}{1} \exp\left\{\frac{-23.14(P-1)}{RT}\right\}, \qquad (19)$$

allowing CO_2 solubility to be predicted at pressures > 1kbar (Table 9).

As discussed for molecular water, the validity of a Henrian model for CO_2 solubility in equilibrium with H_2O-CO_2 mixtures can best be investigated on a plot of $X^mCO_2/(X^mCO_2)^\circ$ versus $f_{CO_2}/(f_{CO_2})^\circ$ (Figure 11). All data fall within 2-σ errors of the 1:1 line, even at the CO_2-rich end of the vapor composition, where the enhancement of CO_2 solubility was expected to be the greatest.

Unless carbon dissolves in the melt as another undetected form, these results suggest Henrian behavior for CO_2; that is, the solubility of CO_2 in the basaltic melt is essentially proportional to the fugacity of CO_2, with the same constant of proportionality, whether the vapor contains pure CO_2 or H_2O+CO_2 (or as indicated in Figure 5, CO+CO_2). Our results do not support the widely held view that water enhances the solubility of carbon dioxide in basaltic melts. Thus, degassing processes in basaltic magmas that are rich in both water and carbon dioxide (e.g., from the Mariana Trough; Newman, 1989) can be accurately modelled using our results in the end-member systems and the assumption of Henry's law as discussed below.

We emphasize that these results may not be precisely comparable to previous studies that have reported non-Henrian behavior of CO_2 (i.e., an enhancement of CO_2

solubility by the addition of water) because our experiments were conducted at significantly lower total pressures (compare, for example, Mysen, 1976; Brey and Green, 1976; Eggler and Rosenhauer, 1978). Also, errors in the previous studies may have been introduced by having the H_2O and CO_2 concentrations measured on bulk samples, rather than in glasses.

5. Implications for modelling of basaltic magma degassing

The solubility relations determined in this study can be used to calculate degassing paths of H_2O- and CO_2-bearing basaltic magmas for a variety of conditions relevant to submarine and subaerial eruptions. Since there are three species (three unknowns) to be described, we require three equations. Degassing of water (dissolved as OH and molecular H_2O) and carbon dioxide (dissolved as carbonate) from basaltic magmas can be described using three nonlinear equations describing mass balance, fractionation, and speciation. The relations have been incorporated in a computer program (Appendix 3) that calculates both closed (where the exsolved vapor remains in contact with the melt throughout degassing) and open (where the vapor is effectively removed from the melt at each degassing step) system degassing paths.

I have performed closed system degassing calculations using initial H_2O concentrations of 0.1, 0.3, 0.6, 1.0, and 2.0 wt.% and CO_2 contents of 500 ppm. This range in compositions can be thought of in terms of either variable source region compositions (low water contents for MORB and higher water contents for arc-related basalts) or varying degrees of fractional crystallization of a MORB magma initially containing 0.1 wt.% H_2O; for example, a residual melt after 95% crystallization would contain 2 wt.% H_2O. For these calculations, I have assumed that each melt starts with a CO_2 content of 500 ppm, as would be expected if it had resided in a vapor-saturated magma chamber at about 2 km below the seafloor. For comparison with the closed system calculations, I have performed open system degassing calculations using an

initial H_2O concentration of 1.0 wt.% and initial CO_2 contents of 500 ppm and 1.0 wt.%. An individual calculation determines the degassing path of a packet of basaltic magma at a given pressure and 1200°C; degassing proceeds until saturation is reached. Trends in the vapor-saturated H_2O, CO_2, and vapor compositions with pressure are shown in Figures 12-16. A summary of the vapor-saturated data from closed system degassing calculations is given in Table 10.

Figure 12 shows the variation of H_2O contents with pressure during closed system degassing in basaltic melts saturated with a mixed H_2O-CO_2 vapor phase. Melts having initial water contents <2.0 wt.% and initial CO_2 contents of 500 ppm are undersaturated with respect to water at 1000 bars. As pressure decreases, degassing of a CO_2-rich vapor phase proceeds with negligible loss of water until the water content closely approaches the water solubility curve. The pressure at which significant loss of water, arbitrarily chosen to be 10% of the initial amount, occurs is summarized below:

$H_2O°$	P (bars)	Water Depth (m)
.1	<1	undersat at atm. P
.3	10	100
.6	33	330
1.0	100	1000
2.0	370	3700

These calculations show that H_2O concentrations in typical MORB (~0.1-0.3 wt. % H_2O) will not be modified by degassing during eruption on the seafloor unless erupted in water depths shallower than about 100 m. Oceanic island basalts containing slightly higher water contents (~0.3-1.0%) may begin exsolving H_2O at eruption depths of 100-1000 m. Water concentrations in water-rich arc or back-arc related magmas (up to about

2 wt. %) may be modified by degassing during eruption at water depths as deep as several thousand meters.

In contrast to the behavior of water, the low solubility of CO_2 causes CO_2 to exsolve continuously from basaltic melts as pressure drops (Figure 13). Based on the calculations, MORBs erupted on the seafloor in equilibrium with a vapor phase are predicted to have CO_2 concentrations within errors of the solubility curve for pure CO_2, whereas water-rich magmas will exsolve sufficient H_2O to reduce significantly the fugacity of CO_2 in the vapor, resulting in lower dissolved CO_2 concentrations. For example, at a pressure of 200 bars (water depth of 2000 m), the CO_2 content of melts saturated with a mixed H_2O-CO_2 vapor phase and initially containing 2.0 wt.% H_2O will be about half the value of a melt saturated with pure CO_2. These predictions are consistent with the low observed CO_2 contents in Mariana trough basalts (Newman, 1989).

Figure 14 shows the covariation of CO_2 and H_2O during closed system degassing. The dashed lines show the degassing path for a given initial H_2O and CO_2 composition. For example, at 800 bars a melt initially containing 1.0 wt.% H_2O and 500 ppm CO_2 will be saturated with a mixed H_2O-CO_2 vapor phase at 0.999 wt.% H_2O and 328 ppm CO_2. As the pressure decreases, CO_2 is lost preferentially with respect to H_2O until a pressure of about 100 bars is reached. Saturation values for closed system degassing for melts having a range in initial H_2O concentrations at constant pressure and initial CO_2 content are shown in solid lines. At a given pressure and initial CO_2 content, the proportion of H_2O in the exsolved vapor will be directly proportional to the initial H_2O content of the melt. Thus, for basaltic melts having a range in H_2O contents and erupted at similar water depths, we would expect to observe a negative correlation between H_2O and CO_2 contents. Such a negative correlation is observed in basaltic glasses from the Mariana back-arc basin (Newman, 1989).

Variations in the vapor phase composition with closed system degassing are shown in Figure 15. The calculations show that the vapor phase in equilibrium with MORB at depths typical for midoceanic ridges (1000-3000 m) is >90% CO_2, consistent with measurements of vapor compositions of vesicles (Killingley and Muenow, 1975; Moore et al., 1977; Delaney et al., 1978; Jambon and Zimmermann, 1987). A water-rich vapor phase can be exsolved in a midoceanic ridge setting from residual melts formed by >90% fractional crystallization and having water contents >1.0 wt.%. This water-rich vapor may be preserved as water-rich vesicles in erupted fractionated lavas or as trapped water-rich vapor inclusions in late stage minerals in oceanic gabbros, such as apatite.

The differences in degassing paths for open versus closed system degassing are shown in Figures 16 and 17. During open system degassing, the vapor is effectively removed from the system after each degassing step; therefore, the system has no "memory" of the initial conditions as degassing proceeds. Thus, the open system degassing paths are identical for melts initially having H_2O contents of 1.0 wt.% and CO_2 contents of 500 ppm and 1.0 wt.%. In general during open system degassing, CO_2 is rapidly removed from the melt with negligible loss of water until the H_2O solubility is reached; for a melt initially containing 1 wt.% H_2O, significant water loss (10% of the initial H_2O) does not occur until a pressure of 80 bars is reached. The closed system degassing path for melt with an initial volatile content of 1.0 wt.% H_2O and 500 ppm CO_2 is similar to the open system case (10% of the initial H_2O has been lost by 95 bars), because the concentration of CO_2 is small compared to the that of H_2O. Also shown on Figure 16, is the closed system degassing path for a melt initially having equal concentrations (1 wt.%) of H_2O and CO_2. In this case, significant water loss occurs at higher pressures (10% of the initial H_2O has been lost by 450 bars) than the open system cases, because the large volume of exsolved CO_2 remains in contact with

the melt, requiring exsolution of more H_2O to produce the appropriate f_{H_2O} to be in equilibrium with the melt.

Figure 17 shows CO_2 versus H_2O for open and closed system degassing. Degassing paths are comparable to the dashed lines on Figure 14. Results for open system degassing (dashed lines) are identical regardless of the initial CO_2 concentration. During closed system degassing, degassing paths are a strong function of initial H_2O and CO_2 concentrations. The pressure at which significant loss of water begins increases as the initial concentration of CO_2 increases.

The results of these calculations are qualitatively similar to those of Shilobreyeva et al. (1983), Gerlach (1986), and Newman (1989, 1990) for basaltic systems and by Newman et al. (1988) for rhyolitic systems, but are based specifically on the thermodynamic models for water and carbon dioxide in mid-ocean ridge basalt at 1200°C as determined in this study. Predictions based on these calculations will be tested by examination of the variation in H_2O and CO_2 contents in suites of natural basaltic glasses (Chapters 2 and 3).

6. Conclusions

A series of experiments have been performed to determine the solubilities of H_2O and CO_2 and the nature of their mixing behavior in basaltic liquid at temperature and pressures relevant to seafloor eruption. The major conclusions of the study are:

1) Molar absorptivities for basaltic glass for the 4500 cm^{-1} band for hydroxyl groups and for the 5230 and 1630 cm^{-1} bands of molecular water were calibrated to be 0.67 ± 0.04, 0.62 ± 0.08, and 25 ± 3 L/mole-cm, respectively.

2) Both molecular water and carbon dioxide appear to follow Henry's law over the range of vapor compositions and pressures (<1 kbar) investigated.

3) Experimental results for water solubility in MORB at pressures from 200-980 bars, a range relevant to seafloor eruption, are consistent with those of previous studies

at higher pressures. Total water concentrations and the speciation of water in vapor-saturated basaltic melt are fit by a regular ternary solution model with the coefficients for albitic glasses, where the activity of water in the melt is given by Henry's law for molecular water. At pressures higher than about 1 kbar, the effect of the molar volume of water in the melt ($V^{0,m}_{H_2O}$) on the activity of water in vapor-saturated melts is no longer negligible; a ($V^{0,m}_{H_2O}$) of ~12 cm^3/mole fits the data of Hamilton et al. (1964).

4) Water does not enhance the solubility of CO_2 in basaltic melts over the pressures (200-980 bars) and temperature (~1200° C) investigated.

5) These results provide a simple basis for interpreting the water and carbon contents of submarine magmas and for assessing factors controlling degassing on ascent and emplacement.

7. Acknowledgements

This work was supported by NSF grant NSF EAR-8811406. I would like to thank David Joyce, Tom Stanton, Gordon Moore, Hanna Nevaskil, Gisli Gimundsson, Tracy Paul, Jeff Roberts, Vivian Pan, and Alison Pawley at ASU and George Rossman, Sieger Van der Laan, John Beckett, Mike Baker, Sally Newman, Phil Ihinger, David Bell, Diane Knott, and Laurie Watson at Caltech for their assistance and support.

References

Armstrong, J.T. (1982) New ZAF and a-factor correction procedures for the quantitative analysis of individual microparticles. *in* K.F.J. Heinrich, Ed., Microbeam Analysis -- 1982, San Francisco Press, San Francisco, pp. 175-180.

Armstrong, J.T. (1988) Quantitative analysis of silicate and oxide materials: Comparison of Monte Carlo, ZAF, and $\phi(\rho z)$ procedures. *in* D.E. Newbury, Ed., Microbeam Analyses -- 1988, San Francisco Press, San Francisco, pp. 239-246.

Bartholomew, R.F, B.L. Butler, H.L. Hoover, and C.K. Wu (1980) Infrared spectra of a water-containing glass. Am. Cer. Soc. J., **63,** 481-485.

Bell, P.M., H.K. Mao, and R.A. Weeks (1976) Optical spectra and electron paramagnetic resonance of lunar and synthetic glasses: A study of the effects of controlled atmosphere, composition, and temperature. Proc. Lunar Sci. Conf. **7**th, 2543-2559.

Bevington, P.R. (1969) Data reduction and error analysis for the physical sciences. McGraw-Hill, New York, p. 336.

Bigeleisen, J., M.L Perlman, and H.C. Prosser (1952) Conversion of hydrogenic materials to hydrogen for isotopic analysis. Analyt. Chem., **24**, 1356-1357.

Brey, G.P. and D.H. Green (1975) The role of CO_2 in the genesis of olivine melilitite. Contrib. Mineral. Petrol., **49**, 93-103.

Brey, G.P. and D.H. Green (1976) Solubility of CO_2 in olivine melilitite at high pressures and role of CO_2 in the Earth's upper mantle. Contrib. Mineral. Petrol, **55**, 217-230.

Burnham, C.W. and N.F. Davis (1971) The role of H_2O in silicate melts: I. P-V-T relations in the system NaAlSi3O8-H2O to 1 kilobars and 1000°C, Am. J. Sci., **270**, 54-79.

Burnham, C.W., J.R. Holloway, and N.F. Davis (1969) Thermodynamic properties of water to 1000°C and 10,000 bars. Geol. Soc. Amer. Spec. Paper **132**, 96 pp.

Byers, C.D., D.W. Muenow, and M.O. Garcia (1983) Volatiles in basalts and andesites from the Galapagos spreading center, 85° to 86°W. Geochim. Cosmochim. Acta, **47**, 1551-1558.

Byers, C.D., D.M. Christie, D.M. Muenow, and J.M. Sinton (1984) Volatile contents and ferric-ferrous ratios of basalt, ferrobasalt, andesite and rhyodacite glasses from the Galapagos 95.5°W propagating rift. Geochim. Cosmochim. Acta, **48**, 2239-2245.

Carmichael, I.S.E. and M.S. Ghiorso (1986) Oxidation-reduction relations in basic magma: A case for homogeneous equilibria. Earth Planet. Sci. Lett., **78**, 200-210.

Christie, D.M., I.S.E. Carmichael, and C.H. Langmuir (1986) Oxidation states of mid-ocean ridge basalt glasses. Earth Planet. Sci. Lett., **79**, 397-411.

Deines, P., R. H. Nafziger, G.C. Ulmer, E. Woermann (1974) Temperature-oxygen fugacity tables for selected gas mixtures in the system C-H-O at one atmosphere total pressure. Bulletin of the Earth and Mineral Sciences Experiment Station, **88**, The Pennsylvania State University, University Park, Pennsylvania.

Delaney, J.R., D.W. Muenow, and D.G. Graham (1978) Abundance and distribution of water, carbon and sulfur in the glassy rims of submarine pillow basalts. Geochim. Cosmochim. Acta, **42**, 581-594.

Des Marais, D.J. (1985) Carbon exchange between the mantle and the crust, and its effect upon the atmosphere: Today compared to Archean time. Geophys. Monograph, **32**, 602-611.

Dixon, J. E., E. Stolper, and J. R. Delaney (1988) Infrared spectroscopic measurements of CO_2 and H_2O glasses in the Juan de Fuca Ridge basaltic glasses, Earth Planet. Sci. Lett., **90**, 87-104.

Eggler, D.H. and M. Rosenhauer (1978) Carbon dioxide in silicate melts: II. Solubilities of CO_2 and H_2O in $CaMgSi_2O_6$ (diopside) liquids and vapors at pressures to 40 kb. Amer. J. Sci., **278**, 64-94.

Fine, G. and E. Stolper (1986) Carbon dioxide in basaltic glasses: Concentrations and speciation. Earth Planet. Sci. Lett., **76**, 263-278.

Gerlach, T.M. (1986) Exsolution of H_2O, CO_2, and S during eruptive episodes at Kilauea Volcano, Hawaii. J. Geophys. Res., **91**, 12177-12185.

Goldman, D.S. and J.I. Berg (1980) Spectral study of ferrous iron in Ca-Al-borosilicate glass at room and melt temperatures, J. Non-Cryst. Solids, **38** & **39**, 183-188.

Grove, T.L. (1981) Use of FePt alloys to eliminate the iron loss problem in 1 atmosphere gas mixing experiments: theoretical and practical considerations. Contrib. Mineral. Petrol., **78**, 298-304.

Guggenheim, E.A. (1952) Mixtures. Oxford University Press, Oxford, 270 pp.

Hamilton, D.L., C.W. Burnham, and E.F. Osborn (1964) The solubility of water and effects of oxygen fugacity and water content on crystallization in mafic magmas. J. Petrol., **5**, 21-39.

Hodges, F.W. (1974) The solubility of H_2O in silicate melts. Carnegie Inst. Wash. Year Book, **73**, 251-255.

Holloway, J.R. (1971) Internally-heated pressure vessels. *in* Ulmer, G.C. (ed.) Research Techniques for high pressure and high temperature. New York: Springer-Verlag, pp. 217-258.

Holloway, J.R. (1977) Fugacity and activity of molecular species in supercritical fluids. *in* Fraser, D. (ed.) Thermodynamics in Geology. Boston: D. Reidel, pp. 161-181.

Holloway, J.R. and C.F. Lewis (1974) CO_2 solubility in hydrous albite liquid at 5 kbar. EOS, **55**, 483.

Holloway, J.R., V. Pan and G. Gudmundsson (1992) Melting experiments in the presence of graphite: Oxygen fugacity, ferric/ferrous ratio and dissolved CO_2. European Jour. Mineral. (in press).

Holloway, J.R., J.E. Dixon, and A.R. Pawley (1992) An internally-heated, rapid-quench vessel. Am. Mineral. (in press).

Ihinger, P.D. (1991) An experimental study of the interaction of water with granitic melt. Ph.D. thesis, California Institute of Technology, 188 pp.

Jambon, A. and J.L. Zimmermann (1987) Major volatiles from a North Atlantic MORB glass and calibration to He: A size fraction analysis. Chem. Geol., **62**, 177-189.

Joyce, D.B. and J.R. Holloway (1992) An experimental investigation of the thermodynamic properties of H_2O - CO_2 - NaCl fluids at high pressures and temperatures. Geochim. Cosmochim. Acta (submitted).

Kadik, A.A., Ye.B. Lebedev, and N.I. Khitarov (1971) Voda V silikatnykh rasplavov [Water in silicate melts]- Nauka, Moscow.

Kadik, A.A., O.A. Lukanin, Ye.B. Lebedev, and E.Ye. Korovughkina (1972) Solubility of H_2O and CO_2 in granite and basalt melts at high pressures. Geoch. Internat., **9**, 1041-1051.

Khitarov, N.I., E.B. Lebedev, E.V. Rengarten, and R.V. Arsenieva (1959) Comparative characteristics of the solubility of water in basaltic and granitic melts. Geoch. (Geokhimiya), **5**, 479-492.

Kilinc, A., I.S.E. Carmichael, M.L. Rivers, and R.O. Sack (1983) Ferric-ferrous ratio of natural silicate liquids equilibrated in air. Contrib. Mineral. Petrol., **83**, 136-140.

Killingley, J.S. and D.M. Muenow (1975) Volatiles from Hawaiian submarine basalts determined by dynamic high temperature mass spectrometry. Geochim. Cosmochim. Acta, **39**, 1467-1473.

Kress, V.C. and I.S.E. Carmichael (1991) The compressibility of silicate liquids containing Fe_2O_3 and the effect of composition, temperature, oxygen fugacity and pressure on their redox states. Contrib. Mineral. and Petrol., **108**, 82-92.

Lange, R. and I.S.E. Carmichael (1989) Ferric-ferrous equilibria in Na_2O-FeO-Fe_2O_3-SiO_2 melts: Effects of analytical techniques on derived partial molar volumes. Geochim. Cosmochim. Acta, **53**, 2195-2204.

Lange, R. and I.S.E. Carmichael (1990) Thermodynamic properties of silicate liquids with emphasis on density, thermal expansion and compressibility. *in* Modern Methods of Igneous Petrology: Understanding Magmatic Processes, Reviews in Mineralogy. **24**, 25-64.

Love, G., M.G. Cox, and V.D. Scott (1978) A versatile atomic number correction for electron-probe microanalysis. J. Phys., D **11**, 7-27.

Mathez, E.A. (1984) Influence of degassing on oxidation states of basaltic magmas. Nature, **310**, 371-375.

Mattey, D. (1991) Carbon dioxide solubility and carbon isotope fractionation in basaltic melt. Geochim. Cosmochim. Acta, **55**, 3467-3473.

Moore, J.G. (1965) Petrology of deep-sea basalt near Hawaii. Amer. J. Sci., **263**, 40-52.

Moore, J.G. (1970) Water content of basalt erupted on the ocean floor. Contrib. Mineral. Petrol., **28**, 272-279.

Moore, J.G. (1979) Vesicularity and CO_2 in mid-ocean ridge basalt. Nature, **282**, 250-253.

Moore, J.G. and J.-G. Schilling (1973) Vesicles, water, and sulfur in Reykjanes Ridge basalts. Contrib. Mineral. Petrol., **41**, 105-118.

Moore, J.G., J.N. Batchelder, and C.G. Cunningham (1977) CO_2-filled vesicles in mid-ocean basalt. J. Volcanol. Geotherm. Res., **2**, 309-327.

Mysen, B.O. (1976) The role of volatiles in silicate melts: Solubility of carbon dioxide and water in feldspar, pyroxene, and feldspathoid melts to 30 kb and 1625°C. Amer. J. Sci., **276**, 969-996.

Mysen, B.O. and D. Virgo (1980a) Solubility behavior of CO_2 in melts on the join $NaAlSi_3O_8$-$CaAl_2Si_2O_8$-CO_2 at high pressures and temperatures: A Raman spectroscopic study, Amer. Mineral., **65**, 1166-1175.

Mysen, B.O. and D. Virgo (1980b) Solubility mechanisms of carbon dioxide in silicate melts: A Raman spectroscopic study. Amer. Mineral., **65**, 885-899.

Nakamoto, K. (1978) Infrared and Raman spectra of inorganic and coordination compounds, 3rd edition. Wiley, New York, 448 pp.

Newman, S. (1989) Water and carbon dioxide contents in basaltic glasses from the Mariana Trough, EOS, Trans. Am. Geophys. Un. **70**, 1387.

Newman, S. (1990) Water and carbon dioxide contents of back arc basin basalts. V.M. Goldschmidt Conf. 1990 Prog. and Abstr., 69.

Newman, S., E.M. Stolper, and S. Epstein (1986) Measurement of water in rhyolitic glasses: Calibration of an infrared spectroscopic technique. Amer. Mineral., **71**, 1527-1541.

Newman, S., S. Epstein, and E. Stolper (1988) Water, carbon dioxide, and hydrogen isotopes in glasses from the ca. 1340 A.D. eruption of the Mono Craters, California: Constraints on degassing phenomena and initial volatile content. J. Volcanol. Geotherm. Res., **35**, 75-96.

Pan, V., J. R. Holloway and R. L. Hervig (1991) The pressure and temperature dependence of carbon dioxide solubility in tholeiitic basalt melts. Geochim. Cosmochim. Acta, **55**, 1587-1595.

Pawley, A.R. and J.R. Holloway (1991) Experimental study of the solubility of CO + CO_2 in basalt, with applications to early atmosphere/magma ocean equilibria. Lunar Planet. Sci. XXII, 1043-1044.

Pawley, A.R., J.R. Holloway, and P. McMillan (1992) The effect of oxygen fugacity on the solubility of carbon-oxygen fluids in basaltic melt. Earth and Planet. Sci. Lett. (submitted).

Prigogine, I. and R. Defay (1954) Chemical Thermodynamics. Everett, C.H. (trans). Longmans Green and Co., New York, 543 pp.

Reed, S.J.B. (1965) Characteristic fluorescence correction in electron-probe microanalysis. Brit. J. Appl. Phys., **16**, 913-926.

Sato, M. (1978) Oxygen fugacity of basaltic magmas and the role of gas-forming elements. Geophys. Res. Lett., **5**, 447-449.

Sato, M. and T.L. Wright (1966) Oxygen fugacities directly measured in magmatic gases. Science, **153**, 1103-1105.

Scholze, H. (1960) Zur Frage der Unterscheidung zwischen H_2O-Molekeln und OH-Gruppen in Gläsern und Mineralen. Naturwissenschaften, **47**, 226-227.

Scholze, H. (1966) Gasses and water in glass. Glass Industry, **47**, 546-551, 622-628.

Sharma, S.K. (1979) Structure and solubility of carbon dioxide in silicate glasses of diopside and sodium melilite composition at high pressures from Raman spectroscopic data, Carnegie Institute of Washington Year Book, **78**, 532-537.

Sharma, S.K., T.C. Hoering, and H.S. Yoder (1979) Quenched melts of akermanite compositions with and without CO_2-characterization by Raman spectroscopy and gas chromatography, Carnegie Institute of Washington Year Book, **78**, 537-542.

Shaw, H.R. (1964) Theroretical solubility of H_2O in silicate melts: quasi-crystalline models. J. Geol., **72**, 601-617.

Shilobreyeva, S.N., A.A. Kadik, and O.A. Lukanin (1983) Outgassing of ocean-floor magma as a reflection of volatile conditions in the magma generation region. Geokhimiya, **9**, 1257-1274.

Silver, L.A. (1988) Water in silicate glasses, Ph.D Thesis, California Institute of Technology, Pasadena, Ca, 310 pp.

Silver, L.A. and E. Stolper (1985) A thermodynamic model for hydrous silicate melts. J. Geol., **93**, 161-178.

Silver, L.A. and E.M. Stolper (1989) Water in albitic glasses. J. Petrol., **30**, 667-709.

Silver, L.A., P.D. Ihinger, and E.M. Stolper (1990) The influence of bulk composition on the speciation of water in silicate glasses. Contrib. Mineral. Petrol., **104**, 142-162.

Stolper, E. (1982a) Water in silicate glasses: An infrared spectroscopic study. Contrib. Mineral. Petrol., **81**, 1-17.

Stolper, E. (1982b) The speciation of water in silicate melts. Geochim. Cosmochim. Acta, **46**, 2609-2620.

Stolper, E. (1989) Temperature dependence of the speciation of water in rhyolitic melts and glasses. Amer. Mineral., **74**, 1247-1257.

Stolper, E.M. and J.R. Holloway (1988) Experimental determination of the solubility of carbon dioxide in molten basalt at low pressure. Earth Planet. Sci. Lett., **87**, 397-408.

Stolper, E., L.A. Silver, and R.D. Aines (1983) The effects of quenching rate and temperature on the speciation of water in silicate glasses (abs). EOS, **64**, 339.

Van der Laan, S.R. and A.F. Koster van Groos (1991) Platinum-rich alloys in experimental petrology applied to high pressure research on hydrous iron-bearing systems. Amer. Mineral., **76**, 1920-1929.

Wasserburg, G.J. (1957) The effect of H_2O in silicate systems. J. Geol., **65**, 15-23.

Wilson, A.D. (1960) The micro-determination of ferrous iron in silicate minerals by a volumetric and a colormetric method. Analyst, **85**, 823-827.

Table 1: Experiment Summary

Run	Comments	P (bars)	T (°C)	±°C	Run duration	rev?	Fe-loss control	Fe in foil (wt. %)	f_{O_2} control	X_{H_2}	Quench rate (°C/sec)
JED 7H	IHPV	206	1196	16	2 hrs 30 min	no	Fe-Pt alloy foil	7.7	Shaw membrane	1.95	~8
JED 8H	IHPV	201	1205	16	5 hrs	yes	Fe-Pt alloy foil	8.2	Shaw membrane	2.10	"
JED 9H	IHPV	300	1200	15	4 hrs 30 min	yes	Fe-Pt alloy foil	6.9	Shaw membrane	1.93	"
JED 17H	RQ-IHPV	717	1182	27	3 hr	no	Fe-Pt alloy foil	9.2	H_2/Ar mix	1.49	100s
JED 17M	RQ-IHPV, 1	717	1182	27	3 hr	no	Fe-Pt alloy foil	9.39	H_2/Ar mix	1.49	"
JED 18M	RQ-IHPV, 1	980	1197	1	3 hrs 5 min	no	Fe-Pt alloy foil	7.7	H_2/Ar mix	1.49	"
JED 20H	RQ-IHPV	310	1199	6	6 hrs	yes	Fe-Pt alloy foil	8.62	H_2/Ar mix	1.49	"
JED 20M	RQ-IHPV	310	1199	6	6 hrs	yes	Fe-Pt alloy foil	8.55	H_2/Ar mix	1.49	"
JED 21H	RQ-IHPV	507	1198	4	5 hrs 30 min	yes	Fe-Pt alloy foil	5.99	H_2/Ar mix	1.49	"
JED 21M	RQ-IHPV	507	1198	4	5 hrs 30 min	yes	Fe-Pt alloy foil	8.08	H_2/Ar mix	1.49	"
JED 32A	RQ-IHPV	515	1199	5	2 hrs	no	pure Pt garbage can		pure Ar	0	"
JED 33A	RQ-IHPV, 1	503	1197	7	2 hrs	no	pure Pt garbage can		pure Ar	0	"
JED 33B	RQ-IHPV, 1	503	1197	7	2 hrs	no	pure Pt garbage can		pure Ar	0	"
JED 34B	RQ-IHPV, 1	507	1199	5	2 hrs	no	pure Pt garbage can		pure Ar	0	"
JED 35B	RQ-IHPV, 1	504	1196	8	2 hrs	no	pure Pt garbage can		pure Ar	0	"

Notes: IHPV means runs were performed in a conventional internally heated pressure vessel. RQ-IHPV runs were performed in a rapid quench internally heated pressure vessel. 1 indicates that vapor was lost from the capsule during or after quench as determined by bead of water on outside of capsule, sometimes with CO_2 bubbles still streaming through, or by audible hiss of vapor loss upon puncture of capsule.

Table 1 (cont.)

Run	starting material	basalt added (g)	H_2O added (g)	oxal. acid dihyd. added (g)	oxalic acid added (g)	Ag-oxalate added (g)	tot. H_2O+CO_2 added (g)	wt. loss after run (g)
JED 7	powdered TT152-21-35,	0.09090	0.0026	0	0	0	0.0026	0
JED 8	QFM-3, 960°C, 20 hrs	0.09059	0.0042	0	0	0	0.0042	0
JED 9	"	0.09070	0.0038	0	0	0	0.0038	0.0012
JED 17H	"	0.10135	0.01029	0	0	0	0.01029	0
JED 17M	"	0.10086	0	0	0.01235	0	0.01207	0.00078
JED 18M	"	0.09218	0	0.0177	0	0	0.0174	?
JED 20H	"	0.07125	0.006	0	0	0	0.0060	0
JED 20M	"	0.07090	0	0.00613	0	0	0.0060	0
JED 21H	"	0.08900	0.00877	0	0	0	0.00877	0
JED 21M	"	0.09282	0	0.01028	0	0	0.00992	0.0001
JED 32A	powdered TT152-51-3,	0.04186	0.00086	0	0	0.02804	0.0090	?
JED 33A	NiNiO, 900°C, 36hrs	0.04435	0.00127	0	0	0.02031	0.00715	0.00597
JED 33B	"	0.05330	0.00306	0	0	0.00868	0.00558	0.00382
JED 34B	"	0.05297	0.0029	0	0	0.00515	0.0044	0.002
JED 35B	"	0.07212	0.0093	0	0	0.01812	0.00607	0.00514

Notes: H_2O added as pure distilled H_2O. Oxalic acid dihydrite: $H_2C_2O_4 \cdot 2H_2O$. Oxalic acid: $H_2C_2O_4$. Ag-Oxalate: $Ag_2C_2O_4$. A "?" for weight loss indicates that portion of capsule of unknown weight sintered to capsule holder causing rupture of capsule when removing it from run assembly.

Table 1 (cont.)

Run	H_2O added (moles)	CO_2 added (moles)	X_{H_2O}-vapor, initial	X_{CO_2}-vapor, initial	vapor comp.	X_{H_2O}-vapor, final	X_{CO_2}-vapor, final
JED 7	0.00014	0	1	0	pure H_2O added	1	0
JED 8	0.00023	0	1	0	pure H_2O added	1	0
JED 9	0.00021	0	1	0	pure H_2O added	1	0
JED 17H	0.00057	0	1	0	pure H_2O added	1	0
JED 17M	0	0.000137	0	1	mol. H_2O in melt	0.075	0.925
JED 18M	0.000281	0.000281	0.5	0.5	mass balance	0.416	0.584
JED 20H	0.000333	0	1	0	pure H_2O added	1	0
JED 20M	0.000097	0.000097	0.5	0.5	manometry	0.387	0.613
JED 21H	0.000487	0	1	0	pure H_2O added	1	0
JED 21M	0.00016	0.00016	0.5	0.5	manometry	0.405	0.595
JED 32A	0.000048	0.000185	0.206	0.794	mol. H_2O in melt	0.138	0.862
JED 33A	0.00007	0.000134	0.343	0.657	mol. H_2O in melt	0.238	0.762
JED 33B	0.00017	0.000057	0.749	0.251	mol. H_2O in melt	0.615	0.385
JED 34B	0.000161	0.000034	0.826	0.174	mol. H_2O in melt	0.580	0.420
JED 35B	0.000052	0.000119	0.242	0.758	mol. H_2O in melt	0.055	0.945

Table 1 (cont.)

Run	f_{H_2O} (bars)	f_{CO_2} (bars)	$f^{\circ}_{H_2O}$ (bars)	$f^{\circ}_{CO_2}$ (bars)	FeO* (wt. %)	FeO (wt. %)	Fe_2O_3 (wt. %)
JED 7	204.9	0	204.9		12.0 assumed	9.57	2.70
JED 8	200	0	200		12.0 assumed	9.71	2.54
JED 9	298.1	0	298.1		12.0 assumed	8.72	9.69
JED 17H	709.2	0	709.2		13.07	9.41	4.06
JED 17M	47.2	775.1	709.2	838.5	12.13	10.02	2.34
JED 18M	377.4	689.7	972.7	1214	11.46	9.79	1.86
JED 20H	308.3	0	308.3		11.85	9.47	2.64
JED 20M	116	201	308.3	331.2	11.94	6.56	5.98
JED 21H	503.2	0	503.2		11.39	9.11	2.53
JED 21M	195.6	330.9	503.2	565.4	11.89	10.00	2.09
JED 32A	65	495.1	511.1	575.4	10.08		
JED 33A	111.4	424.8	499.3	560.5	10.39	4.15	6.79
JED 33B	301.5	207.2	499.3	560.5	10.26	1.95	9.23
JED 34B	285.7	229.1	503.2	565.4	9.88	0.48	10.44
JED 35B	25	530.7	500.2	561.7			

Notes: All fugacities were calculated using a modified Redlich-Kwong equation of state (Holloway, 1977). f_{H_2O} and f_{CO_2} calculated using final mole fractions of H_2O and CO_2 in the vapor, $f^{\circ}_{H_2O}$ and $f^{\circ}_{CO_2}$ calculated for pure H_2O and CO_2 vapor phase compositions.

Table 2: Major element compositions, oxygen fugacities, and densities of quenched basaltic glasses

Run (#avg.)	17H (6)	17M (8)	18M (7)	20H (5)	20M (6)	21H (5)	21M (4)	32A (4)	33A (2)	28B (4) (failed)	29B (5) (failed)	32B (4) (failed)	TT152-21-35 (start. mat.)	TT152-51-3 (start. mat.)
SiO_2	49.03	50.84	50.86	50.88	50.73	50.29	50.65	48.87	49.77	52.08	55.71	49.41	50.81	50.53
TiO_2	1.78	1.85	1.76	1.70	1.77	1.76	1.74	1.40	1.49	1.55	1.48	1.46	1.84	1.61
Al_2O_3	13.57	14.10	13.92	14.06	14.03	13.92	14.03	14.47	14.82	15.62	16.37	14.71	13.70	14.87
FeO*	13.07	12.13	11.46	11.85	11.94	11.39	11.88	10.08	10.39	5.77	1.86	10.68	12.44	11.93
MgO	6.72	6.87	6.73	6.82	6.82	6.74	6.69	7.09	7.20	7.94	6.97	7.16	6.67	6.43
CaO	10.69	11.03	10.75	10.95	10.98	10.86	10.87	11.83	12.06	13.42	12.42	12.12	11.53	12.29
Na_2O	2.54	2.64	2.58	2.72	2.59	2.63	2.62	2.72	2.76	2.88	3.33	2.68	2.68	2.98
K_2O	0.08	0.09	0.08	0.08	0.09	0.07	0.08	0.09	0.11	0.13	0.20	0.11	0.15	0.15
MnO	0.20	0.22	0.21	0.22	0.23	0.24	0.22	0.19	0.21	0.23	0.20	0.19	0.22	0.20
H_2O	2.56	0.50	1.85	1.74	1.05	2.42	1.43	0.91	0.86	0.38	0.46	0.61		
CO_2	0.00	0.03	0.03	0.00	0.01	0.00	0.01	0.02	0.02	0.01	0.01	0.01		
Total	100.24	100.3	100.23	101.02	100.24	100.32	100.22	97.67	99.69	100.01	99.01	99.14	100.04	100.99
FeO	9.41	10.02	9.79	9.47	6.56	9.11	10.00		4.15					
Fe_2O_3	4.07	2.34	1.86	2.64	5.98	2.53	2.09		6.93					
log f_{O_2}	-6.72	-7.93	-8.13	-7.38	-5.01	-7.37	-7.94		-5.92					
ρ (g/cm^3)	2.86	2.88	2.83	2.84	2.86	2.83	2.85	2.84	2.84	2.77	2.66	2.86		

Notes: FeO* is total iron as FeO. FeO determined by wet chemistry (see text), Fe_2O_3 determined by (FeO*-FeO)/0.9. Oxygen fugacities calculated using Kilinc et al. (1983). Glass densities calculated using Gladstone-Dale rule and the Church-Johnson equation as described by Silver (1988). Major element analyses of starting materials courtesy of J. Delaney (unpublished data).

Table 3: Molar Absorptivity Calibration for Molecular Water and Hydroxyl Groups

Calibration	ε^{5230}	ε^{4500}	ε^{1630}
mol. water^{5230} + OH^{4500} = tot. water^{3550}	0.62 ± 0.08	0.65 ± 0.06	
mol. water^{1630} + OH^{4500} = tot.water^{3550}		0.68 ± 0.06	25 ± 3
mol. water^{1630} = mol. water^{5230}	from 1		25 ± 3
Mean values	0.62 ± 0.08	0.67 ± 0.04	25 ± 3

Table 4: Spectroscopic data for total water, molecular water, and hydroxyl groups

Run	Thick. (μm)	3550 cm^{-1} Abs	3550 cm^{-1} H_2O (wt. %)	X_{H_2O}	5230 cm^{-1} Abs	5230 cm^{-1} H_2O, mol (wt. %)	$X_{H_2O,\ mol}$	4500 cm^{-1} Abs	4500 cm^{-1} OH (wt. %)	X_{OH}	1630 cm^{-1} Abs	1630 cm^{-1} H_2O, mol (wt. %)	$X_{H_2O,\ mol}$
7H	170	1.2680	1.272	0.0255	0.00277	0.282	0.0057	0.00931	0.878	0.0352			
7H	132	1.2390	1.243	0.0249	0.00246	0.251	0.0051	0.00948	0.895	0.0358			
7H	160	1.2560	1.261	0.0253	0.00253	0.257	0.0052	0.00989	0.933	0.0374			
7H	172	1.2650	1.268	0.0254	0.00266	0.271	0.0055	0.00967	0.912	0.0365			
7H	32	1.2700	1.274	0.0255									
7H	31	1.3310	1.335	0.0268									
7H	32	1.2890	1.294	0.0259									
8H	190	1.3590	1.364	0.0273	0.00331	0.338	0.0068	0.00962	0.908	0.0363			
8H	197	1.5680	1.572	0.0314	0.00414	0.422	0.0085	0.01041	0.982	0.0391			
8H	51	1.1610	1.169	0.0235							0.122	0.3074	0.0062
8H	156	1.4420	1.447	0.0290	0.00331	0.338	0.0068	0.01040	0.981	0.0392			
8H	153	1.7250	1.731	0.0345	0.00342	0.349	0.0071	0.01060	1.001	0.0400			
8H	84	1.3820	1.387	0.0278									
8H	82	1.3430	1.347	0.0270									
9H	153	1.8530	1.872	0.0373	0.00528	0.542	0.0110	0.01247	1.184	0.0470			
9H	103										0.15920	0.405	0.0082
9H	254				0.00501	0.514	0.0104	0.01199	1.140	0.0453			
9H	58	1.7100	1.729	0.0345							0.18620	0.474	0.0096
9H	83	1.4360	1.451	0.0290							0.17830	0.454	0.0092
9H	132	1.7500	1.768	0.0353									
9H	133	1.7820	1.801	0.0359									
9H	97	1.6990	1.717	0.0343									
9H	84	1.6000	1.617	0.0323									
9H	77	1.7250	1.743	0.0348									
9H	78	1.7900	1.809	0.0361									
9H	67	1.8150	1.834	0.0366									
9H	70	1.8110	1.830	0.0365									
17H	58	1.6970	1.709	0.0341							1.697	1.7086	0.0341
17H	58	1.6910	1.703	0.0340							1.691	1.7027	0.0340
17H	56	1.7300	1.742	0.0348							1.730	1.7421	0.0348
17H	58	1.6810	1.693	0.0338							1.681	1.6928	0.0338
17H	287				0.00485	0.496	0.0100	0.01194	1.131	0.0449			
17H	274				0.00453	0.464	0.0094	0.01178	1.116	0.0444			
17H	287				0.00433	0.443	0.0090	0.01211	1.147	0.0456			
17H	291				0.00451	0.461	0.0093	0.01174	1.112	0.0442			

Notes: Absorbance data normalized to a sample thickness of 100 μm. Mole fractions of dissolved water species are calculated on a single oxygen basis as follows:

(1) the mole fraction of total water in the melt (X_B) and the mole fraction of molecular water in the melt are calculated by:

$$X^m_{H_2O} = \frac{wt\%\ H_2O / 18.015}{\left(wt\%\ H_2O / 18.015 + (100 - wt\%\ H_2O) / 36.594 \right)}$$

(2) the mole fraction of OH in the melt is calculated by:

$$X^m_{OH} = 2\left(X_B - X^m_{H_2O,\,mol} \right)$$

Table 4 (cont.)

Run	Thick. (μm)	3550 cm^{-1} Abs	3550 cm^{-1} H_2O (wt. %)	X_{H_2O}	5230 cm^{-1} Abs	5230 cm^{-1} H_2O, mol (wt. %)	X_{H_2O}, mol	4500 cm^{-1} Abs	4500 cm^{-1} OH (wt. %)	X_{OH}	1630 cm^{-1} Abs	1630 cm^{-1} H_2O, mol (wt. %)	X_{H_2O}, mol
20H	58	1.6970	1.709	0.0341							0.20590	0.522	0.0106
20H	58	1.6910	1.703	0.0340							0.19860	0.504	0.0102
20H	56	1.7300	1.742	0.0348							0.18750	0.476	0.0096
20H	58	1.6810	1.693	0.0338							0.19050	0.475	0.0096
20H	287				0.00485	0.496	0.0100	0.01194	1.131	0.0449			
20H	274				0.00453	0.464	0.0094	0.01178	1.116	0.0444			
20H	287				0.00433	0.443	0.0090	0.01211	1.147	0.0456			
20H	291				0.00451	0.461	0.0093	0.01174	1.112	0.0442			
21H	68	2.1350	2.158	0.0429									
21H	64	2.2370	2.261	0.0449									
21H	56	2.2070	2.230	0.0443									
21H	65	2.1910	2.213	0.0440							0.35200	0.896	0.0180
21H	66	2.2060	2.229	0.0443							0.37210	0.948	0.0191
21H	232				0.00806	0.828	0.0167	0.01520	1.444	0.0568			
21H	230				0.00792	0.813	0.0164	0.01404	1.334	0.0526			
21H	230				0.00828	0.850	0.0171	0.01389	1.320	0.0520			
21H	259				0.00805	0.827	0.0167	0.01368	1.300	0.0512			
21H	228				0.00850	0.872	0.0176	0.01372	1.304	0.0514			
17M	168	0.4518	0.448	0.0091							0.00833	0.021	0.0004
17M	178	0.4955	0.492	0.0099							0.01011	0.025	0.0005
17M	176	0.4943	0.491	0.0099							0.01136	0.028	0.0006
17M	202	0.4916	0.488	0.0099							0.01188	0.030	0.0006
17M	168	0.4488	0.445	0.0090	0.00020	0.020	0.0004	0.00371	0.346	0.0140			
17M	178	0.4955	0.492	0.0099	0.00024	0.024	0.0005	0.00391	0.365	0.0148			
17M	176	0.4966	0.493	0.0100	0.00027	0.027	0.0006	0.00437	0.408	0.0165			
17M	202	0.5094	0.506	0.0102									
18M	64	1.8047	1.823	0.0364									
18M	64	1.8234	1.842	0.0367									
18M	62	1.8484	1.868	0.0372									
18M	64	1.7813	1.800	0.0359									
18M	64	1.7906	1.810	0.0361									
18M	270				0.00493	0.506	0.0102	0.01531	1.454	0.0576	0.20070	0.511	0.0103
18M	271				0.00462	0.474	0.0096	0.01694	1.716	0.0679	0.20300	0.517	0.0104
18M	290				0.00548	0.563	0.0114	0.01452	1.380	0.0546	0.20900	0.532	0.0107
18M	300				0.00524	0.538	0.0109	0.01275	1.211	0.0481	0.20470	0.521	0.0105
18M	298				0.00449	0.461	0.0093	0.01459	1.386	0.0550	0.19660	0.501	0.0105

Table 4 (cont.)

Run	Thick. (μm)	3550 cm^{-1} Abs	3550 cm^{-1} H_2O (wt. %)	X_{H_2O}	5230 cm^{-1} Abs	5230 cm^{-1} H_2O, mol (wt. %)	$X_{H_2O,\ mol}$	4500 cm^{-1} Abs	4500 cm^{-1} OH (wt. %)	X_{OH}	1630 cm^{-1} Abs	1630 cm^{-1} H_2O, mol (wt. %)	$X_{H_2O,\ mol}$
20M	78	1.0744	1.074	0.0216									
20M	79	1.0785	1.078	0.0217									
20M	82	1.0634	1.063	0.0214									
20M	80	1.0725	1.072	0.0215									
20M	76	1.0158	1.015	0.0204									
20M	222	1.0248	1.025	0.0206							0.06495	0.164	0.0033
20M	174	0.9655	0.965	0.0194							0.07010	0.177	0.0036
20M	200	1.0000	1.000	0.0201							0.06950	0.175	0.0036
20M	190	1.0053	1.005	0.0202							0.06990	0.176	0.0036
20M	203	0.9704	0.970	0.0195	0.00152	0.154	0.0031	0.00930	0.874	0.0351			
20M	222	1.0721	1.072	0.0215	0.00201	0.205	0.0041	0.00949	0.892	0.0358			
20M	174	1.0253	1.025	0.0206	0.00171	0.174	0.0035	0.00942	0.886	0.0355			
20M	200	1.0550	1.054	0.0212	0.00174	0.177	0.0036	0.00988	0.929	0.0373			
20M	190	1.0263	1.026	0.0206	0.00157	0.159	0.0032	0.00946	0.889	0.0357			
20M													
21M	75	1.4080	1.413	0.0283									
21M	75	1.4040	1.409	0.0282									
21M	73	1.4055	1.410	0.0282									
21M	71	1.3986	1.403	0.0281									
21M	236				0.00370	0.378	0.0076	0.01061	1.001	0.0399	0.13260	0.335	0.0068
21M	239				0.00298	0.304	0.0061	0.01178	1.111	0.0443	0.13350	0.338	0.0068
21M	235				0.00316	0.322	0.0065	0.01139	1.074	0.0429	0.13700	0.347	0.0070
21M	240				0.00315	0.321	0.0065	0.01109	1.047	0.0418	0.12920	0.327	0.0066
32A	179	0.7620	0.767	0.0155							0.03073	0.078	0.0016
32A	179	0.8648	0.871	0.0175	0.00093	0.095	0.0019	0.00703	0.665	0.0268			
32A	196	0.7551	0.760	0.0153							0.02985	0.076	0.0015
32A	194	0.7773	0.783	0.0158							0.03015	0.077	0.0016
32A	194	0.8634	0.870	0.0175	0.00085	0.087	0.0018	0.00836	0.792	0.0319			
32A	179	0.9318	0.939	0.0189	0.00100	0.102	0.0021	0.00762	0.722	0.0290			
33A	143	0.8140	0.819	0.0165							0.04378	0.111	0.0023
33A	141	0.8404	0.846	0.0170							0.04610	0.117	0.0024
33A	141	0.9504	0.957	0.0193	0.00160	0.163	0.0033	0.00766	0.725	0.0291			
33A	141	0.8298	0.835	0.0168							0.04681	0.119	0.0024
33A	141	0.9447	0.951	0.0191	0.00136	0.139	0.0028	0.00784	0.743	0.0299			
33A	159	0.8170	0.822	0.0166							0.04277	0.109	0.0022

Table 4 (cont.)

Run	Thick. (μm)	3550 cm^{-1} Abs	3550 cm^{-1} H_2O (wt. %)	X_{H_2O}	5230 cm^{-1} Abs	5230 cm^{-1} H_2O, mol (wt. %)	$X_{H_2O,\ mol}$	4500 cm^{-1} Abs	4500 cm^{-1} OH (wt. %)	X_{OH}	1630 cm^{-1} Abs	1630 cm^{-1} H_2O, mol (wt. %)	$X_{H_2O,\ mol}$
33A	159	0.9459	0.952	0.0192	0.00179	0.183	0.0037	0.00712	0.674	0.0271			
33A	163	0.7951	0.801	0.0161							0.04448	0.113	0.0023
33A	61	0.8287	0.834	0.0168							0.04393	0.112	0.0023
33A	59	0.8619	0.868	0.0175							0.04754	0.121	0.0024
33A	58	0.8095	0.815	0.0164							0.03790	0.096	0.0020
33A	64	0.8086	0.814	0.0164							0.03292	0.085	0.0017
33A	65	0.7639	0.769	0.0155							0.03000	0.076	0.0015
33A	61	0.9279	0.935	0.0188									
33A	58	0.9035	0.910	0.0183									
33B	27	1.6556	1.667	0.0333							0.17340	0.440	0.0089
33B	27	1.6611	1.672	0.0334							0.17340	0.440	0.0089
33B	28	1.6125	1.624	0.0324							0.16650	0.422	0.0085
33B	173	1.7156	1.727	0.0345	0.00429	0.439	0.0089	0.01316	1.246	0.0495			
34B	327										0.16150	0.410	0.0083
34B	322										0.16830	0.427	0.0086
34B	321										0.12150	0.308	0.0062
34B	42	1.4143	1.424	0.0285							0.12740	0.323	0.0065
34B	42	1.6321	1.644	0.0328							0.16910	0.429	0.0087
34B	42	1.4857	1.496	0.0299							0.14580	0.370	0.0075
34B	151	1.6172	1.627	0.0325	0.00424	0.434	0.0088	0.01324	1.254	0.0499	0.13840	0.351	0.0071
34B	151	1.6927	1.705	0.0340	0.00397	0.407	0.0082	0.01377	1.304	0.0518	0.15890	0.403	0.0082
34B	151	1.5974	1.608	0.0321	0.00397	0.407	0.0082	0.01351	1.279	0.0509	0.15890	0.403	0.0082
34B	150										0.17130	0.435	0.0088
35B	78	0.3500	0.348	0.0070							n.d.		
35B	76	0.3415	0.340	0.0069							n.d.		
35B	94	0.3862	0.384	0.0078							n.d.		
35B	88	0.3546	0.353	0.0071							n.d.		
35B	92	0.3571	0.348	0.0070							n.d.		
35B	94	0.4043	0.403	0.0082							n.d.		
35B	88	0.3852	0.383	0.0077							n.d.		

Table 5: Estimates of the partial molar volume of H_2O in silicate liquids

Composition	V_{H_2O} (cm^3/mol)	P range (kbars)	T range (°C)	Reference
$NaAlSi_3O_8$	17-22	3-8	1000	Burnham & Davis (1971)
$NaAlSi_3O_8$	~22	1-8	1000	Silver et al. (1990)
$KAlSi_3O_8$	~25	1-7	900-1340	Silver et al. (1990)
Ca-Al-silicate	~16	1-5	1180	Silver et al. (1990)
$CaMgSi_2O_6$	~17	20	1240	Hodges (1974)
Basalt	~12	1-8	1100-1200	this study
Rhyolite	~0	<1.5	850	Silver et al. (1990)

Table 6: Spectroscopic data for carbon dissolved as carbonate in the quenched basaltic glasses

Run	Spectrum	Thick. (μm)	Reference subtracted	1515 cm^{-1} Abs	1515 cm^{-1} ppm	1515 cm^{-1} X_{CO_2}	1430 cm^{-1} Abs	1430 cm^{-1} ppm	1430 cm^{-1} X_{CO_2}
17M	0.001	168	519	0.076429	311	2.58E-04	0.076667	312	2.58E-04
17M	0.002	178	519	0.075843	309	2.56E-04	0.077247	315	2.61E-04
17M	0.003	176	2135	0.071591	292	2.41E-04	0.078977	322	2.66E-04
17M	0.004	202	2135	0.071535	292	2.41E-04	0.072525	296	2.45E-04
18M	0.001	269	519	0.077323	321	2.62E-04	0.072862	302	2.46E-04
18M	0.001	269	2135	0.072119	299	2.44E-04	0.068401	284	2.32E-04
18M	0.002	271	519	0.070849	294	2.40E-04	0.064207	266	2.17E-04
18M	0.003	290	2135	0.067586	280	2.28E-04	0.061379	254	2.07E-04
18M	0.003	290	519	0.078621	326	2.66E-04	0.074828	311	2.53E-04
18M	0.004	300	2135	0.072000	299	2.44E-04	0.069000	286	2.33E-04
18M	0.004	300	519	0.074667	310	2.53E-04	0.065333	271	2.21E-04
18M	0.005	298	519	0.080201	332	2.71E-04	0.072819	302	2.46E-04
18M	0.005	298	2135	0.066443	275	2.25E-04	0.062081	257	2.10E-04
20M	0.001	222	0	0.013514	56	4.59E-05	0.018018	74	6.12E-05
20M	0.001	222	519	0.014189	58	4.75E-05	0.015946	66	5.40E-05
20M	0.002	174	0	0.019540	80	6.61E-05	0.021839	90	7.42E-05
20M	0.002	174	2135	0.016782	69	5.64E-05	0.017701	72	5.96E-05
20M	0.003	200	0	0.017000	70	5.72E-05	0.019000	78	6.45E-05
20M	0.003	200	2135	0.017750	72	5.96E-05	0.018000	73	6.04E-05
20M	0.003	200	2135	0.016200	67	5.48E-05	0.014700	61	5.00E-05
20M	0.004	190	0	0.015789	65	5.32E-05	0.020000	82	6.77E-05
20M	0.004	190	2135	0.018526	75	6.20E-05	0.018316	75	6.20E-05
20M	0.004	190	2135	0.018421	75	6.20E-05	0.021053	86	7.09E-05
20M	0.005	203	0	0.017734	72	5.96E-05	0.020690	85	7.01E-05
20M	0.005	203	2135	0.016010	66	5.40E-05	0.016010	66	5.40E-05
20M	0.005	203	2135	0.016010	66	5.40E-05	0.019704	81	6.69E-05
21M	0.001	236	0	0.031356	129	1.05E-04	0.033051	137	1.12E-04
21M	0.001	236	2135	0.030085	124	1.01E-04	0.030085	124	1.01E-04
21M	0.001	236	2135	0.029237	121	9.90E-05	0.029237	121	9.90E-05
21M	0.001	236	2135	0.031356	129	1.05E-04	0.031356	129	1.05E-04
21M	0.001	236	2135	0.029661	122	9.98E-05	0.029322	121	9.90E-05
21M	0.002	239	0	0.025105	103	8.45E-05	0.029289	121	9.90E-05
21M	0.002	239	2135	0.030126	124	1.01E-04	0.029289	121	9.90E-05

Notes: Absorbance data normalized to a sample thickness of 100 μm. For many samples, the background subtraction was checked by

comparing absorbances measured on the same spectrum but having a different decarbonated reference glass subtracted. 2135 is a devolatilized glass of TT152-21-35; 519 is a devolatilized glass of a Mid-Atlantic Ridge basaltic glass; 0 is no reference subtracted. The

mole fraction of CO_2 in the melt is calculated by: $$X^{m}_{CO_2} = \frac{ppmCO_2 \times 10^{-4} / 44.01}{\left(ppmCO_2 \times 10^{-4} / 44.01 + \left(100 - ppmCO_2 \times 10^{-4} - wt\%\ H_2O \right) / 36.594 \right)}$$

Table 6 (cont.)

Run	Spectrum	Thick. (μm)	Reference subtracted	1515 cm^{-1} Abs	1515 cm^{-1} ppm	1515 cm^{-1} X_{CO_2}	1430 cm^{-1} Abs	1430 cm^{-1} ppm	1430 cm^{-1} X_{CO_2}
21M	0.002	239	2135	0.031799	131	1.07E-04	0.032218	133	1.09E-04
21M	0.003	235	0	0.028085	116	9.5E-05	0.025532	105	8.62E-05
21M	0.003	235	2135	0.030638	126	1.03E-04	0.029787	123	1.01E-04
21M	0.003	235	2135	0.033957	140	1.14E-04	0.031404	130	1.06E-04
21M	0.003	235	2135	0.034894	143	1.18E-04	0.031915	132	1.08E-04
21M	0.004	240	0	0.029167	120	9.82E-05	0.030833	127	1.04E-04
21M	0.004	240	2135	0.030000	124	1.01E-04	0.029167	120	9.82E-05
32A	0.001	179	2135	0.044693	184	1.52E-04	0.051117	211	1.74E-04
32A	0.002	196	2135	0.045306	187	1.55E-04	0.051888	214	1.77E-04
32A	0.003	194	2135	0.049175	203	1.68E-04	0.054588	226	1.86E-04
33A	0.001	143	2135	0.045455	188	1.55E-04	0.046853	193	1.59E-04
33A	0.002	141	2135	0.043262	178	1.47E-04	0.049291	204	1.68E-04
33A	0.003	141	2135	0.043617	180	1.49E-04	0.047518	196	1.62E-04
33A	0.004	159	2135	0.043522	179	1.48E-04	0.047799	197	1.63E-04
33A	0.005	163	2135	0.045399	187	1.54E-04	0.050920	210	1.73E-04
33A	0.001	61	2135	0.048689	201	1.66E-04	0.049672	205	1.69E-04
33A	0.002	59	2135	0.049576	205	1.69E-04	0.054153	224	1.84E-04
33A	0.003	58	2135	0.045172	186	1.54E-04	0.053103	220	1.81E-04
33A	0.004	64	2135	0.042500	172	1.42E-04	0.051719	210	1.73E-04
33A	0.005	65	2135	0.044000	181	1.5E-04	0.052615	218	1.80E-04
33B	0.001	173	2135	0.015607	64	5.24E-05	0.017341	72	5.88E-05
33B	0.002	173	2135	0.013873	57	4.67E-05	0.016185	67	5.48E-05
33B	0.003	173	2135	0.011561	47	3.87E-05	0.015607	64	5.24E-05
34B	0.001	327	2135	0.014373	59		0.014373	59	
34B	0.002	322	2135	0.011180	46		0.015528	64	
34B	0.003	321	2135	0.016822	70		0.017757	73	
34B	0.004	42	2135	0.014286	59	4.85E-05	0.014286	59	4.85E-05
34B	0.001	151	2135	0.017219	71	5.81E-05	0.016556	68	5.56E-05
34B	0.002	151	2135	0.013245	55	4.51E-05	0.019868	82	6.69E-05
34B	0.003	151	2135	0.014570	60	4.92E-05	0.017881	74	6.05E-05
34B	0.004	150	2135	0.014667	60		0.014667	60	
35B	0.001	78	2135	0.045385	185	1.54E-04	0.048462	198	1.64E-04
35B	0.002	76	2135	0.054474	222	1.84E-04	0.057237	234	1.94E-04
35B	0.003	94	2135	0.055851	228	1.89E-04	0.059681	244	2.02E-04
35B	0.004	88	2135	0.049773	204	1.69E-04	0.053864	220	1.83E-04
35B	0.005	92	2135	0.057609	235	1.95E-04	0.059783	245	2.03E-04

Table 7: Summary of H_2O and CO_2 data

Run	f_{H_2O} (bars)	total H_2O 3550 cm^{-1} (wt. %)	H_2O, mol 5230 cm^{-1} (wt. %)	$X_{H_2O, mol}$	OH 4500 cm^{-1} (wt. %)	X_{OH}	total H_2O $OH+H_2O_{mol}$ (wt. %)	X_B	f_{CO_2}	CO_2 (ppm)	X_{CO_2}
35B	25	0.40 ± 0.01	n.d.	0	0.47 ± 0.06	0.0191	0.47	0.0095	530.7	223 ± 16	0.000186
17M	47.2	0.48 ± 0.02	0.02 ± 0.00	0.0005	0.37 ± 0.03	0.0151	0.4	0.008	775.1	306 ± 9	0.000255
32B	46.3	0.61 ± 0.01	0.07 ± 0.02	0.0014	0.50 ± 0.01	0.0203	0.57	0.0115			
32A	64.9	0.89 ± 0.04	0.09 ± 0.01	0.0019	0.73 ± 0.06	0.0292	0.82	0.0165	495.1	204 ± 16	0.00017
33A	111.1	0.95 ± 0.00	0.16 ± 0.02	0.0033	0.71 ± 0.04	0.0287	0.88	0.0177	424.8	197 ± 15	0.000164
20M	116	1.02 ± 0.04	0.18 ± 0.02	0.0035	0.89 ± 0.02	0.0359	1.07	0.0215	201	72 ± 7	0.00006
7H	204.9	1.28 ± 0.03	0.27 ± 0.01	0.0054	0.91 ± 0.02	0.0362	1.17	0.0235			
21M	195.6	1.41 ± 0.00	0.33 ± 0.03	0.0067	1.06 ± 0.05	0.0422	1.39	0.0278	330.9	125 ± 8	0.000104
8H	199.95	1.43 ± 0.18	0.36 ± 0.04	0.0073	0.97 ± 0.04	0.0386	1.33	0.0267			
34B	285.4	1.65 ± 0.05	0.42 ± 0.02	0.0084	1.28 ± 0.02	0.0509	1.69	0.0338	229.1	64 ± 6	0.000053
33B	301.9	1.73 ±	0.44 ±	0.0089	1.25 ±	0.0495	1.69	0.0336	207.2	62 ± 6	0.000052
20H	308.3	1.71 ± 0.02	0.47 ± 0.02	0.0094	1.13 ± 0.02	0.0448	1.59	0.0318			
18M	377.4	1.83 ± 0.03	0.51 ± 0.04	0.0103	1.43 ± 0.18	0.0567	1.94	0.0386	689.7	293 ± 20	0.000244
9H	298.05	1.74 ± 0.12	0.53 ± 0.02	0.0107	1.16 ± 0.03	0.0461	1.69	0.0337			
21H	503.2	2.23 ± 0.05	0.84 ± 0.02	0.0169	1.34 ± 0.06	0.0528	2.18	0.0433			
17H	709.2	2.49 ± 0.15	0.90 ± 0.07	0.0182	1.85 ± 0.05	0.0726	2.76	0.0544			

Table 8: Calculated water speciation and solubility data

P (bars)	f_{H_2O} (bars)	$X_{H_2O,\ mol}$	X_{OH}	X_B	H_2O, mol (wt.%)	OH (wt.%)	H_2O, total (wt.%)
1	1.000	0.00003	0.0044	0.00223	0.0015	0.1083	0.1099
5	4.999	0.00016	0.00942	0.00487	0.0076	0.2324	0.2401
10	9.998	0.00031	0.01293	0.00677	0.0153	0.3192	0.3346
25	24.986	0.00077	0.01932	0.01044	0.0381	0.4780	0.5165
50	49.946	0.00154	0.02577	0.01443	0.0760	0.6385	0.7155
100	99.794	0.00307	0.03374	0.01993	0.1512	0.8376	0.9913
200	199.238	0.00606	0.04314	0.02763	0.2993	1.0736	1.3796
300	298.426	0.00899	0.04914	0.03356	0.4446	1.2250	1.6809
400	397.460	0.01186	0.05353	0.03862	0.5872	1.3357	1.9393
500	496.407	0.01466	0.05693	0.04313	0.7273	1.4219	2.1707
600	595.386	0.01742	0.05967	0.04725	0.8650	1.4913	2.3832
700	694.481	0.02012	0.06193	0.05108	1.0006	1.5488	2.5817
800	793.781	0.02277	0.06384	0.05469	1.1340	1.5973	2.7692
900	893.376	0.02538	0.06549	0.05812	1.2656	1.6392	2.9482
1000	993.353	0.02794	0.06688	0.06138	1.3953	1.6747	3.1190
2000	2031.960	0.05182	0.07426	0.08895	2.6200	1.8630	4.5860
3000	3190.161	0.07377	0.07632	0.11192	3.7727	1.9156	5.8418
4000	4526.357	0.09489	0.07622	0.13300	4.9080	1.9131	7.0218
5000	6091.760	0.11579	0.07496	0.15327	6.0564	1.8809	8.1823

Fugacity of pure water was calculated using a modified Redlich-Kwong equation of state (Holloway, 1977). Activity of water in the melt ($X_{H_2O,\ mol}$) was calculated using Equation 16. Speciation and solubilities were calculated using a regular solution model (Equation 12).

Table 9: CO_2 solubility data

P (bars)	f_{CO_2} (bars)	CO_2 (ppm)
0	0.00	0
100	102.13	46
200	208.67	92
300	319.81	138
400	435.76	185
500	556.72	232
600	682.91	279
700	814.53	327
800	951.80	375
900	1095.00	423
1000	1244.20	472
2000	3127.11	982

Table 10: Summary of Saturation Values for Closed System Degassing

P (bars)	F closed	H_2O (wt.%)	CO_2 (ppm)	X_{H_2O} in vapor	X_{CO_2} in vapor	P (bars)	F closed	H_2O (wt.%)	CO_2 (ppm)	X_{H_2O} in vapor	X_{CO_2} in vapor
		0.100	500.0					0.300	500.0		
1000	0.991	0.100	473.0	0.000	1.000	1000	0.996	0.300	470.2	0.009	0.991
950	0.982	0.100	448.5	0.000	0.999	950	0.993	0.300	445.7	0.009	0.991
900	0.974	0.100	424.2	0.000	0.999	900	0.990	0.300	421.3	0.010	0.990
850	0.966	0.100	399.9	0.000	0.999	850	0.987	0.300	397.0	0.010	0.990
800	0.958	0.100	375.7	0.000	0.999	800	0.984	0.300	372.8	0.011	0.989
750	0.950	0.100	351.6	0.000	0.999	750	0.980	0.300	348.7	0.011	0.989
700	0.941	0.100	327.6	0.001	0.999	700	0.977	0.300	324.7	0.012	0.988
650	0.933	0.100	303.7	0.001	0.999	650	0.974	0.300	300.7	0.013	0.987
600	0.925	0.100	279.8	0.001	0.999	600	0.971	0.300	276.9	0.014	0.986
550	0.917	0.100	256.1	0.001	0.999	550	0.968	0.300	253.1	0.015	0.985
500	0.909	0.100	232.4	0.002	0.998	500	0.965	0.300	229.4	0.017	0.983
450	0.901	0.100	208.8	0.002	0.998	450	0.962	0.300	205.8	0.018	0.982
400	0.893	0.100	185.3	0.002	0.998	400	0.959	0.300	182.2	0.020	0.980
350	0.885	0.100	161.9	0.002	0.998	350	0.955	0.300	158.8	0.023	0.977
300	0.877	0.100	138.5	0.003	0.997	300	0.952	0.300	135.4	0.027	0.973
250	0.869	0.100	115.2	0.003	0.997	250	0.949	0.299	112.1	0.032	0.968
200	0.861	0.100	92.0	0.004	0.996	200	0.945	0.299	88.8	0.039	0.961
150	0.853	0.100	68.8	0.005	0.995	150	0.942	0.299	65.6	0.051	0.949
100	0.844	0.100	45.7	0.008	0.992	100	0.937	0.299	42.5	0.074	0.926
90	0.843	0.100	41.1	0.009	0.991	90	0.936	0.298	37.9	0.081	0.919
80	0.841	0.100	36.5	0.010	0.990	80	0.934	0.298	33.3	0.090	0.910
70	0.839	0.100	31.9	0.011	0.989	70	0.933	0.298	28.7	0.102	0.898
60	0.837	0.100	27.2	0.013	0.987	60	0.931	0.297	24.1	0.117	0.883
50	0.835	0.100	22.6	0.015	0.985	50	0.929	0.297	19.5	0.138	0.862
40	0.833	0.100	18.0	0.019	0.981	40	0.925	0.296	14.9	0.169	0.831
30	0.831	0.100	13.4	0.024	0.976	30	0.920	0.294	10.3	0.219	0.781
20	0.827	0.099	8.8	0.035	0.965	20	0.907	0.291	5.8	0.318	0.682
10	0.820	0.099	4.2	0.064	0.936	10	0.851	0.273	1.6	0.572	0.428
5	0.808	0.097	1.9	0.118	0.882	5	0.701	0.225	0.3	0.786	0.214
1	0.703	0.085	0.2	0.428	0.572	1	0.344	0.110	0.0	0.903	0.097

F is the fraction of volatiles remaining in the melt: $(H_2O^m + CO_2^m)/(H_2O^{tot} + CO_2^{tot})$.

Table 10 (cont.)

P (bars)	F closed	H_2O (wt.%)	CO_2 (ppm)	X_{H_2O} in vapor	X_{CO_2} in vapor	P (bars)	F closed	H_2O (wt.%)	CO_2 (ppm)	X_{H_2O} in vapor	X_{CO_2} in vapor
		0.600	500.0					1.000	500.0		
1000	0.997	0.600	457.8	0.037	0.963	1000	0.997	1.000	424.6	0.110	0.890
950	0.995	0.600	433.3	0.039	0.961	950	0.995	0.999	400.2	0.115	0.885
900	0.994	0.600	409.0	0.041	0.959	900	0.994	0.999	376.0	0.121	0.879
850	0.992	0.600	384.7	0.044	0.956	850	0.993	0.999	351.8	0.128	0.872
800	0.990	0.600	360.5	0.046	0.954	800	0.992	0.999	327.8	0.135	0.865
750	0.989	0.600	336.4	0.049	0.951	750	0.991	0.999	303.8	0.144	0.856
700	0.987	0.600	312.3	0.052	0.948	700	0.990	0.998	279.9	0.153	0.847
650	0.985	0.599	288.4	0.056	0.944	650	0.988	0.998	256.2	0.164	0.836
600	0.983	0.599	264.6	0.060	0.940	600	0.987	0.998	232.5	0.176	0.824
550	0.982	0.599	240.8	0.066	0.935	550	0.986	0.997	208.9	0.191	0.809
500	0.980	0.599	217.2	0.071	0.929	500	0.984	0.997	185.4	0.207	0.793
450	0.978	0.599	193.6	0.078	0.922	450	0.982	0.996	162.0	0.228	0.772
400	0.976	0.599	170.1	0.087	0.913	400	0.981	0.995	138.7	0.253	0.747
350	0.974	0.598	146.6	0.098	0.902	350	0.978	0.994	115.5	0.284	0.716
300	0.972	0.598	123.3	0.113	0.887	300	0.976	0.992	92.4	0.327	0.673
250	0.970	0.597	100.0	0.133	0.867	250	0.972	0.989	69.5	0.385	0.615
200	0.967	0.597	76.8	0.163	0.837	200	0.966	0.983	46.9	0.471	0.529
150	0.963	0.595	53.7	0.212	0.788	150	0.951	0.970	25.2	0.607	0.393
100	0.955	0.591	30.8	0.307	0.693	100	0.895	0.913	7.5	0.812	0.188
90	0.953	0.590	26.2	0.337	0.663	90	0.868	0.886	5.3	0.849	0.151
80	0.949	0.588	21.7	0.377	0.623	80	0.834	0.851	3.6	0.880	0.120
70	0.945	0.585	17.3	0.425	0.575	70	0.792	0.808	2.4	0.904	0.096
60	0.937	0.581	12.9	0.489	0.511	60	0.744	0.759	1.6	0.922	0.078
50	0.924	0.573	8.7	0.574	0.426	50	0.687	0.701	1.0	0.936	0.064
40	0.897	0.556	5.0	0.682	0.318	40	0.622	0.635	0.6	0.947	0.053
30	0.837	0.519	2.2	0.798	0.202	30	0.546	0.558	0.3	0.956	0.044
20	0.721	0.448	0.7	0.882	0.118	20	0.454	0.463	0.1	0.963	0.037
5	0.387	0.240	0.0	0.946	0.054	10	0.328	0.335	0.0	0.970	0.030
1	0.177	0.110	0.0	0.960	0.040	5	0.236	0.240	0.0	0.974	0.026
						1	0.108	0.110	0.0	0.978	0.022

Table 10 (cont.)

P (bars)	F closed	H_2O (wt.%)	CO_2 (ppm)	X_{H_2O} in vapor	X_{CO_2} in vapor	P (bars)	F open	H_2O (wt.%)	CO_2 (ppm)	X_{H_2O} in vapor	X_{CO_2} in vapor
								1.000	500.0		
1000	0.992	1.993	267.3	0.442	0.558	1000	0.997	1.000	424.5	0.000	1.000
950	0.990	1.991	244.0	0.463	0.537	950	0.996	1.000	400.2	0.000	1.000
900	0.989	1.989	220.8	0.486	0.515	900	0.994	0.999	375.9	0.117	0.883
850	0.987	1.987	197.9	0.511	0.489	850	0.993	0.999	351.8	0.063	0.937
800	0.986	1.984	175.1	0.539	0.461	800	0.992	0.999	327.7	0.119	0.881
750	0.984	1.981	152.5	0.571	0.429	750	0.991	0.999	303.8	0.120	0.880
700	0.981	1.977	130.2	0.605	0.395	700	0.990	0.999	279.9	0.122	0.879
650	0.978	1.971	108.3	0.644	0.356	650	0.989	0.999	256.1	0.219	0.781
600	0.973	1.963	86.9	0.686	0.314	600	0.988	0.998	232.4	0.176	0.824
550	0.967	1.950	66.4	0.736	0.264	550	0.987	0.998	208.8	0.225	0.775
500	0.956	1.930	47.4	0.790	0.210	500	0.985	0.998	185.3	0.182	0.818
450	0.939	1.896	31.0	0.845	0.155	450	0.984	0.998	161.8	0.234	0.766
400	0.910	1.838	18.7	0.892	0.108	400	0.983	0.997	138.4	0.240	0.760
350	0.868	1.753	10.9	0.925	0.075	350	0.982	0.997	115.1	0.293	0.707
300	0.813	1.643	6.4	0.946	0.054	300	0.980	0.997	91.9	0.308	0.692
250	0.749	1.514	3.7	0.960	0.040	250	0.979	0.996	68.8	0.442	0.558
200	0.676	1.365	2.1	0.969	0.031	200	0.977	0.995	45.7	0.488	0.512
150	0.591	1.194	1.1	0.975	0.025	150	0.975	0.994	22.8	0.682	0.318
100	0.489	0.988	0.4	0.980	0.020	100	0.967	0.987	0.5	0.989	0.011
90	0.466	0.941	0.3	0.981	0.019	90	0.925	0.944	0.0	1.000	0.000
80	0.441	0.890	0.2	0.982	0.018	80	0.875	0.893	0.0	1.000	0.000
70	0.414	0.837	0.2	0.983	0.017	70	0.822	0.839	0.0	1.000	0.000
60	0.386	0.779	0.1	0.984	0.016	60	0.765	0.780	0.0	1.000	0.000
50	0.354	0.716	0.0	0.984	0.016	50	0.702	0.716	0.0	1.000	0.000
40	0.319	0.645	0.0	0.985	0.015	40	0.632	0.645	0.0	1.000	0.000
30	0.279	0.563	0.0	0.986	0.014	30	0.552	0.563	0.0	1.000	0.000
20	0.230	0.465	0.0	0.987	0.013	20	0.456	0.465	0.0	1.000	0.000
5	0.119	0.240	0.0	0.989	0.011	5	0.236	0.240	0.0	1.000	0.000
1	0.054	0.110	0.0	0.989	0.011	1	0.108	0.110	0.0	1.000	0.000

Vapor compositions for open system degassing are less reliable than those for closed system degassing because of very small quantities of H_2O and CO_2 degassed during each step.

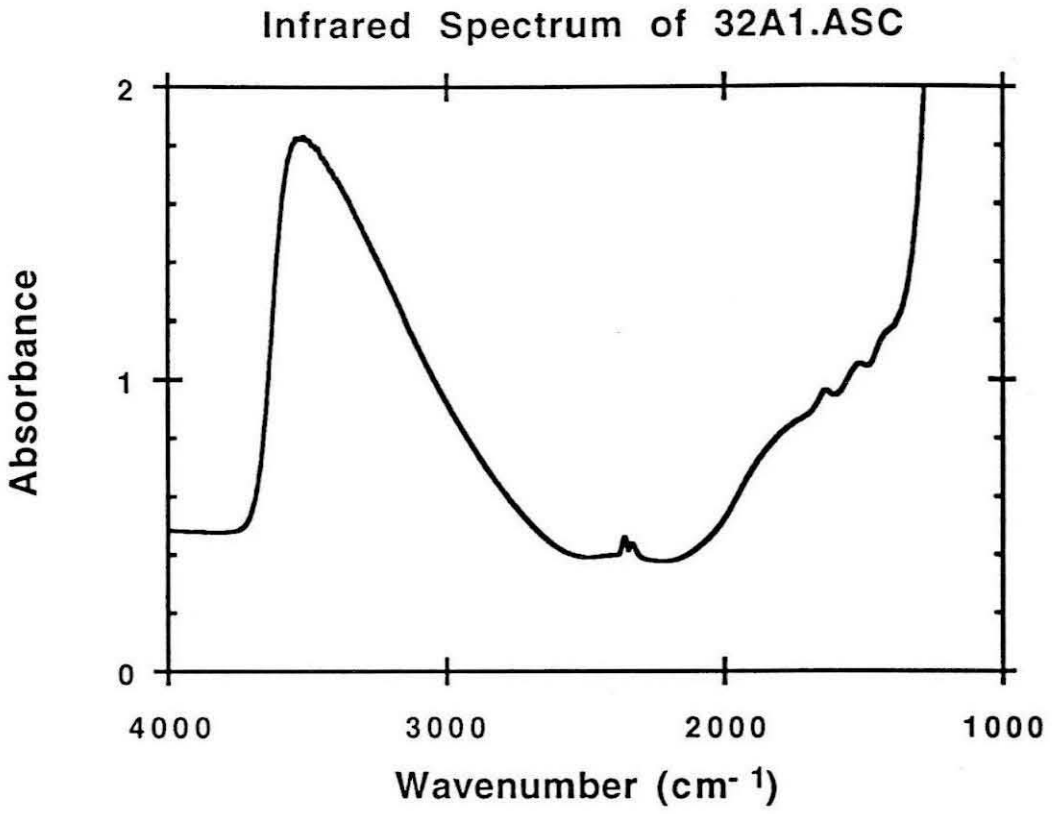

Figure 1a: Infrared spectrum showing typical absorptions of total water (3550 cm^{-1}), molecular water (1630 cm^{-1}), and carbonate bands (1515 and 1430 cm^{-1}). Small peaks at about 2350 cm^{-1} are absorptions by atmospheric CO_2.

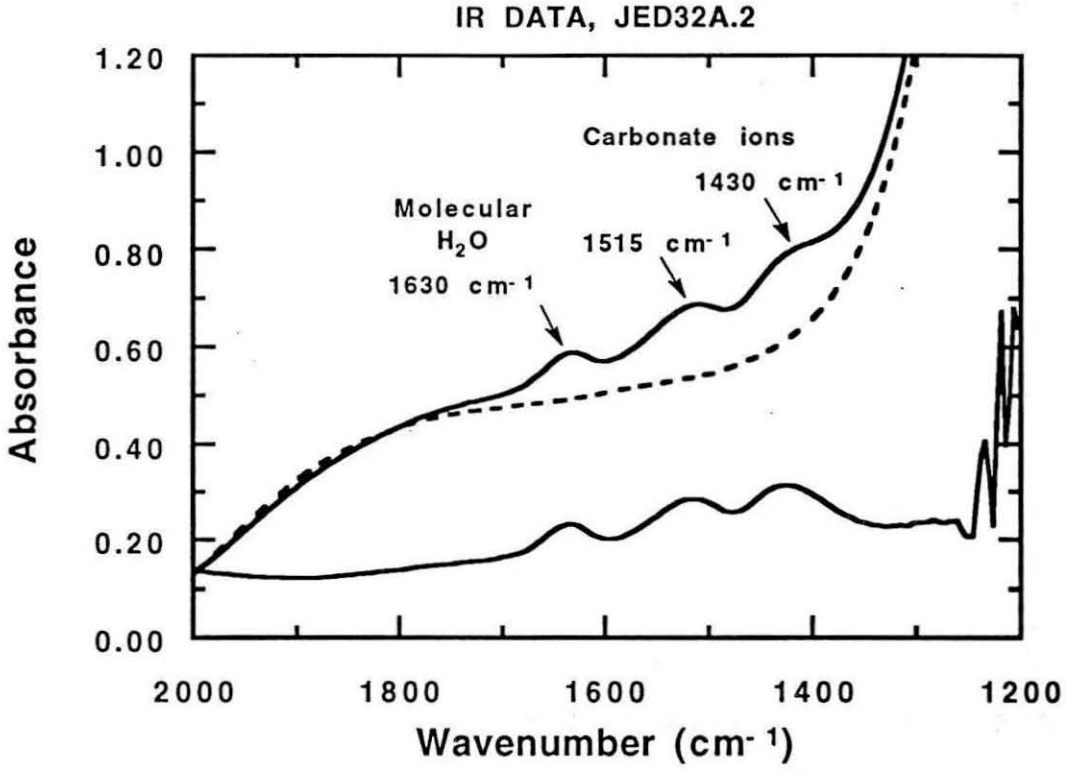

Figure 1b: Typical near-infrared spectrum of basalt showing the absorptions of molecular water at 5230 cm^{-1} and hydroxyl groups at 4500 cm^{-1} superposed on the broad absorbtions at 9500 and 5500 cm^{-1} corresponding to the crystal-field transitions in octahedrally and tetrahedrally coordinated Fe^{2+} ions.

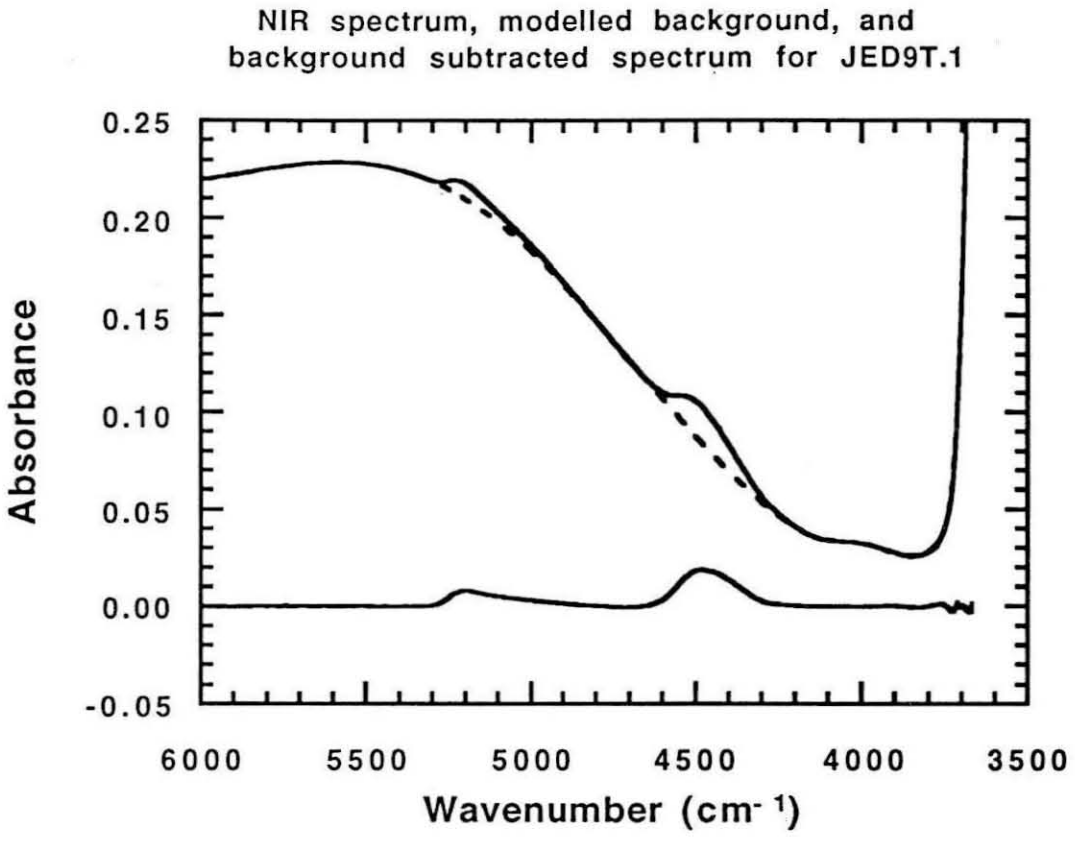

Figure 2: Typical background subtracted near-infrared spectrum. The backgrounds were modeled as a sum of 5 Gaussian curves: two for the Fe absorptions centered at about 9500 and 5500 cm^{-1}, one centered at about 4000 cm^{-1}, and two to fit the left hand shoulder of the 3550 cm^{-1} absorption.

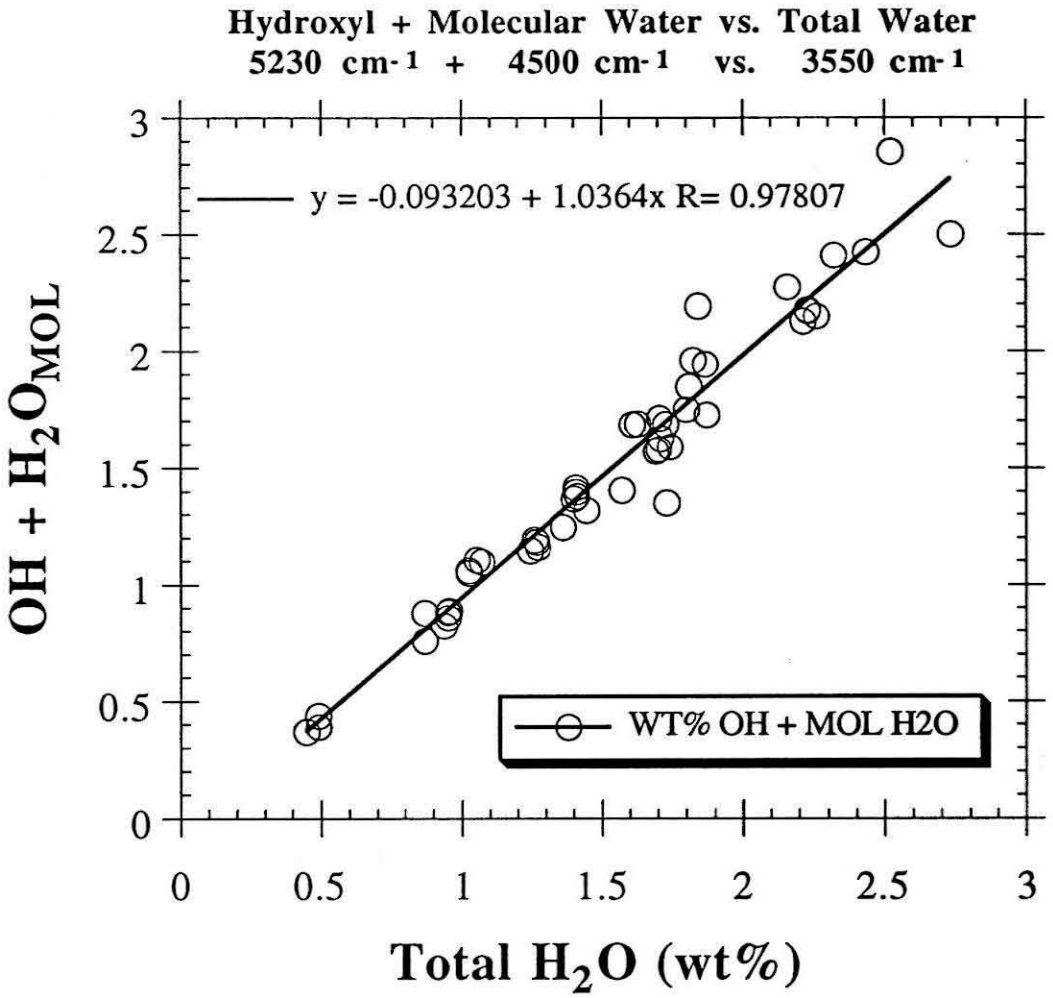

Figure 3: OH + molecular H_2O (5230 cm^{-1}) vs. total H_2O (3550 cm^{-1}) showing the internal consistency of the calibration of the molar absorptivities. Because the 5230, 4500, and 3550 cm^{-1} data were measured on the same spectrum, data from individual spectra are shown.

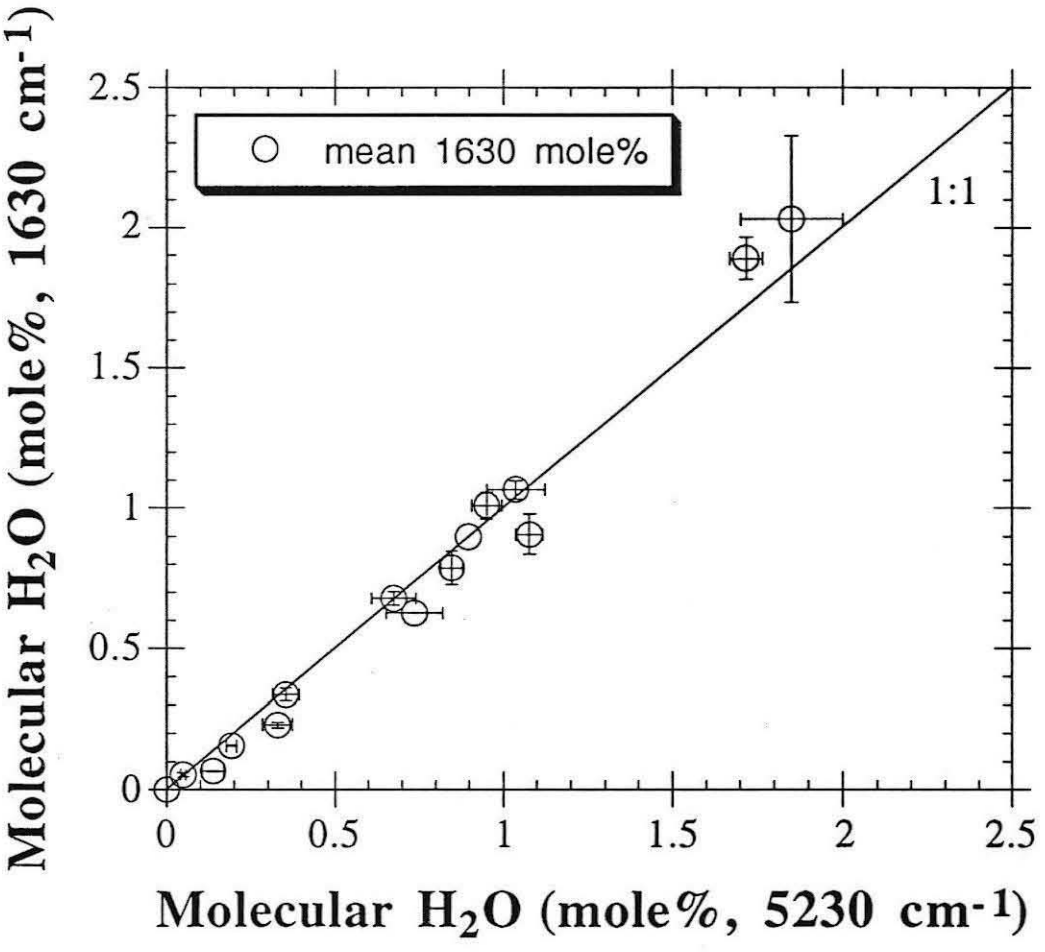

Figure 4: 5230 vs. 1630 cm^{-1} demonstrating the internal consistency of the molar absorptivity calibrations. Because the 1630 and 5230 cm^{-1} data are measured on different spectra (infrared vs. near-infrared), these data are reported in terms of means and standard deviations for each run.

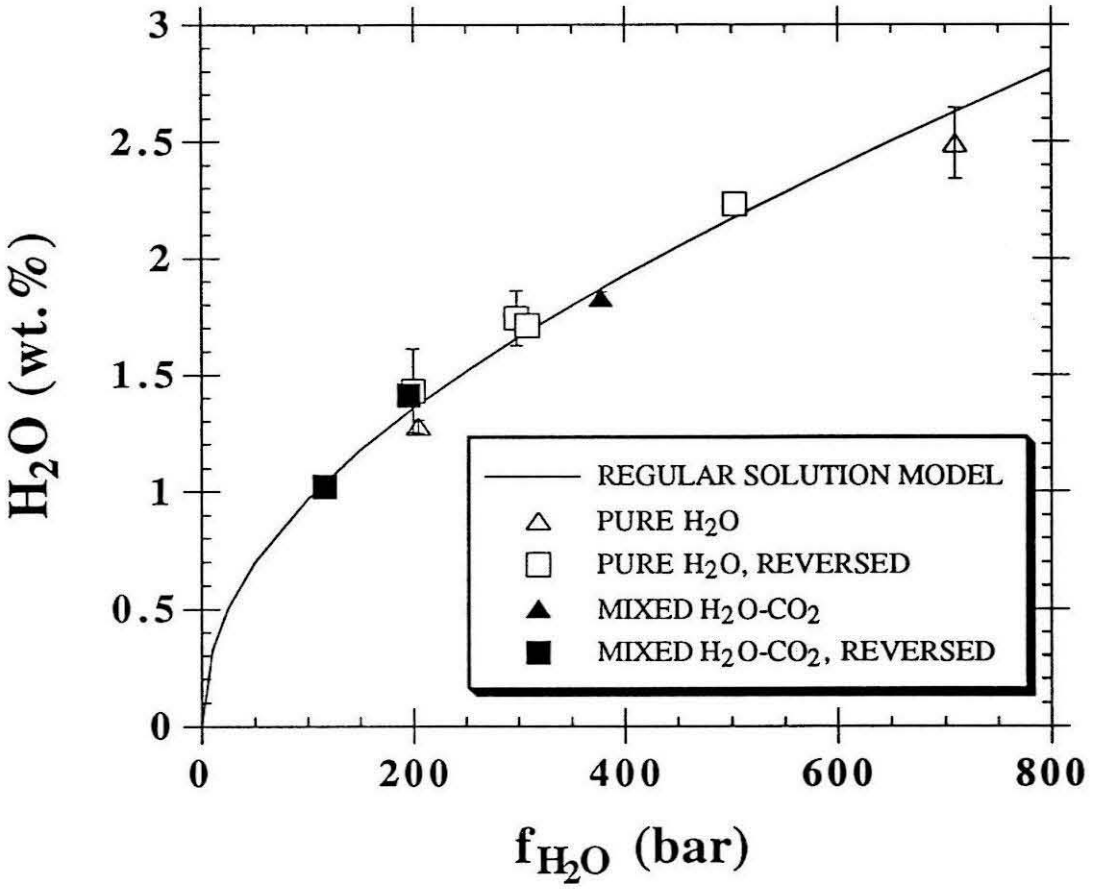

Figure 5: Comparison of molecular H_2O (wt.%) in MORB liquids in equilibrium with "pure" H_2O and mixed H_2O-CO_2 fluids. Error bars are 1 standard deviation of the mean for all analyses of glasses from a run. Symbols with no error bar have errors smaller than the size of the symbol. Curve calculated using a regular ternary solution model with the coefficients for albitic glasses (Silver and Stolper, 1989), where the activity of water in the melt is given by Henry's law for molecular water.

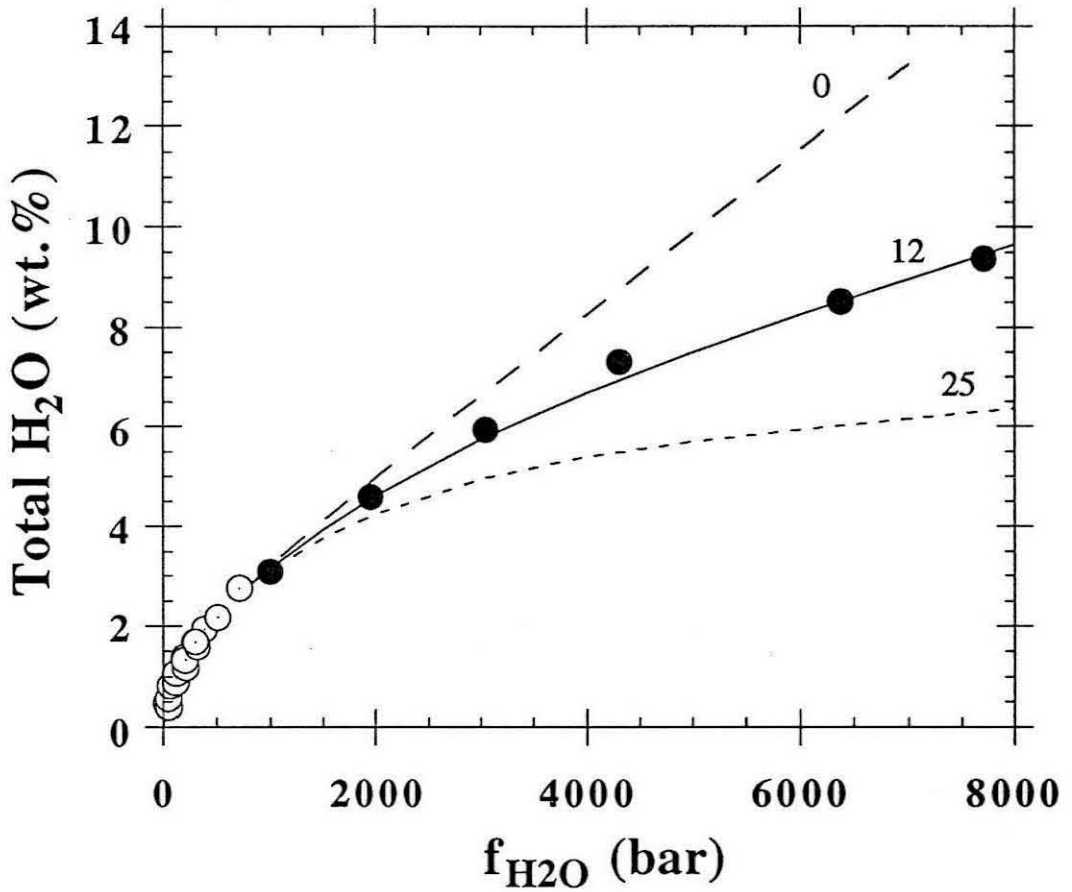

Figure 6: Comparison of new experimental results for the solubility of H_2O (wt.%) in MORB's (open circles) with previous results on a Columbia River basalt (filled circles, Hamilton et al., 1964). Curves calculated using the activity formulations of the regular solution model discussed in the text; numbers next to curves are the values of $V^{0,m}_{H_2O}$. A $V^{0,m}_{H_2O}$ of 12 cm^3/mole provides the best fit to the data.

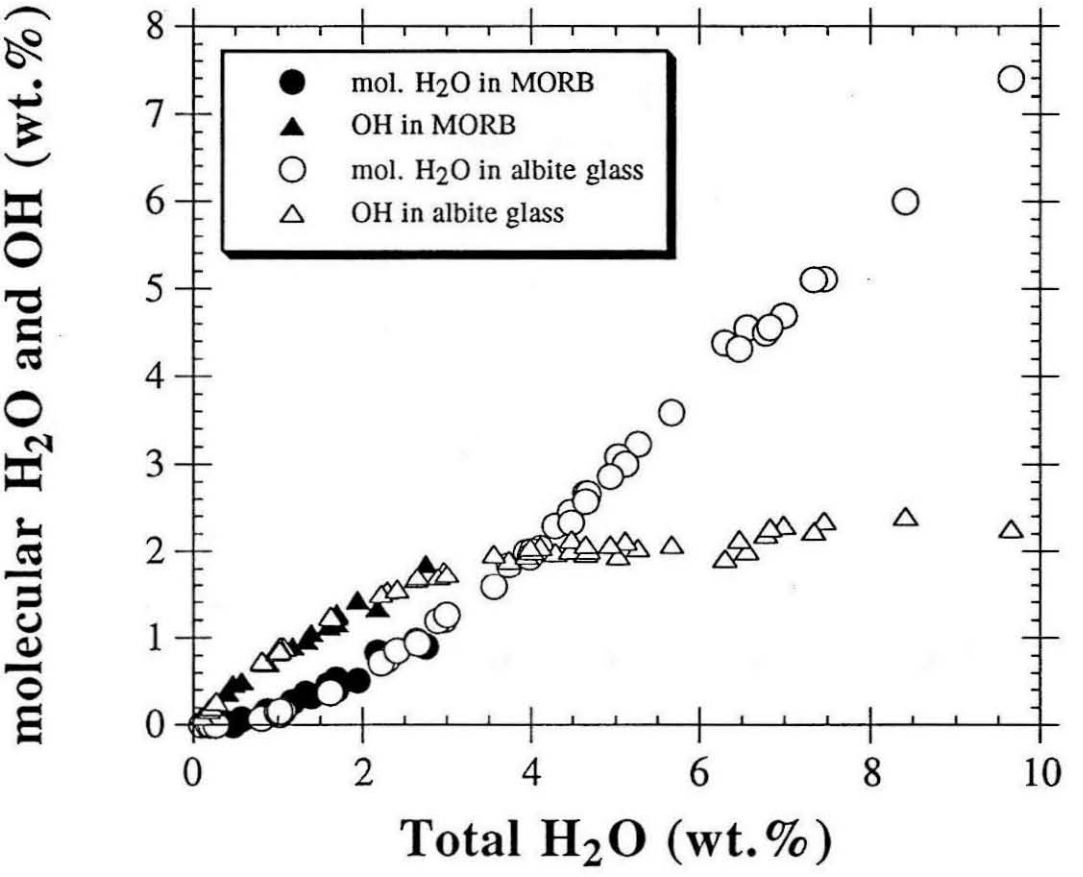

Figure 7a: The concentrations of water dissolved as molecular H_2O (circles) and as OH groups (triangles) as functions of total water (sum of mol. H_2O and OH). Albite samples synthesized in piston cylinder apparatus; data from Silver and Stolper (1989). MORB data from this study.

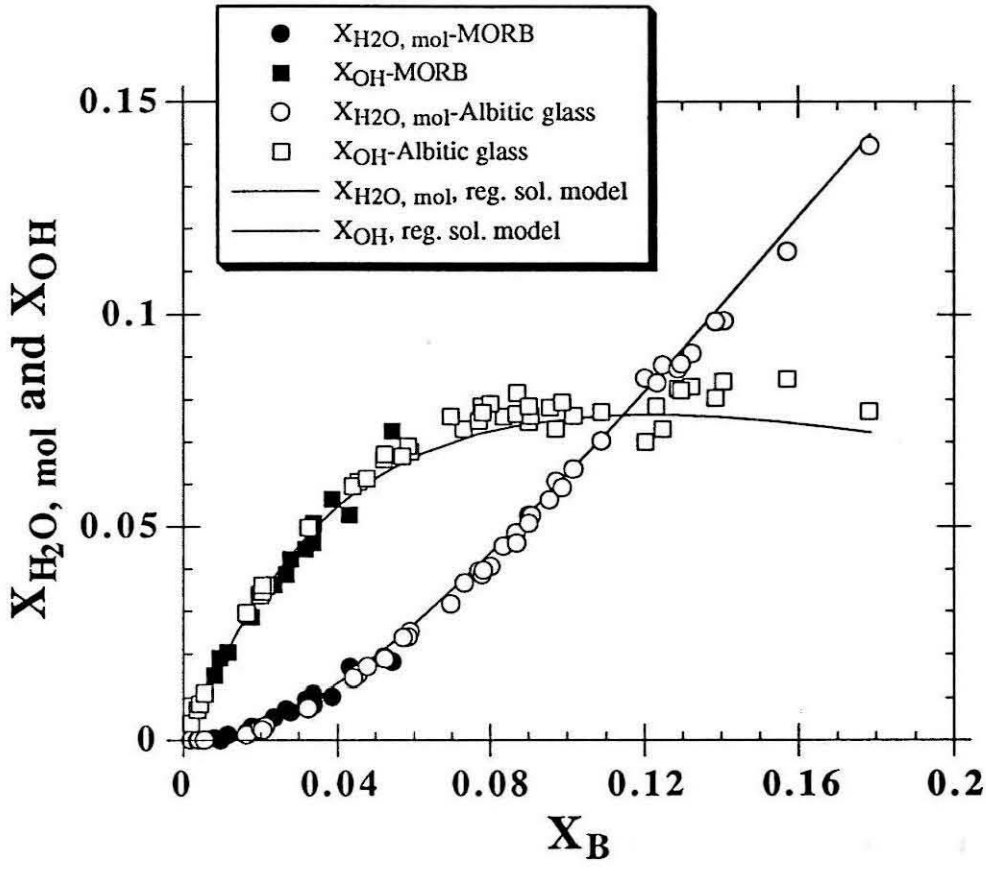

Figure 7b: Mole fractions of molecular water and hydroxyl groups as a function of mole fraction of total dissolved water. Curves generated using a regular solution model and the coefficients for albitic glass from Silver and Stolper (1989), where the activity of water in the melt is given by Henry's law for molecular water.

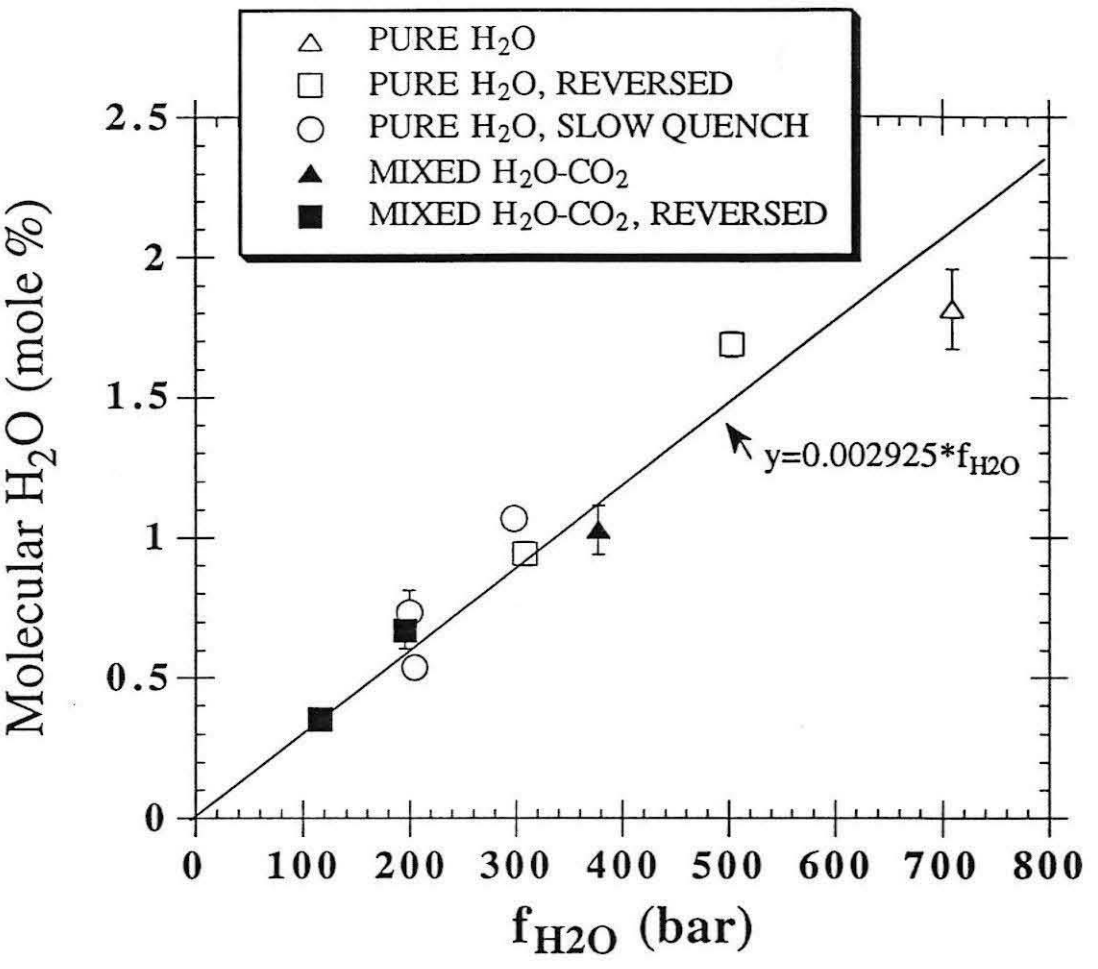

Figure 8: Linear relationship between molecular H_2O, determined from the 5230 cm^{-1} absorbance, and f_{H_2O} indicates Henrian behavior over pressure range investigated. Error bars are 1-σ errors; symbols with no error bars have errors smaller than the size of the symbol.

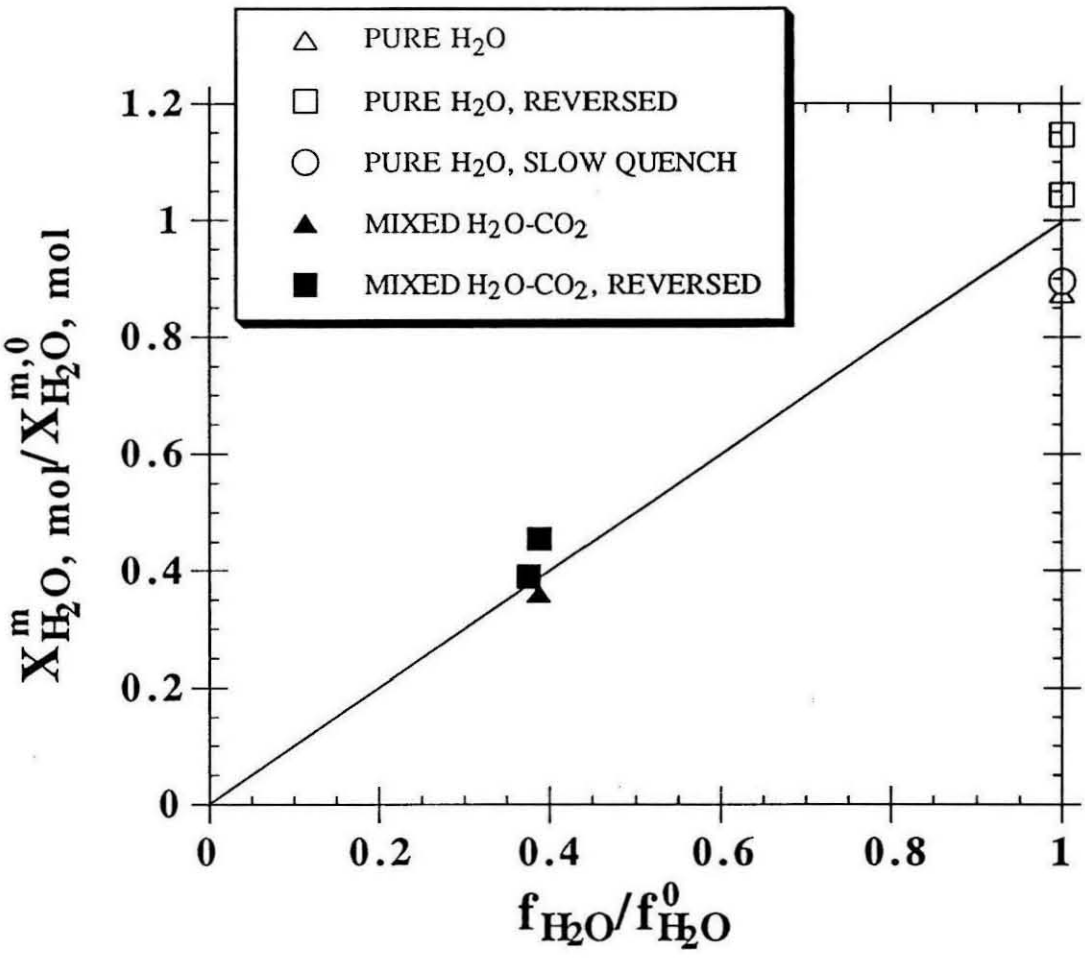

Figure 9: Plot of $X_{H_2O}/X_{H_2O}°$ vs. $f_{H_2O}/f_{H_2O}°$ showing that the ratio of the amount of molecular water dissolved in a melt in equilibrium with mixed H_2O-CO_2 vapor phase with respect to that dissolved in the melt in equilibrium with a pure H_2O vapor phase is equal to the ratio of the water fugacities in the mixed and pure vapors.

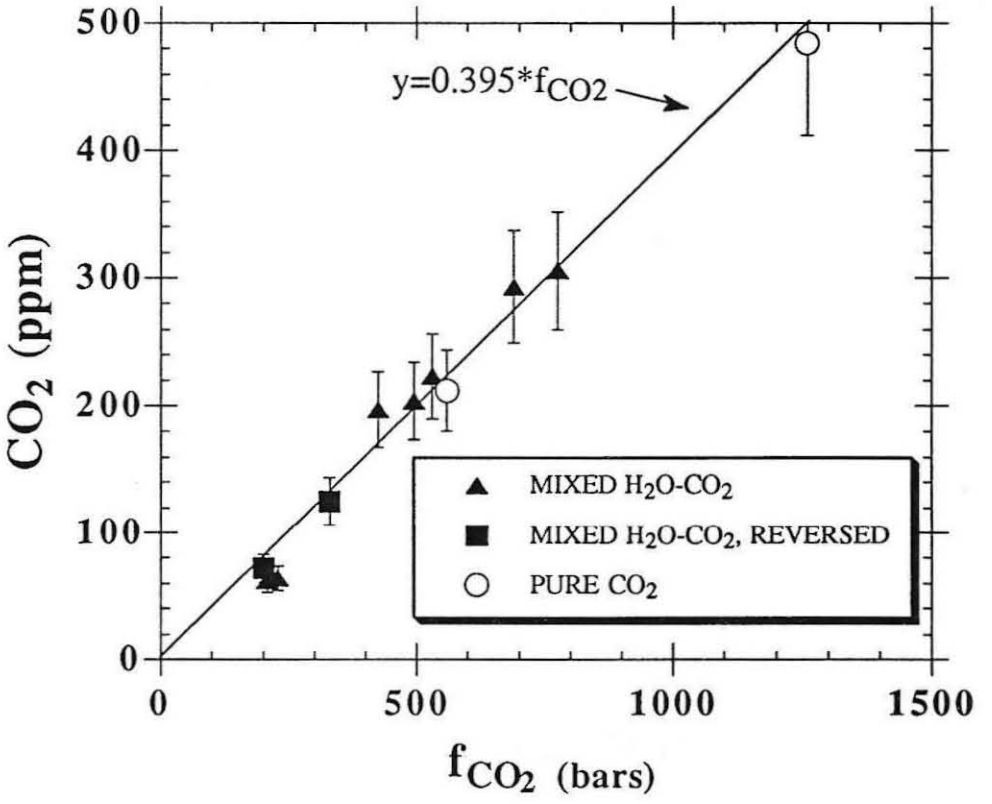

Figure 10: Plot of CO_2 (ppm) vs. f_{CO_2} showing that the solubility of carbon dioxide is a simple function of f_{CO_2} regardless of the composition of the vapor. Errors are 15% of the amount present.

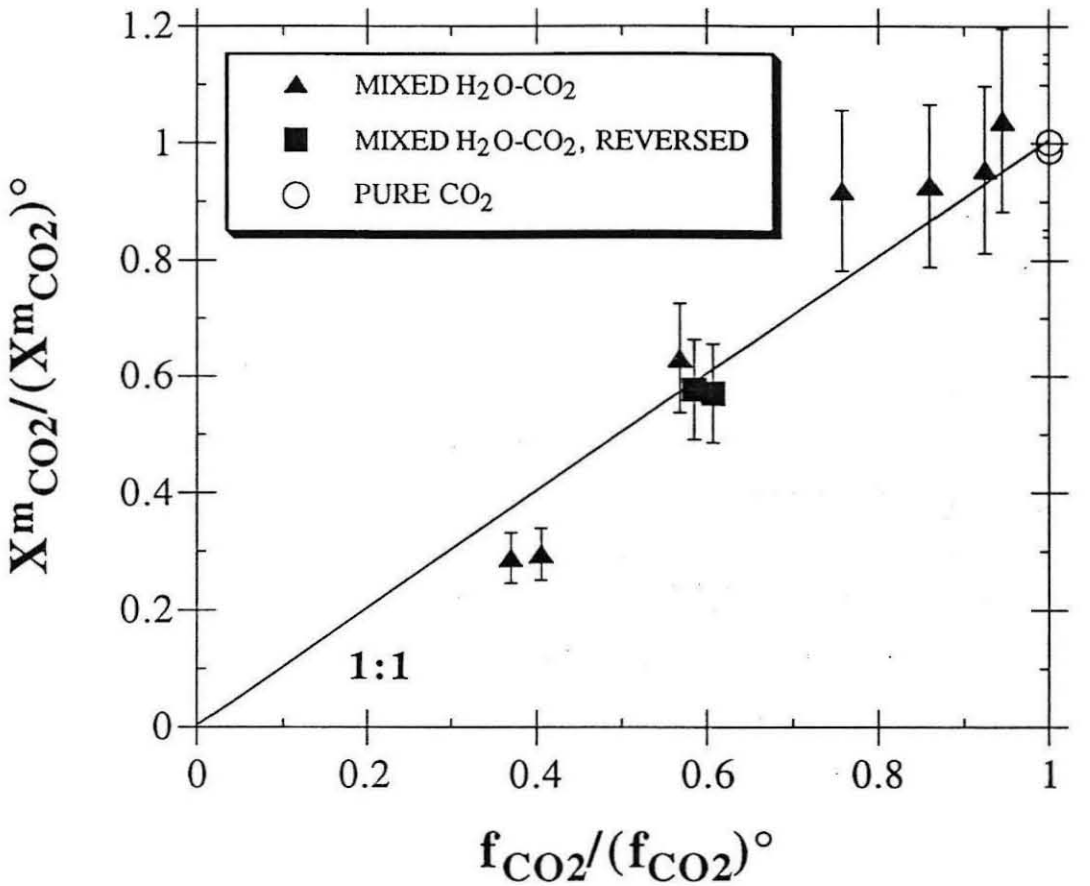

Figure 11: $X_{CO_2}/X_{CO_2}^{\circ}$ vs. $f_{CO_2}/f_{CO_2}^{\circ}$ showing that the ratio of the amount of carbon dioxide dissolved in a melt in equilibrium with mixed H_2O-CO_2 vapor phase with respect to that dissolved in the melt in equilibrium with a pure CO_2 vapor phase is equal to the ratio of the CO_2 fugacities in the mixed and pure vapors. Errors are 15% of the amount present.

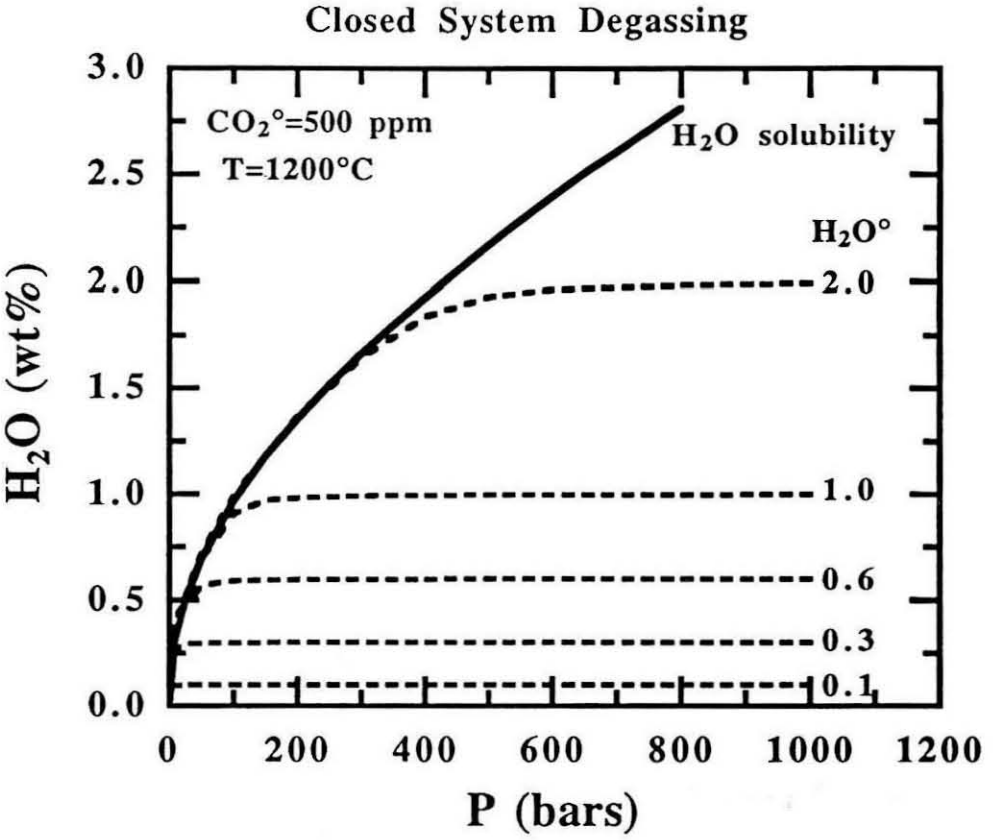

Figure 12: H_2O vs. P in vapor saturated basaltic melts for closed system degassing of melts initially containing 500 ppm CO_2 and a range of H_2O contents (0.1-2.0 wt.%). Solid line is solubility of water in equilibrium with pure water vapor. Dashed lines are degassing paths for melts with different initial water concentrations.

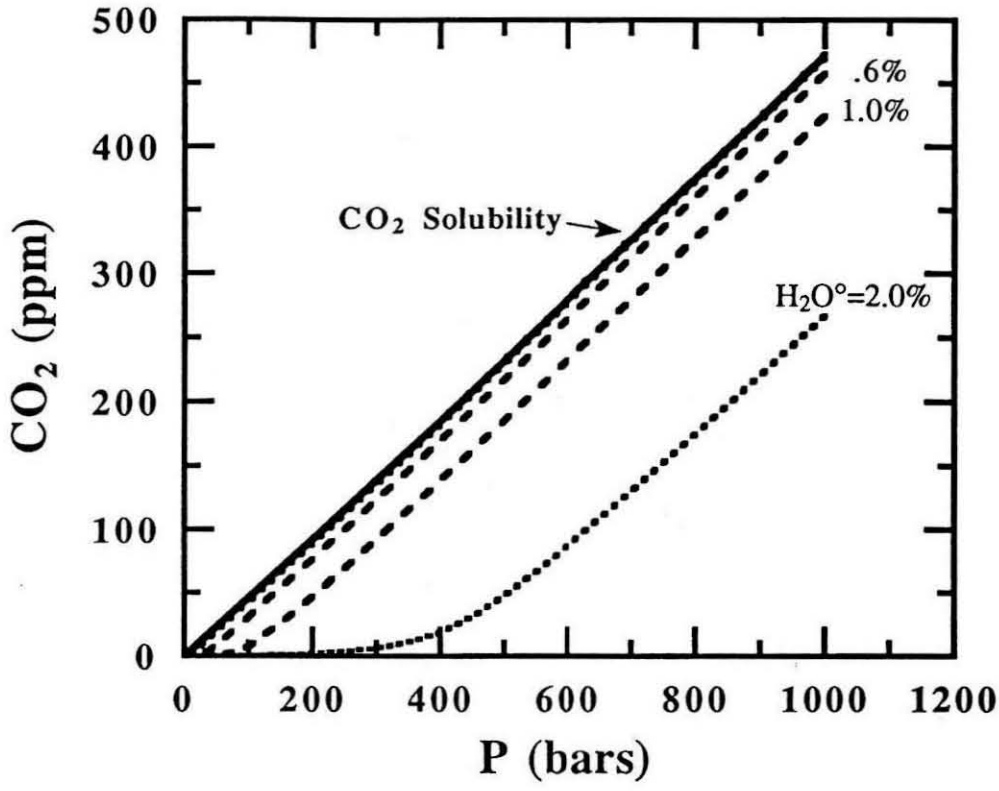

Figure 13: Vapor saturated values of CO_2 vs. P for closed system degassing of basaltic melts at 1200°C and initially containing 500 ppm CO_2 and a range of H_2O contents (0.1-2.0 wt.%). The trends for melts containing 0.1 and 0.3 wt.% H_2O overlap with the trend for pure CO_2 solubility (solid line).

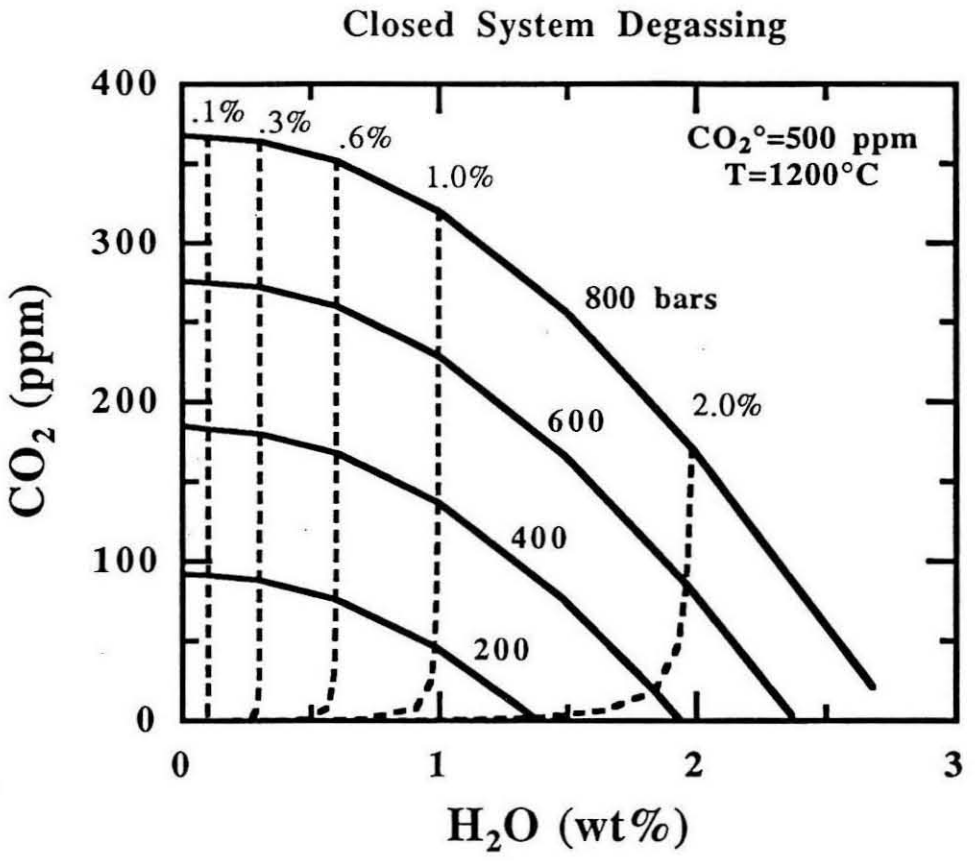

Figure 14: Inverse correlation between CO_2 and H_2O at constant pressure during closed system degassing. Solid lines are lines of constant pressure. Dashed lines represent degassing paths for different initial water contents with decreasing P.

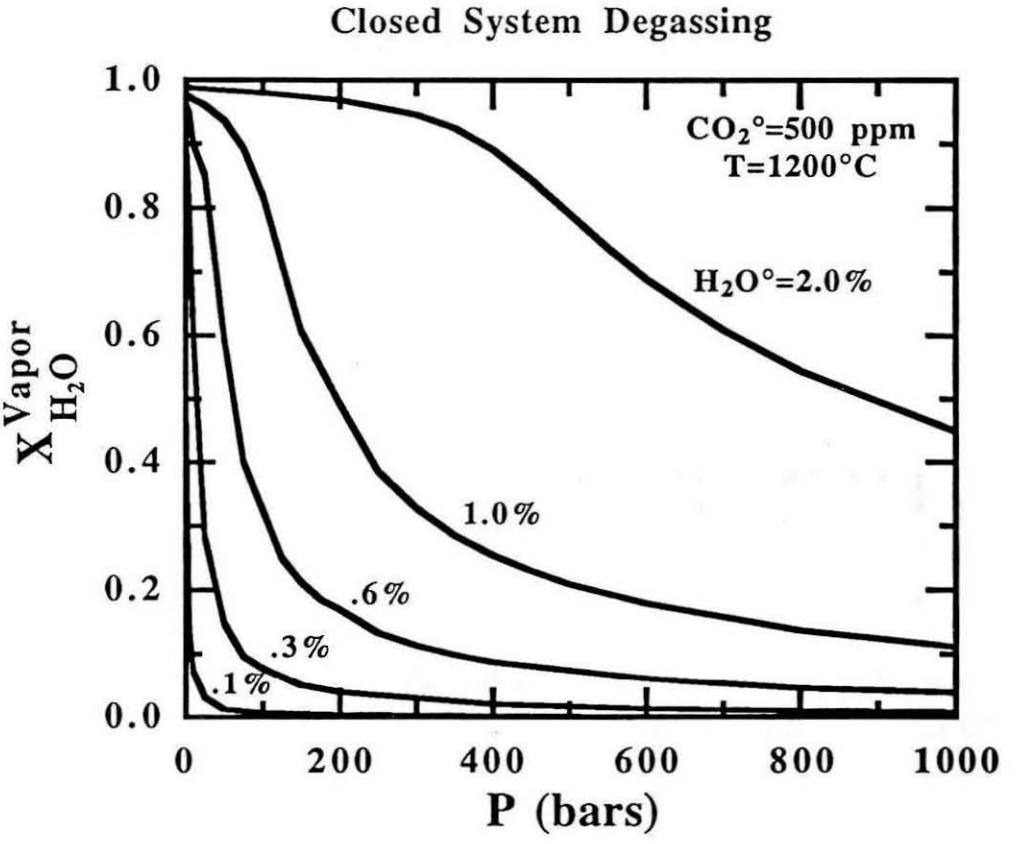

Figure 15: Variation in composition of mixed H_2O-CO_2 vapor phase in equilibrium with basaltic melt during closed system degassing. Numbers next to curves represent initial water content of magma.

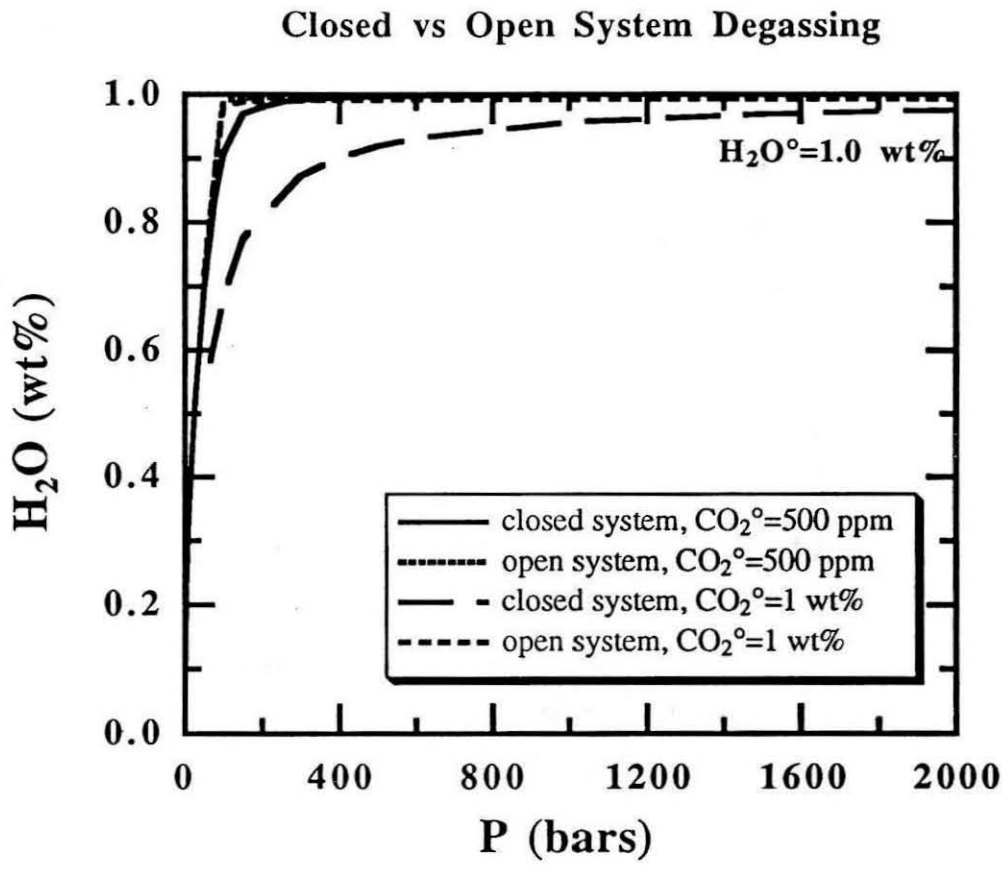

Figure 16: H_2O versus P for open and closed system degassing of basaltic melts with initial water contents of 1.0 wt.%. Results of closed and open system degassing are shown for two different initial CO_2 contents of 500 ppm and 1.0 wt.%. Saturation values for H_2O along the open system degassing paths (short-dashed lines) are identical regardless of the starting composition with negligible water loss until a pressure of about 80 bars is reached. Saturation values for H_2O are lower for the closed system degassing paths and are dependent on the initial composition

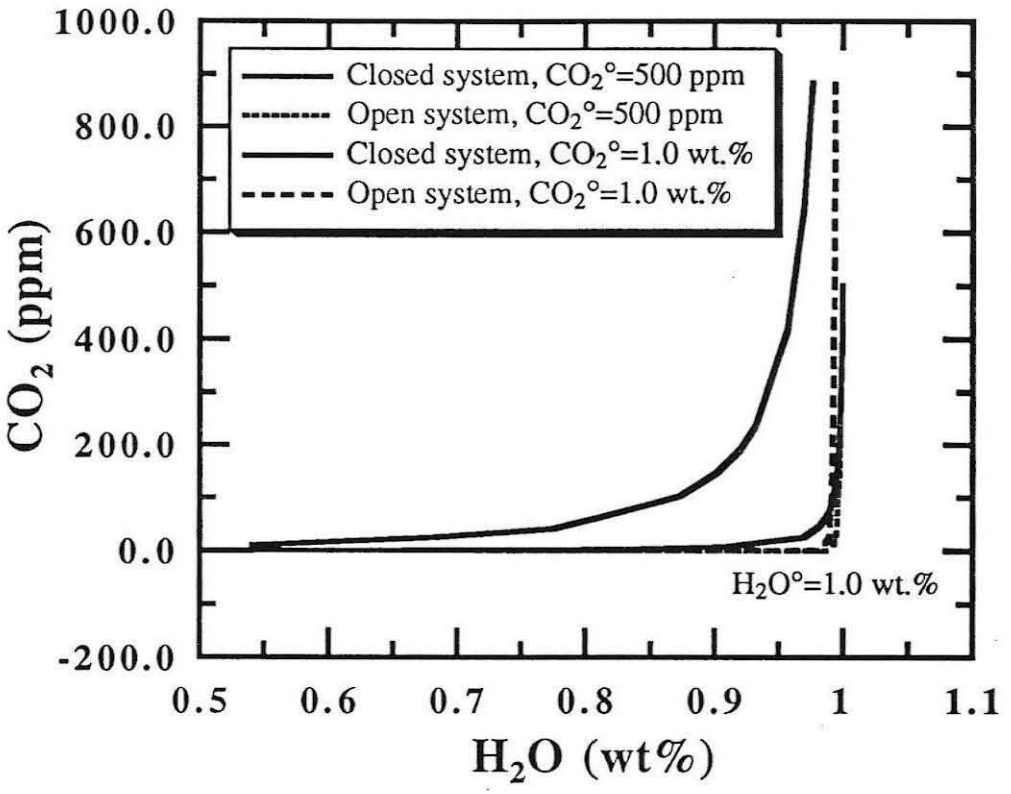

Figure 17: CO_2 versus H_2O for open and closed system degassing. Degassing paths are comparable to the dashed lines on Figure 14. Results for open system degassing (dashed lines) are identical regardless of the initial CO_2 concentration. During closed system degassing, degassing paths are a strong function of initial H_2O and CO_2 concentrations. The pressure at which significant loss of water begins increases as the initial concentration of CO_2 increases.

Chapter 2

INFRARED SPECTROSCOPIC MEASUREMENTS OF CO_2 and H_2O IN JUAN DE FUCA RIDGE BASALTIC GLASSES

(published as Dixon, J.E., E. Stolper, and J.R. Delaney (1988) Earth Planet. Sci. Lett., 90, 87-104.)

ABSTRACT

Dissolved H_2O and CO_2 contents in basaltic glasses from the Juan de Fuca Ridge and neighboring seamounts were determined by infrared spectroscopy. CO_2 contents range from about 45 to 360 ppm by weight, with carbonate ion complexes the only detectable form of dissolved carbon. Samples erupted at a given depth exhibit a large range in dissolved CO_2 contents that we interpret to be the result of variable amounts of degassing. The lowest CO_2 contents at each depth are in reasonable agreement with the experimentally determined CO_2 solubility curve for basalt at low pressures. All glasses with CO_2 values higher than the experimentally determined solubility at the eruption depth are oversaturated because of incomplete degassing. The highest CO_2 contents are spatially associated with the local topographic highs for each ridge segment. Lavas from relatively deep areas may have had greater opportunity to degas during ascent from a magma chamber or during lateral flow in dikes or seafloor lava flows. The highest observed CO_2 concentrations are from the axial seamount and lead to an estimate of a minimum depth to the magma chamber of 2.7 kilometers beneath the ridge axis.

H_2O contents vary from 0.07 to 0.48 wt %, with hydroxyl groups the only detectable form of dissolved water. Water contents correlate positively with FeO*/MgO and the highest water contents are found in the incompatible element enriched Endeavour segment lavas. Variations in ratios of water to other incompatible elements suggest that water has a bulk partition coefficient similar to La during partial melting (D~0.01).

INTRODUCTION

The solubility of CO_2 in silicate liquids is so small at low pressures that most, if not all, terrestrial basaltic magmas exsolve a CO_2-rich vapor as they near the earth's surface. Since CO_2 solubility is roughly linear with pressure at low pressures and the pressure on erupting submarine magma is a linear function of water depth, an approximately linear correlation between depth of eruption and concentration of CO_2 dissolved in the melt is expected provided that magma is able to degas as it rises from depth or as it is emplaced on the ocean floor. In addition, for magmas having the same bulk CO_2 content but erupted at different water depths, a strong negative correlation between depth of eruption and vesicularity is expected. In contrast, H_2O is highly soluble in basaltic liquids even at low pressure. Thus, when mid-ocean ridge basalt (MORB) is erupted in water deeper than about 500 m, little of the water partitions into the vapor phase and water contents are not expected to correlate with eruption depth or extent of degassing [1-4].

The expectation of a positive correlation between extent of CO_2 degassing and eruption depth has had an important influence on thinking about volatile contents and eruptive behavior of submarine magmas. Moore and his coworkers [1-3, 5, 6] have have written extensively on volatiles in submarine basalt and, in particular, have documented the expected negative correlation between vesicularity and eruption depth for individual suites. There also have been several claims, based on samples from a wide range of localities, that CO_2 contents in submarine basaltic glasses are positively correlated with depth [7-9]. In fact, in the absence of experimental determinations of CO_2 solubility in basalts at low pressure, Harris [7] and Des Marais and Moore [8] used observed relationships between depth and CO_2 concentration in basaltic glasses to constrain the pressure dependence of CO_2 solubility in basaltic melts.

Despite the attractiveness of this framework for thinking about the behavior of CO_2 in submarine basalt, there is still considerable uncertainty about CO_2 contents of basaltic glasses. Measurements by different techniques on the same samples can vary by more than an order of magnitude, and causes of these discrepancies are the subject of much debate [10-14]. Using an infrared spectroscopic technique that is specific to carbon dioxide dissolved in the glass, Fine and Stolper [10] showed that dissolved CO_2 contents in submarine basaltic glasses are lower than previously reported and uncorrelated with depth. However, because unrelated samples from a wide range of localities were compared, these results do not give an optimum test of whether there exists a linear correlation between eruption depth and dissolved CO_2 content.

In this study, we measured dissolved CO_2 and H_2O contents of a petrologically and geologically well characterized suite of basaltic glasses from the Juan de Fuca Ridge and neighboring seamounts [15-31] using the infrared spectroscopic technique of Fine and Stolper [10]. Covering a range of eruption depths along a single ridge axis, these samples provide an ideal opportunity to examine the relationship between depth and dissolved CO_2 content in a set of closely related samples. We will show that the expected correlation between dissolved CO_2 content and depth is not observed, probably because many magmas erupted in this area rose so rapidly from depth that there was not enough time for them to degas fully. Comparison of volatile contents with other parameters also leads to insights into the factors controlling the volatile element geochemistry of mid-ocean ridge magmas.

GEOLOGIC SETTING

The Juan de Fuca Ridge is a medium-rate spreading center with a half spreading rate of approximately 30 mm/yr. Based on high resolution bathymetry, Delaney et al. [26] divided the Juan de Fuca Ridge into eight segments roughly 50 km in length (Figure 1).

The northernmost Endeavour segment is offset 30 km to the west of the remainder of the Juan de Fuca Ridge (segments 1-7 numbered from south to north) at the Cobb Offset, an area of overlapping spreading centers caused by northward propagation of segment 7 into the Juan de Fuca Plate [17, 18, 22]. The Juan de Fuca Ridge south of the Cobb Offset is bisected by an axial seamount at the intersection of the Cobb-Eickleburg Seamount chain and the ridge [16]. Segments 1 through 3 and 6 through 4 shift progressively westward toward the axial seamount in a symmetric pattern (Figure 1) [16]. The neovolcanic zone is shallowest at the summit caldera of the axial seamount (1425 m) and deepens to ~2200 m toward the distal ends of segments 3 and 4. Segments 2 and 5 are deeper (2200 to 2700 m) and have broad axial rift valleys 7 to 10 km wide. Segments 1 and 6 have extremely linear and narrow axial rift valleys less than 1.5 km wide. There is a good correlation between shallow topography, hydrothermal activity, and voluminous recent volcanic eruptions [23, 28].

The distribution of seamounts is highly asymmetric with most on the Pacific Plate. The Cobb-Eickleberg seamount chain is the largest and longest-lived seamount chain in the area and is thought to have a hotspot origin [15, 32, 33]. There are also many short chains and isolated volcanoes, not associated with hotspots, that were probably produced close to the ridge axis [15, 34, 35]. Davis and Karsten [25] hypothesized that the asymmetric generation of non-hotspot seamounts is related to the rapid ridge-perpendicular migration rate of the Juan de Fuca Ridge over a heterogeneous source region.

Geochemistry

South of the Cobb Offset the lavas are tholeiites characterized by low K_2O (<0.30 wt %) and variable iron and titanium enrichment probably caused by up to 50 % fractional

crystallization of olivine, plagioclase, and clinopyroxene in the approximate proportions of 1:5:1, respectively [16, 26, 30]. The most highly evolved lavas are ferrobasalts that occur near the Juan de Fuca Ridge-Blanco Fracture Zone intersection (southern end of segment 1) and 20 to 30 km south of the Cobb propagating rift tip (northern end of segment 6) [16]. Although the Cobb-Eickleburg Seamount chain has been proposed as a hotspot trace [e.g., 36], no systematic trends along the ridge away from the axial seamount have been found in trace elements [30], rare earth elements (REE) [19], or Sr-isotopes [20]. Basalts from segments 1-7 of the Juan de Fuca Ridge have low $^{87}Sr/^{86}Sr$ ratios of 0.70233 to 0.70267 [20] characteristic of depleted MORB source regions, but their trace element contents and ratios are transitional between enriched and depleted MORB [30]. (We use "enriched" and "depleted" only to refer to chemical composition, and do not imply that a particular physical process relates the various mantle source regions.) For example, the Zr/Nb ratios are ~20, intermediate between high ratios of >35 for depleted MORB and low ratios of ~10 for enriched MORB [37]. Similarly, La/Sm ratios range from 0.5 to 0.9, higher than a range of 0.3 to 0.5 more typical of depleted MORB [e.g., 38, 39].

The lavas from the Endeavour segment are geochemically distinct, and are tholeiites characterized by high concentrations of incompatible elements [26, 30]. For example, the average K_2O content is about double that south of the Cobb Offset. They also have lower total FeO and higher SiO_2 and Na_2O contents for a given MgO content. Differences in major elements between Endeavour segment lavas and those south of the Cobb Offset may reflect generation of the magmas parental to the Endeavour segment lavas by smaller degrees of partial melting at shallower depths in the mantle [e.g., 40]. Ratios of highly incompatible elements are typical of enriched MORB. The samples are slightly light REE enriched (La/Sm > 1) and have Zr/Nb ratios that range from 7 to 16 [30]. $^{87}Sr/^{86}Sr$ ratios do not show a similar enrichment (0.70243 to 0.70259), perhaps reflecting a relatively recent source region enrichment [20].

The seamount lavas are tholeiites with compositions similar to those of the lavas from the Juan de Fuca Ridge south of the Cobb Offset [24].

SAMPLES

Most samples were selected from dredge hauls from cruises 063, 152, 170, and 175 of the R/V T. Thompson (University of Washington) and cruise 81-017 of the R/V Hudson (University of British Columbia). Additional samples from the axial seamount (Pisces 1326) were obtained by submersible. Ridge crest samples are from dredges spaced approximately 10 km apart. Seamount samples are from Cobb-Eickleberg, Vance, Springfield, and Heck seamount chains, and the Explorer Seamount (Figure 1). Compared to ridge crest samples, seamount sample depths are less well known because of downslope transport and large depth ranges sampled by dredging. The glasses analyzed in this study are from splits of glasses used in other petrologic studies [16, 19-21, 24, 30, 41].

ANALYTICAL TECHNIQUES

Glass chips were doubly polished to a thickness of approximately 100 μm. Each glass chip was placed over a 400 μm in diameter aperture, positioned so that the infrared beam passed through pale brown glass avoiding crystals, devitrified zones, and vesicles. Transmission infrared spectra in the 4000 to 1200 cm^{-1} (2.5 to 8.3 microns) range were collected on a Nicolet 60SX FTIR spectrometer [42]. Typically, 2000 to 2048 scans were collected for each spectrum. The spectrum of an anhydrous, decarbonated sample of TT152-43-19, melted at 1 atm on a Pt loop at 1315°C at QFM and then quenched in water, was subtracted from the sample spectra as a background correction.

The concentrations of H_2O and CO_2 were determined according to the Beer-Lambert law from the intensities of the 3535 cm^{-1} and 1515-1435 cm^{-1} bands [10, 42] using the molar absorption coefficent and integral molar absorption coefficient for CO_2 dissolved as carbonate in basaltic glass from Fine and Stolper [10]. The molar absorption coefficient for H_2O in basaltic glass is taken to be 63 ± 5 L/mol-cm (P. Dobson, S. Newman, S. Epstein, and E. Stolper, unpublished results).

Volume percent and size distribution of vesicles were determined for some samples. Analysis was done in reflected light on polished thin sections by counting numbers of vesicles contained in areas of 0.3 cm^2 (100 adjacent fields of view with a 20X objective) or 1.3 cm^2 (100 adjacent fields of view with a 10X objective; used only for samples with vesicles >600 μm in diameter). The diameter of each vesicle was measured at the vesicle-surface intersection and its area calculated. The volume percent of vesicles for each sample was calculated by dividing the area of vesicles by the total area examined. Bubbles that overlapped adjacent fields of view were counted if they intersected the bottom or left boundary and ignored if they intersected the top or right boundary. The glass chips used for infrared analysis were too small to give statistically significant numbers of vesicles, so larger thin sections of the outer glassy rind of the sample were used for vesicle content determinations. The thin sections used for point counting and glass chips used for infrared analysis were often from slightly different locations on the glassy rim of the sample, so that vesicle contents measured in thin sections sometimes differ from those in the glass chips analyzed for volatiles. Where vesicle populations in different thin sections from the same sample are significantly different, they are listed separately in Table 2.

RESULTS

Locations, depths, concentrations of selected major elements, and concentrations of CO_2 (ppm by weight) and H_2O (wt %) are given in Table 1. Vesicle contents of thin sections are given in Table 2. Some of the data are presented graphically in Figures 2-9.

Precision and Accuracy

In order to assess the precision of our CO_2 measurements, several spectra (2-4) were collected on a single glass chip or on texturally similar glass chips from the same split for a number of samples. Repeat spectra on the same glass chip were obtained for 6 samples and yielded CO_2 contents reproducible to within 7 %. Multiple spectra on texturally similar chips from the same split were obtained for 7 samples and yielded CO_2 contents reproducible to within 13 %. These errors are similar to those reported previously using the same technique [10, 42]. The poorer reproducibility for analyses of different glass chips may reflect minor sample heterogeneity. Glasses from the same dredge but with different textural appearance (e.g., amount of devitrification) have concentrations that differ by up to almost 40 % and are listed separately.

Concentrations of water based on multiple spectra from the same glass chip vary less than 3 %. Typical 1Â values for analyses of different chips from the same split are also usually about 3 %, but variations of up to about 20 % are occasionally observed and may reflect sample heterogeneity.

The accuracy of the reported concentrations is limited primarily by uncertainties in the molar absorption coefficients. These are thought to be known to within 15 % or better

for the carbonate bands [10] and to about 10 % for the hydroxyl band at 3535 cm^{-1} in basalts.

Vesicularity

Different thin sections of the same sample can show significant textural heterogeneity (e.g., TT152-29-1). For samples from which several texturally similar thin sections were point counted, the vesicle content listed in Table 2 is the average of the values of the individual thin sections. Vesicles range in size from a few microns to about 1 mm. Large vesicles dominate the total volume percent vesicles, and the diameter of the largest vesicle is roughly correlated with the total volume percent vesicles. Ridge crest samples contain less than 2.3 total volume % vesicles with most having less than 1.5 %. Higher values of up to 3.1 volume % were found for seamount samples. Concentrations of vesicles less than 40 μm in diameter are highest for the ridge crest samples and range up to 0.35 %. For two samples, thin sections cut perpendicular to the cooling surface contained both glassy and devitrified areas. In these two thin sections, the partially devitrified areas are richer in vesicles than the glassy areas.

CO_2 Contents

The only form of dissolved carbon dioxide found in these samples is carbonate ion complexes, in agreement with the results of Fine and Stolper [10]. CO_2 concentrations range from 45 to 360 ppm. Two samples did not contain detectable CO_2. One of these, HU81017-31-2, was collected at a depth of 800 m, the shallowest in this study. The other sample, HU81017-2-4, was extremely thin (40 μm) and the lack of detectable CO_2 probably reflects sample thickness instead of an anomalously low CO_2 content.

Figure 2 shows dissolved CO_2 content vs. vesicularity for the samples we studied. In cases where thin sections of the same sample showed a wide range of vesicle contents, the vesicle content plotted on Figure 2 corresponds to data from the thin section most similar in texture to the glass chip analyzed for CO_2. There is no correlation between dissolved CO_2 content and total vesicle content, though all the data are confined to the lower left part of the figure and appear to be approximately bounded by the sort of trend expected for closed system degassing. Samples with the largest bubbles (diameter >1 mm) have low CO_2 contents. Most samples with CO_2 contents greater than 200 ppm have abundant (>0.08 volume %) bubbles less than 40 μm in diameter (Figure 3). Samples analyzed by IR containing more than a dozen bubbles smaller than 40 μm per glass chip (a few mm^2) are labelled on the figures with a "b" next to their symbol.

Glassy rims of pillows typically have a textural gradation from glassy at the margin to inwardly increasing degrees of devitrification [44]. The outer centimeter can be subdivided into four zones: glass (~3 mm thick), glass with isolated spherulites (~4 mm thick), glass with partially coalesced spherulites (~1-2 mm thick), and fully coalesced spherulites (~1-2 mm thick) [44]. Although most glasses analyzed in this study are clear brown glass and probably came from the outer few mm of the glassy rind, a few samples have devitrification rims up to 140 μm thick around phenocrysts. Two different glass chips, one with devitrification rims and the other without, were analyzed at each of two dredge locations (TT170-5 and TT175-61). Even though the aperture was placed to avoid the devitrified rims, the CO_2 contents of glasses from samples with partial devitrification are 70 to 100 ppm lower than those of glasses from undevitrified samples from the same locality. Moreover, the three lowest CO_2 contents in samples from the Endeavour segment (TT175-17-14, TT175-40-3, and TT175-54-4) were measured in glasses with devitrified zones. In the two thin sections that contained the textural gradation from glassy to fully devitrified (TT152-77-6 and TT152-61), the volume percent vesicles measured in glassy

regions of the partially devitrified areas is a few tenths of a percent higher than that in undevitrified areas. Likewise, the difference in vesicle contents between partially devitrified regions and clear glassy regions in two different thin sections of TT170-5 is 0.38 % (1.81 vs. 1.43 volume %). Roughly 120 ppm CO_2 must exsolve to form 0.38 % vesicles, similar to the observed CO_2 depletion of the partially devitrified sample relative to the glassy one. We do not have an explanation for how the glass in samples that are partially devitrified could have become depleted in CO_2. The cooling times for the glassy rinds of pillows are much too fast for significant bubble growth to occur [45] and more work is needed to determine whether our observations on these few samples are significant. Nevertheless, because they appear anomalous, analyses of glasses from partially devitrified samples, shown with a "d" next to them on the figures, are not included in the discussion of the general trends in the data.

CO_2 concentrations are plotted versus depth in Figure 4. Also shown is the best fit solubility curve of CO_2 in basalt at 1200°C for pressures up to 1.5 kilobars determined using infrared spectroscopy [42]. Our measurements of dissolved CO_2 contents do not show a positive correlation with depth. Most glasses have CO_2 concentrations in excess of the experimentally determined solubility for the pressure of eruption. Even including the partially devitrified samples, the lowest CO_2 concentrations at a given depth agree within error with the 250 bar solubility measurements [42]. The only undevitrified sample that falls below the best fit solubility curve is TT152-13, the most fractionated composition analyzed, but even this sample has a CO_2 content within measurement error of the 250 bar solubility.

CO_2 contents of samples south of the Cobb Offset show a weak negative correlation with depth (Figures 5c and 6), exactly opposite the trend expected from the pressure dependence of CO_2 solubility in basalt. The highest CO_2 concentrations occur in

lavas from the axial seamount caldera and range from 237 to 360 ppm. When CO_2 contents are plotted against position along the ridge (Figure 6), the highest CO_2 contents are associated with the local topographic highs for each segment.

Samples from the seamounts and Endeavour segment (Figures 5a and b) tend to have lower CO_2 contents (<220 ppm) than those from south of the Cobb Offset, with the lowest values (excepting the partially devitrified samples) close to the experimentally determined solubility. The highest CO_2 content from the Endeavour segment is spatially associated with the topographic high (Figure 6), but there is no clear negative correlation between CO_2 and depth as is seen for samples south of the Cobb Offset.

CO_2 contents do not correlate with degree of fractionation (FeO*/MgO) or incompatible element enrichment.

$\underline{H_2O}$ Contents

Hydroxyl groups are the only detectable form of dissolved water. H_2O contents vary from 0.07 to 0.48 wt %. Water contents of partially devitrified samples are not significantly different from those in glassy samples (e.g., TT170-5A and -5B). Water contents of the ridge samples correlate positively, though with considerable scatter, with FeO*/MgO ratios (Figure 7), K_2O contents (Figure 8), rare earth element contents (Figure 9a-d), and the concentrations of highly incompatible trace elements such as Zr and Nb (Figure 9e and f). Samples from the Endeavour segment have higher water and incompatible element contents than those south of the Cobb Offset at the same FeO*/MgO ratio. On a plot of H_2O versus La the Endeavour segment samples are colinear with those from south of the Cobb Offset on a line that passes through the origin. When water contents are plotted versus progressively heavier (more compatible) REE, the fields for the

Endeavour segment samples are displaced progressively toward higher water/REE ratios (Figures 9a-c). On a plot of water versus Zr, the Endeavour segment data are roughly colinear with data from south of the Cobb Offset on a line that passes through the origin (Figure 9e), but the Endeavour segment samples have lower H_2O/Nb ratios than samples from south of the Cobb Offset (Figure 9f). The seamount samples have water contents less than 0.3 wt %, similar to samples south of the Cobb Offset.

COMPARISON TO OTHER STUDIES

Splits from some of the samples analyzed in this study have been analyzed for CO_2 by Blank et al. [41] using combustion/manometry. The high temperature portion of their data ranges from 140 to 540 ppm CO_2. Dissolved CO_2 contents of 130 ppm were measured on three "vesicle-free" glasses from the southern Juan de Fuca Ridge near the location of TT152-37 by Brett et al. [46] using thermal and laser vacuum extraction techniques combined with quantitative capacitance manometry. The results from these studies are similar to ours. As discussed in the INTRODUCTION, however, measurements of CO_2 contents of MORBs are not without controversy. Although values determined by infrared spectroscopy [10, this study], combustion/manometry [8, 41], or pyrolysis/manometry [7, 46, 47] are typically less than about 400 ppm by weight, the dissolved CO_2 contents of MORB determined by one pyrolysis/manometry study [48] and vacuum fusion/quadrupole mass spectrometry studies [12, 49-51] on the same or similar samples are a factor of two to an order of magnitude higher. Possible explanations for the higher CO_2 contents obtained by fusion/quadrupole mass spectrometry are discussed elsewhere [10, 11].

Concentrations of water in Juan de Fuca Ridge glasses measured in this study using the infrared spectroscopic technique are consistent with those obtained on MORB glasses

by a variety of other techniques such as the Penfield method, vacuum fusion/mass spectrometry, vacuum fusion/manometry, and gas chromatography [1, 7, 12, 21, 46, 49-52]. The range of H_2O contents found in Juan de Fuca Ridge lavas south of the Cobb Offset (0.15 - 0.36 wt %) is essentially identical to the results reported by Moore [1] obtained using the Penfield method on samples from the same region. Splits from some of the samples analyzed in this study have been analyzed for H_2O and D/H ratios by Kyser and O'Neil [21] using pyrolysis/manometry. There is a good correspondence between the two data sets, although their values are lower by about 0.02 to 0.11 wt % H_2O.

CO_2 VERSUS DEPTH

The most significant aspect of our data on dissolved CO_2 contents is that many of the glasses contain CO_2 in excess of its solubility for the hydrostatic pressure at the depth of eruption [see also 10, 42]. The simplest explanation for the existence of glasses supersaturated with respect to CO_2-rich vapor is that they rose from depth and erupted on such short time scales that vapor exsolution did not proceed to completion prior to quenching. Magmas that rise more slowly to the ocean floor from underlying magma chambers and/or pond near the ocean floor prior to eruption and quenching will have more opportunity to nucleate and grow bubbles. These magmas may reach equilibrium and will contain dissolved CO_2 contents corresponding approximately to the CO_2 solubility at the hydrostatic pressure of the eruption depth.

Since many submarine basaltic glasses are supersaturated with respect to CO_2, estimates of solubility based on observed CO_2 contents of basalts at a given depth [e.g., 7, 8] could yield overestimates of CO_2 solubility. On the other hand, the pressure dependence of CO_2 solubility could be determined by comparing the lowest dissolved CO_2 contents of basalts erupted at different depths.

As expected, the lowest CO_2 concentrations at a given depth lie near the measured solubility curve [42]. Sample TT152-13 has a CO_2 concentration of 56 ± 10 ppm (1Â) and is the only undevitrified sample that falls below the best fit solubility, although within the reported uncertainty it overlaps with the solubility data [42]. This sample is the most highly evolved of the samples we studied, but it is unlikely that CO_2 solubility in a fractionated basaltic melt is significantly different from that in more primitive basaltic melts at the same temperature [53]. However, the approximate liquidus temperature for TT152-13 is 1160°C [C. Langmuir and T. Plank, personal communication], lower than liquidus temperatures for most of the other samples (1190-1240°C) [54]. Since CO_2 solubility may be a strong positive function of temperature [42], this might account for the low CO_2 content of this fractionated basalt.

Based on our interpretion of the extent of CO_2 degassing in submarine basalts, the degree of CO_2 supersaturation provides information about relative ascent rates and lengths of time magmas were at or near the seafloor prior to quenching. Although our sampling is limited, the most supersaturated glasses along each ridge segment (~50 km) occur at the summit and the least supersaturated glasses occur at the deeper, distal ends (Figures 5c and 6). On the scale of the entire Juan de Fuca Ridge (~500 km), the highest CO_2 contents occur in glasses from the axial seamount caldera, the summit of the largest topographic anomaly along the ridge (Figure 6).

The observed correlation between ridge topography and CO_2 supersaturation, opposite the common expectation that CO_2 contents are higher for samples erupted at greater depths, suggests some constraints on the dynamics of magma emplacement. Several factors reflecting directions and rates of magma supply need to be considered. (1) Decreasing CO_2 contents with increasing depth along a single ridge segment may reflect

greater opportunities for degassing during lateral flow away from the zone of magma replenishment, either at the surface or in subaxial rifts, analogous to the Kilauea East Rift Zone [55, 56] or Icelandic fissure eruptions [57]. Evidence in support of lateral transport of magma away from axial highs comes from recent models of magmatic segmentation of mid-ocean ridges [33, 58-60]. Overlapping spreading centers and small ridge crest discontinuities also are interpreted to result from misalignment of magmatic pulses that have propagated laterally away from the shallow zone of magma replenishment [61, 62]. (2) If magma is supplied to the deeper portions of the ridge primarily in a vertical direction, greater degrees of degassing may indicate longer transit times between the magma chamber and the surface, either because the magma chamber is deeper, or ascent rates are lower. (3) The high CO_2 contents of glasses from the summit of the axial seamount may indicate extremely short transit times between the magma chamber and the surface reflecting either a shallower magma chamber or higher ascent rates at this location than at deeper portions of the ridge. Ascent rates along mid-ocean ridges are poorly known, but several models predict that there should be along-strike variations in the depth to the magma chamber. Francheteau and Ballard [59] presented a model in which each accretionary ridge segment is underlain by a magma chamber that is largest and shallowest where the ridge crest is shallowest. The high heat flux associated with a large magma chamber causes thinning of the crustal lid, enhanced hydrothermal circulation, and isostatic uplift. Because the crustal lid is thinnest at the axial high, erupting magmas might be relatively undegassed, as they have traversed the shortest, most direct path from the magma reservoir. Observations of voluminous volcanic outpouring [28] and hydrothermal activity [23] at the shallowest part of each ridge segment of the Juan de Fuca Ridge are consistent with this model. Also, results of seismic reflection studies [31] show that the reflector interpreted to be the top of a magma chamber is deeper relative to the ocean floor where the ridge crest is deeper.

Estimates of depths to magma chambers have been attempted by determining the minimum pressure necessary to keep the dissolved CO_2 in supersaturated melts in solution [42]. This calculation assumes that magmas in the magma chamber were vapor-saturated, that they resided in the magma chamber long enough to have established melt-vapor equilibrium [see 49], and that minimal degassing occurred during ascent and eruption. If any of these assuptions are incorrect, the actual depth to the magma chamber will be greater than our estimate. If the negative correlation between dissolved CO_2 contents and eruption depth reflects more extensive degassing for the deeper samples, the second assumption is violated for most of the samples analyzed in this study. Data from the axial seamount, however, may be appropriate to use in such a calculation, because these samples are the least degassed. The sample with the highest CO_2 content, 360 ppm, has about 300 ppm in excess of the solubility at the pressure of eruption (150 bars). The excess CO_2 could be kept in solution if the pressure were increased to about 900 bars. Using a density of 2.8 g/cm^3 for the oceanic crust, the magma would have been vapor-saturated at a depth beneath the seafloor of 2.7 km, in good agreement with the multi-channel seismic reflection results of 2.3 to 2.5 km beneath segment 1 [31]. We note that seismic reflections probably come from near the roof of the chamber, whereas magmas may erupt from deeper levels, so an exact correspondence between these two depth estimates may not be expected in any case.

In general, CO_2 will exsolve into bubbles that may remain suspended in the liquid ("closed system" degassing) or leave the melt ("open system" degassing). For similar bulk CO_2 contents, a negative correlation between vesicle content and dissolved CO_2 content is expected for samples that degas under closed system conditions. The samples we have studied do not fall on a single closed system path (Figure 2) suggesting either a range of initial CO_2 contents in the melts or that some samples have gained or lost bubbles during or prior to eruption. Although large bubbles can rise long distances in magma on eruptive time scales and thus need not be conserved, small bubbles are probably conserved on these

time scales. For example, in 30 minutes a 0.0010 cm (10 μm) diameter bubble in basaltic melt will rise only about 0.004 cm, while a 0.10 cm (1000 μm) bubble will rise 40 cm. Thus small vesicles probably record locally closed system behavior during rapid eruptions. The high concentrations of small vesicles in the samples with CO_2-rich glasses (Figure 3) and the decoupling of their concentration from the concentration of large vesicles (Figure 2) may reflect this kind of behavior. Detailed study of bubble size distributions and CO_2 contents of MORB glasses in the context of knowledge of rates of bubble nucleation and growth may provide quantitative constraints on timescales of magma transport [42, 45]. Measurements of CO_2-zoning profiles in glass adjacent to small vesicles would also be valuable.

DISCUSSION OF H_2O DATA

The amount of water that partitions into the vapor phase is small in submarine eruptions deeper than about 500 m [1-4]. Consequently water contents, unlike CO_2 contents, are not expected to be significantly affected by degassing and can be used to gain insight into the behavior of water during crystal-liquid fractionation processes. It is beyond the scope of this paper to try to explain all the geochemical variations along the Juan de Fuca Ridge, but we briefly discuss water contents in the context of data for other trace and minor elements and existing petrogenetic models.

Chemical variation in Juan de Fuca Ridge basalts has been ascribed to a combination of variations in source region chemistry, degrees of partial melting, and amounts of fractional crystallization and magma mixing [16, 26, 27, 30]. Based on major and trace element data, Liias [30] concluded that the most primitive Endeavour segment lavas could be derived by 7 to 9 % partial melting of a lherzolitic source region with REE

contents 2X chondritic values. The most primitive lavas from the Juan de Fuca Ridge south of the Cobb Offset could be formed from higher degrees of partial melting (10 to 30 %) of a lherzolitic source region depleted relative to that for the Endeavour segment lavas. He also concluded that to generate the wide range of highly incompatible ratios found in lavas south of the Cobb Offset, the source region must be heterogeneous on a scale of hundreds of meters to several kilometers.

The association of high water contents with incompatible element enriched Endeavour segment lavas (Figures 7-9) is consistent with previous studies of H_2O in MORB [1, 52] and implies that water behaves as an incompatible component during magma generation. The systematic behavior of water with respect to other incompatible components allows constraints to be placed on the behavior of water during partial melting. In particular, the proportionality between water and La contents (Figure 9a) for all samples from the Juan de Fuca ridge implies that these components were not fractionated during partial melting, and thus that they have similar bulk partition coefficients (we assume here that the source regions of the Endeavour segment and segments 1-7 are related and their compositional differences were generated by previous igneous processing including extraction and/or addition of a basaltic component). Assuming the lherzolitic source regions are composed of 60% olivine, 30% orthopyroxene, and 10% clinopyroxene [30] and using mineral/melt partition coefficients for La from Bender et al. [63], the bulk partition coefficients of water and La are estimated to be about 0.01. This result is similar, but not identical, to those of Michael [64] for lavas from the Explorer Ridge and the Pacific-Nazca Ridge. Although both his and our studies lead to the conclusion that water behaves like a light rare earth element, he finds water to have a partition coefficient similar to those of Ce and Nd, i.e., somewhat higher than that of La.

Initial water contents of mantle sources of Juan de Fuca ridge lavas can be estimated based on the similar behavior of La and H_2O. This is done by multiplying the initial estimated La contents in the source regions by the near constant H_2O/La ratio of the lavas of about 500. Using source compositions in Liias [30], the enriched source with a La content of 0.66 ppm (2X chon.) would have a water content of 330 ppm, and the transitional source with a La content of 0.50 ppm (1.5X chon.) would have an estimated water content of 250 ppm. These water contents for MORB mantle source regions are similar to those estimated by Byers et al. [51] for the Galapagos Spreading Center and Michael [64] for the Pacific-Nazca and Explorer Ridges on the basis of batch melting calculations assuming reasonable degrees of partial melting (10-30 %).

Equilibrium batch partial melting paths of hypothetical Juan de Fuca ridge source regions [66] have been calculated based on these estimates of water content and the source region compositions of Liias [30]; see caption to Figure 8. These are shown in Figures 8 and 9 along with the effects of fractional crystallization at low pressures. It is clear that the behavior of water relative to other incompatible trace elements can be explained to first order in the context of these simple extensions of Liias's models given a DH_2O of 0.01. For Endeavour segment lavas, about 7-20 % melting of a relatively enriched source (slightly larger than partial melting estimates of Liias [30]) followed by up to about 40 % fractional crystallization can account for most of the data. For Juan de Fuca lavas south of the Cobb Offset, 15-30 % melting of a relatively depleted source followed by up to 50 % fractional crystallization can explain most of the data. We emphasize, however, that although partial melting and fractional crystallization can account for the major trends in the data for lavas from the Juan de Fuca Ridge, important roles for local source variation and/or magma mixing cannot be ruled out [27, 30].

According to this analysis, the H_2O content of the "anhydrous" residue after extraction of MORBs from mantle source regions (provided that melt extraction is 100% efficient) would be on the order of 10 ppm. Assuming that the residual mantle phases during MORB genesis are olivine and pyroxene in the approximate proportions 60:40 [30] and given that the water contents of mantle olivines are at the ppb level [65], this suggests that the residual pyroxenes contain a few tens of ppm dissolved water. The pyroxene/liquid partition coefficient for water during partial melting leading to MORB genesis may thus be as high as 0.03. The small variations in the incompatibility of water during MORB genesis that have been observed [i.e., this study, 64] might reflect variable olivine/pyroxene ratios in MORB source regions. If orthopyroxene tended to concentrate water relative to clinopyroxene, or if water partitions approximately equally between the two pyroxenes (in contrast to most incompatible elements), variations in pyroxene proportions and degree of partial melting could also influence the partition coefficient for water.

CONCLUSIONS

(1) Dissolved CO_2 concentrations of basaltic glasses from the Juan de Fuca Ridge and neighboring seamounts have been measured using infrared spectroscopy and range from 45 to 360 ppm by weight. Samples erupted at a given depth exhibit a wide range in dissolved CO_2 contents, with many samples significantly supersaturated with respect to CO_2-rich vapor at the depth of eruption. Supersaturated glasses probably quenched from magmas that ascended and erupted on timescales too short to degas fully. Samples with the lowest dissolved CO_2 contents at a given depth measured in this study lie near the experimentally determined solubility curve for basaltic melt [42], suggesting that these samples degassed to the equilibrium solubility value.

(2) CO_2 contents of samples south of the Cobb Offset correlate negatively with eruption depth. The highest CO_2 contents for each ridge segment are spatially associated with local topographic highs. Magmas erupted at local axial highs may be least degassed because they traveled directly upward from an underlying magma chamber. Magmas erupted along deeper sections of the ridge may be more degassed because they traveled longer distances from deeper magma chambers or laterally away from magma chambers underlying the axial highs in subaxial dikes or seafloor lava flows.

(3) Dissolved water contents were also determined by infrared spectroscopy and range from 0.07 to 0.48 wt %. Water behaves like La (D ~ 0.01) during magma genesis in the mantle beneath the Juan de Fuca Ridge. The concentration of water in residual "anhydrous" mantle after MORB extraction is on the order of 10 ppm, which is probably concentrated in pyroxene. Variable pyroxene/olivine ratios in peridotitic source regions may translate into variable partition coefficients for water during magma genesis. Water also behaves like an incompatible element during lower pressure crystal/liquid fractionation processes. Endeavour segment lavas could have been produced by about 7-20 % partial melting of a mantle source region containing about 330 ppm water followed by up to 40 % fractional crystallization at low pressures. Juan de Fuca Ridge lavas south of the Cobb Offset could have been derived by larger degrees of partial melting (10 to 30 %) of a source region containing about 250 ppm water followed by up to 50 % fractional crystallization at low pressures.

ACKNOWLEDGEMENTS

We thank P. Rosener for assistance in infrared spectroscopic analyses and D. Burnett for assistance in the vesicle content determinations. C. Langmuir encouraged us to

delve into controls of water content variations, though he is not responsible for our interpretations. J. Blank generously shared her data with us and discussed aspects of her work on the same samples. We also thank T. Plank and C. Langmuir for calculating the liquidus temperature of TT152-13. We are grateful to J. Moore and C. Langmuir for their thoughtful reviews. The research at Caltech was performed under NSF Grants EAR-8417434 and EAR-8618229 (EMS). Samples were collected with support of NSF Grants OCE79-25041, OCE81-11413, and OCE83-09812 (JRD). Caltech Division of Geological and Planetary Science Contribution Number 4573.

References

1. J. G. Moore, Water content of basalt erupted on the ocean floor, Contrib. Mineral. Petrol. 28, 272-279, 1970.
2. J. G. Moore and J. -G. Schilling, Vesicles, water, and sulfur in Reykjanes Ridge basalts, Contrib. Mineral. and Petrol. 41, 105-118, 1973.
3. J. G. Moore, J. N. Batchelder and C. G. Cunningham, CO_2-filled vesicles in mid-ocean basalt, J. Volc. and Geotherm. Res. 2, 309-327, 1977.
4. A. Jambon and J. L. Zimmermann, Major volatiles from a North Atlantic MORB glass and calibration to He: A size fraction analysis, Chem. Geol. 62, 177-189, 1987.
5. J. G. Moore, Petrology of deep-sea basalt near Hawaii, Am. J. Sci. 263, 40-52, 1965.
6. J. G. Moore, Vesicularity and CO_2 in mid-ocean ridge basalt, Nature 282, 250-253, 1979.
7. D. M. Harris, The concentration of CO_2 in submarine tholeiitic basalts, J. Geol. 89, 689-701, 1981.
8. D. J. Des Marais and J. G. Moore, Carbon and its isotopes in mid-oceanic basaltic glasses, Earth Planet. Sci. Lett. 69, 43-57, 1984.
9. H. Sakai, D. J. Des Marais, A. Ueda, and J. G. Moore, Concentrations and isotope ratios of carbon, nitrogen and sulfur in ocean-floor basalts, Geochim. Cosmochim. Acta 48, 2433-2441, 1984.
10. G. Fine and E. Stolper, Carbon dioxide in basaltic glasses: Concentrations and speciation, Earth Planet. Sci. Lett. 76, 263-278, 1986.
11. D. J. Des Marais, Carbon abundance measurements in oceanic basalts: the need for a consensus, Earth Planet. Sci. Lett. 79, 21-26, 1986.
12. C. D. Byers, M. O. Garcia, and D. W. Muenow, Volatiles in basaltic glasses from the East Pacific Rise at 21° N: implications for MORB sources and submarine lava flow morphology, Earth Planet. Sci. Lett. 79, 9-20, 1986.

13. H. Craig, Comment on "Carbon isotope systematics of a mantle hotspot: a comparison or Loihi Seamount and MORB glasses" by R.A. Exley, D.P. Mattey, D.A. Clague and C.T. Pillinger, Earth Planet. Sci. Lett. 82, 384-386, 1987.

14. R. A. Exley, D. P. Mattey and C. T. Pillinger, Low temperature carbon components in basaltic glasses--reply to comment by H. Craig, Earth Planet. Sci. Lett. 82, 387-390, 1987.

15. S. M. Barr, Seamount chains formed near the crest of the Juan de Fuca Ridge, northeast Pacific Ocean, Marine Geol. 17, 1-19, 1974.

16. J. R. Delaney, H. P. Johnson, and J. L. Karsten, The Juan de Fuca Ridge--Hotspot--Propagating rift system: New tectonic, geochemical, and magnetic data, J. Geophys. Res. 86, 11,747-11,750, 1981.

17. R. N. Hey, A new class of "pseudofaults" and their bearing on plate tectonics: a propagating rift model, Earth Planet. Sci. Lett. 37, 321-325, 1977.

18. R. N. Hey, F. K. Duennebier, and W. J. Morgan, Propagating rifts on mid-ocean ridges, J. Geophys. Res. 85, 3647-3658, 1980.

19. J. -G. Schilling, B. Cousens, R. L. Chase, J. R. Delaney, Juan de Fuca-Explorer Ridge: Rare earth contents, EOS Trans. AGU 63, 1154, 1982.

20. J. S. Eaby, D. A. Clague, and J. R. Delaney, Sr isotopic variations along the Juan de Fuca Ridge, J. Geophys. Res. 89, 7883-7890, 1984.

21. T. K. Kyser and J. R. O'Neil, Hydrogen isotope systematics of submarine basalts, Geochim. Cosmochim. Acta 48, 2123-2133, 1984.

22. D. S. Wilson, R. N. Hey, and C. Nishimura, Propagation as a mechanism of reorientation of the Juan de Fuca Ridge, J. Geophys. Res. 89, 9215-9225, 1984.

23. K. Crane, F. Aikman, R. Embley, S. Hammond, A. Malahoff, and J. Lupton, The distribution of geothermal fields on the Juan de Fuca Ridge, J. Geophys. Res. 90, 727-744, 1985.

24. J. L. Karsten and J. R. Delaney, Comparison of glass geochemistry from seamount and adjacent ridge crest lavas: Juan de Fuca Ridge, EOS Trans. AGU 66, 1109, 1985.

25. E. E. Davis and J. L. Karsten, On the cause of the asymmetric distribution of seamounts about the Juan de Fuca ridge: ridge-crest migration over a heterogeneous asthenosphere, Earth Planet. Sci. Lett. 79, 385-396, 1986.

26. J. R. Delaney, J. L. Karsten, and S. R. Hammond, Petrology and tectonics of the Juan de Fuca Ridge, EOS Trans. AGU 67, 888, 1986.

27. J. E. Dixon, D. A. Clague, and J. -P. Eissen, Gabbroic xenoliths and host ferrobasalt from the southern Juan de Fuca Ridge, J. Geophys. Res. 91, 3795-3820, 1986.

28. E. S. Kappel and W. B. F. Bryan, Volcanic episodicity and a non-steady state rift valley along northeast Pacific spreading centers: Evidence from Sea MARC I, J. Geophys. Res. 91, 13,925-13,940, 1986.

29. J. L. Karsten and J. R. Delaney, Hot spot/migrating ridge crest interaction-Juan de Fuca style, EOS Trans. AGU 67, 1254, 1986.

30. R. Liias, Geochemistry and petrogenesis of basalts erupted along the Juan de Fuca Ridge, Ph.D. Thesis. University of Massachusetts. Amherst, Ma., 264 pp., 1986.

31. J. L. Morton, N. H. Sleep, W. R. Normark, and D. H. Tompkins, Structure of the southern Juan de Fuca Ridge from seismic reflection records, J. Geophys. Res. 92, 11,315-11,326, 1987.

32. J. T. Wilson, Evidence from ocean islands suggesting movement in the earth, Phil. Trans, R. Soc. Lond. A 258, 145-165, 1965.

33. P. R. Vogt and G. L. Johnson, Transform faults and longitudinal flow below the mid-oceanic ridge, J. Geophys. Res. 80, 1399-1428, 1975.

34. C. R. B. Lister, Crustal magnetization and sedimentation near two small seamounts west of the Juan de Fuca Ridge, northeast Pacific, J. Geophys. Res. 76, 4824-4841, 1971.

35. R. G. Currie, E. E. Davis, R. P. Riddihough, and B. S. Sawyer, Juan de Fuca Ridge atlas: preliminary Seabeam bathymetry, Energy, Mines and Resources, Canada, Earth Phys. Branch Open File 85-1, 1985.

36. W. J. Morgan, Plate motions and deep mantle convection, in Studies in Earth and Space Sciences, Hess Volume, Mem. 132, edited by R. Shagan et al., Geological Society of America, Boulder, Colo., 1973.

37. A. J. Erlank and E. J. D. Kable, The significance of incompatible elements in Mid-Atlantic Ridge basalts from 45°N with particular reference to Zr/Nb, Contrib. Mineral. Petrol. 54, 281-291, 1976.

38. J. -G. Schilling, Sea-floor evolution: rare-earth evidence, Phil. Trans. Roy. Soc. Lond. A. 268, 663-706, 1971.

39. W. M. White and W. B. Bryan, Sr-isotope, K, Rb, Cs, Sr, Ba, and rare-earth geochemistry of basalts from the FAMOUS area, Geol. Soc. Am. Bull. 88, 571-576, 1977.

40. E. M. Klein and C. H. Langmuir, Global correlations of ocean ridge basalt chemistry with axial depth and crustal thickness, J. Geophys. Res. 92, 8089-8115, 1987.

41. J. G. Blank, J. R. Delaney, and D. J. Des Marais, Carbon in basaltic glass from the Juan de Fuca Ridge, EOS Trans. AGU 67, 1253. 1986.

42. E. Stolper and J. R. Holloway, Experimental determination of the solubility of carbon dioxide in molten basalt at low pressure, Earth Planet. Sci. Lett. 87, 397-408, 1988.

43. E. Stolper, The speciation of water in silicate melts, Geochim. Cosmochim. Acta 46, 2609-2620, 1982.

44. R. J. Kirkpatrick, Processes of crystallization in pillow basalts, Hole 396B DSDP Leg 46, Init. Rep. Deep Sea Drill. Proj. 46, 271-282, 1978.

45. E. B. Watson, M. A. Sneeringer, and A. Ross, Diffusion of dissolved carbonate in magmas: Experimental results and applications, Earth and Planet. Sci. Lett. 61, 346-358, 1982.

46. R. Brett, H. T. Evans, Jr., E. K. Gibson, Jr., J. W. Hedenquist, M.-V. Wandless, and M. A. Sommer, Mineralogical studies of sulfide samples and volatile concentrations of basalt glasses from the southern Juan de Fuca Ridge, J. Geophys. Res. 92, 11,373-11,379, 1987.

47. D. P. Mattey, R. H. Carr, I. P. Wright, and C. T. Pillinger, Carbon isotopes in submarine basalts, Earth Planet. Sci. Lett. 70, 196-206, 1984.

48. F. Pineau and M. Javoy, Carbon isotopes and concentrations in mid-oceanic ridge basalts, Earth Planet. Sci. Lett. 62, 239-257, 1983.

49. J. R. Delaney, D. W. Muenow, and D. G. Graham, Abundance and distribution of water, carbon and sulfur in the glassy rims of submarine pillow basalts, Geochim. Cosmochim. Acta 42, 581-594, 1978.

50. C. D. Byers, D. W. Muenow, and M. O. Garcia, Volatiles in basalts and andesites from the Galapagos Spreading Center, 85° to 86° W, Geochim. Cosmochim. Acta 47, 1551-1558, 1983.

51. C. D. Byers, D. M. Christie, D. M. Muenow, and J. M. Sinton, Volatile contents and ferric-ferrous ratios of basalt, ferrobasalt, and andesite and rhyodacite glasses from the Galapagos 95.5° W propagating rift, Geochim. Cosmochim. Acta 48, 2239-2245, 1984.

52. P. J. Michael and R. L. Chase, The influence of primary magma composition, H_2O and pressure on mid-ocean ridge basalt differentiation, Contrib. Mineral. Petrol. 96, 245-263, 1987.

53. F. J. Spera and S. Bergman, Carbon dioxide in igneous petrogenesis: I. Aspects of the dissolution of CO_2 in silicate liquids, Contrib. Mineral. Petrol. 74, 55-66, 1980.

54. L. A. Silver and J. R. Delaney, Melting experiments on Juan de Fuca Ridge basalts: Implications for petrogenesis, EOS Trans. AGU 64, 888, 1983.

55. J. P. Eaton, Crustal structure and volcanism in Hawaii, in The Crust of the Pacific Basin, Geophys. Monogr. Ser. 6 (edited by E.T.Endo), AGU, Washington, D. C., 13-29, 1962.

56. T. M. Gerlach, Exsolution of H_2O, CO_2, and S during eruptive episodes at Kilauea Volcano, Hawaii, J. Geophys. Res. 91, 12,177-12,185, 1986.

57. H. Sigurdsson, and S. R. J. Sparks, Lateral magma flow within rifted Icelandic crust, Nature 274, 126-130, 1978.

58. B. T. R. Lewis, Periodicities in volcanism and longitudinal magma flow on the East Pacific Rise at 23°N, Geophys. Res. Lett. 6, 753-756, 1979.

59. J. Francheteau and R.D. Ballard, The East Pacific Rise near 21°N, 13°N and 20°S: inferences for along-strike variability of axial processes of the mid-ocean ridge, Earth Planet. Sci. Lett. 64, 93-116, 1983.

60. K. Crane, The spacing of rift axis highs: dependence upon diapiric processes in the underlying asthenosphere?, Earth Planet. Sci. Lett. 72, 405-414, 1985.

61. K. Macdonald, J.-C. Sempere, and P. J. Fox, East Pacific Rise from Siqueiros to Orozco fracture zones: Along-strike continuity of axial neovolcanic zone and structure and evolution of overlapping spreading centers, J. Geophys. Res. 89, 6049-6069, 1984.

62. K. C. Macdonald, J.-C. Sempere, P. J. Fox, and R. Tyce, Tectonic evolution of ridge-axis discontinuities by the meeting, linking, or self-decapitation of neighboring ridge segments, Geology 15, 993-997, 1987.

63. J. F. Bender, C. H. Langmuir, and G. N. Hanson, Petrogenesis of basalt glasses from the Tamayo Region, East Pacific Rise, J. Petrol. 25, 213-254, 1984.

64. P. J. Michael, Concentration, behavior and storage of water in the suboceanic upper mantle: Implications for metasomatism, EOS Trans. AGU 68, 443-444, 1987.

65. G. H. Miller, G. R. Rossman, and G. E. Harlow, The natural occurrence of hydroxide in olivine, Phys. Chem. Minerals. 14, 461-472, 1987.

66. D. M. Shaw, Trace element fractionation during anatexis, Geochim. Cosmochim. Acta 34, 237-243, 1970.

67. W. M. White and J.-G. Schilling, The nature and origin of geohemical variation in Mid-Atlantic Ridge basalts from the Central North Atlantic, Geochim. Cosmochim. Acta 42, 1501-1516, 1978.

68. H. Johnson and M. Holmes, Evolution in plate tectonics: The Juan de Fuca Ridge, Geol. Soc. Am., DNAG, eastern Pacific Volume, Fig. 4, in press.

TABLE 1

SAMPLE	COM-MENTS	LOCATION	DEPTH FROM (m) *e	TO (m) *e	LATITUDE ('N)	LONGITUDE ('W)	SiO2 (wt %) *f	TiO2 (wt %) *f	Na2O (wt %) *f	K2O (wt %) *f	P2O5 (wt %) *f	Mg# *g	FeO*/MgO *h	H2O (wt %)	H2O (+/-, #) *i	CO2 (ppm)	CO2 (+/-, #) *i
JUAN DE FUCA RIDGE, SEGMENTS 1-7																	
TT152-37	b, l	S1	2335	2340	44.617	130.395	50.6	1.9	2.8	0.23	0.25	48	2.0	0.23	(0.00, 4)	203	(14, 4)
TT152-43-19	k	S1	2282	2282	44.996	130.205	50.7	1.4	2.4	0.13	0.12	58	1.3	0.16	(0.00, 2)	209	(11, 2)
TT152-44		S2	2375	2425	45.134	130.186	50.6	1.3	2.4	0.17	0.12	60	1.2	0.18	(0.01, 3)	108	(13, 3)
TT152-77-7		S3	1920	2060	45.671	130.061	47.9	1.3	2.8	0.03	0.11	63	1.1	0.17	(-, 1)	171	(18, 1)
TT152-77-6		S3	1920	2060	45.671	130.061	47.7	1.3	2.6	0.04	0.08	63	1.1	0.16	(-, 1)	178	(20, 1)
TT152-55-25	b	AXIAL	1530	1559	45.938	130.002	49.4	1.4	2.8	0.16	0.13	54	1.5	0.23	(0.02, 2)	265	(26, 2)
TT170-5A	b, d	AXIAL	1425	1545	45.947	130.027	49.2	1.5	2.8	0.18	0.12	54	1.5	0.22	(-, 1)	137	(00, 1)
TT170-5B	b	AXIAL	1425	1545	45.947	130.027	49.2	1.5	2.8	0.18	0.12	54	1.5	0.21	(-, 1)	237	(31, 1)
PISCES1326-2A	b	AXIAL	1554	1554	45.983	130.051	50.4	1.5	2.9	0.18	0.12	54	1.5	0.30	(-, 1)	360	(35, 1)
PISCES1326-2B	b	AXIAL	1554	1554	45.983	130.051	50.4	1.5	2.9	0.18	0.12	54	1.5	0.22	(0.01, 2)	311	(28, 2)
TT152-61		S5	2220	2337	46.075	129.893	49.2	1.7	2.9	0.16	0.16	51	1.7	0.36	(0.02, 4)	087	(11, 4)
TT152-72		S5	2200	2265	46.285	129.726	50.3	1.3	2.3	0.09	0.11	56	1.4	0.27	(-, 1)	088	(02, 1)
TT152-65	b	S5	2295	2320	46.353	129.684	50.9	1.2	2.5	0.07	0.11	56	1.4	0.15	(-, 1)	234	(11, 1)
TT152-29-1	b, k	S6	2310	2360	46.862	129.292	49.6	1.6	2.6	0.10	0.13	52	1.6	0.20	(-, 1)	221	(11, 1)
TT152-21	b, l	S6	2410	2520	46.926	129.264	50.6	1.9	2.6	0.16	0.18	48	1.9	0.36	(0.01, 3)	225	(20, 3)
TT152-13		S6	2625	2625	47.204	129.124	50.5	2.4	2.7	0.15	0.23	43	2.3	0.33	(0.00, 2)	056	(10, 1)
HU81017-6-11	l	S6	2529	2529	47.22	129.092	50.6	2.0	2.7	0.19	0.18	48	1.9	0.31	(0.06, 2)	107	(00, 1)
TT152-11-21		S7	2640	2690	47.541	128.954	50.5	1.8	2.3	0.21	0.21	52	1.7	0.29	(0.01, 2)	099	(08, 2)
TT152-78-1	b	S7	2340	2345	47.661	128.975	50.9	1.3	2.6	0.13	0.12	59	1.3	0.18	(-, 1)	211	(13, 1)
ENDEAVOUR SEGMENT																	
HU81017-11		END	2569	2569	47.62	129.265	51.1	1.5	3.2	0.10	0.16	59	1.2	0.29	(0.00, 2)	116	(11, 2)
TT175-40-3	a, d	END-SE	2251	2736	47.702	129.208	50.6	1.6	3.1	0.25	0.18	57	1.4	0.39	(-, 1)	045	(9, 1)
HU81017-2-4		END	2470	2470	47.726	129.244	51.6	1.9	3.0	0.44	0.33	50	1.8	0.48	(-, 1)	n. d.	n. d.
TT170-70-21		END	2181	2201	47.878	129.145	50.0	1.5	2.8	0.17	0.18	59	1.3	0.22	(0.01, 3)	090	(12, 3)
TT175-28-27		END	2121	2322	47.949	129.103	50.8	1.7	2.9	0.54	0.24	55	1.5	0.46	(-, 1)	186	(14, 1)
TT175-20-30	a	END	2102	2151	47.953	129.108	51.4	1.7	2.7	0.54	0.25	56	1.4	0.39	(-, 1)	094	(20, 1)
TT175-54-4	a, d	END	2052	2241	47.954	129.115	51.8	1.8	3.0	0.39	0.06	55	1.4	0.38	(-, 1)	049	(08, 1)
TT175-17-14		END	2003	2190	47.984	129.085	50.7	1.6	2.7	0.36	0.20	55	1.5	0.33	(-, 1)	073	(03, 1)
TT175-31		END	2181	2201	48.021	129.065	52.0	1.7	2.9	0.50	0.22	58	1.3	0.38	(0.03, 2)	141	(13, 2)
W8408A-3D	a	END	2270	2365	48.391	129.077	49.9	1.2	2.4	0.16	0.12	62	1.1	0.20	(-, 1)	124	(36, 1)
SEAMOUNTS																	
TT175-92-9	a	PURITY	2054	2327	45.611	130.632	48.9	1.4	2.8	0.08	0.08	64	1.0	0.18	(-, 1)	107	(12, 1)
TT175-90	c	COURAGE	1727	1832	45.676	130.829	50.5	1.6	2.8	0.26	0.17	56	1.4	0.29	(-, 1)	066	(13, 1)
TT170-36-3		BBE	1639	1662	45.967	130.274	48.6	1.2	3.0	0.06	0.11	60	1.2	0.13	(-, 1)	065	(18, 1)
TT175-89	d	HUMILITY	1872	2052	46.034	131.268	51.0	1.6	3.0	0.16	0.13	54	1.5	0.24	(0.00, 3)	203	(17, 3)
TT175-74-10		GLUT	1594	1922	47.141	131.463	50.2	1.4	2.7	0.19	0.12	62	1.1	0.19	(-, 1)	089	(17, 1)
TT175-71		LUST	1997	2003	47.501	131.515	49.0	1.4	2.9	0.22	0.14	57	1.3	0.26	(0.02, 2)	104	(11, 2)
TT175-39-3		HOAS W	2101	2777	47.695	129.405	50.2	0.9	1.9	0.00	0.06	65	1.0	0.07	(0.00, 2)	219	(33, 2)
TT175-61-11	d	E. SPGFD	1367	2171	47.901	129.642	50.1	1.3	2.6	0.03	0.06	58	1.3	0.07	(0.00, 2)	114	(13, 2)
TT175-61-20	b	E. SPGFD	1367	2171	47.901	129.642	49.6	1.5	2.9	0.10	0.13	55	1.5	0.16	(0.02, 2)	186	(20, 2)
JLK 71-15-8-1		END SMT	1772	1772	48.283	129.083	51.2	1.1	2.4	0.04	0.06	60	1.2	0.09	(-, 1)	205	(08, 1)
JLK 70-16-5-23	d	E. HECK	1574	1574	48.317	129.201	50.8	0.9	2.3	0.02	0.04	64	1.0	0.12	(-, 1)	106	(00, 1)
HU81017-31-2	B	EXPL	800	800	48.561	130.942	47.9	1.3	2.9	0.04	0.11	61	1.2	0.30	(0.01, 2)	n. d.	n. d.
TT063-34-7	d	EXPL	2370	2770	48.963	131.033	47.1	1.3	2.9	0.16	0.10	59	1.3	0.26	(-, 1)	117	(09, 1)

Legend for Table 1

a: major elements are for different samples or averages of several samples from the same location. b: more than a dozen vesicles <40 μm present in the glass chip analyzed by IR. c: phenocrysts and/or quench crystals present in glass. d: partially devitrified. e: depths corrected using Handbook of Ocean., 1966, p. 74, region 24. f: major elements obtained on glasses using Univ. of Washington 5-channel ARL-EMS electron microprobe (Delaney, unpublished data). g: 100 X Mg/(Mg + Fe^{2+}), Mg and Fe in atomic proportions. h: FeO* = total iron as FeO, both FeO* and MgO in wt.%. i: Water concentrations were determined using the height of the 3535 cm-1 peak, and where more than one spectrum was available we have reported the average and standard deviation. First value in parentheses is the standard deviation (1-σ), second value is the number of spectra used to calculate average. j: For each spectrum, we measured separately the intensities of the 1515 and 1435 cm^{-1} peaks plus the total area under the doublet and calculated a CO_2 concentration from each measurement. The CO_2 contents are averages of all the CO_2 concentrations measured from all spectra on texturally similar glass chips from the same split. The reported error in the CO_2 contents used to calculate the average. First value in parenthese is the standard deviation (1-σ), second value is the number of spectra used to calculate average. k: H_2O and CO_2 contents from Fine and Stolper [10]. l. average H_2O and CO_2 contents include analyses from Fine and Stolper [10].

TABLE 2: VESICLE CONTENTS MEASURED ON THIN SECTIONS

SAMPLE	COMMENTS	VOL % VESICLES TOTAL*		VOL % VESICLES < 40 microns*		VESICLES PER CM2*		DIAMETER LARGEST VESICLE (microns)
SEGMENTS 1-7								
TT152-37		1.02	(0.15, 4)	0.18	(0.05, 4)	630	(80, 4)	140
TT152-43-19		1.72		0.00		34		1020
TT152-44		0.95		0.02		70		480
TT152-77-6A	g to d, p	0.29		0.03		140		120
TT152-77-6B	d to s, same ts	0.55		0.02		160		220
TT152-55-25	b	0.44	(0.09, 3)	0.22	(0.00, 3)	570	(50, 3)	90
TT170-5A	g, b, p	1.43	(0.08, 2)	0.07	(0.01, 2)	290	(70, 2)	340
TT170-5B	d, b, diff. ts, p	1.81		0.08		320		370
P1326-2	b	0.35		0.12		380		140
TT152-61A	g, p	0.19		0.01		70		170
TT152-61B	d, same ts	0.72		0.00		10		680
TT152-65	b	1.36	(0.25, 2)	0.14	(0.04, 2)	770	(70, 2)	130
TT152-29-1A	g	0.37		0.00		40		390
TT152-29-1B	d, diff. ts	0.02		0.00		30		50
TT152-29-1C	b, diff. ts, p	0.78	(0.15, 3)	0.33	(0.04, 3)	1540	(150, 3)	100
TT152-13		2.26		0.01		50		1030
TT152-11-21		0.28		0.00		40		310
TT152-78-1	b	1.38		0.35		1210		90
ENDEAVOUR SEG.								
TT175-40-3	d, b	0.91	(0.05, 2)	0.03	(0.01, 2)	580	(90, 2)	270
TT170-70-21		1.05		0.03		100		650
TT175-20-30	b	0.95		0.07		520		200
SEAMOUNTS								
TT170-36-3		0.04		0.00		30		90
TT175-74-10		2.70		0.02		80		680
TT175-71		3.07		0.01		70		620

Notes:

* first value in parentheses is standard deviation (1-sigma), second value is number of thin sections averaged.

b: most bubbles <40 microns d: partially devitrified g: glassy s: spherulitic p: thin section with texture most similar to glass chip analyzed for volatiles; data from this thin section are plotted on Figures 2 and 3.

A, B, C: distinguish point counts on distinct areas of the same sample, either on the same thin section (same ts) or different thin sections (diff ts).

Figure 1: Map showing location of some of the seamounts and mid-oceanic ridge segments in the northeast Pacific (modified from Delaney, in prep). S1-S7 and Endeavour refer to segments of the Juan de Fuca Ridge. Names of seamounts or seamount chains from which we have samples are also given.

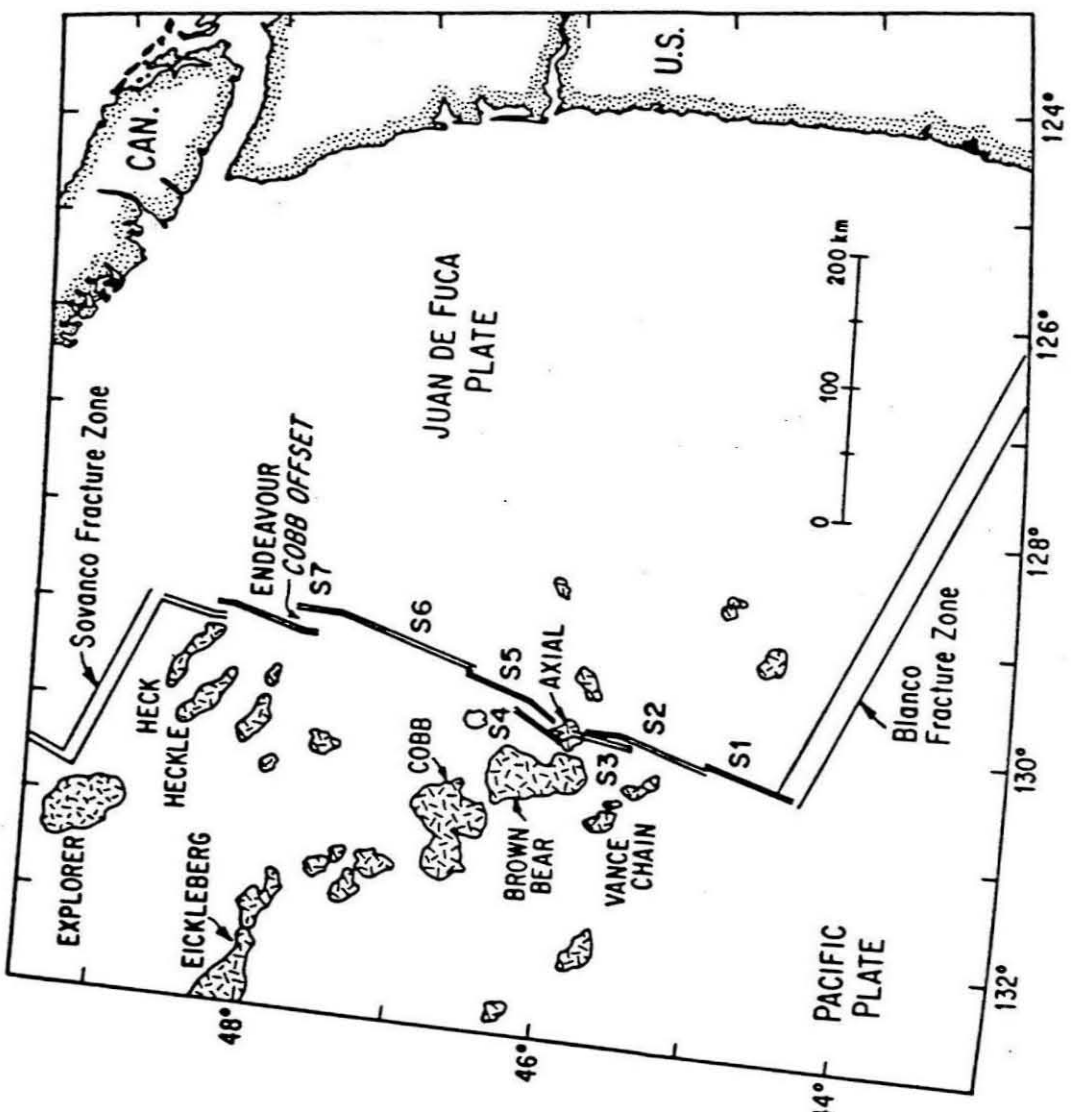
CAN.
U.S.
Sovanco Fracture Zone
ENDEAVOUR
COBB OFFSET
JUAN DE FUCA
PLATE
S7
S6
S5
S4
S3
S2
S1
AXIAL
HECK
HECKLE
EICKLEBERG
EXPLORER
COBB
BROWN
BEAR
VANCE
CHAIN
Blanco
Fracture Zone
PACIFIC
PLATE
0
100
200 km
48°
46°
44°
132°
130°
128°
126°
124°

Figure 2: Dissolved CO_2 content versus total volume percent vesicles measured on thin sections. CO_2 contents were not measured on the same thin sections used for vesicle content determinations. If different thin sections of the same sample had a range in vesicle contents, then the vesicle content plotted corresponds to the thin section most similar in texture to the glass chip analyzed for CO_2. "b" indicates samples with more than a dozen bubbles <40 μm in diameter present in the glass chip analyzed for CO_2. "d" indicates that the glass chip analyzed for CO_2 was partially devitrified. Samples from segments 1-7 are represented by open squares, from the Endeavour segment by filled diamonds, and from off-ridge seamounts by filled squares. The increase in vesicle content expected for a given amount of closed system CO_2 degassing is shown as the heavy arrow. The calculation was done assuming the ideal gas law, a glass transition temperature of 1000°C, a pressure of 200 bars, a gas composed of 90% CO_2, and a basalt density of 2.8 g/cm^3 The position of the arrow is arbitrary.

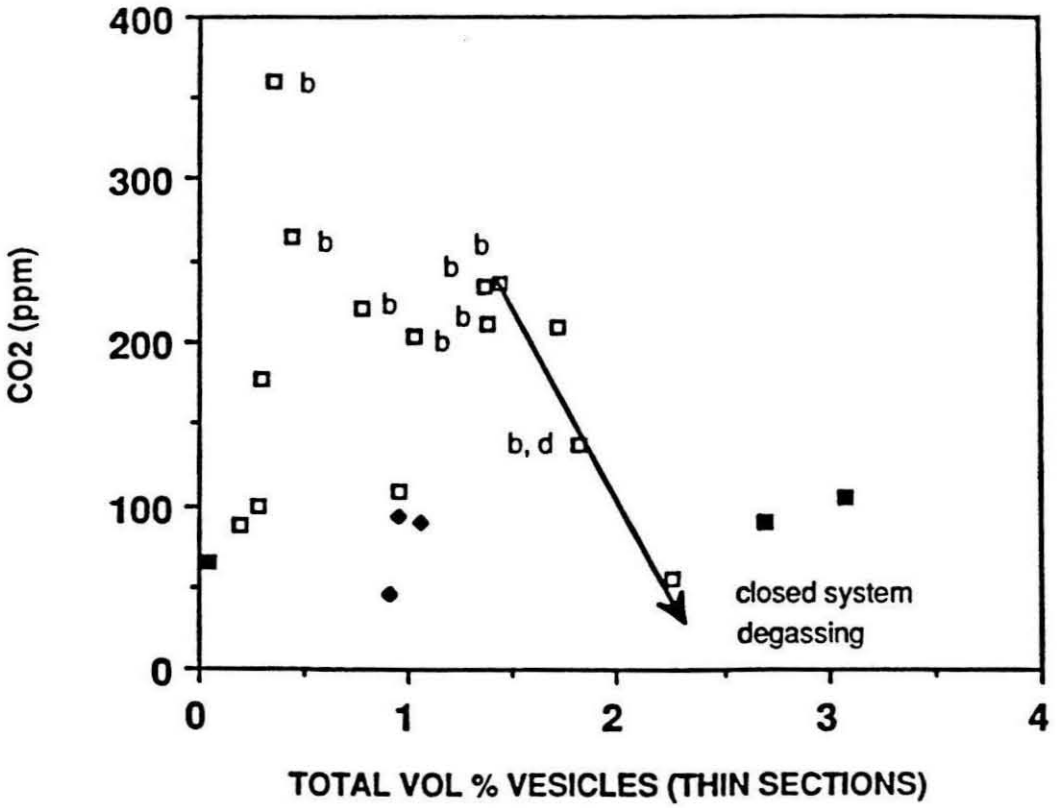
400
300
200
100
0
CO2 (ppm)
0
1
2
3
4
TOTAL VOL % VESICLES (THIN SECTIONS)
b
b
b
b
b
b
b
b, d
closed system
degassing

Figure 3: Dissolved CO_2 content versus volume percent vesicles <40 μm in diameter for samples shown in Figure 5. Small bubbles are most abundant in samples containing >200 ppm CO_2. Symbols and "b" and "d" are the same as in Figure 2.

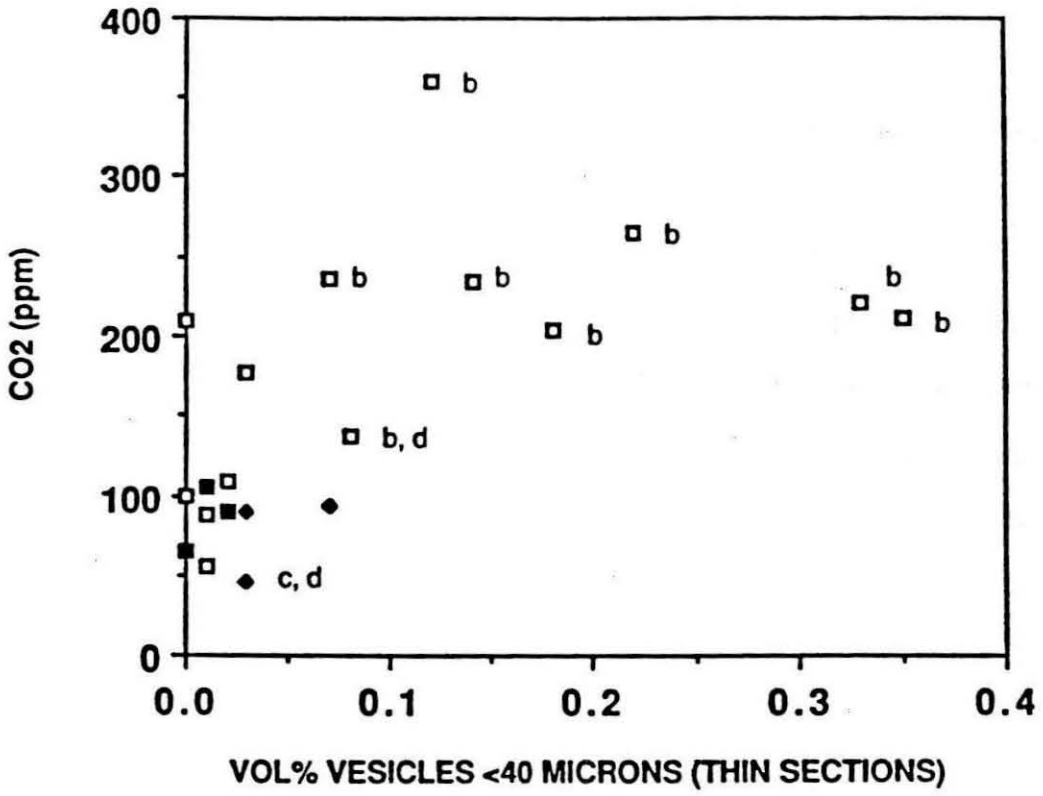
400
300
200
100
0
CO2 (ppm)
0.0
0.1
0.2
0.3
0.4
VOL% VESICLES <40 MICRONS (THIN SECTIONS)
b
b
b
b
b
b
b
b, d
c, d

Figure 4: Dissolved CO_2 contents versus depth for samples from the Juan de Fuca Ridge and adjacent seamounts. CO_2 solubility in basalt at 1200°C (10m H_2O = 1 bar) from Stolper and Holloway [42]. Note most samples have CO_2 contents in excess of solubility. Except for the partially devitrified samples, the lowest CO_2 contents at a given depth usually lie near the experimentally determined solubility curve. Typical error bars (1Â) are shown on a few points and are about 10 % of the amount present. Depth ranges are shown as error bars for those dredges that sample depth ranges larger than the depth range represented by the width of the symbols.

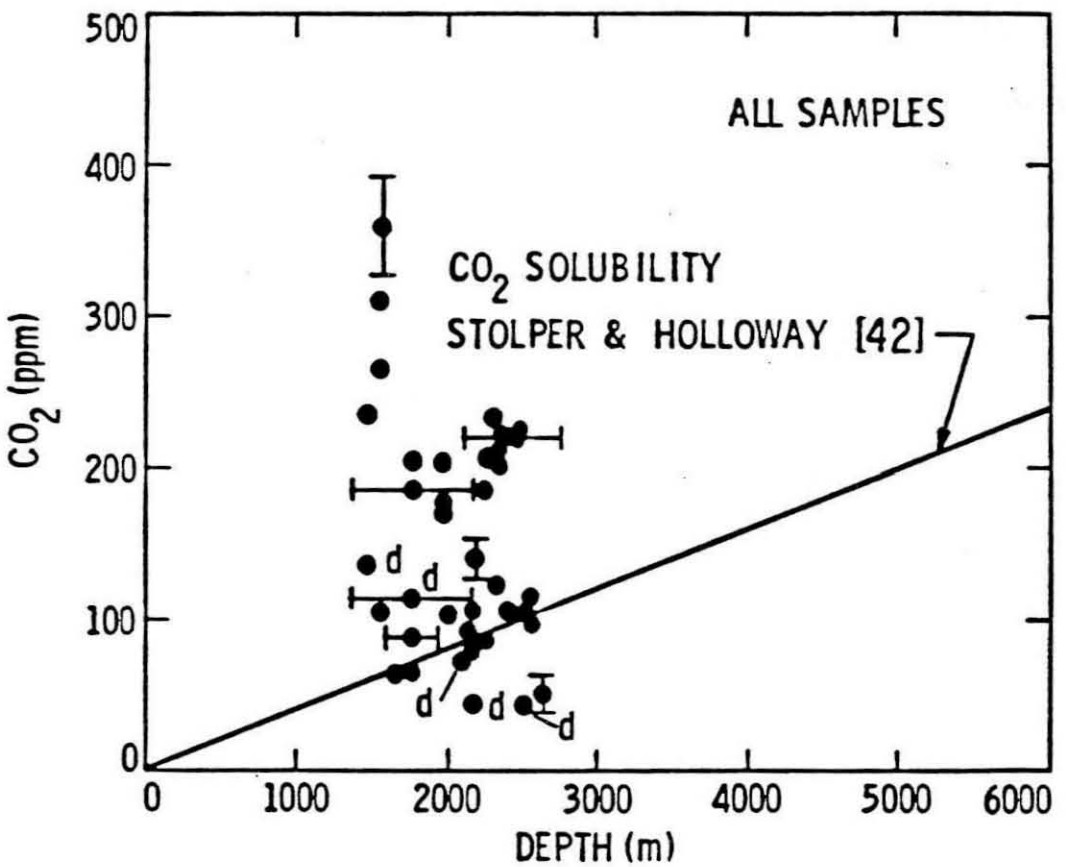
ALL SAMPLES
CO_2 SOLUBILITY
STOLPER & HOLLOWAY [42]
CO_2 (ppm)
DEPTH (m)
0
100
200
300
400
500
0
1000
2000
3000
4000
5000
6000
d
d
d
d
d

Figure 5: Dissolved CO_2 contents versus depth. Typical error bars (1Â) are shown on a few points. Solid line is best fit solubility curve for basaltic liquid at 1200°C [42]. Symbols are the same as in Figure 2. (a) Seamount samples. (b) Samples from Endeavour segment. Note lowest dissolved CO_2 contents are from devitrified glasses. (c) Samples south of the Cobb Offset. Note negative correlation (especially when partially devitrified samples are neglected) between dissolved CO_2 content and depth of eruption. Depth ranges are shown as error bars for those dredges that sample depth ranges larger than the depth range represented by the width of the symbols.

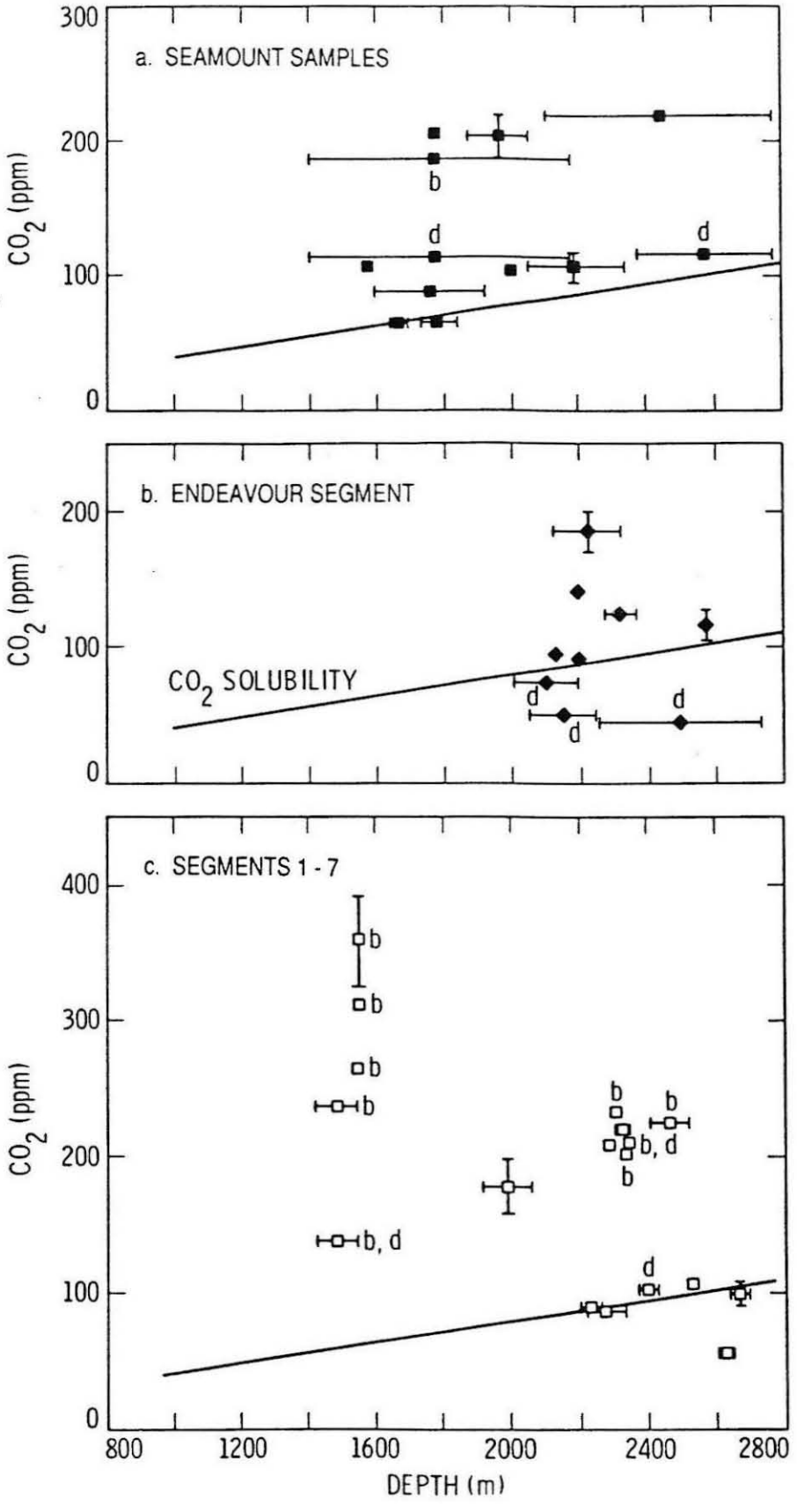
a. SEAMOUNT SAMPLES
b. ENDEAVOUR SEGMENT
CO2 SOLUBILITY
c. SEGMENTS 1 - 7
CO2 (ppm)
DEPTH (m)
0
100
200
300
400
800
1200
1600
2000
2400
2800
b
d
b, d

Figure 6: Dissolved CO_2 contents and generalized ridge topography [68] versus latitude. Note that high CO_2 contents correlate with shallow topography on individual ridge segments and over entire ridge. Vertical dashed lines connect high CO_2 values to their sample location. Symbols are the same as in Figure 2.

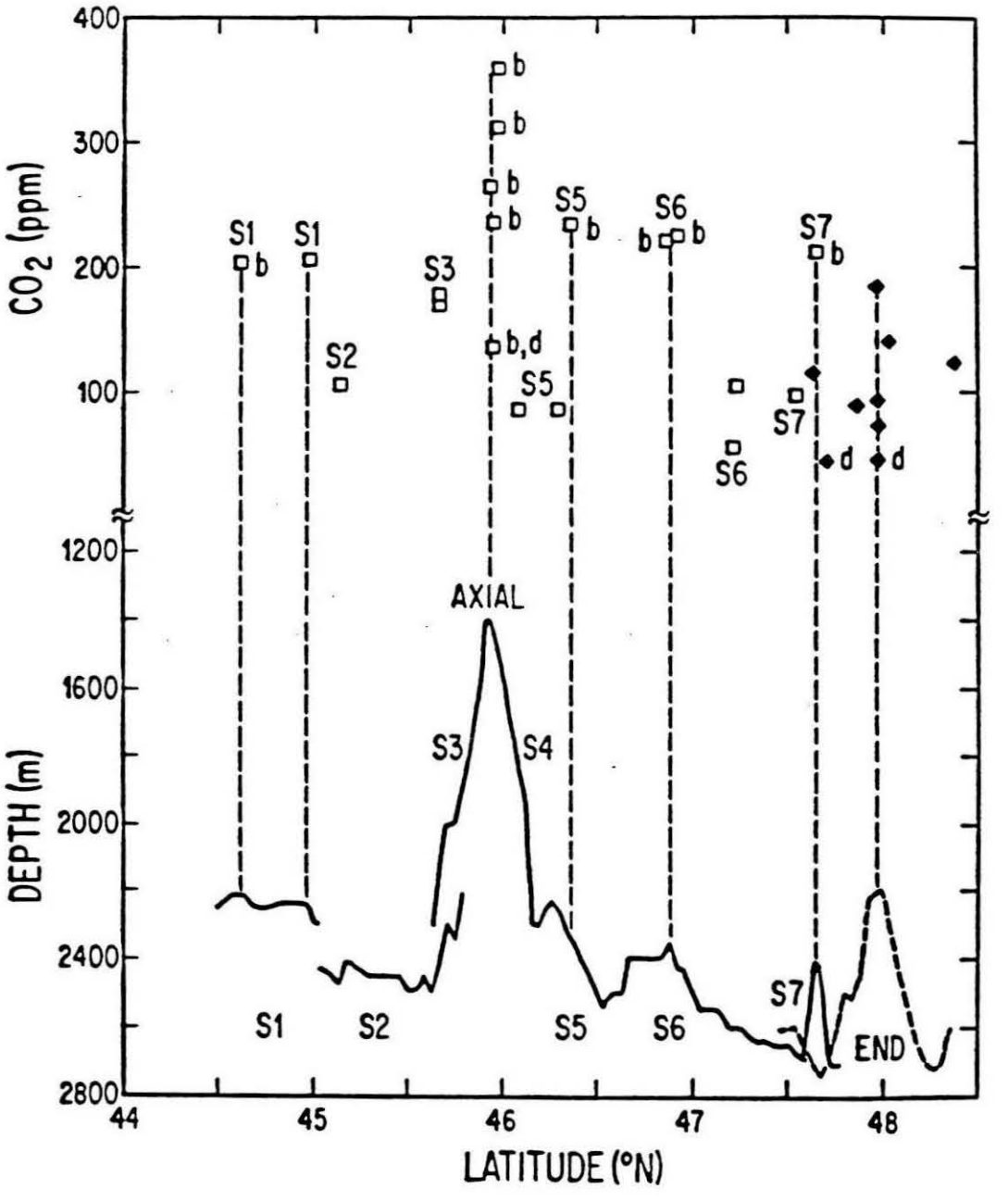
400
300
200
100
1200
1600
2000
2400
2800
CO_2 (ppm)
DEPTH (m)
44
45
46
47
48
LATITUDE (°N)
S1
S1
S2
S3
S5
S6
S7
b
b,d
d
AXIAL
S3
S4
S1
S2
S5
S6
S7
END

Figure 7: Dissolved H_2O contents versus FeO*/MgO. Symbols same as in Figure 2. Water contents increase with increasing FeO*/MgO. Endeavour segment samples have higher water contents at the same FeO*/MgO than samples from segments 1-7. Trends produced by 20% fractional crystallization of olivine, plagioclase, and clinopyroxene in proportions 1:5:1, respectively, are shown. In fractional crystallization models for major and trace elements [30], this assemblage provided the best fit to the data.

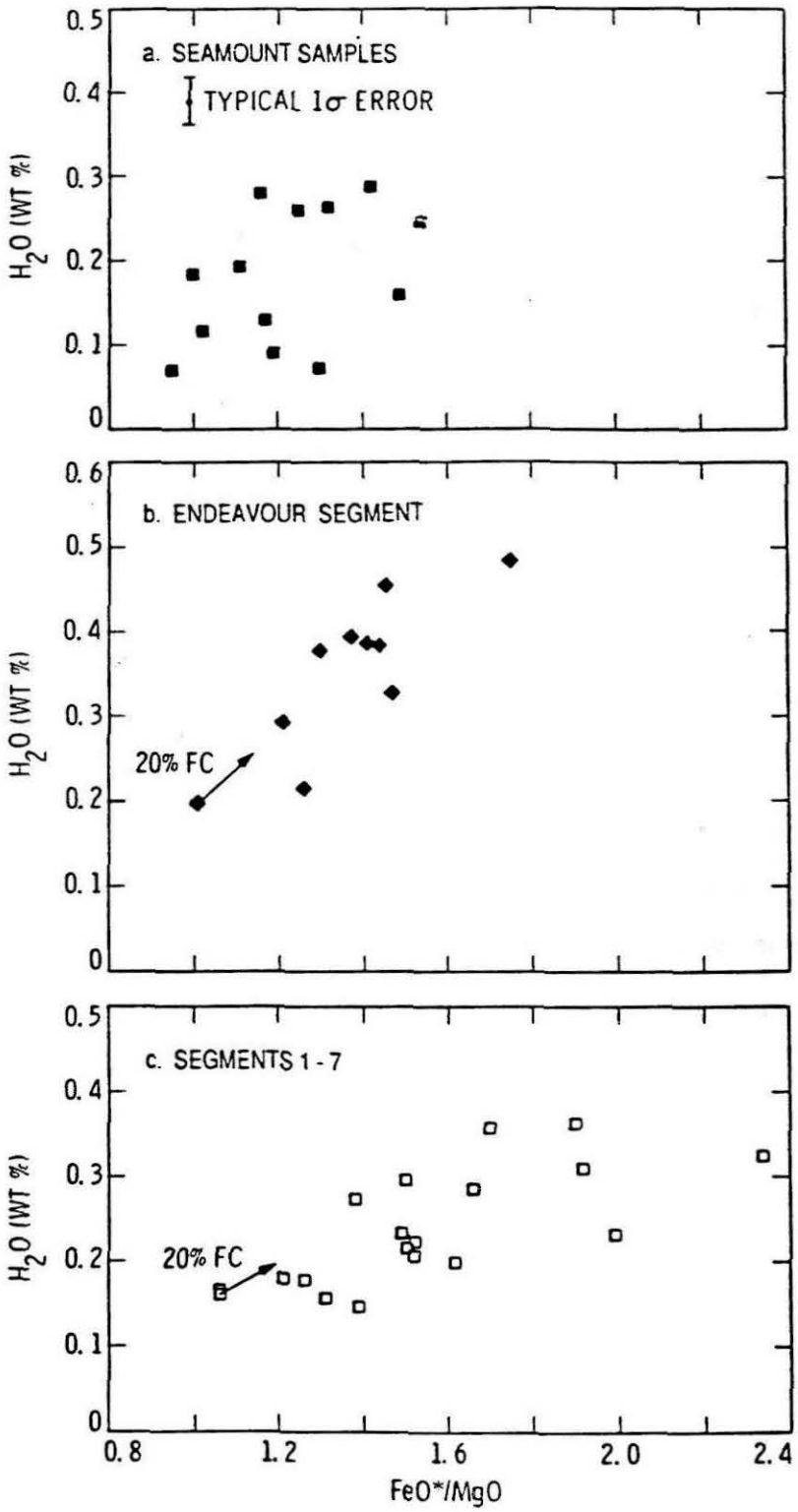
a. SEAMOUNT SAMPLES
TYPICAL 1σ ERROR
b. ENDEAVOUR SEGMENT
20% FC
c. SEGMENTS 1 - 7
20% FC
H2O (WT %)
FeO*/MgO
0.5
0.4
0.3
0.2
0.1
0
0.6
0.8
1.2
1.6
2.0
2.4

Figure 8: Dissolved H_2O versus K_2O contents. Symbols are the same as in Figure 2. Water contents correlate positively with K_2O contents. Endeavour segment lavas have higher water and K_2O contents along with lower (on average) H_2O/K_2O ratios. Partial melting models were calculated using a bulk partition coefficient of 0.001 for K [67] and 0.01 for H_2O (see text). Ticks on the partial melting lines are at 5, 8, 10, 15, 20, and 30 percent partial melting. Bulk K_2O contents in the mantle sources were estimated to be 180 ppm for the transitional source and 300 ppm for the enriched source, by calculating the source composition needed to produce the K_2O contents found in the most primitive lavas using batch melting equations [66] and assuming amounts of partial melting as constrained by other trace elements [30]. Estimation of bulk H_2O values for mantle sources described in text. Fractional crystallization of 50% of a 1:5:1 mixture of olivine, plagioclase, and clinopyroxene, respectively, are shown as arrows attached to the 20% partial melt composition from a transitional source for segments 1-7 and seamounts and to the 10% partial melt composition from an enriched source for the Endeavour segment.

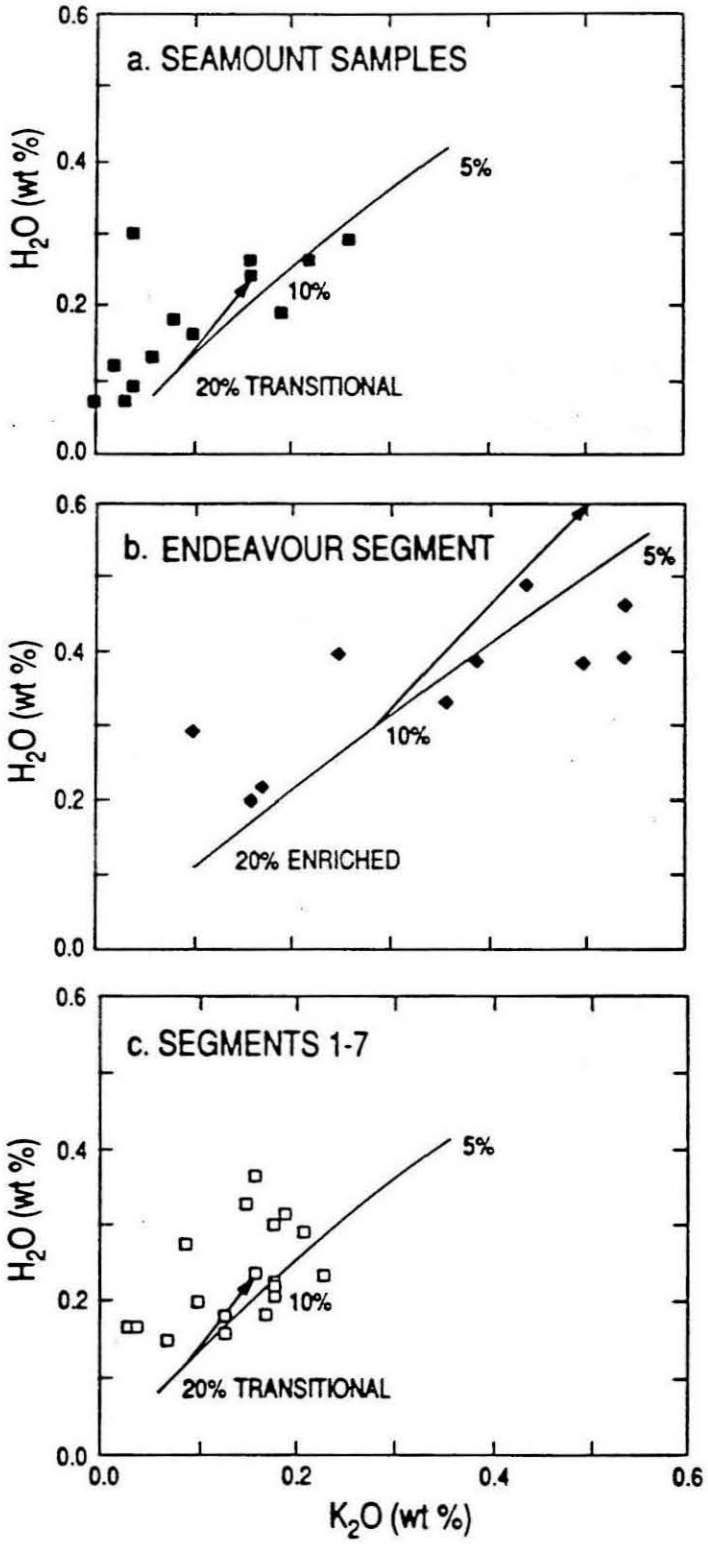
a. SEAMOUNT SAMPLES
5%
10%
20% TRANSITIONAL
b. ENDEAVOUR SEGMENT
5%
10%
20% ENRICHED
c. SEGMENTS 1-7
5%
10%
20% TRANSITIONAL
H2O (wt %)
K2O (wt %)
0.0
0.2
0.4
0.6

Figure 9: Dissolved H_2O in glasses (this study) versus REE and trace element data in whole rock powders (Liias, [30]; instrumental neutron activation analysis, X-ray fluoresence). Symbols are the same as in Figure 2. For the Endeavour segment, common samples were not analysed by us and by Liias [30], so water contents of samples analysed for REE were estimated based on major element chemistry and the observed good correlations between water, FeO*/MgO, TiO_2, and K_2O contents. Batch melting calculations shown using an enriched source [30] for Endeavour segment (solid line) and a transitional source [30] for segments 1-7 (south of the Cobb Offset) (dashed line) with ticks at 5, 8, 10, 15, 20, and 30 percent partial melting. Most partition coefficients (solid/liquid) are from Bender et al. [63] assuming ol:opx:cpx in the proportions of 60:30:10 in the residue. A partition coefficient of 0.005 was used for Nb because it provided a better fit to the data than the value of 0.06 calculated from data in Bender et al. [63]. Fractional crystallization of 50% of a 1:5:1 mixture of olivine, plagioclase, and clinopyroxene, respectively, are shown as arrows attached to the 20% partial melt composition from a transitional source for segments 1-7 and to the 10% partial melt composition from an enriched source for the Endeavour segment.

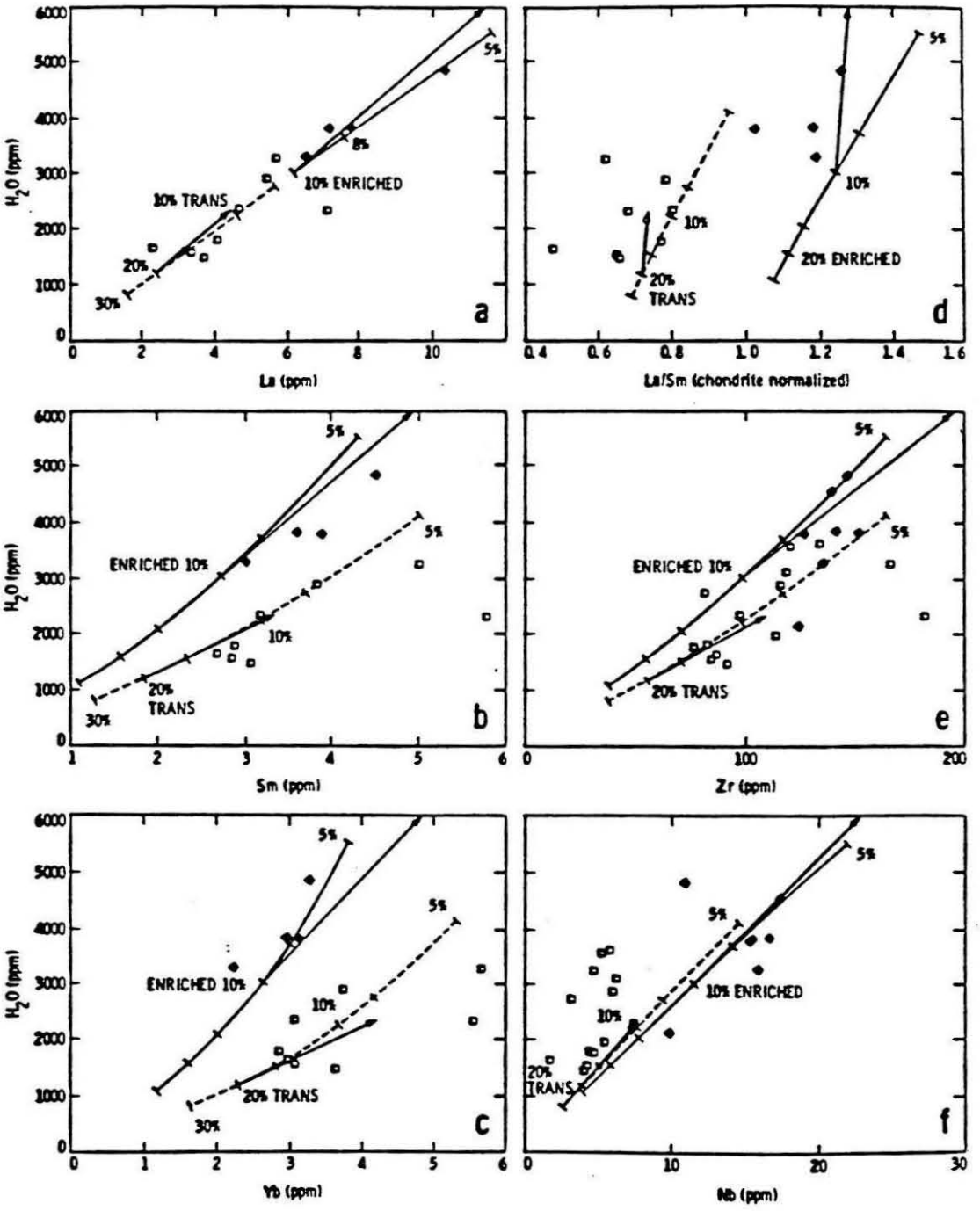
H_2O (ppm)
La (ppm)
10% TRANS
20%
30%
10% ENRICHED
5%
8%
a
La/Sm (chondrite normalized)
10%
20% TRANS
20% ENRICHED
d
Sm (ppm)
ENRICHED 10%
20% TRANS
b
Zr (ppm)
e
Yb (ppm)
c
Nb (ppm)
f

Post publication note

Incorporation of my revised CO_2 solubility values, about 20% higher than the Stolper and Holloway (1988) values, results in only trivial modifications to the conclusions presented in this paper. Most of the glasses remain supersaturated with respect to CO_2, and the samples with the lowest CO_2 contents are still within errors of the CO_2 solubility curve. A revised estimate for the depth to the magma chamber using the new CO_2 solubility is as follows: The highest CO_2 contents of 360 ppm would be redissolved at a pressure of 760 bar. Subtraction of 150 bar hydrostatic pressure leaves a lithostatic pressure of 610 bars. Assuming a crustal density of 2.8 g/cm^3, the depth to the magma chamber would be 2.2 km. This revised estimate is in better agreement with estimates based on seismic reflection than the previous estimate of 2.7 km.

Chapter 3

DEGASSING HISTORY OF WATER, SULFUR, AND CARBON IN SUBMARINE LAVAS FROM KILAUEA VOLCANO, HAWAII

(published as Dixon, J.E., D.A. Clague, and E.M. Stolper (1991) J. Geol., 99, 371-394)

ABSTRACT

Major, minor, and dissolved volatile element concentrations were measured in tholeiitic glasses from the submarine portion (Puna Ridge) of the east rift zone of Kilauea Volcano, Hawaii. Dissolved H_2O and S concentrations display a wide range relative to nonvolatile incompatible elements at all depths. This range cannot be readily explained by fractional crystallization, degassing of H_2O and S during eruption on the seafloor, or source region heterogeneities. Dissolved CO_2 concentrations, in contrast, show a positive correlation with eruption depth and typically agree within error with the solubility at that depth. We propose that most magmas along the Puna Ridge result from (1) mixing of a relatively volatile-rich, undegassed component with magmas that experienced low pressure (perhaps subaerial) degassing during which substantial H_2O, S, and CO_2 were lost, followed by (2) fractional crystallization of olivine, clinopyroxene, and plagioclase from this mixture to generate a residual liquid; and (3) further degassing, principally of CO_2 for samples erupted deeper than 1000 m, during eruption on the seafloor. The degassed end member may form at upper levels of the summit magma chamber (assuming less than lithostatic pressure gradients), during residence at shallow levels in the crust, or during sustained summit eruptions. The final phase of degassing during eruption on the seafloor occurs slowly enough to achieve melt/vapor equilibrium during exsolution of the typically CO_2-rich vapor phase. We predict that average Kilauean primary magmas with 16.0 % MgO contain ~0.47 wt. % H_2O, ~900 ppm S, and have δD values of ~-30 to -40‰. Our model predicts that submarine lavas from wholly submarine volcanoes (i.e., Loihi), for which there is no opportunity to generate the degassed end member by low pressure degassing, will be enriched in volatiles relative to those from volcanoes whose summits have breached the sea surface (i.e., Kilauea and Mauna Loa).

INTRODUCTION

Water and sulfur are much more soluble in basaltic liquids than carbon dioxide. These solubility differences, combined with volcanic gas emission data, have been used to develop two stage models of the outgassing of Kilauea magmas (e.g., Gerlach and Graeber 1985; Greenland et al. 1985; Gerlach 1986). The first stage occurs in the summit magma chamber where most of the CO_2 and lesser amounts of SO_2 and H_2O degas. The second stage occurs during subaerial eruptions where most of the remaining CO_2, SO_2, and H_2O degasses. A second stage of degassing of H_2O and S is not expected to occur in magmas erupted along Kilauea's submarine rift zones deeper than about 1000 meters because the pressure at the depth of eruption is sufficient to prevent exsolution of significant H_2O and S. Consequently, these submarine magmas have been thought to contain concentrations of H_2O and S that have been largely unchanged on eruption. Previous studies of H_2O and S in Hawaiian submarine basaltic glasses (e.g., Moore and Fabbi 1971; Killingley and Muenow 1975; Muenow et al. 1979; Harris and Anderson 1983; Kyser and O'Neil 1984; Byers et al. 1985; Garcia et al. 1989) have focused on constraining their concentrations and using these data to make inferences about their concentrations in primitive magmas and heterogeneities in mantle source regions. We will show, however, based on new measurements of major and minor element and dissolved H_2O, CO_2, and S concentrations in a suite of tholeiitic glasses from the submarine portion of the east rift zone of Kilauea Volcano, Hawaii (hereafter referred to as the Puna Ridge), that even many submarine magmas from Kilauea have lost water and sulfur during complex degassing histories and that inferences regarding volatile concentrations in primitive Hawaiian magmas and mantle source regions may require revision.

GEOLOGIC SETTING

The Puna Ridge is the submarine portion of the 130 km long east rift zone of Kilauea Volcano. It extends 75 km from the shoreline at Cape Kumukahi to the east-northeast to a depth of roughly 5400 m (fig. 1). Lonsdale (1989) presented a detailed geomorphic analysis of the ridge based on high-resolution geophysical techniques and photography. This data set allows a more detailed interpretation than earlier work (Moore 1965; Moore and Fiske 1969; Fornari et al. 1978) and shows that the Puna Ridge is structurally similar to the subaerial portion of the east rift zone. In particular, it contains en-echelon eruptive fissures, pit craters, open fissures, grabens aligned along the axis of the rift, and small shields and steep-sided cones. The main difference between the submarine and subaerial portions of the rift is the steeper gradient along the axis of the submarine rift: the subaerial gradient of 23 m/km steepens to 50 m/km near the shoreline and to 100 m/km at a depth of about 2800 m (Lonsdale 1989).

Most of the rift zone consists of pillow lava flows and pillow joint-block talus (Moore and Fiske 1969; Fornari et al. 1978; Lonsdale 1989), although many of the dredged samples consist of flat to slightly curved slabs of lava with a glassy rim on the top, but not bottom, surface. These fragments are probably from hollow lava tubes in tube-fed lobate flows like the one illustrated by Fornari et al. (1978, fig. 8 bottom right). Lonsdale (1989) noted that sheet-like flows are more common along the deeper parts of the rift and dredge data confirm this observation (Clague et al. 1988).

SAMPLE LOCATIONS

Dredge locations and depths are listed in Table 1 and shown in Figure 1 except for dredges SU49-66 and SU51-66, located just south of the southern boundary of Figure 1. Along-rift dredges recovered samples (dominantly pillows) erupted in the submarine environment (Table 1). The off-rift dredges recovered samples (dominantly glassy basaltic sand and scoria) from rubble-covered slopes of the volcano or from the submarine part of

the 1960 Kapoho flow (Table 1). The fragmental material sampled by the off-rift dredges is believed to be shattered, quenched lava formed by subaerial flows reaching the sea, and vitric ash formed by phreatic processes (Moore and Fiske 1969). Thirteen of the dredges were recovered from the Puna Ridge by the *Pioneer* in 1962 (Moore, 1965). Four dredges were recovered by the *Surveyor* in 1966; three of these are from the flanks of Kilauea and the fourth is located slightly off the axis of the Puna Ridge (Moore and Fiske 1969). The latest five dredges, recovered by the *R/V Farnella* in 1988, were located mainly to fill in gaps in the earlier dredge programs (Clague et al. 1988). One of these, D5, was recovered off the rift axis from a large inflated sheet flow that ponded in the Hawaiian Deep at the base of the Puna Ridge and was discovered by a recent GLORIA side-scan sonar survey (Holcomb et al. 1988). Based on the GLORIA image this flow could have erupted from the Puna Ridge at any depth greater than about 4000 m. One additional sample was collected by the submersible Makalii off the coast of Cape Kumikahi. Though the depth of collection is well known, an exact location is unavailable because of lack of reliable navigation during the dive. Several of the along-rift dredges (SU56, 1688, D43, and 1714) are located slightly off the axis of the Puna Ridge and may have erupted up to 700 m shallower than the depths at which they were dredged. The uncertainty in eruption depth for these dredges is not large enough to significantly affect our conclusions.

Microprobe analyses of the glasses, petrography, and apparent age based on palagonite alteration were used to identify distinguishable flow units within individual dredges. Several flow units contain abundant crystal clusters ranging in size from large glomerocrysts to small gabbroic xenoliths about 1 cm in diameter that were also used to distinguish flow units. Most dredges recovered samples of only a single flow, but dredges D45, 1742, SU56-66, D43, and 1697 recovered two flow units, and D42 recovered three flow units.

ANALYTICAL TECHNIQUES

Modal analyses were performed on thin sections by point counting (1000 counts). Glass chips (1-3 mm in diameter) representative of each flow unit were selected for microprobe analysis, cast into epoxy mounts, and prepared as doubly-polished thin sections. The translucent, pale brown glassy rims were analyzed for major and minor elements on the 9-spectrometer ARL SEMQ microprobe at the U. S. Geological Survey, Menlo Park, using natural and synthetic standards (VG-2 for SiO_2, Al_2O_3, FeO, MgO, CaO, and Na_2O; orthoclase for K_2O; apatite for P_2O_5; barite for S; TiO_2 for TiO_2; and Mn_2O_3 for MnO). Polished thin sections of glass inclusions in crystals were also prepared and analyzed. All glasses were analyzed using a slightly defocused beam (roughly 5 μm spot size was used to avoid abundant phenocrysts and microphenocrysts), 10 nA beam current, 15 kV accelerating potential, and a total count time of 100 s for S, K_2O, P_2O_5, and Al_2O_3, and 200 s for the remaining elements. Each analysis is the average of 3-5 point analyses of glasses from a single sample; many reported analyses are averages of multiple samples from the same flow unit as indicated in Tables 3 and 4. The use of barite as the standard for S gives results about 15% lower than obtained using a sulfide (pyrrhotite or troilite) standard. This standard was used to improve agreement with previous results for samples from the same flow units analyzed by other techniques (see discussion in results section). Precision of the microprobe analyses is estimated from the means and standard deviations of 19 analyses of Juan de Fuca glass standard VG-2 and 15 analyses of Makoupuhi (Kilauea) glass standard A99 (Table 2). Analyses of different glass chips from the same flow unit agree within the analytical precision.

Dissolved H_2O and CO_2 concentrations were determined by transmission infrared spectroscopy (FTIR) on doubly polished glass chips using the procedures and calibrations described by Dixon et al. (1988). This microbeam technique allows us to avoid vesicles, crystals, and areas of seawater alteration that may affect analyses of bulk samples. Where more than one spectrum was measured on glasses from the same flow unit, we report the

average H_2O content and standard deviation. Dissolved H_2O concentrations based on two spectra from the same glass chip and from different glass chips from the same flow unit are reproducible to within 6% of the amount present. The intensities of the carbonate (CO_3^{2-}) peaks (1515 and 1435 cm^{-1}) were measured separately after numerical subtraction of the spectrum of Kilauea Iki lava lake glass 79-6-190.3 (a glass containing no detectable dissolved CO_2) and a concentration was calculated from the intensity of each peak. The dissolved CO_2 contents are averages of all of the CO_2 concentrations measured from all spectra on glass chips from the same flow unit. For samples with dissolved CO_2 contents greater than 50 ppm, analyses on the same and different glass chips from the same flow unit are reproducible to within 8% of the amount present. Dissolved CO_2 contents less than 50 ppm are near the limits of detection and are reproducible to no better than about 70% of the amount present.

The accuracy of the reported H_2O and CO_2 concentrations is limited primarily by uncertainties in the molar absorption coefficients. These values are known to within 15% for the carbonate bands (Fine and Stolper 1986) and to about 10% for the hydroxyl band at 3535 cm^{-1} in basalts.

RESULTS AND DISCUSSION OF DATA

Microscopic Petrography.-All analyzed samples have glassy rims. The modal abundances in the along-rift samples (Table 3) are highly variable but only 3 mineral assemblages are found: 1) olivine + clinopyroxene + spinel + glass; 2) olivine + clinopyroxene + plagioclase + spinel + glass; and 3) olivine + clinopyroxene + plagioclase + orthopyroxene + spinel + glass. Four samples have assemblage (1), ten have assemblage (2), and twelve have assemblage (3). The modal data demonstrate the crystal-rich character of many of the samples and the unusual occurrence of small amounts of clinopyroxene and plagioclase in olivine-rich (>10% modal olivine) samples. Clague et al. (1990) present detailed mineral chemistry and whole-rock compositions of these lavas and

discuss their formation processes. The glassy rinds of the off-rift samples contain abundant microlites and are texturally distinct from the other submarine samples. This texture is typical of subaerially degassed lavas that have quenched below sealevel (see discussion in Moore and Clague, 1987).

Olivine, and less commonly plagioclase, clinopyroxene, and orthopyroxene phenocrysts contain translucent, pale brown glass inclusions. Glass inclusions up to about 200 μm in diameter are present in both euhedral and resorbed phenocrysts. Many of the inclusions in olivine contain single euhedral crystals of Cr-rich spinel, and some include a small vapor bubble. No sulfide phase was seen in any inclusions. CO_2-rich fluid inclusions in olivine, like those observed in dunite xenoliths from Hawaii (Roedder 1965), were not observed.

Moore (1965) studied a subset of these samples and showed that down to depths of 800 m, Puna Ridge basalts have greater than 10 percent vesicles and bulk densities less than 2.8 g/cm^3. Below 800 m the vesicles become smaller and less abundant and the bulk densities increase slowly with depth from 2.8 to 3.0 g/cm^3. Our modal data, when uncertainties in eruption depth are considered, support his observations. The vesicle content is less than 2 vol% at 2000-5500 m depth. At shallower levels, vesicle content increases with decreasing depth to nearly 35 vol% in a lava collected at 490 m.

Major and Minor Elements.-The glassy rims analyzed in this study are tholeiitic in composition and have low (≤ 7 wt. %) MgO contents (Tables 3 and 4). Glass compositions are uncorrelated with eruption depth and more and less fractionated samples occur with equal frequency at all depths. Glass compositions of the along-rift samples are plotted on MgO-variation diagrams in Figure 2 with model liquid lines of descent calculated using the procedures of Grove and Baker (1984) (see caption of fig. 2 for details). The compositions of the off-rift samples are similar to those of the along-rift samples. Al_2O_3 and CaO contents decrease with decreasing MgO content, whereas FeO*, Na_2O, K_2O,

P_2O_5, and TiO_2 contents increase with decreasing MgO content. The FeO* contents of the most fractionated samples (MgO < 5.5 wt. %) are lower and their P_2O_5 and K_2O contents are higher than the values expected based on the calculated liquid line of descent. The analytical errors for SiO_2 (1σ = 0.30-0.43) are large enough to mask any trends that may be present. Analyses of Na_2O, P_2O_5, Al_2O_3, and CaO are generally within error of subaerial lavas with similar MgO contents (Wright and Fiske 1971). At the same MgO content, our SiO_2 analyses are higher and our FeO, TiO_2, and K_2O analyses are lower than those of Wright and Fiske (1971).

The K_2O/P_2O_5 ratio for the glasses included in this study is nearly constant with an average and 1s value of 1.61 ± 0.12 (fig. 3). Whole-rock XRF analyses of many of the same samples give an average K_2O/P_2O_5 ratio of 1.79 ± 0.07 (Clague et al. 1990), similar to values determined by wet-chemistry on whole-rock samples for prehistoric Kilauean lavas (1.70 ± 0.06) and the 1840 Kilauea picrite (1.84 ± 0.06), but lower than the 1959 Kilauea Iki lavas (2.05 ± 0.06) (Wright 1971). Variations in incompatible element ratios comparable in magnitude to these variations in K_2O/P_2O_5 in lavas from many different eruptions of Kilauea have been observed during a single sustained eruption of Mauna Ulu (Hofmann et al. 1984).

Dissolved H_2O.-Dissolved H_2O contents in along-rift glasses range from 0.11 to 0.85 wt. %. Dissolved H_2O contents in the two off-rift (subaerially degassed) glasses analyzed by FTIR are 0.09 wt. %. Flow 1742a has a H_20 content (0.11 wt. %)) similar to those of these subaerial samples, even though it was dredged along the axis of the Puna Ridge at a depth of 1400 m. Samples having dissolved H_2O contents less than 0.35 wt. % contain only OH^- groups. Based on the presence of an absorption at 1630 cm^{-1} in glasses with total water contents greater than 0.35 wt. %, we conclude that both molecular H_2O and OH^- groups are present in these glasses. The molar absorption coefficient for the molecular water band at 1630 cm^{-1} in basaltic glass is not well known, but using the values

for rhyolitic and albitic glasses (Newman et al. 1986; Silver and Stolper 1989), we estimate that no more than 10% of the total dissolved water is present as molecular H_2O. Dissolved molecular H_2O is present in Kilauean tholeiitic glasses at slightly lower total H_2O contents than in mid-ocean ridge basalt (MORB) glasses; for example, no molecular H_2O was detected in glasses from the Juan de Fuca Ridge having dissolved H_2O contents up to 0.48 wt. % (Dixon et al. 1988).

Water concentrations in samples from a few of the same dredges analyzed in this study have been analyzed previously by other techniques. The data of Moore (1965) and Kyser and O'Neil (1984) have been corrected for the mass fraction of phenocrysts in their whole-rock samples using our modal data (see caption to fig. 4). In general there is good agreement between the different data sets (fig. 4a). Almost all the H_2O concentrations measured by Moore (1965) using the Penfield method, Harris (1981) and Kyser and O'Neil (1984) using vacuum fusion/manometry, and Killingley and Muenow (1975) and Muenow et al. (1979) using vacuum fusion/mass spectrometry on glass separates, are within 30% of our values. However, the analysis of sample 1712 by Harris (1981) is 57% lower than ours and the analysis of 1717 by Moore (1965) is 70% higher than ours.

H_2O contents show a weak correlation with depth (fig. 5a) that is unrelated to the solubility curve for pure water in basalt at 1100°C based on an extrapolation of the high pressure data of Hamilton et al. (1964) to the low pressures relevant to these depths of eruption. Nearly the entire range of H_2O values occurs within the depth range of 1400 to 1600 m. Samples erupted in water depths shallower than 1000 m fall near the solubility curve (Hamilton et al. 1964) and are probably saturated with respect to water. These samples, however, are not the ones with the lowest H_2O contents. Samples erupted deeper than 1000 m are greatly undersaturated with respect to pure water.

H_2O contents are plotted versus MgO and K_2O contents in figs. 6a and b. In general, H_2O contents increase with decreasing MgO and increasing K_2O contents, but the scatter in the H_2O data is two to three times greater than in the K_2O data at a given MgO

content (fig. 2). The observed scatter in the H_2O concentrations is reflected in the variable H_2O/K_2O ratios that range from 0.24 to 1.49, in contrast to the nearly constant P_2O_5/K_2O ratios (fig. 3). We have subdivided the samples into three arbitrary groups based on their H_2O/K_2O ratios: (1) low-H_2O/K_2O samples having H_2O/K_2O ratios less than or equal to 0.7; (2) moderate-H_2O/K_2O samples having H_2O/K_2O ratios ranging from 0.7 to 1.0; and (3) high-H_2O/K_2O samples having H_2O/K_2O ratios greater than 1.0. These three groups plot along roughly parallel trends on the H_2O versus K_2O diagram (fig. 6b). H_2O contents samples in each group are weakly negatively correlated with MgO content. Garcia et al. (1989) also found a rough negative correlation between H_2O and MgO in other glasses from the Puna Ridge, but they did not observe H_2O concentrations as low as those in our low H_2O/K_2O group.

Dissolved S.-The S contents of the Puna Ridge glasses range from 220 to 1440 ppm by weight. The values for the off-rift samples (70-240 ppm by weight) are similar to those reported for fountain spatter from Kilauea (Swanson and Fabbi 1973; Gerlach and Graeber 1985) and support the idea that these samples were subaerially degassed. Flow 1742a has a S content (220 ppm) similar to those of the off-rift samples, even though it was dredged along the axis of the Puna Ridge at a depth of 1400 m.

Though the use of a barite standard for microprobe analysis of S results in S values about 15% lower than when a sulfide standard is used (e.g., compare the MORB trend presented in Figure 7 with that of Mathez (1976)), our values still tend to be higher (from 8% lower to 30% higher) than those in samples from the same flow units analyzed using x-ray fluorescence spectrometry (Moore and Fabbi 1971) on 9 whole-rock samples and corrected for the mass fraction of phenocrysts, or using vacuum fusion/mass spectrometry (Killingley and Muenow 1975; Muenow et al. 1979) on 13 glass separates (fig. 4b). Our S concentrations are 18 to 50% higher than those measured using vacuum fusion/manometry on glass separates from 7 samples (Harris 1981; Sakai et al. 1984) and using

combustion/manometry on glass separates from 4 samples (Des Marais and Moore 1984) from the same flow units (fig. 4b). Some of the discrepancies between our measurements of S in the glass and previous analyses of S in bulk samples may be related to the type of sample analyzed; for example, in addition to the glassy rim, the whole-rock samples analyzed by Moore and Fabbi (1971) may have included unknown amounts of the crystalline interior that may have lost some sulfur upon crystallization (Moore and Fabbi 1971). Other discrepancies could reflect analytical techniques; for example, our S concentrations may be systematically high (though the discrepancy would be even worse if a sulfide standard had been used) or perhaps S in not completely released during stepped-heating fusion and combustion techniques. Though the interlaboratory comparison suggests that the accuracy of sulfur determinations is poorly known, the S analyses presented in this study are precise and can be directly compared to the IR analyses of H_2O and CO_2 because both data sets were determined using microbeam techniques on glass.

There is no clear correlation between S concentration and depth (fig. 5b). As is observed for H_2O, the entire range of S contents occurs between 1400 and 1600 m water depth.

S concentrations are plotted against FeO* (total iron reported as FeO) in Figure 7a with the correlation observed in MORB glasses (based on analyses obtained using the same microprobe standards and procedures used here; Clague, unpub. data). S concentrations in Kilauean glasses are lower than MORB glasses at the same FeO* concentration. The samples with the highest S contents at a given FeO* content are within error of the line defined by MORB glasses, which has been interpreted as defining sulfide-saturated liquid compositions (Mathez 1976). Note that the MORB FeO*-S trend shown on Figure 7a is about 15% lower than that of Mathez (1976), presumably due to differences in microprobe standardization for S. Most of the samples with highest S contents belong to our high H_2O/K_2O group. We consider the large range in S contents in Kilauean glasses, which

contrasts with what has been observed in MORB glasses, to be a significant feature of our data set.

There is a positive correlation between H_2O and S (fig. 7b), defined mainly by the 5 members of the low-H_2O/K_2O group. The range of S concentrations reported for other submarine glasses from Kilauea (Garcia et al. 1989) is similar to that spanned by our high- and moderate-H_2O/K_2O samples.

Dissolved CO_2.-Dissolved CO_2 concentrations in the along rift glasses range from below detection limits to 280 ppm. The only form of dissolved CO_2 detected in these samples is carbonate ion complexes. No detectable CO_2 (<10 ppm) was found in the off-rift (subaerially degassed) glasses.

CO_2 contents of some of the same flows analyzed by us have been analyzed by other workers (Muenow et al. 1979; Harris 1981; Des Marais and Moore 1984; Mattey et al. 1984). Although a detailed comparison shows considerable scatter (fig. 4c), our measurements are similar to those of Harris (1981), Des Marais and Moore (1984) and Mattey et al. (1984), but significantly lower than those of Muenow et al. (1979). Such discrepancies in interlaboratory comparisons of CO_2 contents of basaltic glasses are well documented but poorly understood (see Des Marais 1986; Fine and Stolper 1986; Craig 1987; Exley et al. 1987, Stolper and Holloway 1988; Dixon et al. 1988).

CO_2 concentrations are plotted versus depth in Figure 5c along with the experimentally determined solubility curve of CO_2 in basalt at 1200°C for pressures up to 1.5 kbar (Stolper and Holloway 1988). Though scattered, the dissolved CO_2 contents show a positive correlation with depth. The slope of a linear regression line through the data and forced through zero yields a slope of 42 ± 2 (1σ) ppm/km. This value is within error of the slope of 38 ± 2 (1σ) ppm/km for the solubility data of Stolper and Holloway (1988) but lower than a slope of 59 ppm/km for the apparent solubility curve of Harris (1981). Several samples, however, deviate significantly either positively or negatively

from the solubility curve. Dissolved CO_2 contents do not correlate with major or minor element concentrations, or with water contents.

Sample D4, dredged from near the rift zone at a depth of 5470 m, contains about 280 ppm CO_2, approximately 70 ppm CO_2 in excess of the solubility at this depth. Sample D5 is from a voluminous lava flow of uncertain eruption depth located at the base of the rift and contains about 260 ppm CO_2. Based on the similar CO_2 contents of these two samples, we suggest that the lava flows sampled by D4 and D5 erupted at about the same depth; it is possible, and consistent with the distribution of the lava flow (see fig. 1) that D5 erupted in the vicinity of sample D4 and, channelled by the moat, flowed laterally along the base of the rift to its present location.

Our CO_2 data are not in agreement with those of Garcia et al. (1989). Their reported CO_2 concentrations for submarine Kilauean glasses range from 350 to 1350 ppm in excess of the solubility at the depth of eruption, whereas our values are supersaturated by no more than 70 ppm. Their CO_2 concentrations were measured on bulk samples using vacuum fusion/mass spectrometry, a technique that commonly gives CO_2 values much higher than FTIR analyses on the same samples. We emphasize that our analyses are determined using the same technique as those constraining the solubility curve of Stolper and Holloway (1988) and measure only CO_2 dissolved in the glass.

Glass Inclusions.-Analyses of glass inclusions in olivine, plagioclase, clinopyroxene, and orthopyroxene are presented in Clague et al. (1990). Based on major and minor element compositions of these inclusions (Clague et al. 1990), they have crystallized a small (<20%) but variable percentage of their volume onto the walls of the host phase.

The only volatile element we have analyzed in the inclusions is S, which was determined by electron microprobe as in the host glasses. The S contents of glass inclusions range from 220-1380 ppm in 45 analyzed olivine crystals, from 750-1560 ppm

in 4 analyzed plagioclase crystals, from 970-1980 ppm in 4 analyzed clinopyroxene crystals, and is 1400 ppm in a single orthopyroxene crystal. Several small gabbroic xenoliths also contain glass inclusions in olivine (6 analyses ranging from 370-1630 ppm S), clinopyroxene (2 analyses of 680 and 1300 ppm S), and plagioclase (1 analysis of 750 ppm S). Even though the S contents of all these glass inclusions are presumably higher than the S content of the melt that was originally trapped in the crystals (because of the effects of crystallization on the inclusion walls) the facts that some glass inclusions have S contents as low as the lowest value observed in the rind glasses and that enrichments due to crystallization on inclusion walls are ≤20% suggest to us that the host phenocrysts grew from magmas having a wide range of volatile contents. We note that many of the glass inclusion compositions are above the inferred sulfide saturation line in FeO-S (fig. 8b) and that no sulfide phases have been observed in these inclusions, suggesting that sulfide nucleation was inhibited within the inclusions during post-entrapment crystallization of the host phase.

INTERPRETATIONS

Major Element Chemistry.-Wright and Fiske (1971) demonstrated that lavas from Kilauea with MgO >6.8 wt. % plot along olivine-control lines. Puna Ridge glasses generally have lower MgO contents than the lower limit for olivine controlled lavas from Kilauea and define trends distinct from olivine-control lines, but similar or parallel to those for strongly fractionated lavas from Kilauea (Wright and Fiske 1971). In particular, the trends of decreasing CaO and Al_2O_3 with decreasing MgO result from crystallization of clinopyroxene and plagioclase in addition to olivine, as demonstrated by experimental studies of Kilauean lavas (Thompson and Tilley 1969; Helz and Thornber 1987).

The trends in the major element data are generally consistent with fractional crystallization of up to 30% olivine, plagioclase, and clinopyroxene in proportions of 1:5.2:4.9 from a parental magma containing 7.0 wt. % MgO (fig. 2). Although this simple

fractionation model successfully reproduces most of the observed trends in major element chemistry, it cannot account for the low FeO*contents, or the high P_2O_5 and K_2O contents, of the most fractionated samples. Chemical evidence for the fractionation of late-crystallizing phases not on the liquidi of erupted lavas (e.g., oxide crystallization to account for the low FeO contents), and greater increases of incompatible elements with fractionation than can be generated by simple fractional crystallization are characteristics common to many suites of volcanic rocks and may be caused by mixing of residual melts from the crystallizing margins of the magma chamber with well-mixed convecting magma in the interior (Langmuir 1989) or by periodic replenishment of magma bodies that are fractionating and serving as sources of erupted lavas (O'Hara 1977; O'Hara and Mathews 1981). Data on mineral assemblages and their compositions support an explanation of these deviations from simple liquid lines of descent that invokes an important role for magma mixing (Clague et al. 1990). Moreover, as we show below, magma mixing appears to play a critical role in generating the range of volatile contents observed in submarine lavas. Some of the observed deviations in incompatible element concentrations from the simple liquid line of descent may also be related to variable degrees of partial melting or to source region heterogeneity (Wright 1971; Hofmann et al. 1984; Garcia et al. 1989; Clague et al. 1990).

Magma Ascent Rate and CO_2 Supersaturation.-The CO_2 contents of the Puna Ridge glasses, which are approximately saturated with CO_2-rich vapor at their depth of eruption, differ from those for glasses from the East Pacific Rise and Juan de Fuca Ridge (Fine and Stolper 1986; Dixon et al. 1988), where many of the glasses are significantly supersaturated with respect to CO_2-rich vapor at their eruption depth. The CO_2-supersaturated nature of the mid-ocean ridge lavas has been attributed to incomplete degassing during rapid ascent and eruption. The simplest explanation for the correspondence between the dissolved CO_2 contents of most glasses from the Puna Ridge

and the solubility curve is that magmas erupted along the Puna Ridge rose and erupted slowly enough to allow nearly complete exsolution of a CO_2-rich vapor prior to quenching. If this is the case, it implies that magmas along the Puna Ridge typically take more time to travel from a magma reservoir to their final site of quenching on the seafloor than those along the East Pacific Rise and Juan de Fuca Ridge. The predominance of pillow lavas along the Puna Ridge (Lonsdale 1989) is consistent with low effusion rates (Ballard et al. 1979, Holcomb and Clague 1983). The only samples from the Puna Ridge that plot significantly above the solubility curve in Figure 5c are those from the deepest dredges. Incomplete degassing of these samples would be consistent with the observed increase in the proportion of sheet flows, which are thought to erupt at higher effusion rates than pillows (Ballard et al. 1979, Holcomb and Clague 1983), with depth along the rift (Lonsdale 1989).

H_2O and S Contents.-H_2O behaves as an incompatible element during partial melting and fractional crystallization of anhydrous phases; therefore, if these were the only processes affecting the magma composition, H_2O would correlate approximately linearly with other incompatible elements (such as K_2O) as has been found in MORB (e.g., Moore 1970; Michael and Chase 1987; Dixon et al. 1988). The wide range of H_2O and S contents at the same MgO, FeO, and K_2O contents (figs. 6a, 6b, and 7a) demonstrates that processes other than, or in addition to, crystal-liquid fractionation of anhydrous phases influences their concentrations. These samples are so low in H_2O and S that it is unlikely they would be saturated with H- or S-rich crystalline phases, and, as expected, such phases have not been observed in the lavas. Crystallization of hydrous or S-bearing phases, therefore, is also unlikely to have been a major factor in accounting for the observed variations in H_2O and S contents. Moreover, the variations in H_2O/K_2O and S/K_2O ratios of up to a factor of 6 are not likely to be explained by source region heterogeneities because

comparable variations are not observed in ratios of nonvolatile incompatible elements (e.g., K_2O/P_2O_5; see fig. 3).

Exsolution of a vapor phase is one possible mechanism for generating a range in concentrations of volatile components such as H_2O and S while leaving those of nonvolatile incompatible elements unaffected. In order to assess whether degassing during submarine eruption can explain the observed range in H_2O and S, we need to compare the conditions under which substantial amounts of H_2O and S degas from these magmas to those experienced on the seafloor. It is well known that CO_2 exsolves from basaltic magma over a wide range of pressures and dominates the vapor phase at pressures greater than about 100 bar in low-H_2O basalts such as MORB and ocean island tholeiites (Killingley and Muenow 1975; Moore et al. 1977; Delaney et al. 1978; Gerlach and Graeber 1985; Gerlach 1986). Existing solubility data for pure water in basalt (Hamilton et al. 1964) and studies of Kilauean lavas (Moore 1965; Killingley and Muenow 1975; Kyser and O'Neil 1984) indicate that degassing of H_2O and S does not become significant in these melts until pressures lower than about 100 bars are reached (corresponding to water depths shallower than 1000 m or magma column heights less than about 400 m). The fact that the samples from shallower than 1000 m depth have concentrations of H_2O and CO_2 near their solubilities at pressures corresponding to their depths of eruption (figs. 5a and c) is consistent with saturation with respect to a vapor phase containing significant concentrations of both CO_2 and H_2O during submarine eruptions at these depths. Partial degassing on submarine eruption might thus account for depletions in H_2O and S in Puna Ridge glasses erupted shallower than 1000 m, but it cannot be a significant factor in explaining the range of H_2O and S contents of samples erupted deeper than 1000 m.

Another important aspect of the data for samples erupted deeper than 1000 m is that glasses that are low in H_2O and S are not also systematically low in CO_2 (fig. 5c). Thus, the observed range of H_2O and S in the >1000 m samples cannot be a relic of a single episode of low pressure degassing at some point in their evolution prior to their eruption on

the submarine Puna Ridge. If this were the case, the CO_2 contents should be essentially zero, because at pressures low enough to degas substantial quantities of H_2O and S, nearly all of the CO_2 would also exsolve from the melt (Gerlach 1986). The correspondence of most of the CO_2 data to the solubility curve (fig. 5c) is strong evidence that these samples last degassed under submarine conditions near their depths of eruption on the Puna Ridge, and that their preeruptive CO_2 contents were even higher than their current values. These data thus argue strongly that the range of H_2O and S contents observed in samples deeper than 1000 m are not the result of a single episode of low pressure degassing at some point in their history. Note that the off-rift samples do not contain detectable CO_2, consistent with a single stage of subaerial degassing in their evolution.

Our preferred explanation for the observed depletions in H_2O and S that are uncorrelated with nonvolatile incompatible elements is that the lavas we have studied are samples of mixed magmas, one component of which was degassed (i.e., either by actual subaerial eruption or in a shallow magma chamber in which total pressure was less than lithostatic, perhaps by connection through cracks to the surface) and one that was not. Thus, although the magmas we have sampled erupted in submarine environments, they have inherited to varying degrees the characteristic H_2O and S depletions of lavas degassed at low total pressure. Our model is illustrated schematically in Figure 9. In the following sections, we discuss some of the consequences of our model in quantitative terms.

Quantitative Modelling.-We have developed a simple quantitative model that describes the mixing hypothesis presented in the preceding paragraph. We assume that each glass composition can be generated by the following sequence of processes: (1) mixing of undegassed and degassed liquids; (2) fractional crystallization of olivine, clinopyroxene, and plagioclase from this mixture to generate a residual liquid; and (3) further degassing during eruption on the sea floor (principally of CO_2 for eruption depths >1000 m; H_2O and probably S, in addition to CO_2, for eruption depths <1000 m).

For both degassed and undegassed end members, we chose a liquid with a major element composition (shown as "P" in fig. 2; composition listed in caption to fig. 2) similar to the most primitive analyzed glass (MgO ~7.0 wt. %) from the Puna Ridge because glasses with high and low H_2O contents are found at this primitive end of our sample distribution (fig. 6a). In order to be able to account for all of our H_2O data, the H_2O content of the undegassed end member was chosen to be 0.62 wt % and the H_2O content of the degassed end member was chosen to be 0.10 wt %. The S content of the undegassed end member was chosen to be 1200 ppm and that of the degassed end member was chosen to be 200 ppm; these values were chosen such that both end members have an H_2O/S ratio close to the average of 5.1 (see fig. 7b). The CO_2 content of the undegassed end member was chosen to be 480 ppm, which is the minimum value required to account for the highest CO_2 content glasses we have analyzed. The degassed end member is assumed to have no CO_2. The concentrations of H_2O, S, and CO_2 in the degassed end member are close to those measured in the off-rift glasses (Table 4).

The proportions of the two end members and the amount of subsequent fractional crystallization for each sample are listed in Table 5. Because the CaO data show the least scatter with respect to the calculated fractional crystallization trend as discussed above, the amount of fractional crystallization needed to generate the major element composition of the each glass from a parent magma "P" was estimated using its CaO content. The H_2O concentration of the reconstructed parental magma composition for each glass was then calculated by correcting for this amount of fractional crystallization. This H_2O content was then used as the basis for calculating the proportions of degassed and undegassed end members in the parental magma.

Several aspects of this quantitative modelling require clarification. First, the choices of degassed and undegassed end members are not unique. For example, the undegassed end member could have higher H_2O, S, and CO_2 contents if all samples in our collection contain some of the degassed component. Also, the degassed end member could

have lower or higher concentrations depending on the extent of degassing experienced by individual packets of magma. Second, there is nothing in our data set that requires that there are only two end members involved in the mixing process. For example, in one case the mixture could involve two end members that are unfractionated but variably degassed (this is the model we have chosen); in another, fractional crystallization of one or both end members could have preceded degassing of the volatile-depleted end member and mixing, after which more fractional crystallization and mixing could occur; in another, one or both end members could be more primitive (i.e., have higher MgO) than the ones we have chosen. However, since the courses of fractional crystallization and degassing are little affected by each other on the scale we are considering, these additional permutations on the processes we are postulating would have little effect on the outcome of our modelling.

The model we have proposed accounts well for the observed variations in, and correlations among, volatile and nonvolatile elements in Puna Ridge glasses. For example, our model defines, within 2σ errors, a field that encompasses the H_2O, MgO, and K_2O data (figs. 6a and b), although the most fractionated samples have K_2O contents higher and FeO contents lower by more than 1s error than our model. As discussed above, these discrepancies could reflect the inadequacy of modelling complex magma chamber processes by simple fractional crystallization. At this point there is insufficient information to properly constrain the details of these complex processes, but because the solid-liquid partition coefficients of H_2O, S, K_2O and P_2O_5 are similar, these components will covary similarly whether simple fractional crystallization or more complex processes are incorporated into the modelling. In any case, the variability caused by fractional crystallization (or these more complex fractionation processes) is readily distinguishable from that produced by mixing of degassed and undegassed magmas.

The proportion of the degassed end member required to produce the moderate- and high-H_2O group compositions is less than 50%. Note that although three of the five low H_2O/K_2O samples (>50% degassed end member) occur deeper than 1000 m (below the

depth at which significant H_2O and S are lost on submarine eruption), none of the samples in the low H_2O/K_2O group occur deeper than 3000 m (the depth at which a change in slope of the rift axis occurs) suggesting that the proportions of degassed magma within magma reservoirs are greater at shallower levels.

Our model accounts well for the S data (figs. 7a and b), as expected based on the roughly constant H_2O/S ratio of the samples. The positive correlation of H_2O and S is produced by the colinear trends of degassing and fractional crystallization.

The behavior of CO_2 predicted by our model is interesting in that depending upon the proportions of the two end members and the depth of submarine eruption, the magmas may be either supersaturated or undersaturated with respect to CO_2 on eruption. The following examples illustrate this point. Consider a batch of magma residing in a magma chamber at a depth of 4 km beneath the summit of Kilauea (lithostatic load about 1000 bars). A 50/50 mixture of degassed (no CO_2) and undegassed (480 ppm CO_2) magmas will have a CO_2 content of about 240 ppm; undersaturated with respect to CO_2 at this depth in the magma chamber. During lateral injection into the rift system and eruption, the pressure decreases to hydrostatic (300 bars), and the CO_2 solubility decreases from 400 to 110 ppm. Therefore, during eruption the mixed magma will become supersaturated with respect to a vapor phase and exsolution of CO_2-rich vapor will occur. In this way, a magma can both be rich enough in CO_2 to degas on submarine eruption, yet inherit the H_2O and S depletion of shallow degassing (which, as discussed above, would in a single stage process also strip the magma of all its CO_2). However, if the mixing proportions were greater than about 80% of the degassed end member, the mixed magma would have less than 110 ppm, and during eruption on the seafloor, CO_2-rich vesicles would not form.

The behavior of CO_2 in almost all of the Puna Ridge glasses is consistent with our proposed mixing model. Calculated mixing proportions listed in Table 5 lead to the prediction than only 1 sample would be undersaturated with respect to CO_2-rich vapor on eruption. This sample (1742a) contains no detectable CO_2, is the only bubble-free sample

shallower than 5000 m, and, as predicted, falls outside of errors below the solubility curve in Figure 5c. The remaining samples are predicted to contain sufficient CO_2 to become supersaturated with respect to CO_2-rich vapor during eruption. The model does not predict, however, the absence of detectable CO_2 in sample 1689 erupted at a depth of 1600 m. We note that this sample is vesicular (4% vesicles), highly fractionated (5.20 wt. % MgO), and contains an extremely high H_2O content of 0.81 wt. %. Exsolution on eruption of vesicles rich in both H_2O and CO_2 could account at least qualitatively for the characteristics of this sample. It is interesting that the only sample from the Juan de Fuca Ridge that fell significantly below the experimentally-determined CO_2 solubility curve was also the most fractionated of the suite (Dixon et al. 1988), perhaps reflecting a similar effect. It is also possible that sample 1689 has undergone an episode of low pressure degassing followed by migration down the rift system, as suggested by Des Marais and Moore (1984) for selected CO_2-poor samples.

Isotopic Fractionation and Seawater Addition.-Kyser and O'Neil (1984) observed a positive correlation between δD (-73 to -33‰) and H_2O contents (0.24 to 0.56 wt. %) in 10 glassy whole rock samples from the Puna Ridge. They proposed that small amounts of seawater (δD = 0‰) were added to unaltered magma (δD = -80‰) at magmatic temperatures, resulting in increases in both δD and H_2O contents. Seawater addition, however, would not readily explain the covariation of H_2O and S observed in this study. A positive correlation between H_2O content and dD was not found, however, by Garcia et al. (1989) in glasses from four Kilauean tholeiites having a smaller range of δD values (-61 to -74‰) and water contents (0.44 to 0.57 wt. %) than the suite of samples studied by Kyser et al. (1984), nor is there any overlap between the two data sets (fig. 10).

Our model, with minor modifications, can account for the covariation of δD and H_2O contents observed by Kyser and O'Neil (1984). We generated the degassed end

member (0.25 wt. % H_2O and δD of -80‰) from the undegassed end member (0.62 wt. % H_2O and δD of

-35‰) by Rayleigh fractionation using a vapor/melt fractionation factor of 1.050. The fractionation factor needed to fit the data is at the high end of a wide range of values (1.010 to 1.050) suggested for high temperature degassing of basalt (Kyser and O'Neil 1984, Pineau and Javoy 1986) based on the δD values of coexisting glass and vapor in submarine basalts.

Figure 10 shows the range of H_2O contents and δD values predicted by our model of mixing of degassed and undegassed magmas followed by fractional crystallization along with the data of Kyser and O'Neil (1984) and Garcia et al. (1989). Although there is considerable scatter in the observed δD values that cannot be rationalized by any simple model, our model of mixing and fractional crystallization explains the observed range in δD values and their correlation with H_2O content reasonably well. The correspondence between our model and the data of Kyser and O'Neil (1984) is much poorer if we use a more degassed component for our degassed end member composition. If significant, this could suggest that the degassed end member may not typically be as fully degassed as the 0.10 wt. % H_2O component used to generate Figures 6 and 7. Note that our reinterpretation of the data of Kyser and O'Neil (1984) implies that mantle source regions for Hawaiian tholeiites may have δD values as high as ~-30 to -40‰, significantly heavier than the value of -80‰ assumed by other workers (Craig and Lupton 1976; Kyser and O'Neil, 1984) for the mantle source regions for Hawaii and MORB. In a study of another oceanic hotspot, Poreda et al. (1986) conclude that the mantle source regions for Iceland must have δD values heavier than MORB, in the range of -44 to -74‰. Also, in a study of glasses from the East Pacific Rise, Chaussidon et al. (1989) document a positive correlation between δD and $^{143}Nd/^{144}Nd$ ratios and use these data to suggest that the mantle source regions for these lavas have δD values ranging from -55 to -84‰. These

studies suggest that the mantle is heterogeneous with respect to hydrogen isotopes as well as with respect to radiogenic isotopes and concentrations of incompatible elements.

Volatile Content of Primary Magma.-We can estimate the volatile contents of Kilauean primary magma based on the composition of our hypothetical undegassed end member (0.62 wt. % H_2O, 1200 ppm S). Crystallization of about 25% olivine and minor amounts (~1%) of magnesiochromite from an average primary magma composition containing about 16% MgO proposed by Clague et al. (1990) is required to generate the major element composition of the undegassed end member. Thus, correcting for about 25% crystallization, we calculate that such a primary magma would contain about 0.47 wt. % H_2O and 900 ppm S. These values must be considered minimum estimates, because we may not have sampled the undegassed end member composition (i.e., all samples may have some fraction of degassed magma). Also, the degree of partial melting, and consequently the concentrations of incompatible elements, may vary by as much as ±20% from the average value for different batches of magma entering Kilauea (Clague et al. 1990), implying that the initial H_2O content may range from about 0.38 to 0.56 wt. % and the initial S content may range from 720 to 1080 ppm.

Several other approaches can be used to estimate the S content of the primary magma. First, use of the highest S/K_2O ratio in the high S glass inclusions in olivines (0.238) and the K_2O content of the average primary magma (0.39 wt. %), yields an estimate of 930 ppm S in the primary magma. Second, the highest S content in glass inclusions in olivine from tephra erupted near the summit of Kilauea (Clague, unpub. data) is 1300 ppm in a glass with 6.7 wt. % MgO. Correction for about 35% fractional crystallization results in an estimate of 845 ppm S in a primary melt composition.

Our estimated H_2O content is higher than values of 0.32 wt. % by Greenland et al. (1985) based on gas emission data and 0.30 wt. % by Gerlach and Graeber (1985). Our estimate of the S content in the primary magma is nearly identical to that of Greenland et al.

(1985) based on gas emission data but lower than a value of 1300 ppm used by Gerlach and Graeber (1985) based on glass inclusion data of Harris and Anderson (1983) on glass inclusions with about 12% MgO.

Mechanisms for Generation and Recycling of Degassed Magma.-Recycling of magma degassed at shallow levels in the crust may provide a possible mechanism for returning degassed magmas to the interior of the volcano for mixing with relatively undegassed magmas. Since the tops of the Kilauea summit magma chamber and rift zone reservoirs are on average about 2 km beneath the volcano surface (Fiske and Kinoshita 1969; Koyanagi et al. 1976; Ryan et al. 1981; Ryan 1988), corresponding to lithostatic pressures of about 500 to 560 bars (assuming crustal densities of 2.5 to 2.8 g/cm^3), significant amounts of H_2O and S could not be simply lost from these magmas during residence in the magma reservoir, unless the pressure on the magma is much less than lithostatic. Considerable magmatic CO_2 is lost during summit chamber degassing (Gerlach 1980; Gerlach and Graeber 1985; Greenland et al. 1985; Gerlach 1986), and vigorous degassing at eruptive fissures with little or no lava appearing at the surface is commonly observed at Kilauea (Moore and Koyanagi 1969), implying the existence of open pathways from the surface to the magma and less than lithostatic pressures on the magma. The continuous emission of SO_2 from high temperature fumaroles during repose periods at Kilauea provides evidence that sulfur is able to degas even at times when magma does not reach the surface (Casadevall et al. 1980; Gerlach 1980; Harris and Anderson 1983; Greenland et al. 1985) and is consistent with the idea of less than lithostatic pressures in the summit chamber. Another possibility is that CO_2-rich bubbles rising through the magma within the summit magma chamber (Vergniolle and Jaupart 1990) may progressively dehydrate the magma as has been hypothesized for the Bishop Tuff (Anderson et al. 1989). Thus, degassing of magma at depth in the summit magma chamber is one possible

mechanism for generating the degassed component observed in submarine magmas erupted on the Puna Ridge.

Estimates for the amounts of S and H_2O loss during summit chamber degassing are highly varied. Based on measured gas emission and magma supply rates, Greenland et al. (1985) estimate that magma residing in the summit magma reservoir degasses about 18% of its original S. Similar estimates for H_2O cannot be made because of contributions of unknown amounts of meteoric water to the gas emission data, but the near constant H_2O/S ratio shown in our data suggest that the proportion of H_2O degassed could be close to that of S. Gerlach and Graeber (1985) estimate a higher value of 46% for the amount of original S lost during summit degassing, but they may have overestimated the S concentration in the calculated chamber gas composition because of inaccuracies in analytical techniques used to measure S (as discussed above) in their parental (measured by microprobe) and stored (measured by XRF) magma compositions.

Recycling of degassed magma during sustained summit lava lake activity may also provide a mechanism for returning degassed magmas to the summit magma reservoir. Such phenomena have been well-documented during historic eruptions of Kilauea. On a small scale, subaerial lava flows (e.g., the earliest phase of Puu O'o) were observed descending into preexisting open cracks (Wolfe et al. 1987). On a larger scale, the 1919-1920 eruption at Mauna Iki on the southwest rift zone was fed by degassed lava drained from Halemaumau along shallow fissures (Jaggar 1947). The best documented example of lava lake backflow occurred during the Kilauea Iki summit eruption in 1959, for which Richter et al. (1970) observed backflow of lake lava down the vent during and following each of the 17 eruptive phases. Following phase 4 there was little net volume change in the lava lake, suggesting that a volume of lava comparable to that erupted reentered down the vent following each eruptive phase. Another example occurred on Feb. 7, 1960, when the still liquid core of the 1952 lava lake in Halemaumau drained away and resulted in the rapid collapse of the floor of Halemaumau (Richter et al. 1970, p. E70). This collapse and two

smaller subsequent collapses in Halemaumau had a total volume of about 20 million m^3, and this volume of degassed summit lake lava presumably drained into magma reservoirs beneath Kilauea's summit. Degassing of magma within the crust may also occur when magma moves to relatively shallow depths and then returns to the main reservoir; for example, the summit chamber is presently only 1 km below Halemaumau pit crater, and it is not unreasonable is suppose that magmas may reach within 0.5 km or less of the surface as they migrate through pathways in the summit region.

In contrast to the predominance of rift eruptions over the past 70 yrs, the eruptive style of Kilauea during the 1800s, and in fact over much of the last 10,000 years (including the times of eruption of most of the Puna Ridge lavas; Clague et al. 1990), was characterized by vigorous summit activity and formation of sustained summit lava lakes (Holcomb 1987). The predominance of such an eruptive style at the summit over the period in which the Puna Ridge samples erupted is consistent with the important role played by a degassed end member in our model for the generation of the Puna Ridge suite. Periods of sustained summit activity and subsequent catastrophic caldera collapse would provide opportunities for significant quantities of degassed magma to return to the magma reservoir and mix with relatively undegassed magma (perhaps new influxes of primitive magma), followed by lateral injection of the mixed magma into an adjacent rift system. Mixing may also be facilitated by convection in the reservoir initiated by caldera collapse.

Predictions for Other Volcanoes.-We predict that depletions in volatile elements similar to those observed in Puna Ridge glasses should be observed in samples from rift zones of oceanic volcanoes whose summits have breached the sea surface (e.g., Mauna Loa), but not in samples from completely submerged oceanic volcanoes (e.g., Loihi). The H_2O contents of glasses from the submarine rift zone of Mauna Loa do indeed display a wide range at a given MgO content (Garcia et al. 1989), similar to that of Kilauean glasses (fig. 11). In contrast and also as predicted, the H_2O contents of tholeiitic glasses from the

summit of Loihi are higher than those of most glasses from the Mauna Loa submarine rift (Garcia et al. 1989), comparable to our high H_2O/K_2O samples (fig. 11). Similarly, Cl contents in tholeiitic glasses from Loihi are an order of magnitude higher than those in glasses from the submarine rift zones of Kilauea and Mauna Loa (Byers et al. 1985; Garcia et al. 1989). Byers et al. (1985) and Garcia et al. (1989) attributed these differences in H_2O and Cl contents to differences in the volatile element contents of the mantle source regions of Loihi and Mauna Loa parent magmas. While source regions for different Hawaiian volcanoes may indeed differ, the differences between the volatile contents of tholeiitic glasses from Loihi and those from the submarine rifts of Kilauea and Mauna Loa can also be explained by invoking a role for low pressure (perhaps even subaerially) degassed magma in eruptions on the submarine portions of the rift zones of volcanoes whose summits have breached the ocean surface.

CONCLUSIONS

We have presented major and volatile element concentrations in basaltic glasses from the submarine portion of the east rift zone of Kilauea Volcano, Hawaii. Significant features of our data are: (1) H_2O/K_2O ratios are highly variable, in contrast to the nearly constant ratios of nonvolatile incompatible elements (e.g., K_2O/P_2O_5); (2) S contents at a given FeO* are highly variable and often much lower than required for sulfide saturation, in contrast to the simple trends observed in MORB glasses; (3) S contents in glass inclusions are highly variable, and (4) CO_2 contents of most glasses agree within error with CO_2 solubility at the pressure of eruption. These data cannot readily be explained by combinations of fractional crystallization, degassing during submarine eruption, seawater addition, or heterogeneities in the mantle source regions of the magmas.

Our data are consistent with generation of these submarine magmas by: (1) mixing of magmas depleted in H_2O, S, and CO_2 with relatively undegassed magmas (degassed to the extent that occurs on rise into the summit reservoir located at >2-3 km depth beneath the summit of Kilauea); followed by (2) up to 30% fractional crystallization of olivine, clinopyroxene, and plagioclase in the proportions of 1:5.2:4.9 from the mixed magma to generate residual liquid; followed by (3) further degassing upon eruption on the seafloor, principally of CO_2 for eruption depths greater than 1000 m and of CO_2, H_2O and S shallower than 1000 m. The degassed component can be generated in the upper levels of the summit magma chamber, if the summit magma reservoir experiences pressures much less than lithostatic, by a flux of CO_2-rich bubbles rising through the magma, or during sustained summit eruptions and in lava lakes. Mixing of the degassed and undegassed components can occur as degassed magma is returned to the interior of the volcano, perhaps associated with drainbacks of lava lakes developed during sustained summit eruptions. The final phase of degassing during eruption on the seafloor occurs slowly enough to achieve melt/vapor equilibrium during exsolution of the typically CO_2-rich vapor phase.

Based on the characteristics of the undegassed end member required by our mixing model, we predict that Kilauean primary magmas with 16.0% MgO contain ~0.47 wt. % H_2O and ~900 ppm S. We can also explain the observed positive correlation between H_2O contents and δD values (Kyser and O'Neil 1984) if this component has a δD value of about -30 to -40‰, which is much higher than previous estimates of the δD of primitive Hawaiian magmas. We also predict that submarine lavas from wholly submarine volcanoes (i.e., for which there is no opportunity to generate the degassed end member by low pressure degassing) will be enriched in volatiles relative to those from volcanoes whose summits have breached the sea surface. This is consistent with the observed volatile element enrichment in tholeiitic glasses from Loihi relative to submarine glasses from Kilauea and Mauna Loa (Byers et al. 1985; Garcia et al. 1989).

Acknowledgements-We thank Robert Dixon for polishing the glass chips for IR analysis, Walt Friesen for the modal data, and Steve Wessells and Walt Friesen for their assistance with the microprobe analyses. Jim Moore kindly allowed us access to his collection of Kilauea dredged lavas, without which the study would not have been possible. We thank Mike Baker for allowing us to use his fractional crystallization program. Jim Moore, Tom Wright, Terry Gerlach, and two anonymous reviewers provided thoughtful reviews of the manuscript. The research at Caltech was performed under NSF grant EAR-8811406. Caltech Division of Geological and Planetary Science Contribution Number 4832.

REFERENCES CITED

Anderson, A. T.; Newman, S.; Williams, S. N.; Druitt, T. H.; Skirius, C.; and Stolper, E., 1989, H_2O, CO_2, Cl, and gas in Plinian and ash-flow Bishop rhyolite: Geology, v. 17, p. 221-225.

Ballard, R. D.; Holcomb, R. T.; and van Andel, T. J., 1979, The Galapagos Rift at 86°W, 2, Volcanism, structure, and evolution of the rift valley: Jour. Geophys. Res., v. 84, p. 5407-5422.

Byers, C.D.; Garcia, M.O.; and Muenow, D. W., 1985, Volatiles in pillow rim glasses from Loihi and Kilauea Volcanoes, Hawaii: Geochim. Cosmochim. Acta, v. 49, p. 1887-1896.

Casadevall, T. J.; Malinconico L. L.; LeGuern F.; Sato, M.; Stoiber, R.; McGee, K.; and Hazlett, R., 1980, Volcanic gas studies in Hawaii, 1978-1979 (abst.): EOS, v. 61, p. 67.

Chaussidon, M.; Sheppard, S. M. F.; Michard, A., 1989, Hydrogen, sulfur, and neodymium isotope variations in the mantle beneath the EPR at 12°50'N: Epstein 70th Birthday Symposium, California Institute of Technology, p. 94.

Clague, D. A.; Holcomb, R. T.; Torresan, M.; and Ross, S., 1988, Shipboard report for Hawaii GLORIA ground-truth cruise F11-88-HW, 25 Oct.-7 Nov., 1988: U.S. Geological Survey Open-file Report 89-109, 33 p.

————; Moore, J. G.; Friesen, W. F.; and Dixon, J. E., 1990, The mineral chemistry and petrogenesis of submarine lavas from Kilauea's East Rift Zone, Hawaii: Jour. Petrol., in press.

Craig, H., 1987, Comment on "Carbon isotope systematics of a mantle hotspot: a comparison of Loihi Seamount and MORB glasses" by R. A. Exley, D. P. Mattey, D. A. Clague, and C. T. Pillinger: Earth Planet. Sci. Lett., v. 82, p. 384-386.

———, and Lupton, J. E., 1976, Primordial neon, helium, and hydrogen in oceanic basalts: Earth Planet. Sci. Lett., v. 31, 369-385.

Delaney, J. R.; Muenow, D. W.; and Graham, D. G., 1978, Abundance and distribution of water, carbon and sulfur in the glassy rims of submarine pillow basalts: Geochim. Cosmochim. Acta, v. 42, p. 581-594.

Des Marais, D. J., 1986, Carbon abundance measurements in oceanic basalts: the need for a consensus: Earth Planet. Sci. Lett., v. 79, p. 21-26.

———, and Moore, J. G., 1984, Carbon and its isotopes in mid-oceanic basaltic glasses: Earth Planet. Sci Lett., v. 69, p. 43-57.

Dixon, J. E.; Stolper, E.; and Delaney, J. R., 1988, Infrared spectroscopic measurements of CO_2 and H_2O in Juan de Fuca Ridge basaltic glasses: Earth Planet. Sci. Lett., v. 90, p. 87-104.

Exley, R. A.; Mattey, D. P.; and Pillinger, C. T., 1987, Low temperature carbon components in basaltic glasses--reply to comment by H. Craig: Earth Planet. Sci. Lett., v. 82, p. 387-390.

Fine, G. J., and Stolper, E. M., 1986, Dissolved carbon dioxide in basaltic glasses: concentrations and speciation: Earth Planet. Sci. Lett., v. 76, p. 263-278.

Fiske, R. S., and W. T. Kinoshita, 1969, Inflation of Kilauea Volcano prior to its 1967-1968 eruption: Science, v. 165, p. 341-349.

Fornari, D. J.; Malahoff, A.; and Heezen, B. C., 1978, Volcanic structure of the crest of the Puna Ridge, Hawaii: Geophysical implications of submarine volcanic terrain: Geol. Soc. America Bull., v. 89, p. 605-616.

Garcia, M. O.; Muenow, D.; Aggrey, K.; and O'Neil, J., 1989, Major element, volatile and stable isotope geochemistry of Hawaiian submarine tholeiitic basalt: Jour. Geophys. Res., v. 94, p. 10,525-10,538.

Gerlach, T. M., 1980, Evaluation of volcanic gas analyses from Kilauea volcano: Jour. Volcanol. Geotherm. Res., v. 7, p. 295-317.

————, 1986, Exsolution of H_2O, CO_2, and S during eruptive episodes at Kilauea Volcano, Hawaii: Jour. Geophys. Res., v. 91, p. 12,177-12,185.

————, and Graeber, E. J., 1985, Volatile budget of Kilauea volcano: Nature, v. 313, p. 273-277.

Greenland, L. P.; Rose, W. I.; and Stokes, J. B., 1985, An estimate of gas emissions and magmatic gas content from Kilauea volcano: Geochim. Cosmochim. Acta, v. 49, p. 125-129.

Grove, T. L., and Baker, M. B., 1984, Phase equilibrium controls on the tholeiitic versus calc-alkaline differentiation trends: Jour. Geophys. Res., v. 89, p. 3253-3274.

————, and Byran, W. B., 1983, Fractionation of pyroxene-phyric MORB at low pressure: An experimental study: Contrib. Mineral. Petrol., v. 84, p. 293-309.

Hamilton, D. L.; Burnham, C. W.; and Osborn, E. F., 1964, The solubility of water and effects of oxygen fugacity and water content on crystallization in mafic magmas: Jour. Petrol., v. 5, p. 21-39.

Harris, D. M., 1981, The concentration of CO_2 in submarine tholeiitic basalts: Jour. Geol., v. 89, p. 689-701.

————, and Anderson, A. T., 1983, Concentrations, sources, and losses of H_2O, CO_2, and S in Kilauean basalt: Geochim. Cosmochim. Acta, v. 47, p. 1139-1150.

Helz, R. T., and Thornber, C. R., 1987, Geothermometry of Kilauea Iki lava lake, Kilauea Volcano, Hawaii: Bull. Volcanology, v. 49, p. 651-658.

Hofmann, A. W.; Feigenson, M. D.; and Raczek, I., 1984, Case studies on the origin of basalt: III. Petrogenesis of the Mauna Ulu eruption, Kilauea, 1969-1971: Contrib. Mineral. Petrol., v. 88, p. 24-35.

Holcomb, R. T., 1987, Eruptive history and long-term behavior of Kilauea Volcano, *in* Volcanism in Hawaii, U.S. Geological Survey Prof. Paper 1350, p. 261-350.

————, and Clague, D. A., 1983, Volcanic eruption patterns along submarine rift zones: Oceans 83 Proceedings, IEEE, New York, p. 787-790.

————; Moore, J. G.; Lipman, P. W.; and Belderson, R. H., 1988, Voluminous lava flows from Hawaiian volcanoes: Geology, v. 16, p. 400-404.

Jaggar, T. A., 1947, Origin and development of craters: Geol. Soc. America Mem. 21, 508 p.

Jarosewich, E.; Nelen, J. A.; Norberg, J. A., 1979, Electron microprobe reference samples for mineral analyses: Smithsonian Contrib. to the Earth Sciences, no. 20, p. 68-72.

Killingley, J. S., and Muenow, D. M., 1975, Volatiles from Hawaiian submarine basalts determined by dynamic high temperature mass spectrometry: Geochim. Cosmochim. Acta, v. 39, p. 1467-1473.

Koyanagi, R. Y.; Unger, J. D.; Endo, E. T.; and Okamura, A. T., 1976, Shallow earthquakes associated with inflation episodes at the summit of Kilauea Volcano, Hawaii: Bull. Volcanology, v. 39, p. 621-631.

Kyser, T. K., and O'Neil, J. R., 1984, Hydrogen isotope systematics of submarine basalts: Geochim. Cosmochim. Acta, v. 48, p. 2123-2133.

Langmuir, C. H., 1989, Geochemical consequences of *in situ* crystallization: Nature, v. 340, p. 199-205.

Langmuir, C. H.; Vocke, R. D., Jr.; Hanson, G. N.; and Hart, S. R., 1978, A general mixing equation with applications to Icelandic basalts: Earth Planet. Sci. Lett., v. 37, p. 380-392.

Lonsdale, P., 1989, A geomorphological reconnaissance of the submarine part of the East Rift Zone of Kilauea Volcano, Hawaii: Bull. Volcanology, v. 51, p. 123-144.

Mathez, E. A., 1976, Sulfur solubility and magmatic sulfides in submarine basalt glass: Jour. Geophys. Res., v. 81, p. 4269-4276.

Mattey, D. P.; Carr, R. H.; Wright, I. P.; and Pillinger, C. T., 1984, Carbon isotopes in submarine basalts, Earth Planet. Sci. Lett., v. 70, p. 196-206.

Michael, P. J., and Chase, R. L., 1987, The influence of primary magma composition, H_2O and pressure on mid-ocean ridge basalt differentiation: Contrib. Mineral. Pet., v. 96, p. 245-263.

Moore, J. G., 1965, Petrology of deep-sea basalt near Hawaii: American Jour. Sci. v. 263, p. 40-52.

————, 1970, Water content of basalt erupted on the ocean floor: Contrib. Mineral. Pet., v. 28, p. 272-279.

————, and Fiske, R. S., 1969, Volcanic substructure inferred from dredge samples and ocean-bottom photographs, Hawaii: Geol. Soc. America Bull., v. 80, p. 1191-1203.

————, and Koyanagi, R. Y., 1969, The October 1963 eruption of Kilauea Volcano, Hawaii: U.S. Geol. Surv. Prof. Paper 614-C,13 p.

————, and Fabbi, B. P., 1971, An estimate of the juvenile sulfur content of basalt: Contrib. Mineral. Petrol., v. 33, p. 118-127.

————, and Clague, D. A., 1987, Coastal lava flows from Mauna Loa and Hualalai volcanoes, Kona, Hawaii: Bull. Volcanology, v. 49, p. 752-764.

————, Batchelder, J. N.; and Cunningham, C. G., 1977, CO_2-filled vesicles in mid-ocean basalt: Jour. Volcanol. Geotherm. Res., v. 2, p. 309-327.

Muenow, D. W.; Graham, D. G.; Liu, N. W. K.; and Delaney, J. R., 1979, The abundance of volatiles in Hawaiian tholeiitic submarine basalts: Earth Planet. Sci Lett., v. 42, p. 71-76.

Newman, S. N.; Stolper, E. M.; and Epstein, S., 1986, Measurement of water in rhyolitic glasses: Calibration of an infrared spectroscopic technique: America Mineral., v. 71, p. 1527-1541.

O'Hara, M. J., 1977, Geochemical evolution during fractional crystallization of a periodically refilled magma chamber: Nature, v. 266, p. 503-507.

————, and Mathews, R. E., 1981, Geochemical evolution in an advancing, periodically replenished, periodically tapped, continuously fractionated magma chamber: Jour. geol. Soc. Lond., v. 138, p. 237-277.

Pineau, F., and Javoy, M., 1986, The volatile record of a "popping rock" from the Mid-Atlantic Ridge at 15 °N: concentrations and isotopic compositions (abs.): Terra Cognita, v. 6, p. 191.

Poreda, R.; Schilling, J-G.; and Craig, H., 1986, Helium and hydrogen isotopes in ocean-ridge basalts north and south of Iceland: Earth Planet. Sci. Lett., v. 78, p. 1-17.

Richter, D. H.; Eaton, J. P.; Murata, K. J.; Ault, W. U.; and Krivoy, H. L., 1970, Chronological narrative of the 1959-60 eruption of Kilauea Volcano, Hawaii: U.S. Geol. Surv. Prof. Paper 537-E, 73 p.

Roedder, E., 1965, Liquid CO_2 inclusions in olivine-bearing nodules and phenocrysts from basalts: America Mineral., v. 50, p. 1746-1782.

Roedder, P. L., 1974, Activity of iron and olivine solubility in basaltic liquids: Earth Planet. Sci. Lett., v. 23, p. 397-410.

Ryan, M. P.; Koyanagi, R. Y.; and Fiske, R. S., 1981, Modeling the three-dimensional structure of macroscopic magma transport systems: Applications to Kilauea Volcano, Hawaii: Jour. Geophys. Res., v. 86, p. 7111-7129.

————,1988, The mechanics and three-dimensional internal structure of active magma systems: Kilauea volcano, Hawaii: Jour. Geophys. Res., v. 93, p. 4213-4248.

Sakai, H.; Des Marais, D. J.; Ueda, A.; and Moore, J. G., 1984, Concentrations and isotopic ratios of carbon, nitrogen and sulfur in ocean-floor basalts: Geochim. Cosmochim. Acta, v. 48, p.2433-2441.

Silver, L., and Stolper, E., 1989, Water in albitic glasses: Jour. Petrol., v. 30, p. 667-709.

Stolper, E., and Holloway, J. R., 1988, Experimental determination of the solubility of carbon dioxide in molten basalt at low pressure: Earth Planet Sci Lett., v. 87, p. 397-408.

Swanson, D. A., and Fabbi, B. P., 1973, Loss of volatiles during fountaining and flowage of basaltic lava at Kilauea Volcano, Hawaii: Jour. Res. U.S. Geol. Surv., v. 1, p. 649-658.

Thompson, R. N., and Tilley, C. E., 1969, Melting and crystallization relations of Kilauean basalts of Hawaii. The lavas of the 1959-60 Kilauea eruption: Earth Planet. Sci. Lett., v. 5, p. 469-477.

Vergniolle, S., and Jaupart, C., 1990, Dynamics of degassing at Kilauea Volcano, Hawaii: Jour. Geophys. Res., v. 95, p. 2793-2809.

Wilde, P.; Chase, T. E.; Normark, W. R.; Thomas, J. A.; and Young, J. D., 1980, Oceanographic data off the southern Hawaiian Islands: Lawrence Berkeley Laboratory Pub. 359, Lawrence Berkeley Labs, University of California, Berkeley.

Wolfe, E. W.; Garcia, M. O.; Jackson, D. B.; Koyanagi, R. Y.; Neal, C. A.; and Okamura, A. T., 1987, The Puu Oo eruption of Kilauea Volcano, episodes 1-20, January 3, 1983, to June 8, 1984: U.S. Geol. Surv. Prof. Paper 1350, p. 471-508.

Wright, T. L., 1971, Chemistry of Kilauea and Mauna Loa lava in space and time: U.S. Geol. Surv. Prof. Paper 735, 40 p.

————, and Fiske, R. S., 1971, Origin of the differentiated and hybrid lavas of Kilauea Volcano, Hawaii: Jour. Petrol., v. 12, p. 1-65.

TABLE 1

Dredge Locations

Dredge	Depth (m)	Lat. (N)	Long. (W)
	Along-Rift		
1684	490	19° 32.1'	154° 47.4'
1717	550	19° 32.7'	154° 46.7'
D45	740	19° 32.9'	154° 45.4'
1685	760	19° 34.5'	154° 45.5'
1742	1400	19° 36.5'	154° 39.0'
SU56-66	1440	19° 32.0'	154° 42.9'
1689	1600	19° 36.5'	154° 39.0'
1688	1650	19° 36.2'	154° 42.8'
D43	1835	19° 37.1'	154° 36.3'
D42	2235	19° 40.1'	154° 29.9'
1695	2590	19° 42.5'	154° 26.1'
1697	2960	19° 44.1'	154° 24.5'
1699	3410	19° 45.2'	154° 22.2'
1701	3960	19° 44.5'	154° 15.0'
1712	4680	19° 50.2'	154° 18.9'
1706	5000	19° 51.5'	154° 15.2'
1714	5180	19° 49.1'	154° 15.4'
D4	5470	19° 49.6'	154° 08.3'
D5	5490	19° 26.9'	154° 16.3'
	Off-Rift		
SU49-66	840	19° 07.7'	155° 16.5'
SU51-66	1040	19° 12.6'	155° 10.2'
SU57-66	1560	19° 25.3'	154° 48.9'

Dredges 1684 to 1742 recovered by the *Pioneer* in 1962; dredges SUxx-66 recovered by the *Surveyor* in 1966; dredges D4 to D45 recovered by *R/V Farnella* in 1988.

Table 2

Comparison of Wet Chemical and Microprobe Analyses of Glass Standards

	VG-2[1]	VG-2[2] n=19	A-99[1]	A-99[2] n=15
SiO_2	50.81	50.56 ± .30	50.94	51.00 ± .43
Al_2O_3	14.06	14.13 ± .29	12.49	12.71 ± .35
FeO*	11.84	11.69 ± .10	13.30	13.28 ± .12
MnO	.20	.21 ± .01	.15	.20 ± .01
MgO	6.71	6.99 ± .05	5.08	5.11 ± .05
CaO	11.12	11.07 ± .21	9.30	9.26 ± .18
Na_2O	2.62	2.78 ± .06	2.66	2.80 ± .05
K_2O	.19	.19 ± .01	.82	.82 ± .03
P_2O_5	n.a.	.22 ± .02	n.a.	.45 ± .04
TiO_2	1.85	1.82 ± .03	4.06	3.99 ± .06
S	n.a.	.134 ± .008	n.a.	.017 ± .003

[1]wet chemical analyses (Jarosewich et al. 1979)

[2]mean microprobe analysis and 1s standard deviation; The standard values for SiO_2, FeO, MgO, and Na_2O in VG-2 used in the microprobe data reduction program were modified slightly from the reported wet-chemical analysis based on microprobe analysis of VG-2 against other standards and are within the standard deviations reported for our mean analysis.

n.a. = not analyzed

TABLE 3

ANALYSES OF GLASSES FROM THE PUNA RIDGE

Flow Unit	1684	1717	D45a	D45b	1685	1742a	1742b	SU56a	SU56b	1689	1688	D43a	D43b	D42a	D42b	D42c	1695	1697a[d]
Number	1	2	2	5	2	3	2	3	1	1	1	3	3	7	2	3	1	2
Depth (m)	490	550	740	740	890	1400	1400	1440	1440	1600	1650	1835	1835	2235	2235	2235	2590	2960
SiO_2	51.2	51.8	50.7	51.0	50.7	52.2	50.0	52.0	52.2	51.8	51.4	51.0	51.9	51.2	50.9	51.0	51.6	52.4
Al_2O_3	14.2	13.6	14.1	13.8	13.6	13.5	13.8	14.1	14.2	13.6	13.7	14.2	13.6	14.0	13.8	14.4	13.8	13.7
FeO	11.0	11.3	11.2	11.4	11.6	10.9	11.0	10.4	10.9	11.4	11.3	10.2	11.8	10.8	11.2	10.9	10.5	11.1
MnO	.15	.16	.17	.17	.18	.16	.17	.15	.16	.16	.18	.16	.18	.17	.16	.17	.16	.15
MgO	6.37	5.98	6.00	5.86	6.07	6.39	6.41	6.70	5.62	5.20	6.20	6.96	5.65	6.50	6.28	6.49	6.45	6.25
CaO	10.9	10.2	10.6	10.0	10.3	10.3	10.8	10.9	9.63	9.23	10.4	11.1	9.79	10.7	10.5	10.7	10.6	10.4
Na_2O	2.48	2.56	2.69	2.67	2.71	2.52	2.59	2.53	2.83	2.72	2.46	2.40	2.67	2.44	2.53	2.60	2.53	2.62
K_2O	.52	.54	.49	.58	.67	.46	.52	.48	.67	.67	.47	.41	.53	.41	.52	.48	.50	.46
P_2O_5	.33	.37	.32	.32	.40	.31	.32	.30	.41	.48	.31	.27	.33	.28	.36	.30	.29	.27
TiO_2	2.70	2.87	2.72	3.00	3.16	2.80	2.78	2.59	3.10	3.22	2.76	2.42	3.20	2.49	2.72	2.69	2.63	2.81
Total	99.9	99.5	99.0	98.9	99.5	99.6	98.5	100.2	99.8	98.6	99.3	99.2	99.8	99.1	99.1	99.8	99.2	100.2
S (wt %)	.066	.073	.098	.100	.090	.022	.125	.047	.098	.129	.123	.098	.144	.117	.119	.085	.104	.073
H_2O (wt %)[a]	.47	.38	.50	.42	.40	.11	.48	.22	.54	.81	.51	.48	.58	.61	.62	...	.57	...
std. dev.	...	.04	...	...	.01	...	...	.01	.04	.02	...	...	.07	...	...	...	...	...
CO_2 (ppm)[b]	0	0	30	19	29	0	39	71	46	0	57	84	21	117	110	...	118	...
std. dev.	...	...	20	5	15	...	11	7	10	0	8	5	13	10	17	...	30	...
Modal Analyses[c]																		
Vesicles	32.9	15.8	.7	9.8	10.9	0	7.4	2.8	1.4	4.0	2.0	1.7	0.3	.1	1.7	.7	.7	.6
Olivine	1	6	3	5	5	18	6	9	29	10	5	28	12	7	6	3	9	7
Cpx	2	6	3	4	4	1	2	1	2	5	2	<1	10	<1	2	1	<1	4
Opx	...	>1	...	>1	2	...	...	...	>1	<1	...	...	<1	...	...	...	<1	<1
Ptag	<1	4	2	3	5	<1	1	<1	1	4	1	...	11	...	2	<1	<1	5

[a]Calculated using molar absorption coefficient of 63 ± 5 l mol^{-1} cm^{-1} for the 3535 cm^{-1} band in basalt (P. Dobson, S. Newman, S. Epstein, and E. Stolper, unpublished results) and assumed glass density of 2.8 g cm^{-3}. Where more than one spectrum was measured we report the average and standard deviation.

[b]The intensities of the carbonate (CO_3^{2-}) peaks (1515-1435 cm^{-1}) were measured separately after numerical subtraction of the spectrum of Kilauea Iki lava lake glass 79-6-190.3 (a glass containing no detectable dissolved CO_2) and a concentration was calculated from each measurement using a molar absorption coefficient of 375 l mol^{-1} cm^{-1} (Fine and Stolper 1986) and an assumed glass density of 2.8 g cm^{-3}. The dissolved CO_2 contents are averages of all of the CO_2 concentrations measured from all spectra on glass chips from the same split.

[c]Modes give the combined volume percent of phenocrysts, microphenocrysts, xenocrysts, and vesicles in the outer 1.5 cm of the sample, which includes the glassy rims plus a microcrystalline zone adjacent to the glassy rim. All samples contain <1% chromite enclosed in olivine phenocrysts.

[d]Sample 1697 analyzed by Killingley and Muenow (1975) and Muenow et al. (1979) is from flow unit 1697a. Sample 1697 analyzed by Byers et al. (1985) and Harris (1981) is probably from flow unit 1697b. Sample reported as 1712 (4680 m) by Byers et al. (1985) is probably a misidentified sample from dredge 1714 based on their reported microprobe glass analysis.

Table 4

Microprobe Analyses of Subaerially Erupted Kilauean Glasses

Flow Unit	228-3*	SU49	SU51a	SU51b	SU57a	SU57b	SU57c
No. Averaged	1	1	1	1	1	1	1
Depth	220	840	1040	1040	1560	1560	1560
SiO_2	50.6	51.5	51.3	52.0	52.1	51.4	51.2
Al_2O_3	13.5	13.3	14.0	13.8	13.6	13.2	13.7
FeO	11.3	11.8	10.9	11.0	11.1	12.0	11.8
MnO	.20	.19	.16	.16	.15	.18	.18
MgO	5.25	6.32	6.93	6.58	6.45	6.10	6.07
CaO	9.44	10.8	11.2	11.3	11.2	10.6	10.3
Na_2O	2.84	2.47	2.40	2.42	2.50	2.64	2.61
K_2O	.95	.49	.46	.44	.45	.53	.58
P_2O_5	.56	.30	.32	.25	.28	.31	.39
TiO_2	4.28	2.90	2.46	2.52	2.66	2.96	3.13
Total	98.9	100.1	100.1	100.5	100.5	99.9	100.0
S (wt. %)	.024	.015	.007	.011	.017	.013	.010
H_2O (wt. %)				.09		.09	
std.dev.				.00		.00	
CO2 (ppm)				0		0	
std.dev.				0		0	

* 1960 Kapoho flow collected off Cape Kumikahi by the submersible *Makali'i* on dive PP82-228 as sample 3.

Table 5

Mixing and Fractional Crystallization Proportions

Sample	%Deg.	%xtls	model CO_2 (ppm)	model S (wt. %)
1684	34.2	6.0	336	.091
1717	59.2	18.0	239	.074
D45a	34.0	11.4	358	.097
D45b	54.6	20.0	272	.082
1685	55.0	16.4	258	.078
1742a	100.0	16.4	0	.024
1742b	34.2	8.0	343	.093
SU56a	79.6	6.5	105	.043
SU56b	38.1	25.5	399	.110
1689	11.0	30.4	613	.157
1688	35.8	14.9	362	.099
D43a	28.8	2.0	349	.093
D43b	33.8	23.5	415	.113
D42a	13.3	9.7	461	.118
D42b	15.8	13.2	466	.120
1695	22.1	11.4	422	.110
1697b	78.3	11.4	118	.047
1699	0	24.7	637	.159
1701	36.9	29.8	431	.118
1712	40.8	23.0	369	.103
1706	8.7	22.3	564	.143
1714	47.3	14.9	297	.085
D4-13	40.8	11.4	321	.089
D5-8	11.9	11.4	477	.122

The amount of fractional crystallization (%xtls) needed to generate the major element composition of the each glass from a parent magma ("P" on fig. 2 containing 7.0 wt. % MgO and 11.23 wt. % CaO) was estimated using its CaO content (see fig. 2). The proportions of degassed (%Deg with 0.10 wt % H_2O, 200 ppm S, and no CO_2) and undegassed (100-%Deg with 0.62 wt % H_2O, 1200 ppm S, and 480 ppm CO_2) end members were calculated by mass balance using the H_2O content (corrected for %xtls) of the reconstructed parental magma composition for each glass. Model CO_2 and S concentrations for each glass represent our predicted values after mixing and fractional crystallization.

Figure 1. Dredge locations of samples from the Puna Ridge (inset). Bathymetry along the axis of the Puna Ridge and in the Hawaiian Moat at the distal end of the Puna Ridge after Lonsdale (1989), remainder of the bathymetry after Wilde et al. (1980), modified slightly based on data from U.S. Geological Survey cruise F2-88-HW (Clague et al. 1988). Dredge locations from Moore (1965) and Clague et al. (1985) are listed in Table 1. Sample location symbols are: filled circle for dredges by *Pioneer* in 1962, filled triangles for dredges by *Surveyor* in 1966, filled squares for dredges by *R/V Farnella* in 1988, and an open square for a box core by *R/V Farnella* in 1988 that included 5 turbidite layers of submarine erupted glass sand and silt (these glasses are discussed in Clague et al. 1990).

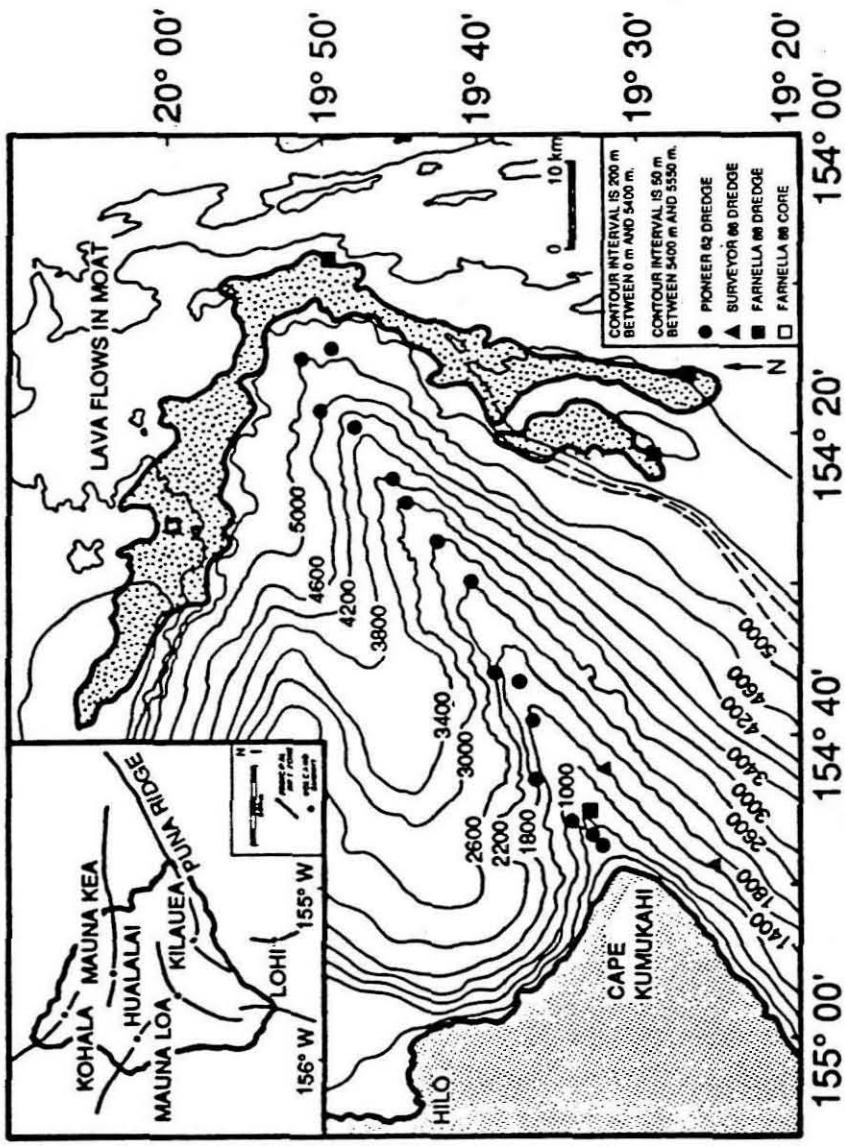
KOHALA
MAUNA KEA
HUALALAI
MAUNA LOA
KILAUEA
PUNA RIDGE
LOHI
155° W
156° W
LAVA FLOWS IN MOAT
HILO
CAPE KUMUKAHI
5000
4600
4200
3800
3400
3000
2600
2200
1800
1000
1400
20° 00'
19° 50'
19° 40'
19° 30'
19° 20'
155° 00'
154° 40'
154° 20'
154° 00'
0
10 km
N
CONTOUR INTERVAL IS 200 m BETWEEN 0 m AND 5400 m.
CONTOUR INTERVAL IS 50 m BETWEEN 5400 m AND 5550 m.
PIONEER 82 DREDGE
SURVEYOR 86 DREDGE
FARNELLA 86 DREDGE
FARNELLA 86 CORE

FIGURE 1

Figure 2. MgO variation diagrams of glass compositions from the Puna Ridge. Solid line represents 0-30% crystal fractionation of olivine, plagioclase, and clinopyroxene in proportions of 1:5.2:4.9 from a parental magma (P). Composition of parental magma (in wt. %) is SiO_2 51.02, Al_2O_3 14.37, FeO 10.12, MnO 0.13, MgO 7.00, CaO 11.23, Na_2O 2.37, K_2O 0.44, P_2O_5 0.28, TiO_2 2.40, S 0.120, H_2O 0.62, CO_2 0.048. Fractional crystallization calculations (following Grove and Baker 1984) were carried out in increments by removing 2 wt. % solids from an initial liquid to give a residual fractionated liquid. Compositions of olivine, plagioclase, and clinopyroxene in equilibrium with the initial liquid were calculated for each increment using Fe-Mg distribution coefficients of 0.30 for olivine (Roedder 1974) and 0.25 for clinopyroxene (Grove and Bryan 1983) and Ca-Na distribution coefficient of 1.5 for plagioclase. The CaO, Al_2O_3, and TiO_2 contents of the clinopyroxene were kept constant at 19.1, 2.49, 0.65 wt. %, respectively, and were chosen to be close to the average composition found in lavas from the Puna Ridge (Clague et al. 1990).

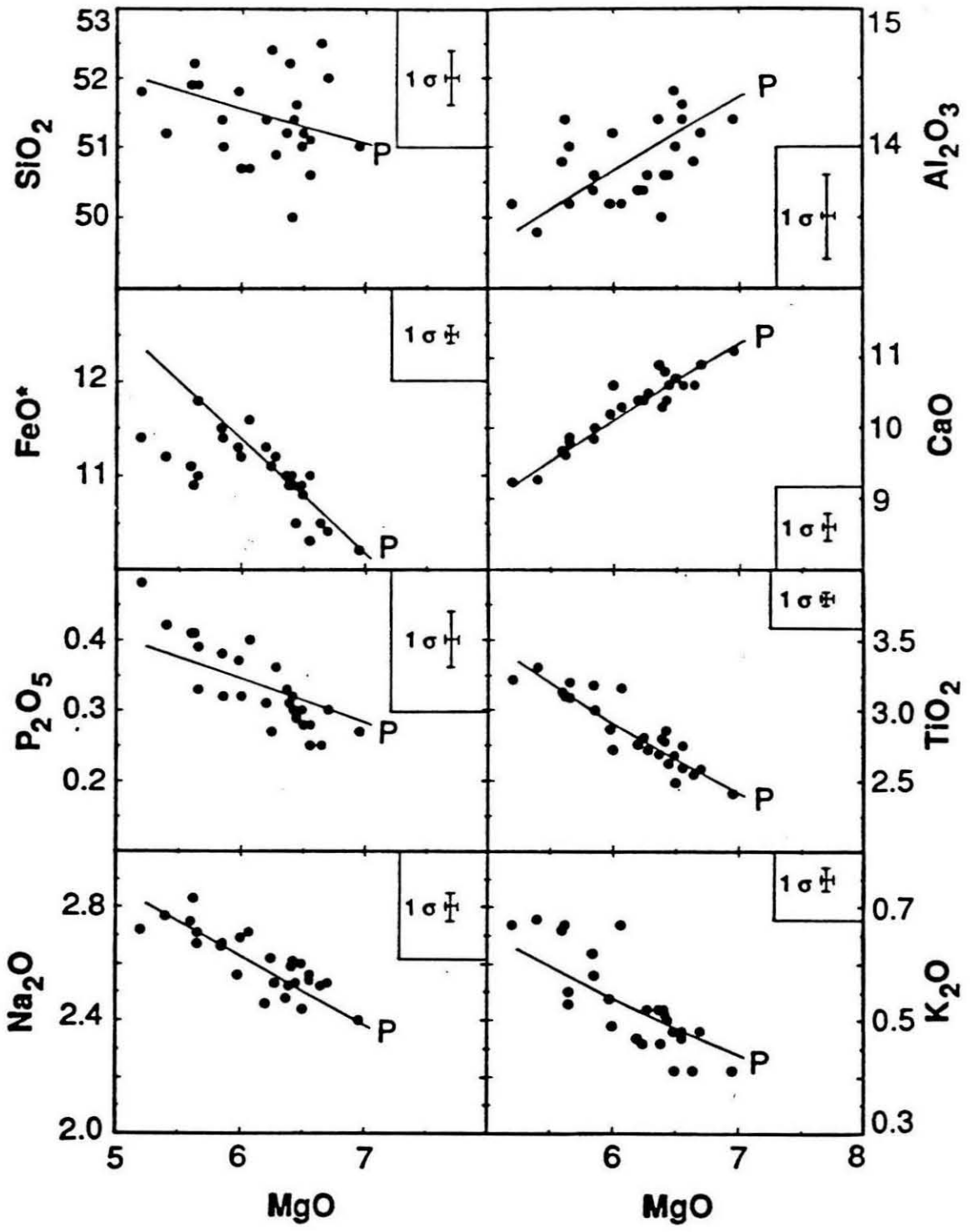
SiO2
53
52
51
50
1σ
P
Al2O3
15
14
FeO*
12
11
CaO
11
10
9
P2O5
0.4
0.3
0.2
TiO2
3.5
3.0
2.5
Na2O
2.8
2.4
2.0
K2O
0.7
0.5
0.3
5
6
7
8
MgO
MgO

FIGURE 2

Figure 3. K_2O versus P_2O_5 for the glass compositions from the Puna Ridge.

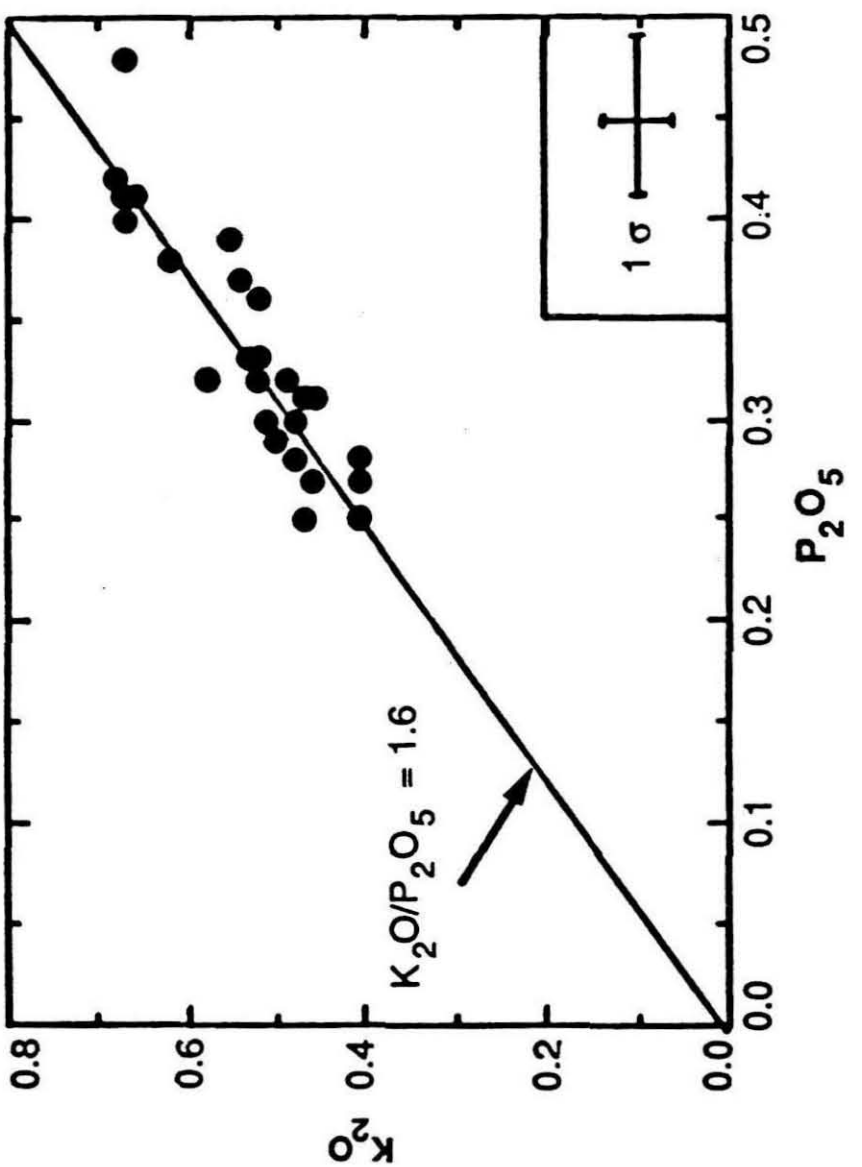

FIGURE 3

Figure 4. Comparisons of volatile element data measured by other techniques and those reported in this study on samples from the same flow units. Filled symbols represent analyses of glassy whole-rock samples. H_2O and S concentrations shown on the figure for whole-rock samples have been corrected for the mass fraction of phenocrysts using our modal data (Table 3) and densities(g/cm^3) of 3.5 for olivine, 3.3 for clinopyroxene, and 2.72 for plagioclase. Open symbols and crosses represent analyses of glass separates. a) H_2O, b) S, c) CO_2.

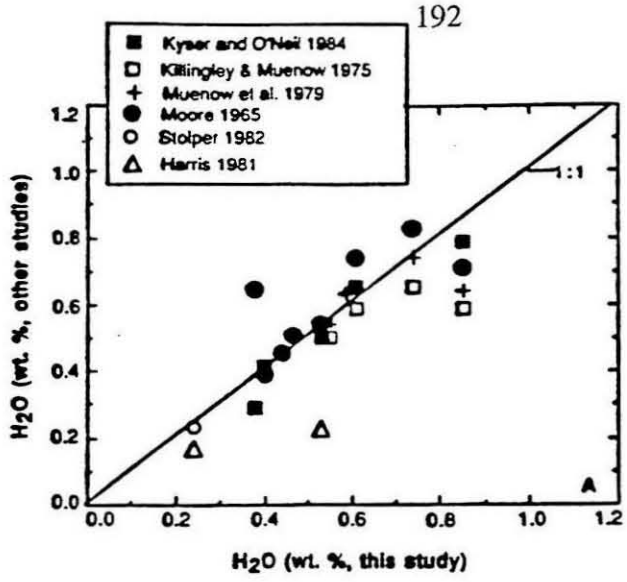
Kyser and O'Neil 1984
Killingley & Muenow 1975
Muenow et al. 1979
Moore 1965
Stolper 1982
Harris 1981
1:1
A
H2O (wt. %, other studies)
H2O (wt. %, this study)

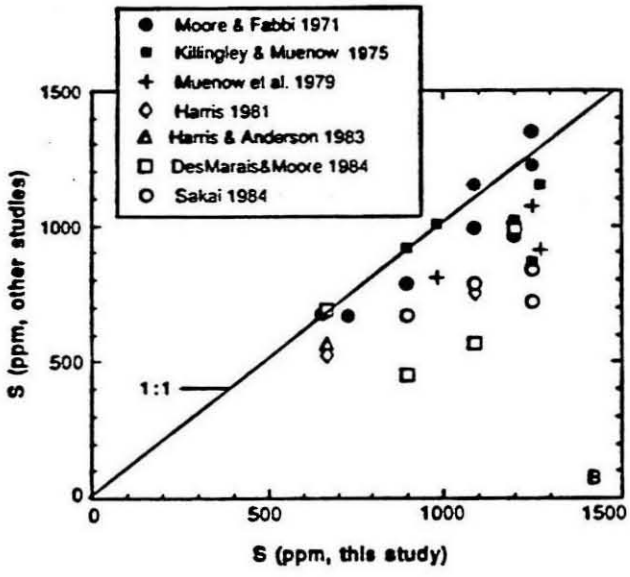
Moore & Fabbi 1971
Killingley & Muenow 1975
Muenow et al. 1979
Harris 1981
Harris & Anderson 1983
DesMarais&Moore 1984
Sakai 1984
1:1
B
S (ppm, other studies)
S (ppm, this study)

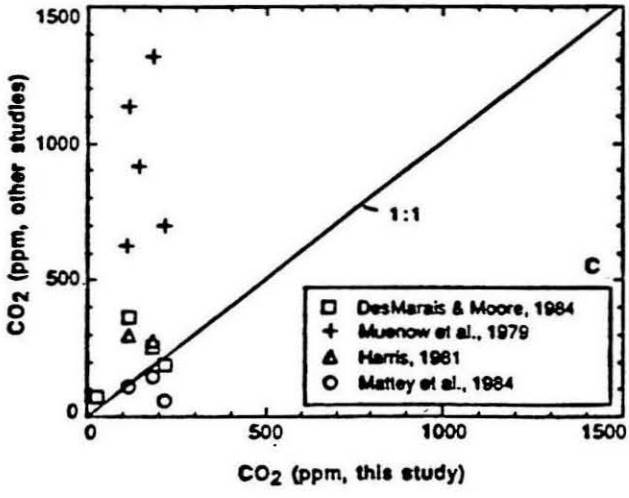
1:1
C
DesMarais & Moore, 1984
Muenow et al., 1979
Harris, 1981
Matley et al., 1984
CO2 (ppm, other studies)
CO2 (ppm, this study)

FIGURE 4

5. a) Dissolved H_2O vs depth. Solubility of pure H_2O in basalt at 1100°C (Hamilton et al. 1964) is an extrapolation of higher pressure data.. b) Dissolved S vs depth. c) Dissolved CO_2 vs depth. Open squares: low-H_2O/K_2O samples with H_2O/K_2O ratios less than or equal to 0.7; Filled circles: moderate-H_2O/K_2O samples with H_2O/K_2O ratios between 0.7 and 1.0; Crosses: high-H_2O/K_2O samples with H_2O/K_2O greater than 1.0. Vertical lines through some symbols show uncertainty in depth of eruption.

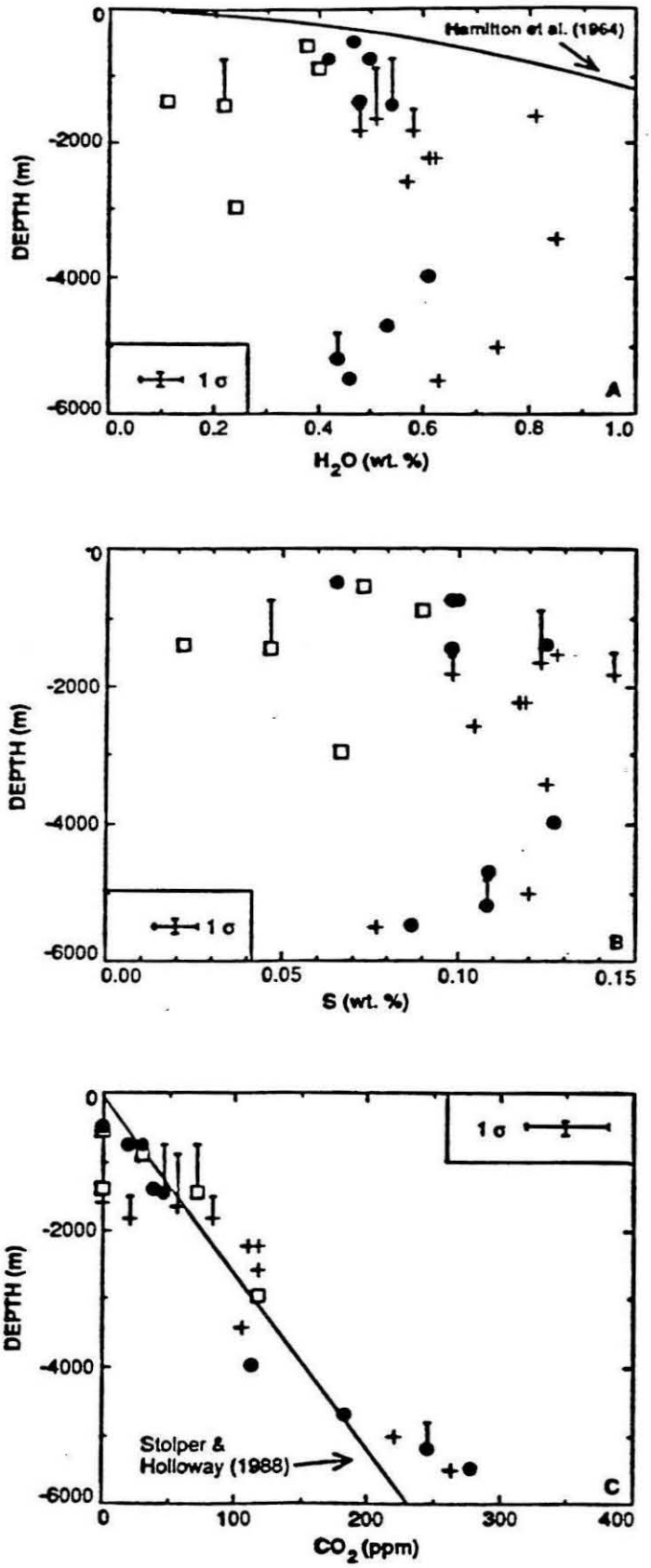
Hamilton et al. (1964)
DEPTH (m)
0
-2000
-4000
-6000
1 σ
A
0.0
0.2
0.4
0.6
0.8
1.0
H2O (wt. %)
B
0.00
0.05
0.10
0.15
S (wt. %)
Stolper &
Holloway (1988)
C
0
100
200
300
400
CO2 (ppm)

FIGURE 5

6. a) Dissolved H_2O vs MgO, b) Dissolved H_2O vs K_2O. Open squares: low-H_2O/K_2O samples with H_2O/K_2O ratios less than or equal to 0.7; Filled circles: moderate-H_2O/K_20 samples with K_2O/H_2O ratios between 0.7 and 1.0; Crosses: high-H_2O/K_2O samples with H_2O/K_2O greater than 1.0; Open triangles: off-rift (subaerially degassed) samples; U: Undegassed end member; D: Degassed end member; Trends resulting from mixing of degassed and undegassed magmas calculated using mixing equations in Langmuir et al. (1978) and shown by open ended arrows. Trends resulting from fractional crystallization (f.c.) shown by solid arrows. Extent of fractional crystallization is constrained by major element models. Grid lines shown at 20% intervals for mixing proportions and 10% intervals for fractional crystallization.

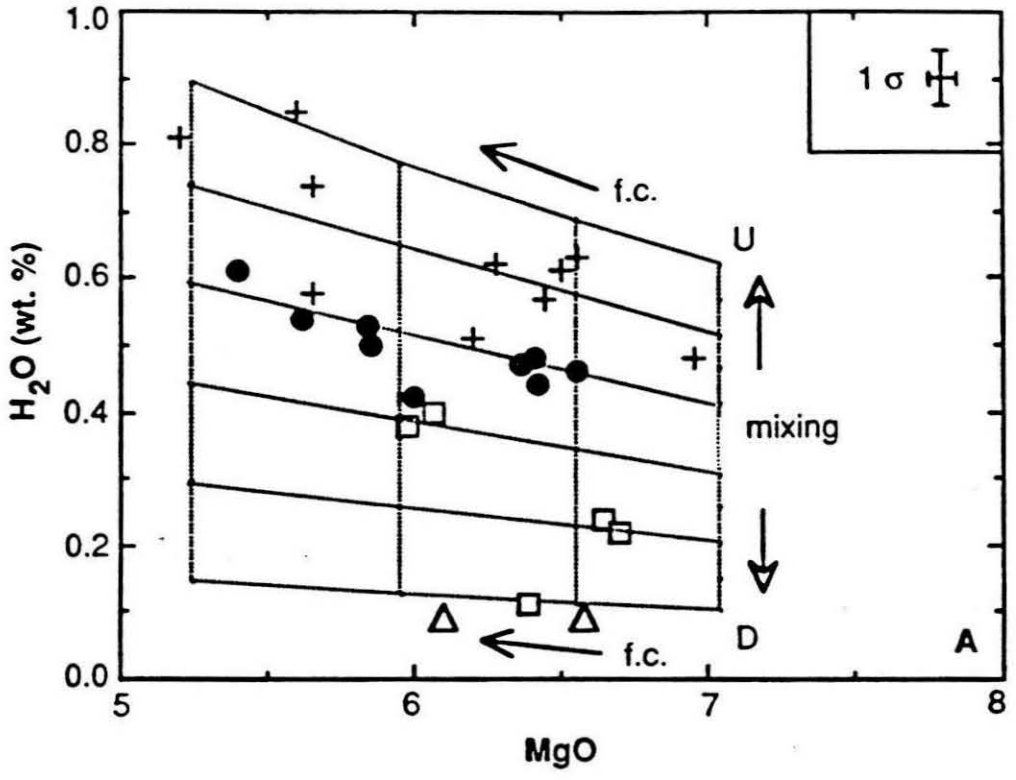
1.0
0.8
0.6
0.4
0.2
0.0
5
6
7
8
H_2O (wt. %)
MgO
1 σ
f.c.
U
mixing
D
f.c.
A

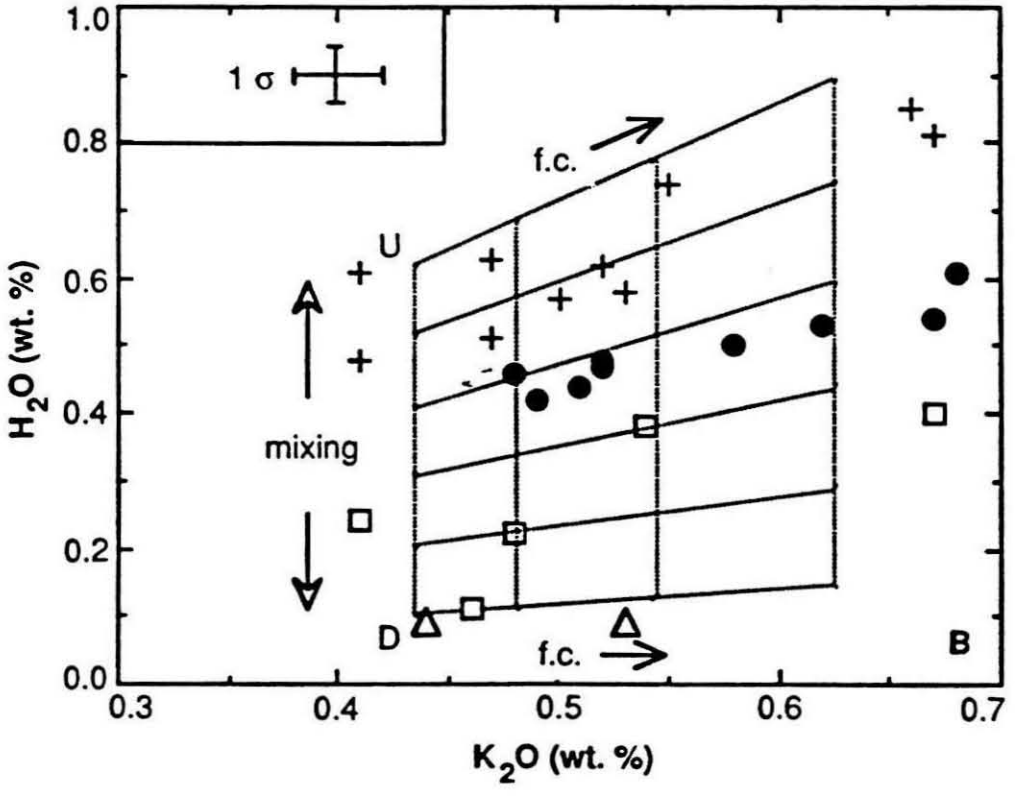
1.0
0.8
0.6
0.4
0.2
0.0
0.3
0.4
0.5
0.6
0.7
H_2O (wt. %)
K_2O (wt. %)
1 σ
f.c.
U
mixing
D
f.c.
B

FIGURE 6

7. a) Dissolved S vs FeO. MORB S trend line is based on microprobe analysis of glasses from Juan de Fuca and Gorda Ridges (D. A. Clague, unpub. data) obtained using the same S standardization as the data in this study and are about 15% lower than those of Mathez (1976), obtained using a sulfide standard for S. The wide range of S concentrations at a given FeO* content in Puna Ridge glasses contrasts with the narrow range observed in MORB glasses. b) Dissolved S vs H_2O. Classification of samples and trends resulting from mixing of degassed and undegassed magmas and fractional crystallization are the same as in Figure 6.

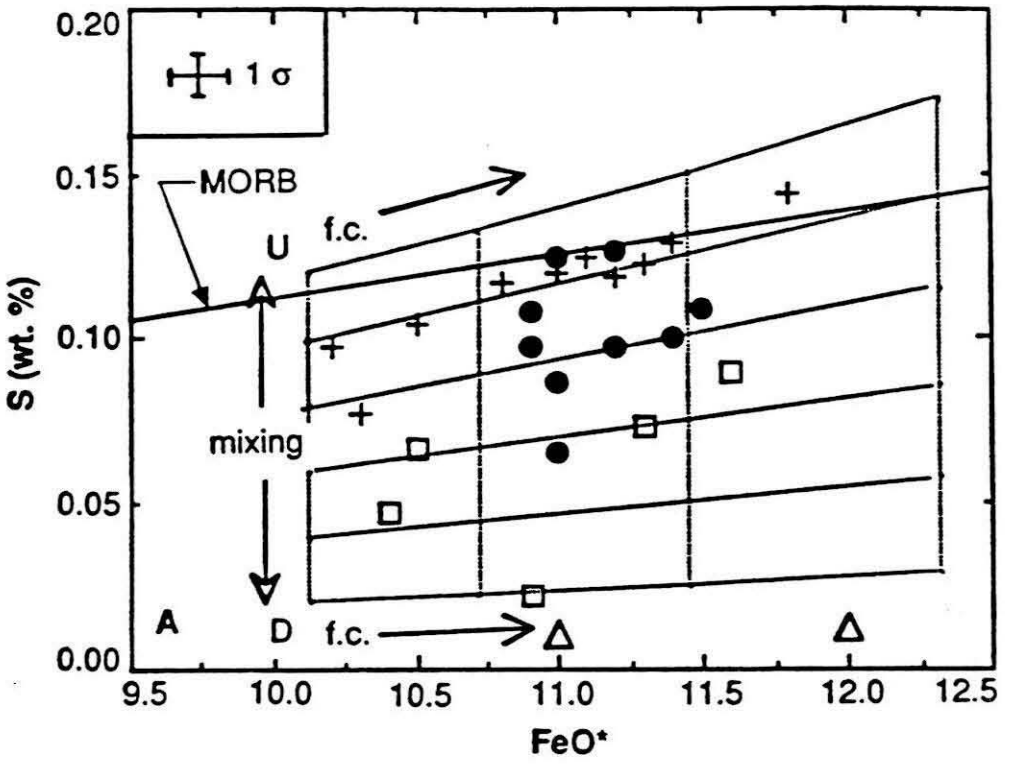
0.20
0.15
0.10
0.05
0.00
S (wt. %)
1 σ
MORB
U
f.c.
mixing
A
D
f.c.
9.5
10.0
10.5
11.0
11.5
12.0
12.5
FeO*

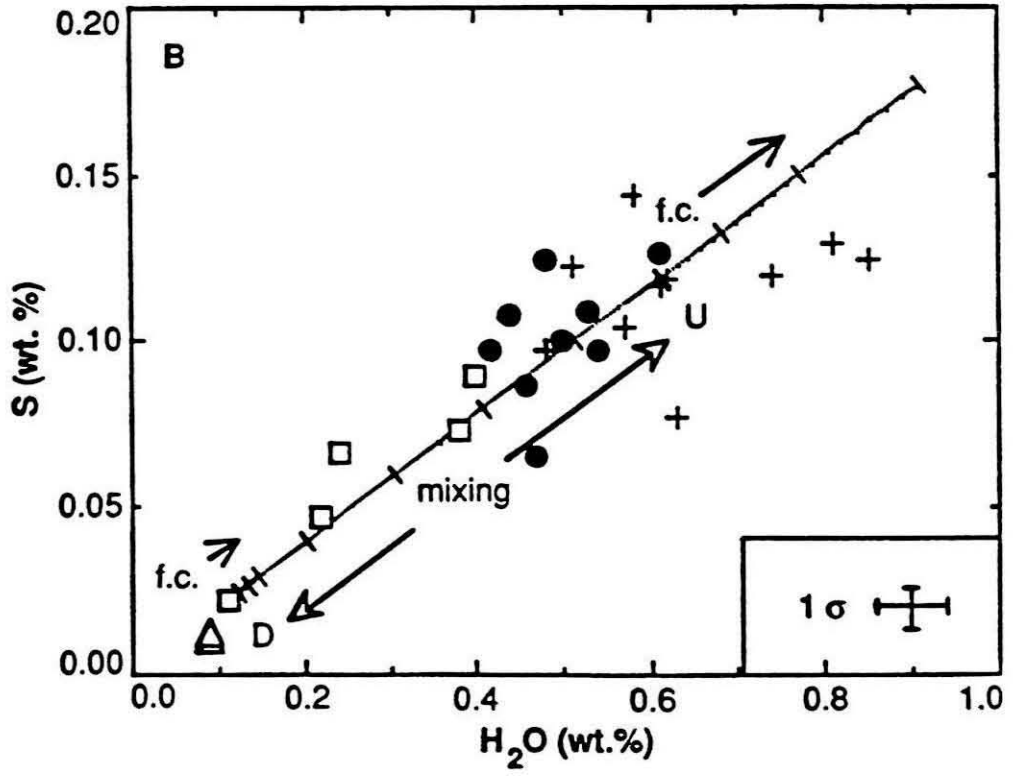
B
0.20
0.15
0.10
0.05
0.00
S (wt. %)
f.c.
U
mixing
f.c.
D
1 σ
0.0
0.2
0.4
0.6
0.8
1.0
H2O (wt.%)

FIGURE 7

8. Dissolved S contents in glass inclusions. Cross-hatched fields surround data from glassy rinds. a) S vs. MgO, b) S vs. FeO*.

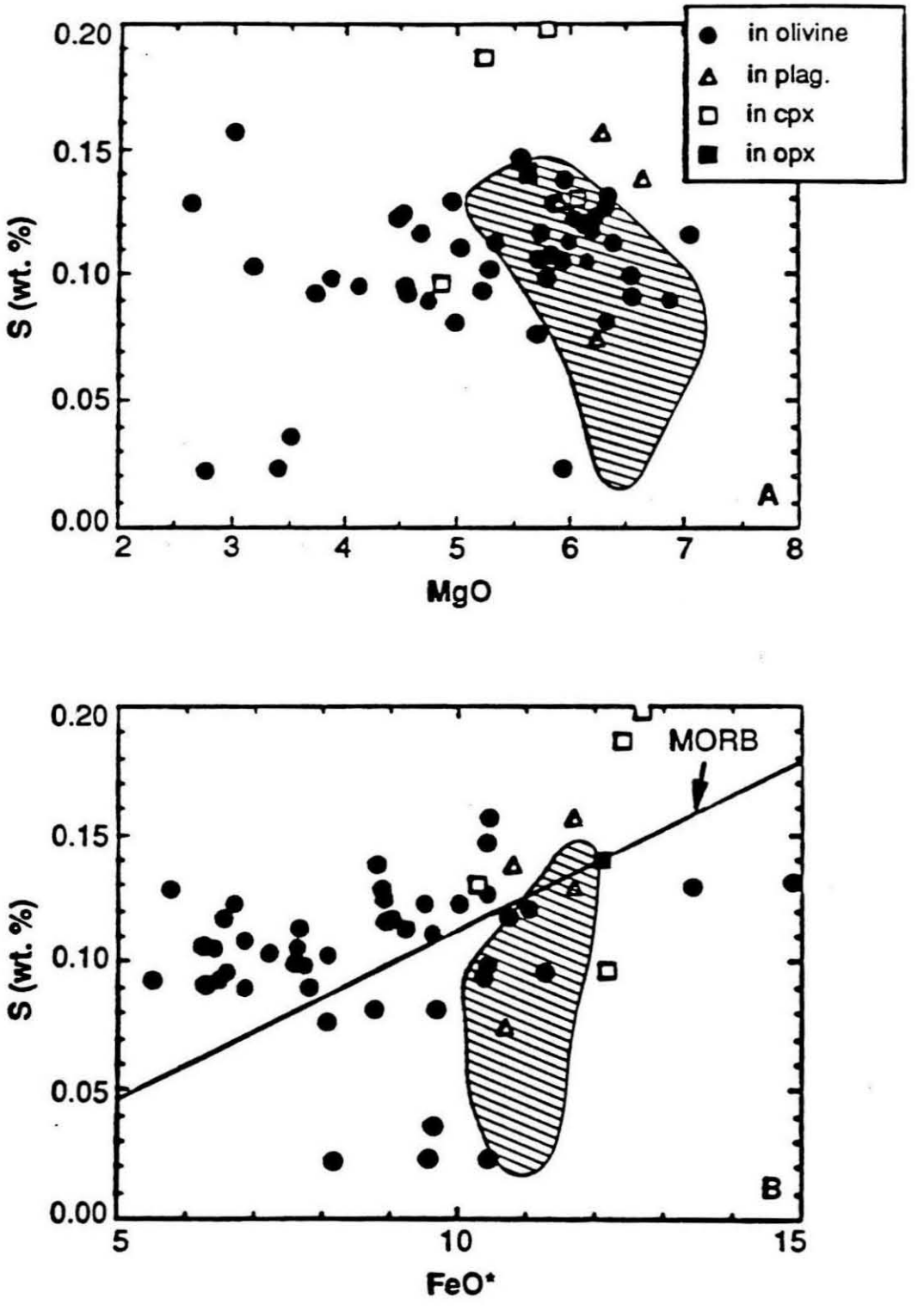
in olivine
in plag.
in cpx
in opx
S (wt. %)
0.20
0.15
0.10
0.05
0.00
2
3
4
5
6
7
8
MgO
A
MORB
S (wt. %)
0.20
0.15
0.10
0.05
0.00
5
10
15
FeO*
B

FIGURE 8

9. Schematic cross-section of Kilauea Volcano (vertical exaggeration 5:1) illustrating our model for the degassing history of Puna Ridge tholeiites. Most magmas erupted along the Puna Ridge result from mixing of a relatively volatile-rich, undegassed component with magmas that experienced low pressure (perhaps subaerial) degassing during which substantial H_2O, S, and CO_2 were lost. The gradient in stippling density from light to dark represents a decrease in the proportion of degassed component with depth in the summit magma reservoir. Olivine, clinopyroxene, and plagioclase are removed from this mixture to generate a residual liquid. Further degassing, principally of CO_2 for samples erupted deeper than 1000 m, occurs during eruption on the seafloor.

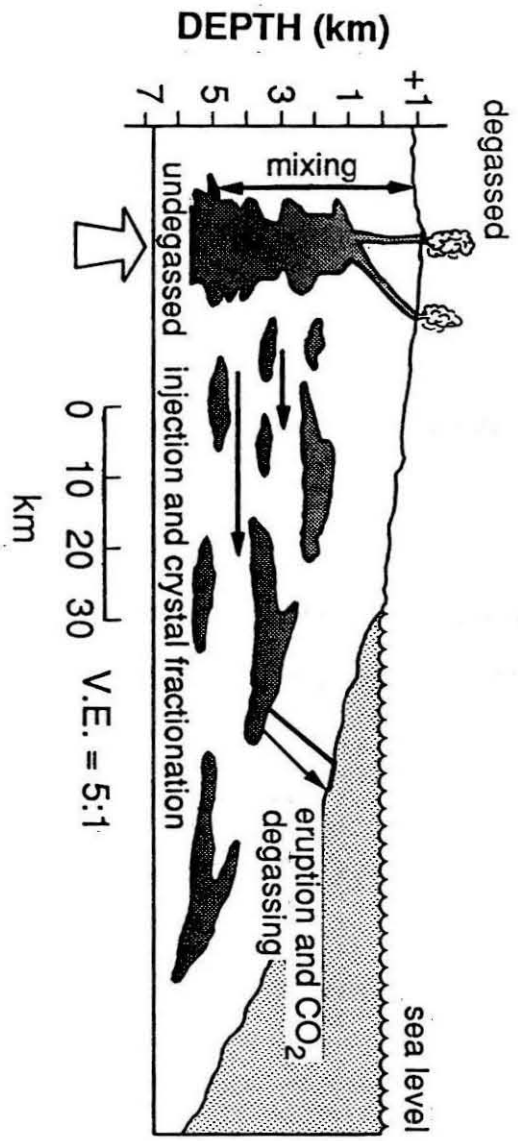
DEPTH (km)
+1
1
3
5
7
degassed
mixing
undegassed
injection and crystal fractionation
eruption and CO_2 degassing
sea level
0 10 20 30
km
V.E. = 5:1

FIGURE 9

10. δD vs. dissolved H_2O. Open squares: Data of Kyser et al. (1984) on glassy whole-rock samples; Filled circles: H_2O concentrations of Kyser et al. (1984) corrected for mass fraction of phenocrysts; Filled triangles: Data of Garcia et al. (1989) on glass separates from Puna Ridge samples. Gridlines for mixing and fractional crystallization model are the same as in Figure 6. The isotopic composition of the degassed end member (D; H_2O = 0.25 wt. %, δD = -80‰.) was calculated from the undegassed end member (U; H_2O = 0.62 wt. %, δD = -35‰) using a Rayleigh fractionation model and a fractionation factor of 1.050.

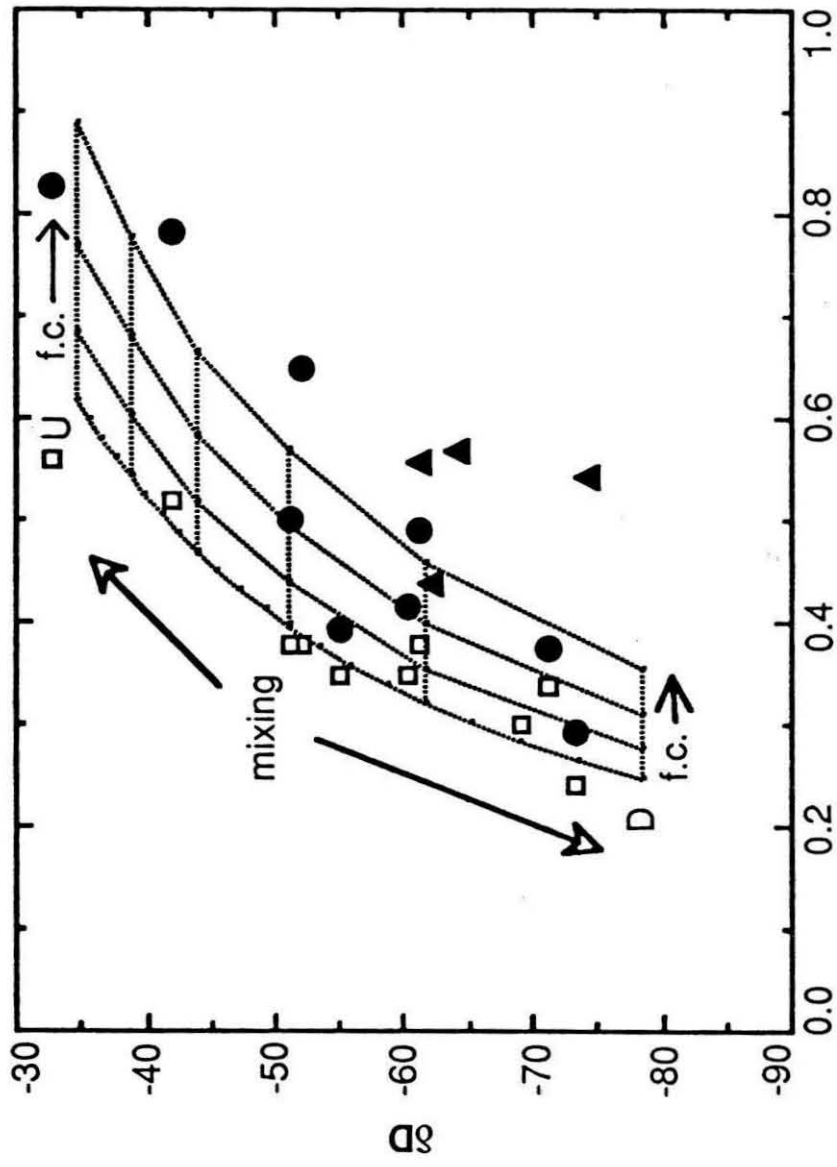

FIGURE 10

11. Comparison of H_2O contents in lavas from Kilauea (symbols; this study), Mauna Loa and Loihi (cross-hatched fields; Garcia et al. 1989). Open squares: low-H_2O/K_2O samples with H_2O/K_2O ratios less than or equal to 0.70; Filled circles: moderate-H_2O/K_20 samples with $0.70< K_2O/H_2O<1.0$; Crosses: high-H_2O/K_2O samples with H_2O/K_2O greater than or equal to 1.0. H_2O contents in samples from Loihi are higher than those from Mauna Loa, and are similar to the H_2O concentrations in our high H_2O/K_2O samples.

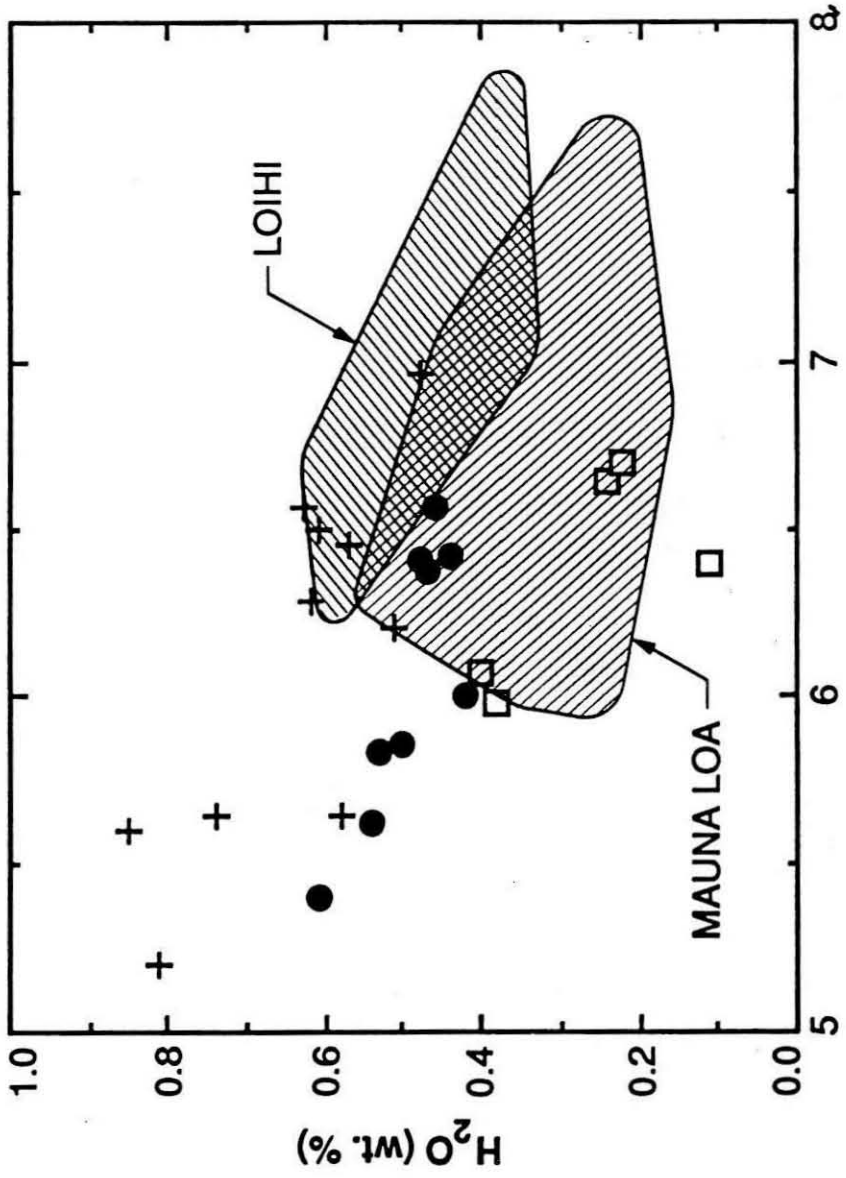

FIGURE 11

Post publication note:

The CO_2 concentrations measured in Puna Ridge glasses are shown below along with the trends calculated from closed system degassing models of basaltic melts (Chapter 1) with initial water contents ranging from 0.1 to 1.0 wt.%. Most data fall within the envelop generated by the upper, $H_2O°$=0.1 wt.% and the lower, $H_2O°$=1.0 wt.% curves. The closed system degassing curve for a melt having $H_2O°$ of 0.6 wt.% (middle dark line) has the same slope as the calculated best fit through the data and the origin (42 ppm/km).

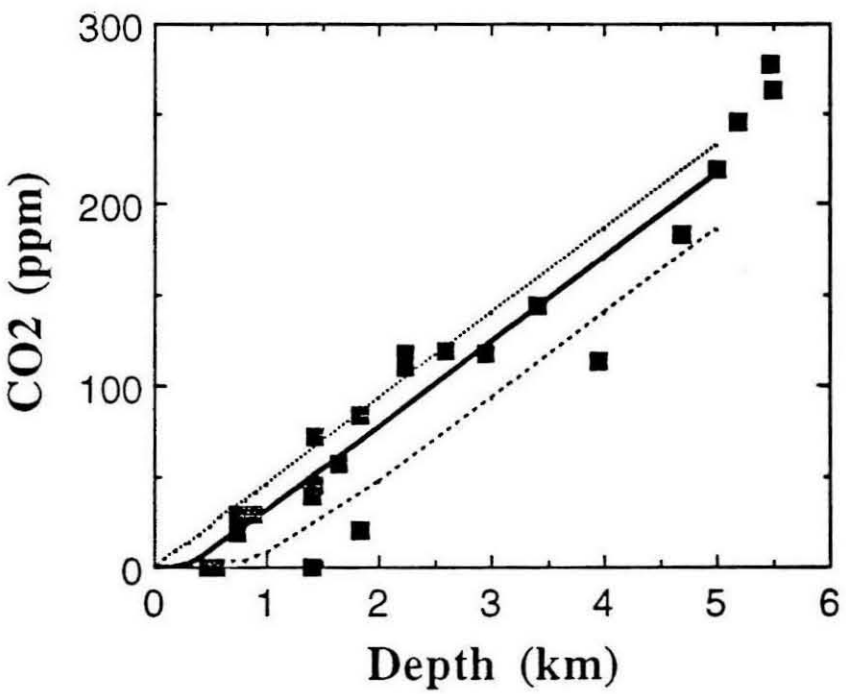

The section in Chapter 3 on δD and H_2O modelling assumes that the linear correlation between δD and H_2O observed by Kyser and O'Neil (1984) is a primary (magmatic) feature of these samples. This assumption leads to our conclusion that the mantle may be as light as -30 to -40‰. Based on the H_2O speciation data (Chapter 1), I

now believe that the glasses with the highest δD values (>50‰) may have had water added by diffusion at low temperatures, and that the correlation observed by Kyser and O'Neil (1984) is a secondary, not a primary feature. If this is true, then the mantle is about -60 to -80‰ and the fractionation factor between melt and vapor for hydrogen isotopes is probabley smaller than assumed in our modelling.

APPENDIX I

An internally-heated, rapid-quench, high pressure vessel

John R. Holloway*, Jackie Eaby Dixon+, and Alison R. Pawley*

*Departments of Chemistry and Geology, Arizona State University, Tempe 85287

+Division of Geological Sciences, California Institute of Technology, Pasadena 91125

Abstract

A pressure vessel and furnace system were designed for "rapid-quench" operation while maintaining the advantages of sample size and hydrostatic loading inherent in an internally-heated, argon-medium vessel (IHPV). The rapid-quench is achieved using the "quench wire" technique common to atmospheric-pressure, quench furnaces; the sample capsules fall from their position in the furnace hot-spot into room temperature argon gas at the bottom of the vessel chamber. The quench rate is several hundred °C sec^{-1} compared to a rate of about 3 °C sec^{-1} in conventional IHPV's. The system operates at temperatures up to at least 1300 °C and pressures up to 1500 bars, conditions specifically chosen to study solubilities of H_2O, CO_2, and other volatiles in low viscosity silicate melts which have shown severe quench effects in IHPV's having "normal" quench rates. Loading and unloading the pressure system is relatively simple and fast.

Introduction

Many phase equilibrium studies are hampered by the inability to "quench in" the chemical and structural identity of one or more phases existing at the pressure - temperature conditions of the experiment. The problem is most prevalent in carbonate, sulfide, and low-viscosity silicate liquids, and in supercritical fluids. The most obvious quench effect in liquids is the formation of quench crystals or the overgrowth of quench rims on stable crystals. These effects can make it difficult or impossible to determine the chemical composition of the stable liquid. Quench effects in supercritical fluids may cause changes in their bulk

composition by precipitation of solids, or may cause changes in abundance of species due to homogeneous reactions. The degree to which a high pressure - temperature assemblage is preserved depends on the quench rate of the experimental apparatus and the properties of the system under study. The quench rate varies widely among the apparatus types commonly used in experimental petrology (Holloway and Wood, 1988). Piston-cylinder and one-atmosphere quench furnaces have relatively high rates while internally-heated and cold-seal pressure vessels have much lower quench rates. The quench rate of cold-seal vessels was dramatically improved by the introduction of rapid-quench systems, first by Rudert et al. (1976), and with recent improvements by Ihinger (1991). Compared to cold-seal vessels, IHPV's offer advantages of higher temperature operation at a given pressure, and generally of larger sample size. However, the slow quench rate of IHPV's has made them unacceptable for studies such as solubility of H_2O in basaltic liquids because the liquid often forms quench crystals. The formation of quench crystals may change the bulk H_2O content of the quench crystal + glass assemblage representing the stable liquid, and it certainly prevents use of analytical techniques such as infrared spectroscopy which rely on the presence of a glassy sample to quantitatively determine dissolved H_2O content. The purpose of this paper is to describe the design and operation of an IHPV which allows quench rates about two orders of magnitude greater than obtainable with conventional designs.

Design objectives

In addition to the primary criterion that the system should obtain the greatest feasible quench rate, several other desired design features were identified. These were: a maximum operating temperature greater than the liquidus of primary basaltic compositions; a stable, isothermal, hot-zone longer than the length of the

sample capsules; a maximum pressure high enough to achieve the solubility range-coverage desired; and finally, ease of operation.

Exploratory designs were tested in an existing IHPV with a 5 cm inside diameter and a 35 cm working length. A furnace consisting of two independently powered resistance elements had an inside diameter of 1.6 cm. The vessel is operated with its long axis vertical, so the furnace elements are positioned one above the other. The "rapid quench" modification is described in detail below. It is based on the quench wire design used in one atmosphere quench furnaces (Shepherd et al., 1909; Osborn and Schairer, 1941), the only difference being the placement of the quench assembly *inside* the IHPV. The quench occurs when the sample drops from the hot spot of the furnace to the bottom of the vessel where the argon was determined to be at room temperature (20-27 °C) by a thermocouple placed at the point where the capsule comes to rest. In this design an open space exists between the sample and the bottom of the vessel to allow the sample to drop. Tests were made at a temperature of 1100 °C from pressures ranging from 500 bars to 5 kbar. It was found that at pressures of up to about 2 kbar the temperature gradient over a 4 cm length was within ±15 °C and stable. At higher pressures severe aperiodic temperature oscillations occured and became larger as pressure increased. The oscillations could not be reduced by changes in the temperature controller settings, nor by changes in the proportion of power between the upper and lower furnace elements. These oscillations were eliminated when the open space below the samples was filled with a solid ceramic rod, and so we infer that they are the result of strong convection of argon gas in the open column. The conclusion from the preliminary tests was that the rapid

quench design would work at pressures below 2 kbar, but that the temperature oscillations precluded operation at higher pressures.

Design

Vessel

An overall schematic of the vessel, furnace and quench assembly is shown in Fig. 1. Because of the upper pressure restriction caused by the temperature oscillations, a 2 kbar operating pressure was chosen. The diameter of the furnace used in the preliminary tests was satisfactory, but we choose a slightly larger vessel inside diameter to allow a small increase in the size of the hole below the sample capsules. The vessel (manufactured by the High Pressure Equipment Co.) is a single-end design with a 5.72 cm ID, a working length of 30 cm, and a 15 cm OD. It is made of AISI 4340 steel heat-treated to 35 on the Rockwell 'C' scale. The vessel was fitted for water cooling by winding 0.96 cm ID copper tubing on the OD of the vessel immediately after coating the vessel with a 3 mm layer of aluminum-filled epoxy cement. The vessel was permanently mounted in a vertical position, open end facing down, so that the open end is at a height of about 1.5 m above the floor. The pressure inlet to the vessel is through its closed end.

Closure-head

The pressure seal on the closure-head is a simple inverted bridgeman type with a rubber o-ring backed by a stainless steel wedge ring (Holloway, 1971). The closure-head contains two lead-throughs for furnace power capable of carrying currents of 25 amps each, and five low-power lead-throughs for thermocouples and the quench-wire electrode. All low-power lead-throughs consist of a wire onto which a tool steel cone is silver soldered. The wires are copper for the

quench electrode lead-through, platinum-compensated for one thermocouple lead-through, and $PtRh_{10}$-compensated for the other three thermocouple lead-throughs. The thermocouple leass and cones are electrically insulated from the head with heat-shrink thermoelastomer plastic tubing. There are three mounting holes for furnace support rods.

Furnace

The furnace is shown schematically in Fig. 1. An outer stainless steel tube has an OD of 5.7 cm, a length of 23 cm, and a wall thickness of 1.3 mm. The furnace has an ID of 2.00 cm. Each of the two windings are about 9 cm in length. The samples are positioned about 1 cm below the boundary between the two windings.

Two winding materials are used, either a 1.02 mm diameter nickle alloy with approximate composition Ni 76 wt %, Cr 16, Fe 8, Mn 0.5, Ti 0.35, Al 0.25 (Kanthal A-1), or 0.5 mm diameter $PtRh_{30}$ alloy. The nickle alloy works well at temperatures of up to 1200 °C, and the Pt alloy is used at higher temperatures.

The furnace ceramic used depends on the element type: for Ni alloy elements the ceramic is a hydraulic-setting type of approximately $CaSiO_3$ composition (Saureisen #75), and in the Pt alloy furnaces a castable alumina-based ceramic (Ceramacast 510, Aremco Products) is used.

Thermocouples

Three Pt-PtRh10 thermocouples are used. They are positioned at three different heights in the hot zone of the furnace (in early experiments at 1200 °C up to five sheathed, type K thermocouples were used to determine the optimum position for the samples.) The three thermocouples share a common negative lead-through to

minimize the number of lead-throughs required. Two-hole thermocouple ceramic insulators (99.9% Al_2O_3) are used to support and electrically insulate the thermocouples.

Quench assembly

The quench assembly is shown schematically in Fig. 1 and details of the quench wire and capsule holder are shown in Fig. 2. The assembly consists of a set of 1.65 cm OD ceramic pieces (Aremcolox 502-1400, Aremco Products), each containing a central 7.1 mm quenching hole and five 1.6 mm holes for the three thermocouples and two quench-wire electrodes. The quench electrodes are made of 0.7 mm Pt wire. One is grounded to the closure-head and the other connected to the copper wire lead-through.The quench wire is isolated from the capsule clamp wire by a thin piece of two hole thermocouple ceramic. Use of the separator minimizes accidental welding of one end of the quench wire to the capsule clamp wire (which is the most usual cause of a failed quench). The capsule clamp is fabricated from a piece of cast Pt rod and provides an easy mechanism for holding the capsule without damaging it.

Operation

Procedure

Setting up an experiment involves hanging the sample capsule on the quench wire, tying the quench wire to the electrodes, and attaching the furnace in place over the quench assembly. The entire furnace/closure-head assembly is then inserted into the vessel. The simple inverted Bridgeman (o-ring) seal allows the closure to be inserted into the vessel by hand.

The run is brought to a starting pressure about 60% of the desired pressure before heating. Power is then applied and temperature increased to set-point over a period of about 20 minutes. The experiment is terminated by connecting an 80000 μF capacitor charged to about 35 volts to the quench wire electrodes. This explosively fuses the quench wire allowing the capsules to fall to the bottom of the quench assembly. A microphone is attached to the bottom exterior of the vessel and its amplified output allows audio confirmation that the capsule has fallen. The power to the furnace is then switched off and the furnace allowed to cool to room temperature.

After bleeding off the argon gas to atmospheric pressure the closure nut is removed and the closure-head/furnace assembly removed by hand from the vessel. Due to the moderate pressures used, the closure seal components have long lifetimes, the rubber o-rings need replacing after 10-20 runs and the stainless steel wedge rings last for up to 100 runs.

Hydrogen Control

For nominally hydrogen-free experiments such as those using fluids in the C - O system (Pawley and Holloway, 1991), pure argon gas is used as the pressure medium. In samples with hydrogen as a component, H_2 fugacity is controlled by using premixed hydrogen-argon gas, following Joyce and Holloway (1991). We have noted that the vessel has a memory effect when switching from argon containing relatively high H_2 to pure argon; a significant amount of hydrogen is observed in the nominally pure argon during a run, as evidenced by high H_2O contents in quenched basaltic glasses. The amount of hydrogen in subsequent pure argon runs is very low. This suggests that a significant amount of hydrogen

dissolves in the components of the pressure system exposed to argon, as noted by Joyce and Holloway (1991).

Furnace Conditions

The optimal proportions of power to the windings are 50% upper and 50% lower. The power consumed at 1200 °C ranges from 400 watts at 200 bars to 500 watts at 1500 bars.

The temperature gradients vary between furnaces, ranging from 0 to 20 °C cm^{-1} over a 1 cm sample length.

Temperature oscillations are on the order of ± 1 °C.

Quench Rate

Use of this system results in an isobaric quench in which the capsule drops from a hot region of relatively low argon density to a cold region of considerably higher argon density (actually there is a small change in pressure observed when the capsule falls due to the displacement of cold argon into hotter regions.) Fig. 3 shows argon density at 25° and 1200 °C as a function of pressure.

The quench rate in this system is difficult to measure directly. We have observed that hydrous basaltic liquids which did not quench to glasses in a conventional IHPV do form excellent glasses in the rapid quench system (Dixon et al., unpublished) demonstrating that the quench is faster in the latter system. Another approach is to calculate the quench rate using a conductive cooling model (see Carslaw and Jaeger, 1959, p. 199). We assume that the argon convects the heat away from the cooling capsule and therefore maintains a

constant temperature of about 25 °C at the outer contact of the capsule. We are most interested in the rate of cooling in the temperature interval between the run temperature (1200 °C) and the glass transition T for the sample. For a liquidus temperature of 1150 °C, the glass transition temperature is about 850-900 °C (Uhlmann and Onorato, 1979), but we have assumed a more conservative value of 700 °C. We can ignore the latent heat of crystallization because the melt is quenching to glass. Also we can neglect the effect of cooling the outer platinum capsule because the thermal diffusivity for platinum (0.25 cm sec^{-1}) is much greater than that for silicate melts (0.01 cm sec^{-1}). With these values, the time needed for the center of a cylinder having a radius of 0.25 cm to reach the glass transition temperature is about 1 sec, resulting in a quench rate of about 500 °C sec^{-1} at the center of the capsule. Though the exact quench rate is a function of time and distance from the capsule wall, we are confident that we have achieved quench rates two orders of magnitude faster that those obtained in conventional internally-heated pressure vessels.

Acknowledgements

This research was supported by NSF grant OCE-88-20131 and NASA grant NAGW-2221. We thank Gary Lofgren and Richard Wendlandt for helpful reviews and David Joyce for helpful discussions.

References

Carslaw, H. S., and Jaeger, J. C. (1959) Conduction of heat in solids, 510 p. Oxford University Press, Oxford.

Dixon, J. E., Stolper, E. S., and Holloway, J. R. (1991) Solubilities of water and carbon dioxide in basaltic magmas. Geological Society of America Abstracts with Programs, 23, A93.

Holloway, J. R. (1971). Internally heated pressure vessels in G. C. Ulmer and H. E. Barnes, Ed., Research Techniques for High Temperature and Pressure, p. 217-257. Springer-Verlag, New York.

Holloway, J. R. (1987) Igneous fluids, in Thermodynamic Modelling of Geological Materials: Minerals, Fluids and Melts. Reviews in Mineralogy, 17, 182-186.

Holloway, J. R., and Wood, B. J. (1988) Simulating the Earth: Experimental Geochemistry, 196 p. Unwin-Hyman, New York.

Ihinger, P. (1991) An experimental study of the interaction of water with granitic melt, Ph. D. Dissertation, California Institute of Technology.

Joyce, D. B., and Holloway, J. R. (1991) Experimentally determined activity-composition relations for H_2O in C-O-H-NaCl fluids by the H_2O fugacity buffer technique. Geological Society of America Abstracts with Programs, 23, A52.

Osborn, E. F., and Schairer, J. F. (1941) The ternary system pseudowollastonite - akermanite - gehlenite. American Journal of Science, 234, 715-763.

Pawley, A. R., and Holloway, J. R. (1991) Experimental study of the solubility of CO + CO2 in basalt, with applications to early atmosphere/magma ocean equilibria. Lunar and Planetary Science Conference Abstracts, 22, 1043-1044.

Rudert, V., Chou, I., and Eugster, H. P. (1976) Temperature gradients in rapid-quench cold-seal pressure vessels. American Mineralogist, 61, 1012-1015.

Shepherd, E. E., Rankin, G. A., and Wright, F. E. (1909) The binary systems of alumina, with silica, lime and magnesia. American Journal of Science, 33, 293-333.

Uhlmann, D. R., and Onorato, P. I. K. (1979) A simplified model for glass formation. Proceedings of the 10th Lunar and Planetary Science Conference, 10, 375-381.

Figure 1. Schematic cross-section of the rapid quench vessel. The ceramic insulators in the furnace interior are not shown here, but are shown in Fig. 2.

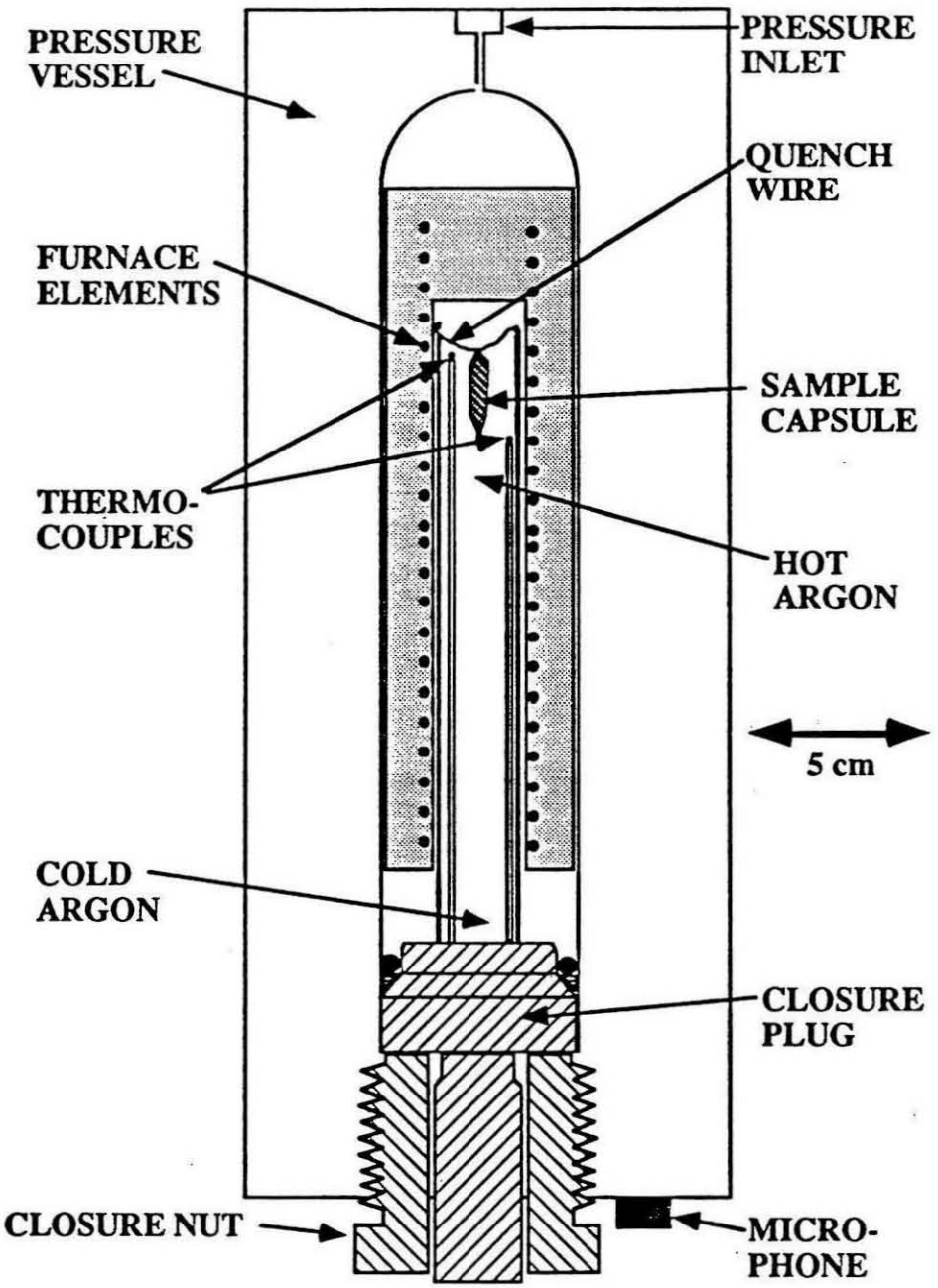
PRESSURE VESSEL
PRESSURE INLET
QUENCH WIRE
FURNACE ELEMENTS
SAMPLE CAPSULE
THERMO-COUPLES
HOT ARGON
5 cm
COLD ARGON
CLOSURE PLUG
CLOSURE NUT
MICRO-PHONE

Figure 1

Figure 2. Detailed views of the quench assembly. **a**. Plan view. **b**. Vertical cross-section.

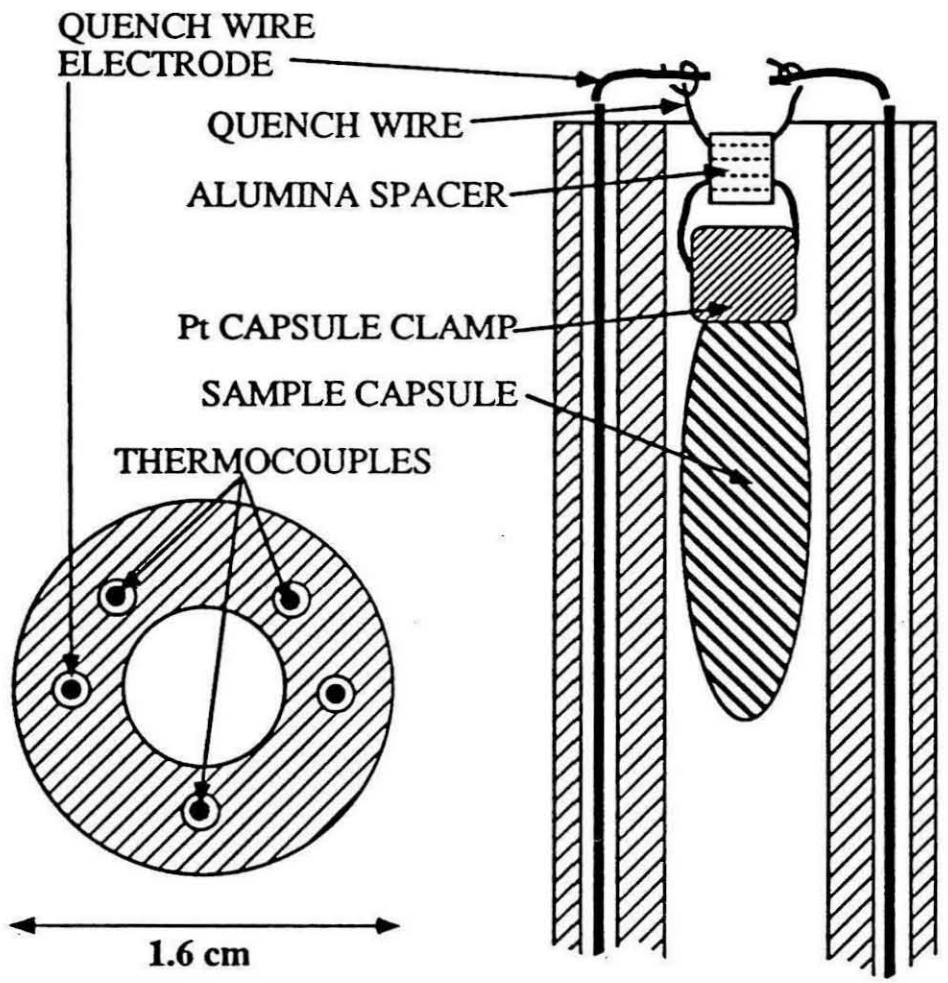
QUENCH WIRE
ELECTRODE
QUENCH WIRE
ALUMINA SPACER
Pt CAPSULE CLAMP
SAMPLE CAPSULE
THERMOCOUPLES
1.6 cm

Figure 2

Figure 3. Variation in the density of argon as a function of pressure along the 25° and 1200°C isotherms. Calculated using a Redlich-Kwong equation of state (Holloway, 1987) with *a* and *b* parameters of 9.54 x 10^6 bar•cm^6•$deg^{1/2}$and 21.6 cm^3, respectively.

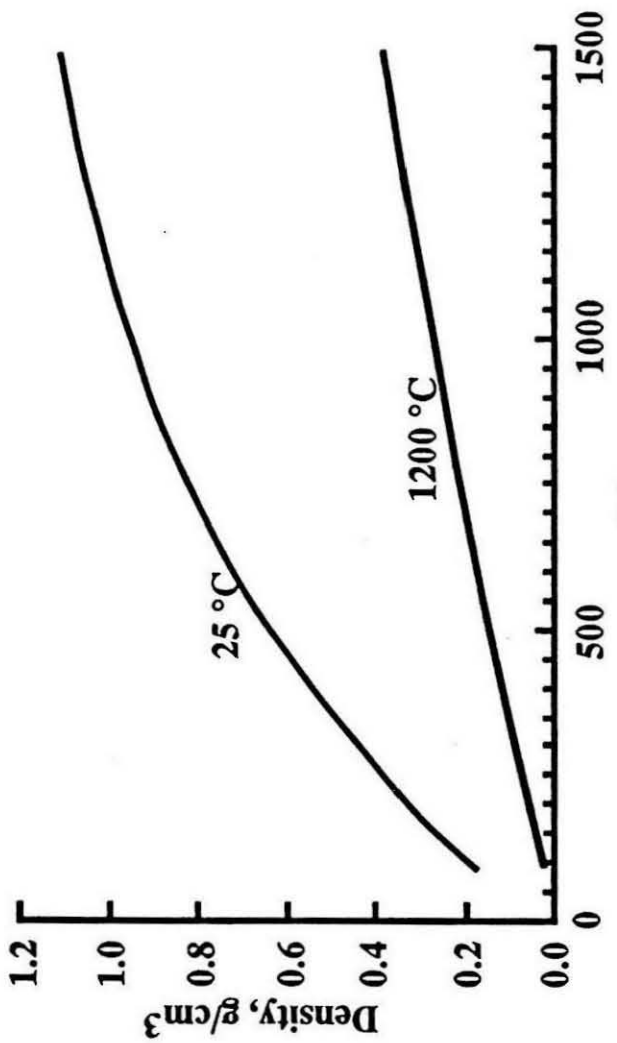
Density, g/cm3
1.2
1.0
0.8
0.6
0.4
0.2
0.0
0
500
1000
1500
P bars
25 °C
1200 °C

Determination of the molar absorptivity for dissolved carbonate in basanitic glass

Jacqueline Eaby Dixon

Division of Geological and Planetary Sciences, California Institute of Technology, Pasadena, California 91125

and

Vivian Pan*

Department of Geology, Arizona State University, Tempe, Arizona 85287

Submitted as a Letter to American Mineralogist

Abstract

Basanitic glasses with known dissolved carbon concentrations have been analyzed using infrared spectroscopy. Carbon is dissolved as carbonate complexes in the glass, giving rise to absorption bands at 1525 and 1425 cm^{-1}. No carbon was observed to be dissolved as molecular carbon dioxide in the glass. Molar absorptivities of 282 ± 6 l/mole-cm were determined for both the 1525 and 1425 cm^{-1} absorption bands. An integrated molar absorptivity of 60,000 ± 700 l/mole-cm^2 was determined using the integrated area under the doublet. These values are about 20% lower than those determined for tholeiitic glasses.

Introduction

Infrared spectroscopy, when accurately calibrated for the composition of interest, can be used as a quantitative tool for measuring the dissolved water and carbon dioxide contents in silicate glasses. Recent studies using infrared spectroscopy to measure the concentrations and speciation of dissolved volatiles in tholeiitic basaltic (Dixon et al., 1988; Dixon et al., 1991) and rhyolitic (Newman et al., 1988) glasses and glass inclusions have shown that these data, combined with accurate knowledge of the solubilities at the pressures of interest, provide powerful constraints on the degassing histories of magmatic systems. Discovery of fresh alkalic glasses on submarine volcanic rocks erupted along the Hawaiian Arch (Clague et al., 1990) has motivated us to extend the calibration of the infrared technique from tholeiitic to more alkalic compostions. In order to use the intensities of infrared absorptions to determine concentrations, the molar absorptivity, or the proportionality constant between the measured absorbance and the concentration (also referred to as the extinction coefficient), for the absorbance band of interest must be known. Molar absorptivites for carbon dissolved as carbonate and molecular carbon dioxide (when present) have been determined in previous studies for

Ca-Mg silicate (including tholeiite, diopside, and anorthite glasses) (Fine and Stolper, 1986) and Na-aluminosilicate (Fine and Stolper, 1985) glasses. This study presents new molar absorptivity determinations for carbon dissolved as carbonate ion complexes in basanitic glass compositions.

Analytical Technique

Glass chips having known concentrations of dissolved carbon were doubly polished to a thickness of about 30 to 60 μm in order to have the absorbances on scale. The position and size of the beam were controlled by placing each glass chip over a 200 μm aperture. Transmission infrared spectra in the 4000-1200 cm^{-1} (2.5 to 8.3 μm) range were collected using the microchamber on a Nicolet 60SX FTIR spectrometer, a globar source, a KBr beamsplitter, a HgCdTe detector, and a mirror velocity of 1.57 cm/s. Typically, 4096 scans were collected for each spectrum. The spectrum of a decarbonated basanite sample (1297D) was subtracted from the sample spectra as a background correction. Absorbance measurements were made on reference subtracted spectra. Determination of the molar absorptivities was done through Beer-Lambert law calibration (see caption to Fig. 2, and discussions in Stolper, 1982; Fine and Stolper, 1985; Fine and Stolper, 1986). The thickness, or path length, is measured by a digital micrometer with a precision of ±1-2 μm. The glass density was calculated to be 2950 g/l using the Gladstone-Dale rule and the Church-Johnson equation as described by Silver (1988).

Characterization of Glasses

Glasses were prepared by quenching CO_2-saturated basanitic melts generated under P-T conditions ranging from 1-20 kbar and 1200-1550°C. In general, the experimental procedures were the same as those in Pan et al. (1991). The starting material is a basanite from Peridot Mesa, San Carlos Arizona (Table 1). The CO_2 source of the samples

(except 3048-7) was a mixture of siderite, calcite, magnesite, and Na_2CO_3. The carbonates were mixed with proportions of reagent grade Al_2O_3 and SiO_2 to yield the correct stoichiometry of the original basanite. Run 3048-7 contained silver oxalate as the CO_2 source. Pan et al. (1991) showed that there was an insignificant effect of using the two different CO_2 sources. The samples were placed in Fe-saturated Pt capsules and runs were performed in a rapid-quench, internally heated gas vessel (3048-7 only) (Holloway et al., 1991) or a non-endloaded piston cylinder apparatus.

The bulk carbon values were obtained using a LECO™ JR-12 Carbon Analyzer. Carbon analysis was done on 18-28 mg of glass hand-picked to be free of bubbles. Analytical precision was determined to be ±0.006 wt.% carbon. The accuracy of these concentrations was confirmed by ion probe and found to be within 10% of the LECO™ measured values (Pan and Holloway, in prep.).

Results

A typical spectrum is shown in Figure 1. Absorbance data for each spectrum are reported in Table 2. All samples have absorptions at 1525 and 1425 cm^{-1} resulting from the ν_3 antisymmetric stretching of CO_2 dissolved as carbonate groups in the glass (Brey and Green, 1975; Sharma, 1979; Sharma et al., 1979; Mysen and Virgo 1980a; Fine and Stolper, 1986). The splitting between the two carbonate bands is 100 cm^{-1}, slightly larger than the 80 cm^{-1} observed for tholeiitic glasses (Fine and Stolper, 1986), but within the range observed for other Ca-Mg silicate glasses (Sharma, 1979; Sharma et al., 1979; Taylor, 1990). Absorbances at 2630 cm^{-1} were not observed, indicating that carbon does not dissolve in these glasses as molecular CO_2, consistent with observations for other Ca-Mg silicate glasses (Brey, 1976; Sharma, 1979; Sharma et al., 1979; Fine and Stolper, 1986; Taylor, 1990).

Absorbances normalized to 100 μm sample thickness are plotted against measured concentrations in Figure 2. There is a linear correlation that goes through the origin between absorbance and concentration using the peak heights of the 1425 and 1525 cm-1 absorbance bands and for the integrated absorbance of the doublet. Linear regression through the data and forced through the origin yields molar absorptivities of 282 ± 6 l/mole-cm for both the 1525 and 1425 cm^{-1} absorption bands and an integrated molar absorptivity of 60,000 ± 700 l/mole-cm^2 using the integrated area under the doublet.

Discussion

Fine and Stolper (1986) determined the molar absorptivity for carbonate dissolved in Ca-Mg silicate glasses (including tholeiite, diopside, and anorthite glasses) to 375 l/mole-cm for both the 1515 and 1435 cm^{-1} absorption bands and the integrated molar absorptivity to be 69,500 ± 700 l/mole-cm^2 using the integrated area under the doublet. Our values for basanite are 25% lower for the molar absorptivity and 14% lower for the integrated molar absorptivity. Pan et al. (1991) have confirmed the molar absorptivity of 375 l/mole-cm for tholeiite using carbon concentrations measured by LECO™ carbon analysis and ion probe, thus showing that the difference in molar absorptivity for tholeiite and basanite is not caused by a systematic bias in the analytical methods used to measure the carbon concentrations in glasses in this study and those in Fine and Stolper (1986).

In general, previous studies have found that the character of the carbonate bands in silicate glasses can be divided into two distinct compositional groups; such that NaAl silicate glasses (albite, jadeite, nepheline glasses) have splittings of about 200 cm^{-1} and molar absorptivities of 200 to 235 l/mole-cm,while CaMg silicate glasses (tholeiite, diopside, anorthite, sodamelilte, and ankerimite) have splittings of about 90 ± 10 cm^{-1} and molar absorptivity of 375 l/mole-cm. These differences are related to the environment of the dissolved carbonate in the silicate melt (see Taylor, 1990). Our

values for both the molar absorptivity and magnitude of splitting of the carbonate bands for basanite are intermediate between values for NaAl silicate glasses and CaMg silicate glasses. This is consistent with the fact that the basanite is richer in alkalies than the tholeiite studied by Fine and Stolper (1986), but the exact nature of the compositional dependence of the molar absorptivity requires more data on the molar absorptivities of other melt compositions covering a range in alkali/alkali earth ratios.

Conclusions

Molar absorptivities of 282 ± 6 l/mole-cm were determined for both the 1525 and 1425 cm^{-1} absorption bands in basanitic glass. An integrated molar absorptivity of 60,000 ± 700 l/mole-cm^2 was determined using the integrated area under the doublet. These values are about 20% lower than those determined for tholeiitic glasses.

Acknowledgements

We thank C. F. Lewis for performing the LECO™ analyses in Prof. C. B. Moore's laboratory at ASU. Experiments performed in J. R. Holloway's lab under NSF grant OCE-88-20131. Infrared spectroscopy work at Caltech performed under EAR-88-11406.

References

Brey, G. (1976) CO_2 solubility mechanisms in silicate melts at high pressures, Contributions to Mineralogy and Petrology, 57, 215-221.

Brey, G. and Green, D. H. (1975) The role of CO_2 in the genesis of olivine melilitite, Contributions to Mineralogy and Petrology, 49, 93-103.

Clague, D. A., Holcomb, R. T., Sinton, J. M., Detrick, R. S., and Torresan, M. E. (1990) Pliocene and Pleistocene alkalic flood basalts on the seafloor north of the Hawaiian islands, Earth and Planetary Science Letters, 98, 175-191.

Dixon, J. E., Stolper, E., and Delaney, J. R. (1988) Infrared spectroscopic measurements of CO_2 and H_2O in Juan de Fuca Ridge basaltic glasses, Earth and Planetary Science Letters, 90, 87-104.

Dixon, J. E., Clague, D. A., and Stolper, E. M. (1991) Degassing history of water, sulfur, and carbon in submarine lavas from Kilauea Volcano, Hawaii, The Journal of Geology, in press.

Fine, G., and Stolper, E. (1985) The speciation of carbon dioxide in sodium aluminosilicate glasses, Contributions to Mineralogy and Petrology, 91, 105-121.

Fine, G., and Stolper, E. (1986) Dissolved carbon dioxide in basaltic glasses: concentrations and speciation, Earth and Planetary Science Letters, 76, 263-278.

Holloway, J. R., Dixon, J. E., and Pawley, A. R. (1991) An internally-heated, rapid-quench vessel, American Mineralogist, submitted.

Mysen, B. O., and Virgo, D. (1980a) Solubility behavior of CO_2 in melts on the join $NaAlSi_3O_8$-$CaAl_2Si_2O_8$-CO_2 at high pressures and temperatures: a Raman spectroscopic study, American Mineralogist, 65, 1166-1175.

Newman, S., Stolper, E. M., and Epstein, S. (1986) Measurement of water in rhyolitic glasses: Calibration of an infrared spectroscopic technique, American Mineralogist, 71, 1527-1541.

Newman, S., Epstein, S., and Stolper E. (1988) Water, carbon dioxide, and hydrogen isotopes in glasses from the ca. 1340 A.D. eruption of the Mono Craters, California: Constraints on degassing phenomena and initial volatile content, Journal Volcanology and Geothermal Research, 35, 75-96.

Pan, V., and Holloway, J. R. Carbon dioxide solubility in basanitic magma, in prep.

Pan, V., Holloway, J. R., and Hervig, R. L. (1991) The pressure and temperature dependence of carbon dioxide solubility of tholeiitic basalt melts, Geochimica Cosmochimica Acta, 55,1587-1595.

Sharma, S. K. (1979) Structure and solubility of carbon dioxide in silicate glasses of diopside and sodium melilite composition at high pressures from Raman spectroscopic data, Carnegie Institite of Washington Year Book, 78, 532-537.

Sharma, S. K., Hoering, T. C., and Yoder, H. S. (1979) Quenched melts of akermanite compositions with and without CO_2 - characterization by Raman spectroscopy and gas chromatography, Carnegie Institute of Washington Year Book, 78, 537-542.

Silver, L. (1988) Water in silicate glasses, 310 p., Ph.D. thesis, California Institute of Technology, Pasadena, California.

Stolper, E. (1982) Water in silicate glasses: An infrared spectroscopic study, Contrib. Mineral. Petrol., 81, 1-17.

Stolper, E., and Holloway, J. R. (1988) Experimental determination of the solubility of carbon dioxide in molten basalt at low pressure, Earth and Planetary Science Letters, 87, 397-408.

Taylor, W. R. (1990) The dissolution mechanism of CO_2 in aluminosilicate melts - infrared spectroscopic constraints on the cationic environment of dissolved $[CO_3]^{2-}$, European Journal of Mineralogy, 2, 547-563.

TABLE 1. Composition Peridot Mesa Basanite, San Carlos

SiO_2	46.82
TiO_2	3.17
Al_2O_3	15.20
Fe_2O_3	0.86
FeO	11.21
MnO	0.23
MgO	9.06
CaO	8.22
Na_2O	4.33
K_2O	1.32
P_2O_5	0.27
Total	100.00

TABLE 2. Infrared data obtained in this study

Sample	CO_2 (wt.%)	Spec#	Band (cm-1)	Intensity (abs)	Band (cm-1)	Intensity (abs)	Area (cm-1)
3048-7	0.080670	1	1523	0.17111	1424	0.16000	35.6220
		2	1522	0.14091	1420	0.13864	27.9091
		3	1528	0.16984	1426	0.16190	34.4127
		4	1521	0.15323	1424	0.14677	30.0484
3048-11	2.4270	1	1530	4.7781	1424	4.7781	1035.6250
		2	1529	4.4656	1423	4.4469	957.5000
		3	1529	4.5967	1420	4.4900	950.3333
3048-13	2.1780	1	1524	4.1140	1431	4.1163	890.8163
		2	1526	4.3227	1425	4.3250	926.8182
		3	1526	4.1213	1423	4.0787	887.8723
3048-16	1.1770	1	1523	2.2956	1425	2.2533	467.3333
		2	1523	2.1909	1426	2.1386	444.5455
		3	1524	2.1702	1428	2.1191	437.8724
3048-15	1.7270	1	1524	3.2400	1426	3.2133	680.6667
		2	1526	3.3033	1425	3.2867	696.0000
		3	1524	3.0036	1424	2.9357	606.4286

Figure 1. Typical spectrum of basanite saturated with CO_2 in the frequency range of 2200 to 1200 cm-1 (5-8 μm wavelength). A reference spectrum of decarbonated basanite 1297 has been subtracted. Carbonate absorption bands are present at 1423 and 1529 cm^{-1}.

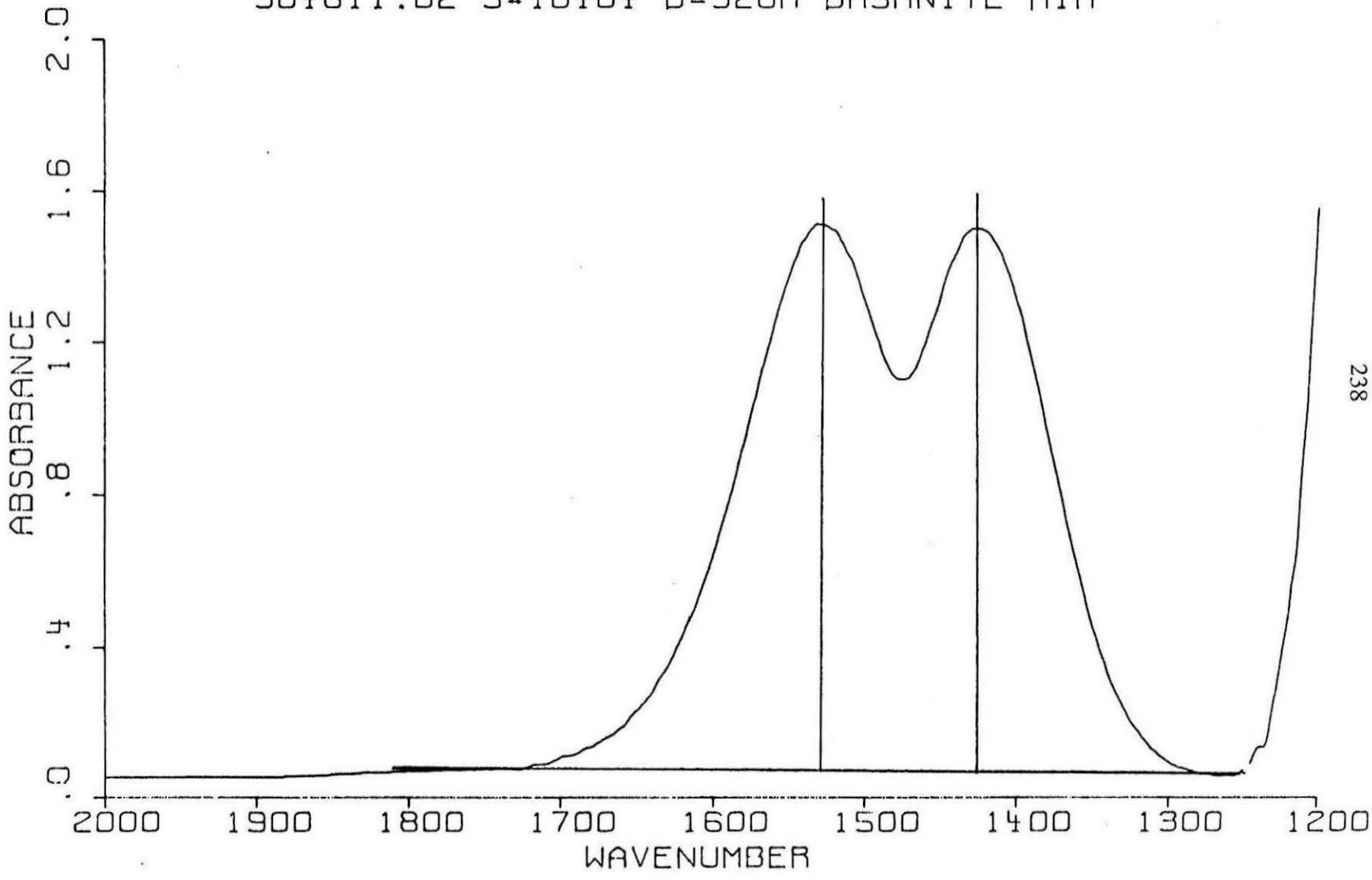
304811.02 S#10404 D=32UM BASANITE MIR
ABSORBANCE
.0
.4
.8
1.2
1.6
2.0
2000
1900
1800
1700
1600
1500
1400
1300
1200
WAVENUMBER
238

Figure 2. Measured carbon concentrations plotted vs. intensities of absorptions normalized to a sample thickness of 100 μm. A. Concentration vs. 1425 cm^{-1} absorbance. B. Concentration vs. 1525 cm^{-1} absorbance. C. Concentration vs. integrated molar absorbance. Concentrations are calculated using Beer-Lambert law:

$$c = \frac{MW \times Abs}{\rho \times d} \times \frac{1}{\varepsilon},$$

where MW is the molecular weight in g/mole, ρ is the glass density in g/l, and d is the sample thickness in cm. The slope of the line on a plot of concentration vs. measured absorbance normalized to 100 μm can be related to the molar absorptivity by:

$$\text{slope} = \frac{MW*10^4}{\rho * \varepsilon}.$$

The molar absorptivites were calculated using a glass density of 2950 g/l and MW of 44.01g/mole.

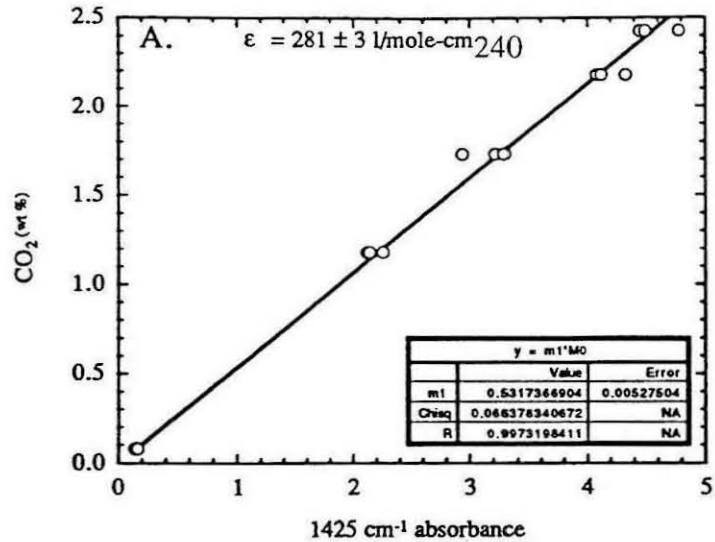
A.
ε = 281 ± 3 l/mole-cm
CO2 (wt %)
1425 cm-1 absorbance
y = m1*M0
Value Error
m1 0.5317366904 0.00527504
Chisq 0.066376340672 NA
R 0.9973198411 NA

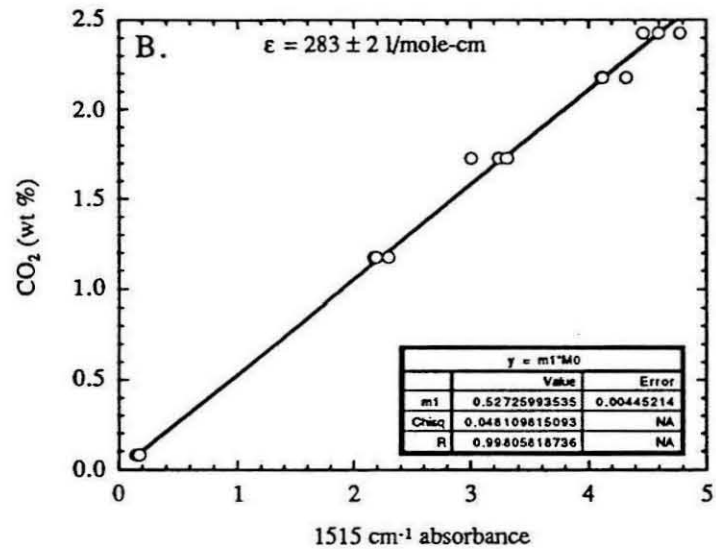
B.
ε = 283 ± 2 l/mole-cm
CO2 (wt %)
1515 cm-1 absorbance
y = m1*M0
Value Error
m1 0.52725993535 0.00445214
Chisq 0.048109815093 NA
R 0.99805818736 NA

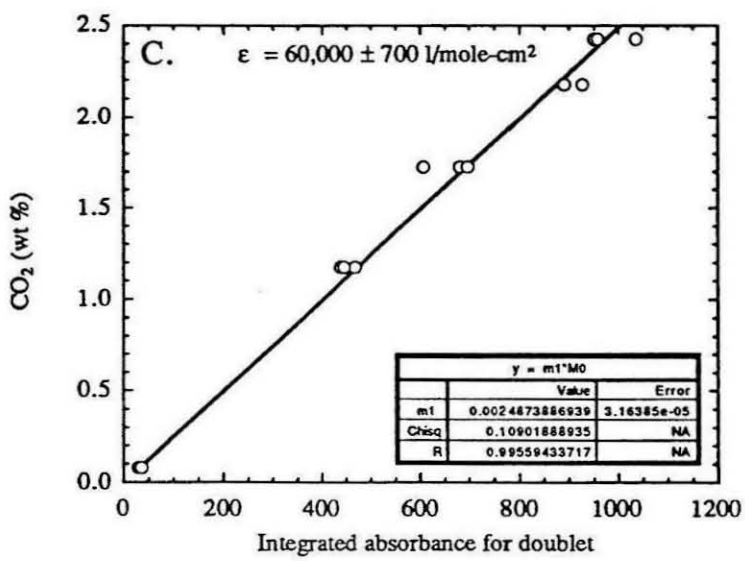
C.
ε = 60,000 ± 700 l/mole-cm2
CO2 (wt %)
Integrated absorbance for doublet
y = m1*M0
Value Error
m1 0.0024873886939 3.16385e-05
Chisq 0.10901888935 NA
R 0.99559433717 NA

Appendix 3

A Method for Calculating Degassing of Water and Carbon Dioxide from Basaltic Magma

Introduction

Degassing of water and carbon dioxide from basaltic magmas can be described using three independent, nonlinear equations describing mass balance, fractionation, and speciation of water in the melt. The analytical problem can be simplified by expressing the governing equations in terms of three coupled, linear, differential equations and solving using standard methods of matrix algebra. This approach is similar to one used to describe D/H fractionation during degassing of water from silicate melts (G. Miller and P. Dobson, personal communication) and has the advantage of allowing solution of both open and closed system degassing problems. The three governing equations and a method for their solution are discussed below. A list of variable definitions is given below.

Definition of Variables

CO_2^{Tot} initial number of moles of CO_2 in the melt

CO_2^m number of moles of CO_2 in the melt

H_2O^{Tot} initial number of moles of H_2O in the melt

H_2O^m number of moles of H_2O in the melt;

OH^m number of moles of OH in the melt

$H_2O^m_{mol}$ number of moles of molecular water in the melt

CO_2^v number of moles of CO_2 in the vapor

H_2O^v number of moles of H_2O in the vapor

X_i^m mole fraction of species i in melt (single oxygen basis);

$$= \frac{N_i^m}{N^m_{H_2O} + N^m_{CO_2} + N_O}, \text{ where } N_O = \frac{100\text{-wt\%}H_2O - \text{wt\%}CO_2}{36.594}$$

X_i^v mole fraction of species i in vapor

a_i^m activity of species i in melt

$a_i^{0,m}$ activity of species i in melt in equilibrium with vapor phase of pure i

f_i fugacity of i in the vapor

f_i^0 fugacity of pure vapor i

$V_i^{0,m}$ molar volume of i in the melt

f fraction of total volatiles remaining in melt (Eqn.1)

β CO_2/H_2O fractionation factor between vapor and melt (Eqn 9)

λ discriminates between open (λ=0) and closed (λ=1) system degassing

y fraction of H_2O present as OH (Eqn. 24)

Governing Equations:

1) Mass balance:

The equation of mass balance is defined in terms of f, the fraction of initial water and carbon dioxide remaining in the melt:

$$f = \frac{H_2O^m + CO_2^m}{H_2O^{Tot} + CO_2^{Tot}}. \qquad (1)$$

Water dissolved in a basaltic melt can exist as hydroxyl groups or as discrete molecules of water. When water enters the melt as hydroxyl groups, one molecule of H_2O reacts with a bridging oxygen to produce 2 hydroxyl groups; therefore, the mass balance equation for H_2O is:

$$H_2O^m = .5OH^m + H_2O^m_{mol}. \qquad (2)$$

Substitution of (2) into (1) gives:

$$f = \frac{.5OH^m + H_2O^m_{mol} + CO_2^m}{H_2O^{Tot} + CO_2^{Tot}} \quad . \tag{3}$$

Differentiating of (3) with respect to f gives:

$$\frac{.5dOH^m}{df} + \frac{dH_2O^m_{mol}}{df} + \frac{dCO_2^m}{df} = H_2O^{Tot} + CO_2^{Tot} \quad . \tag{4}$$

In both open and closed system degassing, we can equate the differential gain of water and carbon dioxide in the vapor with the differential loss from the melt:

$$CO_2^v = CO_2^{Tot} - CO_2^m \tag{5}$$

and

$$H_2O^v = H_2O^{Tot} - H_2O^m = H_2O^{Tot} - .5\ OH^m - H_2O^m_{mol} \, . \tag{6}$$

Differentiating (5) and (6) with respect to f leads to:

$$\frac{dCO_2^v}{df} = \frac{-dCO_2^m}{df} \quad , \tag{7}$$

and

$$\frac{dH_2O^v}{df} = \frac{-dH_2O^m}{df} = \frac{-.5dOH^m}{df} - \frac{dH_2O^m_{mol}}{df} \quad . \tag{8}$$

2) Fractionation

Assuming that both water and CO_2 in the melt are in equilibrium with the vapor phase during each degassing step, and that we have accurate knowledge of their solubilities (Chapter 1), we can express this equilibrium in terms of a single constant ratio of $\beta_{CO_2\text{-}H_2O}$:

$$\beta_{CO_2 H_2O} = \frac{\left(\frac{N^v_{CO_2}}{N^v_{H_2O}}\right)}{\left(\frac{N^m_{CO_2}}{N^m_{H_2O_{mol}}}\right)} \quad . \tag{9}$$

Solubilities are expressed in terms of fugacities and mole fractions of components in the melt; therefore, we need to express β in terms of these variables. Because the denominators cancel, the ratio of the number of moles is the same as the ratio of the mole fractions of H_2O and CO_2.

$$\left(\frac{N^m_{CO_2}}{N^m_{H_2O_{mol}}}\right) = \left(\frac{\frac{N^m_{CO_2}}{N^m_O + N^m_{H_2O} + N^m_{CO_2}}}{\frac{N^m_{H_2O_{mol}}}{N^m_O + N^m_{H_2O} + N^m_{CO_2}}}\right) = \left(\frac{X^m_{CO_2}}{X^m_{H_2O_{mol}}}\right) \tag{10}$$

For the fugacities of H_2O and CO_2 in the vapor phase, we can simplify the calculation by using the Lewis-Randall rule:

$$f_i = X^v_i f^0_i \tag{11}$$

The use of the Lewis-Randall assumption, rather than calculating the fugacities of H_2O and CO_2 using the modified Redlich-Kwong equation of state for H_2O-CO_2 mixtures (Holloway, 1977) results in <20% errors (Table 1). In general, the magnitude of the difference between fugacities calculated using the Lewis-Randall rule instead of the modified Redlich-Kwong equation increases with pressure and decreases with increasing mole fraction of the species in the vapor. At 100 bars pressure, the error is <2%, while

at 1000 bars pressure, the error is as much as 20%. Table 2 shows the magnitude of the error in b caused by using the Lewis-Randall rule to calculate fugacities. In general, the error is less than 15% for conditions relevant to degassing of basaltic magmas.

The ratio of the number of moles of CO_2 and H_2O in the vapor can now be expressed in terms of fugacities by:

$$\left(\frac{N^{v}_{CO_2} f^{0}_{CO_2}}{N^{v}_{H_2O} f^{0}_{H_2O}}\right) = \left(\frac{X^{v}_{CO_2} f^{0}_{CO_2}}{X^{v}_{H_2O} f^{0}_{H_2O}}\right) = \left(\frac{f_{CO_2}}{f_{H_2O}}\right) . \qquad (12)$$

We can define a new variable, β', where:

$$\beta' = \frac{\left(\frac{f_{CO_2}}{f_{H_2O}}\right)}{\left(\frac{X^{m}_{CO_2}}{X^{m}_{H_2O_{mol}}}\right)} = \beta\left(\frac{f^{0}_{CO_2}}{f^{0}_{H_2O}}\right) . \qquad (13)$$

The value of β will be a function of pressure. The pressure dependence of the activity of H_2O and CO_2 in basaltic melts (assuming T to be constant at 1200 °C) is shown below:

$$X^{m}_{H_2O_{mol}} = a^{m}_{H_2O_{mol}} = a^{0,m}_{H_2O_{mol}}(P_0)\,\frac{f_{H_2O}(P)}{f^{0}_{H_2O}(P_0)}\exp\left(\frac{-V^{0,m}_{H_2O}(P-P_0)}{RT}\right) \qquad (14)$$

and

$$X^{m}_{CO_2} = a^{m}_{CO_2} = a^{0,m}_{CO_2}(P_0)\,\frac{f_{CO_2}(P)}{f^{0}_{CO_2}(P_0)}\exp\left(\frac{-V^{0,m}_{CO_2}(P-P_0)}{RT}\right) . \qquad (15)$$

Using a reference pressure (P_0) of 1 bar and data from Chapter 1, then:

$a^{0,m}_{H_2O_{mol}}(P_0) = 3.102 \times 10^{-5}$ $\quad$ $a^{0,m}_{CO_2}(P_0) = 3.817 \times 10^{-7}$

$f^0_{H_2O}(P_0) = 1$ $\quad$ $f^0_{CO_2}(P_0) = 1$

$V^{0,m}_{H_2O} = 12\ cm^3/mole$ $\quad$ $V^{0,m}_{CO_2} = 23.14\ cm^3/mole.$

Substituting in these value into Eqns 14 and 15, and applying the definition of β' gives:

$$\beta = 81.268 \frac{\exp\left(\frac{-12\ (P - 1)}{122{,}488}\right)}{\exp\left(\frac{-23.14\ (P - 1)}{122{,}488}\right)} . \qquad (16)$$

Differentiating of the expression for β (9) with respect to f gives:

$$\beta CO_2^m\left(\frac{dH_2O^v}{df}\right) + \beta H_2O^v\left(\frac{dCO_2^m}{df}\right) - CO_2^v\left(\frac{dH_2O^m_{mol}}{df}\right) - H_2O^m_{mol}\left(\frac{dCO_2^v}{df}\right) = 0 . \qquad (17)$$

The vapor phase abundances can be expressed as:

$$H_2O^v = \lambda\left(H_2O^{Tot} - .5OH^m - H_2O^m_{mol}\right) , \qquad (18)$$

$$CO_2^v = \lambda\left(CO_2^{Tot} - CO_2^m\right) , \qquad (19)$$

where λ=1 for closed system degassing and 0 for open system degassing. Combining Equations 17-19 gives:

$$-.5\beta CO_2^m\left(\frac{dOH^m}{df}\right) + \left[(\lambda-\beta)CO_2^m - \lambda CO_2^{Tot}\right]\left(\frac{dH_2O^m_{mol}}{df}\right)$$
$$+ \left[\beta\lambda\left(H_2O^{Tot} - .5OH^m - H_2O^m_{mol}\right) + H_2O^m_{mol}\right]\left(\frac{dCO_2^m}{df}\right) = 0 . \qquad (20)$$

3) Speciation:

The speciation equation (Eqn. 12, Chapter 1) defines the distribution of water between hydroxyl groups and molecular water species in the melt . An equivalent equation does not exist for CO_2 because CO_2 dissolves in basaltic melts only as carbonate groups. It is convenient to define a variable, y, as the fraction of total water present as OH groups:

$$y = \frac{.5OH^m}{.5OH^m + H_2O^m_{mol}} = \frac{OH^m}{OH^m + 2H_2O^m_{mol}} . \qquad (21)$$

Rearranging and differentiating with respect to f yields:

$$(y - 1)\frac{dOH^m}{df} + 2y\frac{dH_2O^m_{mol}}{df} = \frac{-dy}{df}\left(OH^m + H_2O^m_{mol}\right) . \qquad (22)$$

This equation contains the term dy/df, which must be expressed in terms of dOH^m/df or dH_2O_{mol}/df. Using the chain rule, dOH^m/df can be expressed as:

$$\frac{dOH^m}{df} = \left(\frac{dOH^m}{dy}\right)\left(\frac{dy}{df}\right) . \qquad (23)$$

Therefore, dy/df is equivalent to:

$$\frac{dy}{df} = \frac{\left(\frac{dOH^m}{df}\right)}{\left(\frac{dOH^m}{dy}\right)} . \qquad (24)$$

I have obtained an analytical expression for dOH^m/dy by fitting a 3rd order polynomial through OH^m vs Y data (Figure 1) for albite (Silver and Stolper, 1989). The fit has an R^2 of 0.994 and is given by:

$$X_{OH}^{m} = 0.0770 + 0.00642y + 0.0385y^2 - 0.1209y^3 \quad . \tag{25}$$

The derivative of (25) with respect to y is:

$$\frac{dX_{OH^m}}{dy} = 0.00642 + 0.07694y - 0.3627y^2 \quad . \tag{26}$$

Since:

$$OH^m = X_{OH^m}(N_{H_2O} + N_{CO_2} + N_O) \quad . \tag{27}$$

then:

$$\frac{dOH^m}{dy} = (N_{H_2O} + N_{CO_2} + N_O)(0.00642 + 0.07694y - 0.3627y^2) \quad . \tag{28}$$

Now that dOH^m/dy can be evaluated for each iteration, we can combine (22) and (24) to get the final differential equation for speciation of water in the melt:

$$\left[(y - 1)\left(\frac{dOH^m}{dy}\right) + OH^m + 2H_2O_{mol}^m\right]\left(\frac{dOH^m}{df}\right) + 2y\left(\frac{dOH^m}{dy}\right)\left(\frac{dH_2O_{mol}^m}{df}\right) = 0 \quad . \tag{29}$$

The three final differential equations are:

Mass Balance:

$$\frac{.5dOH^m}{df} + \frac{dH_2O_{mol}^m}{df} + \frac{dCO_2^m}{df} = H_2O^{Tot} + CO_2^{Tot} \quad ; \tag{4}$$

Fractionation:

$$-.5\beta CO_2^m\left(\frac{dOH^m}{df}\right) + \left[(\lambda-\beta)CO_2^m - \lambda CO_2^{Tot}\right]\left(\frac{dH_2O^m_{mol}}{df}\right)$$
$$+\left[\beta\lambda\left(H_2O^{Tot} - .5OH^m - H_2O^m_{mol}\right) + H_2O^m_{mol}\right]\left(\frac{dCO_2^m}{df}\right) = 0 \quad ; \qquad (20)$$

and Speciation:

$$\left[(y-1)\left(\frac{dOH^m}{dy}\right) + OH^m + 2H_2O^m_{mol}\right]\left(\frac{dOH^m}{df}\right) + 2y\left(\frac{dOH^m}{dy}\right)\left(\frac{dH_2O^m_{mol}}{df}\right) = 0 \quad . \qquad (29)$$

These equations can be solved simultaneously for the derivatives $\frac{dOH^m}{df}$, $\frac{dH_2O^m_{mol}}{df}$, and $\frac{dCO_2^m}{df}$. These.derivatives are calculated by casting Equations 4, 20, and 29 into the form of a matrix equation (**AX = B**):

$$\begin{vmatrix} .5 & 1 & 1 \\ -.5\beta CO_2^m & (\lambda-\beta)CO_2^m - \lambda CO_2^{Tot} & \beta\lambda(H_2O^{Tot} - .5OH^m - H_2O^m_{mol}) + H_2O^m_{mol} \\ (y-1)\left(\frac{dOH^m}{dy}\right) + OH^m + 2H_2O^m_{mol} & 2y\left(\frac{dOH^m}{dy}\right) & 0 \end{vmatrix}$$

$$X \begin{bmatrix} \frac{dOH^m}{df} \\ \frac{dH_2O^m_{mol}}{df} \\ \frac{dCO_2^m}{df} \end{bmatrix} = \begin{bmatrix} H_2O^{Tot} + CO_2^{Tot} \\ 0 \\ 0 \end{bmatrix} \quad . \qquad (30)$$

This matrix equation can be solved using standard techniques, and the vector of derivatives can be integrated numerically to yield the abundances of hydroxyl groups, molecular water, and carbon dioxide in the melt.

Discussion of Degassing Program:

A program has been written to calculate the degassing path of a packet of basaltic magma at a given pressure and 1200°C; degassing proceeds until saturation is reached. The calculation begins with a specified pressure, initial water and carbon dioxide contents, and f set to 1. For open system degassing, λ is set to 0 (equivalent to setting H_2O^v and CO_2^v to 0 for each iteration). For closed system degassing, λ is set to 1. The values for $f^0_{H_2O}$, $f^0_{CO_2}$, and β are computed as a function of pressure and remain constant for the remainder of the calculations.

The program next computes the progressive changes in melt and vapor compositions with progressive degassing of increments of initial volatiles present (-df). For each iteration, the concentrations of water species (OH^m and $H_2O^m_{mol}$) and dy/df are calculated. Substitution of the numeric values of y, dy/df, b, and the melt species concentrations OH^m, $H_2O^m_{mol}$, and CO_2^m into Eqn 30 gives a 3X3 matrix equation for $\frac{dOH^m}{df}$, $\frac{dH_2O^m_{mol}}{df}$, and $\frac{dCO_2^m}{df}$. The values of these derivatives are determined using a LU decomposition solution to the matrix equation.

For each iteration, the total volatile content (H_2O and CO_2) drops by an amount -df. The concentrations of the melt species drop by amounts $-df\frac{dOH^m}{df}$, $-df\frac{dH_2O^m_{mol}}{df}$, and $-df\frac{dCO_2^m}{df}$, respectively. The abundances and f are changed by the appropriate amount, and new values of y and dy/df are calculated. The matrix equations are solved again, now using the updated abundances. These steps are repeated until saturation is reached. Saturation is defined by:

$$\frac{a^{m}_{H_2O}}{a^{0,m}_{H_2O}} + \frac{a^{m}_{CO_2}}{a^{0,m}_{CO_2}} = 1 \quad . \qquad (31)$$

where the activities of the species in the melt are the mole fractions of molecular water and carbon dioxide in the melt after each iteration, and the activities of the species in the melt in equilibrium with a pure vapor phase are calculated using Equations 14 and 15.

A copy of the program and sample calculations are included below.

References

Holloway, J.R. (1977) Fugacity and activity of molecular species in supercritical fluids. *in* Fraser, D. (ed.) Thermodynamics in Geology. Boston: D. Reidel, pp. 161-181.

Silver, L.A. and E.M. Stolper (1989) Water in albitic glasses. J. Petrol., **30**, 667-709.

Table 1: Comparison of H_2O and CO_2 fugacities calculated using the MRK equation of state and the Lewis-Randall Rule

P (bars)	$X^{v}_{H_2C}$	$f^{MRK}_{H_2O}$	$f^{LR}_{H_2O}$	% diff.	$f^{MRK}_{CO_2}$	$f^{LR}_{CO_2}$	% diff
100	.01	.975	.998	2.4	101.11	101.09	0.0
100	.1	9.78	9.98	2.0	91.90	91.92	0.0
100	.25	24.61	24.95	1.4	76.49	76.60	0.1
100	.5	49.59	49.90	0.6	50.76	51.07	0.6
100	.75	74.73	74.84	0.2	25.18	25.53	1.4
500	.01	4.49	4.96	10.47	551.15	551.15	0.0
500	.1	45.56	49.64	9.0	500.60	501.05	0.1
500	.25	116.63	124.10	6.4	415.07	417.54	0.6
500	.5	241.01	248.21	3.0	271.28	278.36	2.6
500	.75	369.44	372.31	0.8	130.79	139.18	6.4
1000	.01	8.40	9.93	18.2	1231.76	1231.78	0
1000	.1	85.94	99.34	15.6	1118.26	1119.80	0.1
1000	.25	222.93	248.34	11.4	924.54	933.17	0.9
1000	.5	470.74	496.68	5.5	596.27	622.11	4.3
1000	.75	734.11	745.01	1.5	279.16	311.06	11.4

MRK values calculated using a modified Redlich-Kwong equation of state (Holloway, 1977). LR values calculated using $f_i = X_i f_i^0$.

Table 2

P (bars)	$X^{v}_{H_2C}$	$\left(\frac{f_{CO_2}}{f_{H_2O}}\right)$	$\left(\frac{X^{v}_{CO_2} f^{o}_{CO_2}}{X^{v}_{H_2O} f^{o}_{H_2O}}\right)$	% diff
100	.01	103.70	101.29	-2.3
100	.1	9.397	9.210	-2.0
100	.25	3.108	3.070	-1.2
100	.5	1.024	1.023	-0.1
100	.75	0.337	0.341	+1.2
500	.01	122.751	111.119	-9.5
500	.1	10.988	10.094	-8.1
500	.25	3.559	3.365	-5.5
500	.5	1.126	1.121	-0.4
500	.75	.3540	0.374	+5.6
1000	.01	146.638	124.046	-15.4
1000	.1	13.012	11.272	-13.4
1000	.25	4.147	3.758	-9.4
1000	.5	1.267	1.253	-1.1
1000	.75	0.380	0.418	+10.0

```
100 REM **THIS PROGRAM CALCULATES A DEGASSING PATH FOR A BASALTIC MELT**
REM **WITH A GIVEN TOTAL VOLATILE CONTENT AND EMPLACED AT A GIVEN P AND
T.**
REM **DEGASSING PROCEEDS UNTIL SATURATION IS REACHED.  ONLY FINAL
SATURATION**
REM **VALUES ARE SAVED IN DATA FILE, THEN PROGRAM ITERATES DOWN PRESSURE**
F$ = CHR$(34)
PRINT "INPUT FILENAME FOR STORING OUTPUT DATA:  ":INPUT F$
OPEN F$ FOR OUTPUT AS #1
REM **FIRST INPUT P,T,WTH2O, PPMCO2**
3100 PRINT "INPUT INITIAL H2O CONTENT (WT%):  ":INPUT WTH2O
3200 PRINT "INPUT INITIAL CO2 CONTENT (PPM):  ":INPUT PPMCO2
  WTH2OO=WTH2O
   PPMCO2O=PPMCO2
3300 PRINT "INPUT P (BARS):  ":INPUT P
REM **SET LAMBDA TO 1 FOR CLOSED SYSTEM DEGASSING OR 0 FOR OPEN SYSTEM**
PRINT "DO YOU WANT OPEN (0) OR CLOSED (1) SYSTEM DEGASSING? ENTER 0 OR
1:":INPUT LAMBDA
REM 3400 PRINT "INPUT T (°C):  ":INPUT TEMP
3450   TEMP=1200+273.15
  T=TEMP

REM **INITIAL INCREMENT OF DEGASSING SET TO BE .1%**
  DF=-.001

3500 REM **OBTAIN FUGACITIES OF PURE H2O AND CO2 AT GIVEN P AND T FOR USE IN **
REM **CALCULATION OF BETA USING MRK FROM HOLLOWAY, 1977 AND PRAUSNITZ,
P156**
REM **AND LEWIS-RANDALL RULE SIMPLIFICATION (F=X*F°)**
  R=83.14321
REM **AH IS THE TEMP DEP EQN FOR a FOR H2O, UNITS ARE atm cm^6 R^1/2 mole^-2**
REM **1.01325 IS CONVERSION FROM BARS TO ATM, T IN CELSIUS**
  AH=(1.668E+08-193080!*(T-273.15)+186.4*(T-273.15)^2-.071288*(T-273.15)^3)*1.01325
REM **AC IS TEMP DEP EQN FOR a FOR CO2, T IN CELSIUS**
  AC=1.01325*(7.303E+07-71400!*(T-273.15)+21.57*(T-273.15)^2)
REM **b(H2O)=14.6 cm^3/mole, b(CO2)=29.7**
  B1=14.6
  B2=29.7
REM **AHC IS THE EQN FOR a FOR MIXTURES OF H2O AND CO2**
REM ** INCLUDES LNK, THE EQUILIBRIUM  CONSTANT FOR H2O-CO2 COMPLEX
FORMATION**
REM **T IN DEGREES KELVIN**
REM **(a°H2O*a°CO2)^1/2=4.01248E+07 **
  LNK=-11.071+(5953/T)-(2746000!/T^2)+(4.646E+08/T^3)
  K=EXP(LNK)
  AHC=1.01325*((K*.5*R*R*T^2.5/1.026676)+40124800#)
REM **USES METHOD OF NEWTON  TO ITERATE FOR VOLUME**
FOR X1=0 TO 1 STEP 1
  B=X1*B1+(1-X1)*B2
  A=(X1^2*AH)+(2*X1*(1-X1)*AHC)+((1-X1)^2*AC)
  DEF FNF#(V#)=R*T/(V#-B)-A/((V#*V#+B*V#)*SQR(T))-P
  V2=B+5
  Q=1
  V1=V2
3510 F1=(FNF#(V1+.01)-FNF#(V1))/.01
  V2=V1-Q*FNF#(V1)/F1
  F2=(FNF#(V2+.01)-FNF#(V2))/.01
   IF F2*F1>0 THEN 3520
```

```
  Q=Q/2
3520 IF ABS(V2-V1)<.00001 THEN 3530
  V1=V2
  F1=F2
  GOTO 3510
3530 V#=V2
REM **G1=FUGACITY COEFFICIENT FOR H2O, G2= FOR CO2, SEE PRAUSNITZ P.156**
  G1=LOG(V#/(V#-B))+B1/(V#-B)-2*(X1*AH+(1-X1)*AHC)*LOG((V#+B)/V#)/(R*T^1.5*B)
  G1=G1+(LOG((V#+B)/V#)-B/(V#+B))*A*B1/(R*T^1.5*B^2)-LOG(P*V#/(R*T))
  G1=EXP(G1)
  G2=LOG(V#/(V#-B))+B2/(V#-B)-2*(X1*AHC+(1-X1)*AC)*LOG((V#+B)/V#)/(R*T^1.5*B)
  G2=G2+(LOG((V#+B)/V#)-B/(V#+B))*A*B2/(R*T^1.5*B^2)-LOG(P*V#/(R*T))
  G2=EXP(G2)
  IF X1=0 THEN VCO2=V#
  IF X1=1 THEN VH2O=V#
  IF X1=0 THEN FCO2O#=G2*(1-X1)*P
  IF X1=1 THEN FH2OO#=G1*X1*P
NEXT X1

REM **CALCULATE BETAP AS FUNCTION OF P**
  BETAP=81.268*(EXP(-12*(P-1)/122488!))/(EXP(-23.14*(P-1)/122488!))

REM **CALCULATE BETA FROM BETAP (BETA=BETAP*FH2OO/FCO2O)**
  BETA=BETAP*FH2OO#/FCO2O#

3550 REM **CALCULATE INITIAL (OR TOTAL) NUMBER OF MOLES OF H2O AND CO2**
  NCO2TOT=PPMCO2*.0001/44.009
  NH2OTOT=WTH2O/18.015

3600 REM **CALCULATE NUMBER OF MOLES AND MOLE FRACTIONS OF H2O AND CO2 IN
MELT**
  T=TEMP
  H2OOLD=WTH2O
  CO2OLD=PPMCO2
  NCO2=PPMCO2*.0001/44.009
  NH2O=WTH2O/18.015
  NO=(100-WTH2O-PPMCO2*.0001)/36.594
  XH2O=NH2O/(NH2O+NO+NCO2)
  XCO2M=NCO2/(NCO2+NO+NH2O)
  XO=1-XH2O-XCO2
  XB=NH2O/(NH2O+NO+NCO2)

3610 REM **F=FRACTION OF INITIAL VOLATILES LEFT IN MELT**
  F=(NH2O+NCO2)/(NH2OTOT+NCO2TOT)

3620 REM **FIRST GUESS FOR XOHM CALCULATED BY USING FOURTH ORDER
POLYNOMIAL FIT**
REM **THROUGH ALBITE DATA FOR XOHM VS XH2O**
  XOHMO#=2.1898*XH2O-23.3226*XH2O^2+113.6695*XH2O^3-211.243*XH2O^4
  IF (XH2O-.5*XOHMO#<=0) THEN XOHMO#=2*.98*XH2O
  XOHM#=XOHMO#
REM ** ITERATIVE SOLUTION FOR WATER SPECIATION USING SILVER AND STOLPER,
1989**
REM ** REGULAR SOLUTION MODEL WITH PARAMETERS FOR ALBITE**
3700 K=0
3710 IF (XH2O-.5*XOHM#<=0) THEN XOHM#=(.999*2*XH2O+XOHMO#)/2
  IF (XO-.5*XOHM#<=0) THEN XOHM#=(.999*2*XO+XOHMO#)/2
  IF (XOHM#^2=0) THEN XOHM#=XOHMO#/2
```

```
   A=9.143
   B=-3.295
   C=-6.019
   D=-.572
  FX#=A+B*(XOHM#-1)+2*C*(XO-XOHM#)+2*D*(XH2O-XOHM#)+LOG(XOHM#^2/((XH2O-
.5*XOHM#)*(XO-.5*XOHM#)))
REM **FXP# IS DERIVATIVE OF FX# WITH RESPECT TO XOHM#**
  FXP#=B-2*(C+D)+(2*(XH2O-.5*XOHM#)*(XO-.5*XOHM#)+.5*XOHM#*((XH2O-
.5*XOHM#)+(XO-.5*XOHM#)))/(XOHM#*(XH2O-.5*XOHM#)*(XO-.5*XOHM#))
   DERATH#=FX#/FXP#
  XOHMO#=XOHM#
  XOHM#=XOHM#-DERATH#
   K=K+1
  IF (ABS(DERATH#)>=.00001) THEN GOTO 3710
  XMH2OM#=XH2O-.5*XOHM#

REM ** CALCULATE NOHM AND NMH2OM FROM XOHM AND XMH2OM**
  NMH2OM=XMH2OM#*(NH2O+NCO2+NO)
  NOHM=XOHM#*(NH2O+NCO2+NO)

REM **Y=OH/(OH +MOLH2O)=FRACTION OF WATER AS OH**
  Y=.5*NOHM/(.5*NOHM+NMH2OM)

REM **DOHMDY=DOHM/DY=DERIVATIVE OF 3RD ORDER POLYNOMIAL THROUGH ALBITE
XOH VS Y DATA**
  DOHMDY=(NH2O+NCO2+NO)*(.00642+.07694*Y-.3627*Y^2)

REM **DEFINE COEFFICIENTS FOR LINEAR DIFFERENTIAL EQUATIONS TO BE
CALCULATED IN**
REM **LINEAR EQUATION SOLVER ROUTINE**
REM   DIM A(3,3)
REM   DIM B(3)
REM   DIM X(3)
REM   A(1,1)=.5
REM   A(1,2)=1
REM   A(1,3)=1
REM   A(2,1)=-.5*BETA*NCO2
REM  A(2,2)=(LAMBDA-BETA)*NCO2-LAMBDA*NCO2TOT
REM  A(2,3)=BETA*LAMBDA*(NH2OTOT-.5*NOHM-NMH2OM)+NMH2OM
REM  A(3,1)=(Y-1)*DOHMDY+NOHM+2*NMH2OM
REM  A(3,2)=2*Y*DOHMDY
REM   A(3,3)=0

REM **X(1)=DOHDF**
REM **X(2)=DMH2ODF**
REM **X(3)=DCO2DF**

REM  B(1)=NH2OTOT+NCO2TOT
REM  B(2)=0
REM  B(3)=0

REM **SOLVE 3 LINEAR DIFFERENTIAL EQUATIONS BY LU DECOMPOSITION**
REM **GENERAL LINEAR EQUATION SOLVER**
REM **REF P. 76, J. HEILBORNN, SCIENCE & ENGINEERING PROGRAMS/OSBORNE-
MCGRAW HILL
REM **FACTORIZATION OF A**
REM **INPUT DATA**
GOSUB 420
```

```
REM 1-NORM OF A
GOSUB 860
REM FACTORIZATION OF A
GOSUB 1050
REM ESTIMATION OF CONDITION OF MATRIX A
GOSUB 1640
REM INPUT VECTOR B
280 GOSUB 650
REM SOLVE A*X=B
GOSUB 2440
REM OUTPUT SOLUTION
GOSUB 760
GOTO 5000
REM INPUT DATA
420 N=3
   A(1,1)=.5
   A(1,2)=1
   A(1,3)=1
   A(2,1)=-.5*BETA*NCO2
   A(2,2)=(LAMBDA-BETA)*NCO2-LAMBDA*NCO2TOT
   A(2,3)=BETA*LAMBDA*(NH2OTOT-.5*NOHM-NMH2OM)+NMH2OM
   A(3,1)=(Y-1)*DOHMDY+NOHM+2*NMH2OM
   A(3,2)=2*Y*DOHMDY
   A(3,3)=0
620 RETURN
REM INPUT B ROUTINE
650 B(1)=NH2OTOT+NCO2TOT
   B(2)=0
   B(3)=0
730 RETURN
REM OUTPUT SOLUTION
760 REM PRINT
REM PRINT "SOLUTION"
REM PRINT "**********"
REM FOR I=1 TO N
REM PRINT "X(";I;") = ";B(I)
REM NEXT I
830 RETURN
REM 1 NORM OF MATRIX A
860 A9=0
FOR J=1 TO N
T=0
FOR I=1 TO N
T=T+ABS(A(I,J))
NEXT I
IF T<=A9 THEN 940
A9=T
940 NEXT J
950 RETURN
REM P IS PERMUTATION MATRIX
REM L IS LOWER TRIANGULAR MATRIX
REM U IS UPPER TRIANGULAR MATRIX
1050 I0(N)=1
N1=N-1
IF N1=0 THEN 2150
FOR K=1 TO N1
K1 = K+1
REM FIND PIVOT
```

```
M=K
FOR I=K1 TO N
A1=ABS(A(I,K))
A2=ABS(A(M,K))
IF A1<=A2 THEN 1170
M=I
1170 NEXT I
REM PIVOT LOCATED
I0(K)=M
IF M=K THEN 1250
I0(N)=-I0(N)
REM INTERCHANGE DIAGONAL TERMS
1250 T=A(M,K)
A(M,K)=A(K,K)
A(K,K)=T
REM SKIP STEP IF PIVOT IS ZERO
IF T=0 THEN 1450
REM COMPUTE MULTIPLIERS
FOR I=K1 TO N
A(I,K)=-A(I,K)/T
NEXT I
REM INTERCHANGE AND ELIMINATE BY COLUMNS
FOR J=K1 TO N
T=A(M,J)
A(M,J)=A(K,J)
A(K,J)=T
IF T=O THEN 1440
FOR I=K1 TO N
A(I,J)=A(I,J) + A(I,K)*T
NEXT I
1440 NEXT J
1450 NEXT K
REM PRINT "WANT DET(A) (Y/N) ";
REM INPUT W$
REM IF W$= "N" THEN 1590
REM COMPUTE DETERMINANT
D=1
FOR I=1 TO N
D=D*A(I,I)
NEXT I
D=D*I0(N)
REM PRINT "DET(A) = ";D
1590 RETURN
REM ESTIMATION OF CONDITION OF MATRIX A
1640 IF N>1 THEN 1740
C=1
IF A(1,1)<>0 THEN 2240
GOTO 2380
REM GENERAL CASE
1740 K=1
1750 T=0
IF K=1 THEN 1810
K1=K-1
FOR I=1 TO K1
T=T+A(I,K)*B(I)
NEXT I
1810 E1=1
IF T>=0 THEN 1850
```

```
E1=-1
REM CHECK FOR SINGULARITY
1850 IF A(K,K)=0 THEN 2380
B(K)=-(E1+T)/A(K,K)
K=K+1
IF K>=(N+1) THEN 1910
GOTO 1750
REM SOLVE FOR SYSTEM
1910 FOR K2=1 TO N1
K=N-K2
T=0
K1=K+1
FOR I=K1 TO N
T=T+A(I,K)*B(K)
NEXT I
B(K)=T
M=I0(K)
IF M=K THEN 2040
T=B(M)
B(M) = B(K)
B(K)=T
2040 NEXT K2
Y1=0
FOR I=1 TO N
Y1=Y1+ABS(B(I))
NEXT I
GOSUB 2440
Z1=0
FOR I= 1 TO N
2150 Z1 =Z1+ABS(B(I))
NEXT I
C=A9*Z1/Y1
IF C>=1 THEN 2240
C=1
2240 REM PRINT
REM PRINT "ESTIMATION OF CONDITION OF MATRIX A"
REM PRINT "  C = ";C
REM TEST FOR SINGULARITY
IF C<(C+1) THEN 2350
2340 REM PRINT "A IS SINGULAR TO WORKING PRECISION"
2350 REM PRINT
RETURN
2380 REM PRINT "MATRIX A IS SINGULAR"
GOTO 2680
REM FORWARD SOLUTION
2440 IF N=1 THEN 2660
N1=N-1
FOR K=1 TO N1
K1=K+1
M=I0(K)
T=B(M)
B(M)=B(K)
B(K)=T
FOR I=K1 TO N
B(I)=B(I)+A(I,K)*T
2540 NEXT I
2550 NEXT K
2570 FOR K2=1 TO N1
```

```
K1=N-K2
K=K1+1
B(K)=B(K)/A(K,K)
T=-B(K)
FOR I=1 TO K1
B(I)=B(I)+A(I,K)*T
2640 NEXT I
2650 NEXT K2
2660 B(1)=B(1)/A(1,1)
2670 RETURN
2680 GOTO 5000

5000 REM **CALCULATE NEW NOHM, NMH2OM, NH2O, NCO2**
REM **NOHM=NOHM+DF(DOHM/DF), ECT.**
F=F+DF
DOHMDF=B(1)
DMH2OMDF=B(2)
DCO2DF=B(3)
NOHM=NOHM+DF*DOHMDF
NMH2OM=NMH2OM+DF*DMH2OMDF
NH2O=.5*NOHM+NMH2OM
NCO2=NCO2+DF*DCO2DF
IF NCO2<=0 THEN NCO2=0
WTH2O=NH2O*18.015
PPMCO2=NCO2*44.009/.0001
H2ONEW=WTH2O
CO2NEW=PPMCO2

   NO=(100-WTH2O-PPMCO2*.0001)/36.594
   XH2O=NH2O/(NH2O+NO+NCO2)
   XCO2M=NCO2/(NCO2+NO+NH2O)
   XO=1-XH2O-XCO2
   XB=NH2O/(NH2O+NO+NCO2)
   XOHM=NOHM/(NH2O+NO+NCO2)
   XMH2OM=NMH2OM/(NH2O+NO+NCO2)

IF LAMBDA=0 GOTO 5200

5100 REM **CALCULATE COMPOSITION OF VAPOR PHASE CLOSED SYSTEM**
   NVCO2=NCO2TOT-NCO2
   NVH2O=NH2OTOT-NH2O
   XVCO2=NVCO2/(NVCO2+NVH2O)
   XVH2O=NVH2O/(NVCO2+NVH2O)
   GOTO 6000

5200 REM **CALCULATE COMPOSITION OF VAPOR FOR EACH STEP IN OPEN SYSTEM**
   VCO2=CO2OLD-CO2NEW
   NVCO2=VCO2/(10000*44.01)
   VH2O=H2OOLD-H2ONEW
   NVH2O=VH2O/18.015
   XVCO2=NVCO2/(NVCO2+NVH2O)
   XVH2O=NVH2O/(NVCO2+NVH2O)

6000 REM **IS THE MELT SATURATED?  IF SO, STOP.  IF NOT, CONTINUE**
   REM **MELT IS SATURATED WHEN ACO2/A°CO2 + AH2O/A°H2O = 1**
   AH2OM=XMH2OM
   ACO2M=XCO2M
```

```
6500 REM **ACTIVITY CALCULATIONS INCLUDING CORRECTION FOR MOLAR VOLUME OF
   REM WATER AND CARBON DIOXIDE IN MELT  WITH REF STATE OF 1 BAR, 1200°C**
   AOH2OM=3.102E-05*(FH2OO#/1)*EXP(-12*(P-1)/122488!)
   AOCO2M=3.817E-07*(FCO2O#/1)*EXP(-23.14*(P-1)/122488!)

6700   GH2O=AH2OM/AOH2OM
   GCO2=ACO2M/AOCO2M

7000   REM **IF ONE MORE ITERATION WOULD CAUSE NEGATIVE VALUES FOR H2O OR
CO2 THEN**
   REM **REDUCE THE DEGASSING INCREMENT BY HALF*
   IF (GH2O+GCO2-1<.0001) THEN GOTO 8000
   IF (GH2O+GCO2-1<1) AND (GH2O+GCO2-1>.1) THEN DF=-.0001
   IF (GH2O+GCO2-1<.1) AND (GH2O+GCO2-1>.01) THEN DF=-.00005
   IF (GH2O+GCO2-1<=.01) AND (GH2O+GCO2-1>.001) THEN DF=-.00001
   IF (GH2O+GCO2-1<=.001) AND (GH2O+GCO2-1>.0001) THEN DF=-.000001
   GOTO 3600

8000  WRITE #1,P;TEMP-273.15;WTH2OO;PPMCO2O;FH2OO#;FCO2O#;LAMBDA;BETA;Y;F;B(1);
B(2);B(3);NOHM;NMH2OM;NCO2;XOHM; XMH2OM; XH2O;XCO2M;WTH2O; PPMCO2; NVH2O;
NVCO2; XVH2O;XVCO2; GH2O; GCO2; GH2O+GCO2

IF P=1 THEN GOTO 9000
IF P=5 THEN P=1
IF P=10 THEN P=5
IF P<=100 AND P>10 THEN P=P-10
IF P>=150 THEN P=P-50
PRINT "P=";P
WTH2O=WTH2OO
PPMCO2=PPMCO2O
GOTO 3450

9000 CLOSE #1
GOTO 100
END
```

	P (bars)	T°C	INIT H2O (wt%)	INIT CO2 (PPM)	fH2O (bars)	fCO2 (bars)	lambda	beta	Y=OH/(OH+2MH2O)	F	DOHM/DF	DMH2OM/DF	DCO2M/DF	NOHM	NMH2OM
1	1000.0	1200.0	1.0000	500.00	993.35	1244.2	1.0000	71.053	0.84507	0.99660	0.010114	0.0022096	0.049379	0.093783	0.0085966
2	950.00	1200.0	1.0000	500.00	943.31	1168.8	1.0000	71.501	0.84510	0.99548	0.011134	0.0024319	0.048648	0.093772	0.0085939
3	900.00	1200.0	1.0000	500.00	893.38	1095.0	1.0000	71.956	0.84513	0.99434	0.012314	0.0026889	0.047799	0.093759	0.0085908
4	850.00	1200.0	1.0000	500.00	843.54	1022.8	1.0000	72.416	0.84516	0.99318	0.013674	0.0029848	0.046824	0.093745	0.0085873
5	800.00	1200.0	1.0000	500.00	793.78	951.80	1.0000	72.884	0.84520	0.99201	0.015256	0.0033290	0.045689	0.093729	0.0085834
6	750.00	1200.0	1.0000	500.00	744.10	882.45	1.0000	73.358	0.84524	0.99081	0.017110	0.0037322	0.044358	0.093711	0.0085790
7	700.00	1200.0	1.0000	500.00	694.48	814.53	1.0000	73.838	0.84529	0.98958	0.019290	0.0042058	0.042795	0.093690	0.0085738
8	650.00	1200.0	1.0000	500.00	644.91	748.02	1.0000	74.326	0.84535	0.98830	0.021856	0.0047629	0.040955	0.093666	0.0085679
9	600.00	1200.0	1.0000	500.00	595.39	682.91	1.0000	74.820	0.84541	0.98697	0.024893	0.0054217	0.038777	0.093637	0.0085609
10	550.00	1200.0	1.0000	500.00	545.89	619.15	1.0000	75.321	0.84549	0.98557	0.028473	0.0061970	0.036212	0.093602	0.0085525
11	500.00	1200.0	1.0000	500.00	496.41	556.72	1.0000	75.828	0.84559	0.98408	0.032687	0.0071080	0.033194	0.093560	0.0085423
12	450.00	1200.0	1.0000	500.00	446.93	495.60	1.0000	76.342	0.84571	0.98245	0.037641	0.0081764	0.029649	0.093507	0.0085295
13	400.00	1200.0	1.0000	500.00	397.45	435.76	1.0000	76.863	0.84587	0.98060	0.043422	0.0094187	0.025516	0.093438	0.0085128
14	350.00	1200.0	1.0000	500.00	347.95	377.17	1.0000	77.390	0.84608	0.97846	0.049946	0.010813	0.020859	0.093345	0.0084906
15	300.00	1200.0	1.0000	500.00	298.43	319.81	1.0000	77.924	0.84640	0.97572	0.057214	0.012352	0.015687	0.093206	0.0084573
16	250.00	1200.0	1.0000	500.00	248.86	263.65	1.0000	78.465	0.84690	0.97194	0.064672	0.013899	0.010410	0.092988	0.0084050
17	200.00	1200.0	1.0000	500.00	199.24	208.67	1.0000	79.012	0.84784	0.96565	0.071677	0.015275	0.0055317	0.092572	0.0083070
18	150.00	1200.0	1.0000	500.00	149.55	154.84	1.0000	79.565	0.85015	0.95149	0.077258	0.016123	0.0018930	0.091545	0.0080678
19	100.00	1200.0	1.0000	500.00	99.794	102.13	1.0000	80.124	0.85990	0.89481	0.081671	0.015572	0.00023824	0.087142	0.0070986
20	90.000	1200.0	1.0000	500.00	89.832	91.726	1.0000	80.237	0.86452	0.86819	0.082802	0.015106	0.00013788	0.085012	0.0066611
21	80.000	1200.0	1.0000	500.00	79.866	81.362	1.0000	80.349	0.87045	0.83402	0.084156	0.014488	7.9638e-05	0.082231	0.0061194
22	70.000	1200.0	1.0000	500.00	69.897	71.041	1.0000	80.462	0.87766	0.79236	0.085751	0.013723	4.7235e-05	0.078775	0.0054904
23	60.000	1200.0	1.0000	500.00	59.924	60.764	1.0000	80.576	0.88609	0.74351	0.087590	0.012822	2.8698e-05	0.074631	0.0047972
24	50.000	1200.0	1.0000	500.00	49.947	50.529	1.0000	80.689	0.89574	0.68718	0.089686	0.011785	1.7816e-05	0.069730	0.0040581
25	40.000	1200.0	1.0000	500.00	39.966	40.338	1.0000	80.803	0.90675	0.62231	0.092077	0.010596	1.1137e-05	0.063925	0.0032870
26	30.000	1200.0	1.0000	500.00	29.980	30.190	1.0000	80.917	0.91944	0.54643	0.094842	0.0092178	6.8399e-06	0.056917	0.0024935
27	20.000	1200.0	1.0000	500.00	19.991	20.084	1.0000	81.031	0.93453	0.45407	0.098154	0.0075643	3.9286e-06	0.048074	0.0016839
28	10.000	1200.0	1.0000	500.00	9.9978	10.021	1.0000	81.146	0.95430	0.32826	0.10256	0.0053652	2.0344e-06	0.035490	0.00084973
29	5.0000	1200.0	1.0000	500.00	4.9994	5.0053	1.0000	81.203	0.96816	0.23552	0.10571	0.0037904	1.2575e-06	0.025832	0.00042471
30	1.0000	1200.0	1.0000	500.00	0.99998	1.0002	1.0000	81.249	0.98611	0.10788	0.10990	0.0016946	4.7970e-07	0.012052	8.4870e-05

	NCO2M	XOHM	XMH2OM	XH2OM	XCO2M	WTH2O	PPMCO2	NVH2O	NVCO2	XVH2O	XVCO2	a/a° H2O	a/a° CO2	a/a°(H)+a/a°(C)
1	0.00096471	0.033971	0.0031140	0.020100	0.00034945	0.99962	424.56	2.1104e-05	0.00017142	0.10961	0.89039	0.11145	0.88864	1.0001
2	0.00090939	0.033967	0.0031130	0.020096	0.00032941	0.99947	400.21	2.9515e-05	0.00022674	0.11518	0.88482	0.11675	0.88334	1.0001
3	0.00085427	0.033962	0.0031118	0.020093	0.00030944	0.99930	375.96	3.8948e-05	0.00028186	0.12141	0.87859	0.12263	0.87744	1.0001
4	0.00079938	0.033957	0.0031106	0.020089	0.00028956	0.99911	351.80	4.9409e-05	0.00033675	0.12795	0.87205	0.12919	0.87086	1.0001
5	0.00074477	0.033951	0.0031092	0.020085	0.00026978	0.99890	327.76	6.1251e-05	0.00039137	0.13533	0.86467	0.13655	0.86355	1.0001
6	0.00069031	0.033945	0.0031075	0.020080	0.00025005	0.99865	303.80	7.4800e-05	0.00044582	0.14367	0.85633	0.14488	0.85520	1.0001
7	0.00063607	0.033937	0.0031057	0.020074	0.00023040	0.99837	279.93	9.0443e-05	0.00050006	0.15316	0.84684	0.15438	0.84568	1.0001
8	0.00058207	0.033928	0.0031035	0.020068	0.00021084	0.99804	256.16	0.00010863	0.00055406	0.16392	0.83608	0.16532	0.83477	1.0001
9	0.00052826	0.033918	0.0031010	0.020060	0.00019135	0.99765	232.48	0.00013017	0.00060787	0.17637	0.82363	0.17805	0.82203	1.0001
10	0.00047464	0.033905	0.0030979	0.020051	0.00017193	0.99719	208.88	0.00015582	0.00066149	0.19065	0.80935	0.19306	0.80699	1.0001
11	0.00042124	0.033890	0.0030943	0.020039	0.00015259	0.99663	185.38	0.00018702	0.00071489	0.20736	0.79264	0.21101	0.78903	1.0000
12	0.00036808	0.033871	0.0030897	0.020025	0.00013333	0.99592	161.99	0.00022627	0.00076805	0.22756	0.77244	0.23288	0.76721	1.0001
13	0.00031512	0.033846	0.0030836	0.020007	0.00011415	0.99500	138.68	0.00027771	0.00082101	0.25275	0.74725	0.26008	0.74000	1.0001
14	0.00026240	0.033813	0.0030756	0.019982	9.5052e-05	0.99378	115.48	0.00034639	0.00087373	0.28390	0.71610	0.29486	0.70523	1.0001
15	0.00020998	0.033763	0.0030636	0.019945	7.6064e-05	0.99191	92.411	0.00044917	0.00092615	0.32659	0.67341	0.34078	0.65932	1.0001
16	0.00015794	0.033684	0.0030447	0.019887	5.7214e-05	0.98899	69.508	0.00061112	0.00097819	0.38452	0.61548	0.40416	0.59591	1.0001
17	0.00010663	0.033538	0.0030094	0.019777	3.8630e-05	0.98349	46.928	0.00091625	0.0010295	0.47090	0.52910	0.49651	0.50357	1.0001
18	5.7211e-05	0.033168	0.0029231	0.019507	2.0729e-05	0.96993	25.178	0.0016689	0.0010789	0.60736	0.39264	0.63938	0.36074	1.0001
19	1.8958e-05	0.031592	0.0025734	0.018369	6.1477e-06	0.91282	7.4630	0.0048395	0.0011192	0.81218	0.18782	0.83942	0.16067	1.0001
20	1.1931e-05	0.030828	0.0024155	0.017829	4.3266e-06	0.88575	5.2508	0.0063421	0.0011242	0.84943	0.15057	0.87443	0.12567	1.0001
21	8.1903e-06	0.029830	0.0022199	0.017135	2.9711e-06	0.85094	3.6045	0.0082742	0.0011279	0.88003	0.11997	0.90299	0.097108	1.0001
22	5.5226e-06	0.028589	0.0019925	0.016287	2.0042e-06	0.80848	2.4304	0.010631	0.0011308	0.90388	0.096124	0.92522	0.074882	1.0001
23	3.6377e-06	0.027098	0.0017419	0.015291	1.3209e-06	0.75866	1.6009	0.013397	0.0011325	0.92205	0.077948	0.94251	0.057588	1.0001
24	2.3097e-06	0.025334	0.0014744	0.014141	8.3915e-07	0.70120	1.0165	0.016586	0.0011338	0.93601	0.063985	0.95618	0.043913	1.0001
25	1.3645e-06	0.023241	0.0011950	0.012815	4.9609e-07	0.63502	0.60051	0.020260	0.0011348	0.94696	0.053040	0.96764	0.032458	1.0001
26	6.8565e-07	0.020709	0.00090726	0.011262	2.4947e-07	0.55760	0.30175	0.024557	0.0011354	0.95581	0.044193	0.97833	0.021768	1.0001
27	1.9542e-07	0.017508	0.00061327	0.0093675	7.1172e-08	0.46336	0.086002	0.029789	0.0011359	0.96327	0.036733	0.99078	0.0093172	1.0001
28	0.0000	0.012942	0.00030988	0.0067811	0.0000	0.33498	0.0000	0.036915	0.0011361	0.97014	0.029858	1.0001	0.0000	1.0001
29	0.0000	0.0094297	0.00015503	0.0048699	0.0000	0.24034	0.0000	0.042168	0.0011361	0.97376	0.026236	1.0001	0.0000	1.0001
30	0.0000	0.0044054	3.1022e-05	0.0022337	0.0000	0.11009	0.0000	0.049398	0.0011361	0.97752	0.022482	1.0001	0.0000	1.0001